MODELING AND SIMULATION OF POPULATION BALANCES FOR PARTICULATE PROCESSES

Shamsul Qamar

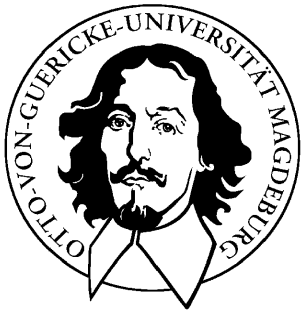

Faculty of Mathematics
Otto-von-Guericke University Magdeburg

Modeling and Simulation of Population Balances for Particulate Processes

HABILITATIONSSCHRIFT
zur Erlangung des akademischen Grades
doctor rerum naturalium habilitatus
(Dr. rer. nat. habil.)

genehmigt

durch die Fakultät für Mathematik
der Otto-von-Guericke Universität Magdeburg

von **Dr. rer. nat. Shamsul Qamar**
geb. am 12. März 1972 in Mardan, Pakistan

Gutachter:
Prof. Dr. Michael Junk
Prof. Dr. Gerald Warnecke
Prof. Dr. Kun Xu

Tag der Einreichung: 25. Juni 2007
Tag der Verteidigung: 31. Januar 2008

Abstract

This work focuses on the modeling and numerical approximations of population balance equations (PBEs) for the simulation of different phenomena occurring in process engineering. The population balance equation (PBE) is considered to be a statement of continuity. It tracks the change in particle size distribution as particles are born, die, grow or leave a given control volume. In the population balance models the one independent variable represents the time, the other(s) are *property coordinate(s)*, e.g., the particle volume (size) in the present case. They typically describe the temporal evolution of the number density functions and have been used to model various processes such as granulation, crystallization, polymerization, emulsion and cell dynamics.

The semi-discrete high resolution schemes are proposed for solving PBEs modeling one and two-dimensional batch crystallization models. The schemes are discrete in property coordinates but continuous in time. The resulting ordinary differential equations can be solved by any standard ODE solver. To improve the numerical accuracy of the schemes a moving mesh technique is introduced in both one and two-dimensional cases.

A model is derived for the batch preferential crystallization of enantiomers with fines dissolution unit. The model is further elaborated by considering the isothermal and non-isothermal conditions. In this model, the crystallization of the preferred enantiomers is assumed to take place in a single crystallizer with a fines dissolution loop. The model is further extended to a coupled batch preferential crystallization process with isothermal and non-isothermal conditions. In this setup, the crystallization of two enantiomers is assumed to take place in two separate crystallizers, coupled by their fines dissolution loops.

The finite volume scheme for one-component pure aggregation model is extended to two-component aggregation model. For this purpose the integro-ordinary differential equation for two-component aggregation is reformulated to a partial differential equation (PDE) coupled with integral equations. The resulting PDE is then solved by a semi-discrete finite volume scheme which also employs the geometric grid discretization technique. Analogous procedure is used for the numerical solution of one-component breakage problem.

The proposed numerical schemes are further investigated by solving PBEs with simultaneous nucleation, growth, aggregation and breakage processes. Two methods are proposed for this purpose. In the first method, a method of characteristics (MOC) is used for growth process while a finite volume scheme for aggregation and breakage processes. In the second method, a semi-discrete finite volume scheme (FVS) is used for all processes.

Various numerical test problems are considered for the underlying models. The numerical results are also validated against available analytical solutions.

Zusammenfassung

Diese Arbeit konzentriert sich auf die Modellierung sowie die numerische Approximation von Populationsbilanzmodellen (PBM), mit deren Hilfe verschiedene Phänomene in der Verfahrenstechnik simuliert werden können. Es behandelt die Änderung in der Größenverteilung gewisser Partikel unter Berücksichtigung von Quell- und Senktermen, Wachstumsansätzen sowie des Austritts aus einem Kontrollvolumen. In den PBM stellen die Zeit und die Partikeleigenschaften (Partikelvolumen oder Partikelgröße) die unabhängigen Variablen dar. Typischerweise beschreiben die PBM die zeitliche Evolution der Teilchenanzahldichte, die in vielen Bereichen der Verfahrenstechnik Anwendung findet. Hierzu zählen die Granulation, die Kristallisation, Polymerisation, Emulsion und die biologische Zellfermentation.

Wir stellen semidiskrete, hochauflösende finite Volumenschemata zur Lösung der PBM für die sogenannte Batch-Kristallisation vor, jeweils für Lösungen auf einem ein- bzw. zweidimensionalen Koordinatenraum. Die semidiskreten Schemata sind diskret in den Eigenschaftskoordinaten, aber kontinuierlich hinsichtlich der Zeit. Die resultierenden gewöhnlichen Differentialgleichungssysteme können dann mit einem gewöhnlichem DGL-Löser berechnet werden. Um die numerische Genauigkeit der Schemata zu erhöhen, haben wir im ein- und zweidimensionalen Fall Gitteradaptionstechniken angewandt.

Es wird ein Modell für die sog. bevorzugte Batch-Kristallisation zur Trennung von Enantiomeren mit Feinkornauflösung hergeleitet. Das Modell wird weiter ausgebaut unter Berücksichtigung isothermer und nichtisothermer Bedingungen. In diesem Modell wird angenommen, dass die Kristallisation von Enantiomeren in einem einzigen Kristallisator mit einem Kreislauf zur Entfernung von Feinkorn und Wiedereinspeisung der wässrigen Lösung stattfindet. Das Modell wird schließlich erweitert, um gekoppelte Kristallisatoren zu behandeln. Diese beiden Kristallisatoren sind nur über zwei Kreisläufe zur Entfernung von Feinkorn gekoppelt.

Das konservative finite Volumenschema für einkomponentige Aggregation wird auf das erweiterte Modell für zwei Komponenten erweitert. Zu diesem Zweck wird die gewöhnliche skalare Integro-Differentialgleichung für zwei Komponenten zu einer partiellen skalaren Erhaltungsgleichung umformuliert, die mit einer Integralgleichung gekoppelt ist. Diese Erhaltungsgleichung wird mit einem semidiskreten finiten Volumenschema gelöst, das auch die geometrische Gitterverfeinerung verwendet. Eine analoges Verfahren wird auch für einkomponentige Zerteilungsvorgänge benutzt.

Die vorgeschlagenen numerischen Schemata sind weiter ausgebaut worden für die gleichzeitige Behandlung von Keimbildung, Wachstum, Aggregation und Zerteilungsvorgängen. Zu diesem Zweck werden zwei Methoden vorgeschlagen: Zum einen ein Charakteristikenverfahren zur numerischen Lösung von Wachstumsprozessen, und zum anderen eine finite

Volumenmethode für Aggregation und Zerteilung. Die zweite semidiskrete Methode ist überdies für alle oben genannten Verfahrensprozesse anwendbar.

Für die zugrungeliegenden Modelle werden verschiedene numerische Testprobleme entwickelt. Hierbei werden die numerischen Ergebnisse mittels bekannter Vergleichslösungen bestätigt.

Acknowledgements

First and foremost, I am highly indebted to my group leader Prof. Gerald Warnecke for giving me an opportunity to pursue postdoctoral studies after completing my Ph.D. studies in his supervision. His invaluable guidance and kind behavior encouraged me to accomplish this research work in a novel and industry related field with a dynamic, multi-cultural and multinational research group. His constant encouragement, technical discussions and advice have helped me immensely to improve my research capabilities and to finish the current postdoctoral thesis in an adequate time.

I am grateful to Prof. Andreas Seidel-Morgenstern for his useful technical discussions and invaluable suggestions. I am also thankful to him for giving me opportunity to collaborate with his research group at the Max-Planck Institute for Dynamic Complex Technical Systems Magdeburg. His advice and constructive criticism was the driving force towards the successful completion of current research work.

I would like to thank Dr. Martin Peter Elsner and Ivan Angelov of the Max-Plank Institute Magdeburg, who spared lot of their precious time for discussion and helped me during our common research work. Their valuable remarks and suggestions enabled me to learn a lot about crystallization process.

I express my deep gratitude to Priv.-Doz. Dr. Matthias Kunik for his kind behavior, invaluable suggestions and guidance. His expertise in analysis have helped me a lot in the research work and to improve my knowledge in this area.

I had a wonderful time with our professors, colleagues and students at the Institute for Analysis and Numerics. Thanks to Prof. Tobiska and Prof. Grunau for their cooperation and support. I am also thankful to my Pakistani friends Ayaz Farooq and Mohammad Zahid Iqbal for their encouragement and help on several occasions.

I am thankful to the reviewers Prof. Michael Junk of the University of Konstanz Germany and Prof. Kun Xu of the Hong Kong University of Science and Technology for their great interest and useful remarks.

I am grateful to my family back home in Pakistan, especially my father Gul-Bad-Shah, for their ambitions for me to get higher education. They always encouraged and supported me, no matter how far we are from each other.

Finally, special thanks to my wife Dr. Qurrat-ul-Ain for her support and extreme desire to complete this degree. She has given me spare time to complete this thesis by taking care of our children Asim, Hammad and Faryal. This work was unthinkable without her support.

Contents

Chapter 1

Introduction

1.1 Overview

Population balance models (PBMs) are encountered in several scientific and engineering disciplines. They can be used to describe the time evolution of one or more property distributions of individuals population. In 1964, they were introduced in the field of chemical engineering by Hulburt and Katz [35] as well as Randolph and Larson [102]. In the late seventies they were reviewed by Ramkrishna [99]. However, their applications were limited due to a lack of computational power. Since high speed computers are available now, they became popular which is reflected by their use in several areas of chemical and biochemical engineering. They are used to study precipitation, polymerization, crystallization, food processes, pharmaceutical manufacture, pollutant formation in flames, particle size distribution (PSD) of crushed material and rain drops, dispersed phase distributions in multiphase flows, and growth of microbial and cell populations.

Population balance equations (PBEs) are similar to our well known mass and energy balance equations. They describe a balance law for the number of individuals of a population, such as crystals, droplets, bacteria etc. What makes PBEs more interesting than the mass balance equations are several phenomena which are responsible for the change in population of the individuals. In addition to the inflow and outflow of particles from a given control volume which is induced by fluid flow, there are several other mechanisms which are responsible for the change of particles population in the same control volume. New particles may be born from a given supersaturated solution. This process increases the population of small particles. Similarly, a particle of smaller size may grow to form a bigger particle and a bigger one may dissolve a bit to make particle of sizes we are considering. Clearly, particles of a given size can also be formed when bigger ones break and smaller ones aggregate to form exactly the size we are looking for.

Due to the above mentioned phenomena the description of the dynamic behavior of the particulate processes essentially involves specifying the temporal change of the particle

property distribution. This distribution is a part of the system state. Hence, particulate processes are inherently distributed parameter systems. Population balance models are usually used to model this class of systems.

In the framework of PBEs, the state of an individual particle is represented by a particle state vector containing *external* coordinates, such as position of a particle in physical space, and *internal* coordinates representing the particle properties, such as particle size, volume etc. If $\mathbf{x}_e$ represents the external and $\mathbf{x}_i$ the internal coordinates, then the particle state vector $\mathbf{x}$ is given by $\mathbf{x} = (\mathbf{x}_e, \mathbf{x}_i)$. A population of particles is characterized by its particle property distribution, which is described mathematically by a *number density function* $f(t, \mathbf{x})$ and is a function of time t and the state vector $\mathbf{x}$. This function represents the (average) number of particles per volume of particle state space. It is understood that this deterministic approach is only reasonable if large populations are considered. It is further assumed that the number density function is sufficiently smooth to be differentiated with respect to its arguments. The actual number of particles in a certain area of the particle state space is determined by the integral of the number density function over this area.

The temporal change of the number density function is described by the *population balance equation* (PBE), which is a partial differential equation (PDE). It describes the change due to continuous *transport* of particles in the state space, e.g. by particle growth, as well as the effect of *birth* and *death* events such as nucleation, breakage or aggregation. The last two processes represent *nonlocal* effects: a particle of certain size breaking into two parts causes two particles to be formed at distant points in particle state space. These phenomena distinguish systems described by population balance equations from spatially distributed systems. From mathematical point of view these effects may lead to integral terms in the partial differential equation, i.e. leads to a partial integro-differential equation. The form of the population balance equation (PBE) is as follows

$$\frac{\partial f(t,\mathbf{x})}{\partial t} + \nabla \cdot (\mathbf{v} f)(t,\mathbf{x}) = \mathcal{B}(\mathbf{x},t) - \mathcal{D}(\mathbf{x},t)\,, \tag{1.1}$$

where the velocity $\mathbf{v}$ is given by

$$\mathbf{v} = \frac{d\mathbf{x}}{dt}\,. \tag{1.2}$$

Here the velocity components related to the external coordinates are the conventional velocity components, while those related to the internal coordinates describe for example, the rate of change of size, or moisture content. In equation (1.1) the terms $\mathcal{B}$ and $\mathcal{D}$ represent the birth and death terms, respectively.

Apart from particle-particle interactions the dispersed phase usually also interacts with its environment, e.g. the continuous liquid phase in crystallization. The state of the continuous phase may influence the rate of growth, birth and death processes and thus affects the particle population. In the other direction, the dispersed particle phase generally affects the

continuous phase, e.g. by mass transfer from liquid to solid due to growth in crystallization or by heat transfer due to the heat transfer of crystallization. Therefore, in general a model for a particulate system consists of a population balance equation, which describes the dispersed phase, coupled with a mass (or mole) balance and an energy balance, which represents the continuous phase. A typical disperse two-phase system is shown in Figure 1.1 taken from Motz et al. [77].

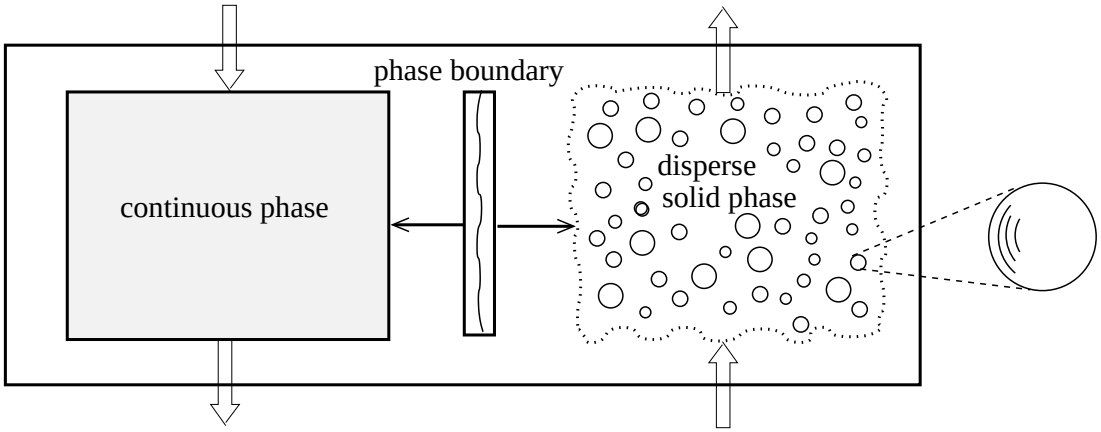

Figure 1.1: Schematic representation of a disperse two phase system.

1.2 Problem and Motivation

In population dynamics the behavior of the individuals of a population, such as crystals, droplets, bacteria etc., are investigated. As described above the birth and death terms are frequently integral functions of the whole population. Therefore, PBEs are generally partial integro-differential equations of hyperbolic or parabolic type. Since analytical solution are available only for limited number of simplified cases, numerical schemes are usually needed. Many studies are therefore focused on the development of accurate and efficient numerical solutions of the population balance equations.

In practical engineering processes, the population density function may extend over orders of magnitudes and the distribution can be very sharp. Hence, the accurate numerical simulation of the population density functions can be challenging for a numerical scheme. This fact motivated several researchers in this field, to develop specialized algorithms for solving PBEs, see for example Ramkrishna [100, 101], Nicmanis and Hounslow [80], and references therein. As a result, several numerical methods were developed which can be roughly divided into five main classes such as method of moments, method of characteristics, method of weight residuals/orthogonal collocation, the Monte Carlo method, and finite difference schemes/discrete population balances.

In the method of moments, instead of the distribution function one calculates its moments, see Marchisio and Fox [71], Barrett and Jheeta [7], Madras and McCoy [67], as well as Vollmer [121]. Under certain conditions, the moment equations are closed, that is, the differential equations for the lower order moments do not depend on the values for high-order moments. This results in small number of ordinary differential equations (ODEs) which can be solved by any high order ODE solver. However, for more complex systems this moments closure condition is violated. The method of characteristics, see Kumar and Ramkrishna [49], solve the population balance equation by finding curves in the $x-t$ plane that reduce the population balance equation to an ODEs. The method is highly efficient when the physics is simple, however the approach does not generalize to more complex systems. The method of weighted residuals, Sing and Ramkrishna [109], approximates the distribution by linear combination of basis functions. This also results in a system of ordinary differential equations (ODEs) which can be solved by one of the available ODE solvers. In this method the basis functions must be carefully tuned to each specific system, if a small number of ODEs is required. Monte Carlo methods track the histories of each individual particle, see Shah et al. [106], Maisels et al. [68], Song and Qiu [111]. The method is computationally suitable for stochastic population balance models, especially for complex systems, see Ramkrishna [100]. However, the method is computationally expensive and of lower order.

In the method of finite differences/discretized population balances, the population balance equation is approximated by a finite difference scheme, see Kumar and Ramkrishna [47]. Numerous discretizations of the PBE with different orders of accuracy have been investigated and applied to various particulate processes, see for example David et al. [15], Gelbard et al. [26], Hounslow [31], Hounslow et al. [33], Kumar and Ramkrishna [49], Litster et al. [62], Marchal et al. [70], as well as Muhr et al. [78]. The method in [47] was recently improved by Kumar et al. [45, 46].

Apart from above methods a commercial software, named PARSIVAL, based on the adaptive hp-Galerkin approach was introduced by Wulkow et al. [122]. This software is user friendly and is able to solve several processes. However, being a black box solver for the user it is difficult to make changes in the software according to the user interest.

The Finite volume schemes, which were originally developed for the gas dynamics, were also applied for the numerical solution of PBEs, see Gunawan et al. [28], Lim et al. [61], Ma et al. [65, 66] and Motz et al. [77]. These schemes have already been used for the numerical solution of hyperbolic systems which arise in astrophysical flows, gas dynamics, detonation waves and multi-phase fluid flows, see [11, 12, 37, 50, 58, 79, 117] and references therein. Further, we have also used finite volume schemes for different hyperbolic systems, see Ain et al. [2], Dreyer and Qamar [16, 17], and Qamar et al. [85]-[88]. These schemes give high order accuracy on coarse grid and resolve sharp discontinuities to avoid numerical diffusion and numerical dispersion which leads to unphysical oscillations. Since these schemes are developed for general purposes, they can be applied to any particular problem

without knowing the details of its physical character. Furthermore, Filbet and Laurençot [23] have proposed a finite volume scheme for single-component aggregation. These authors used a conservation law form of the population balance equation, see e.g. Makino et al. [69] and Smit el al. [110], for aggregation problems which can be readily solved by a finite volume scheme. This special reformulation was a great achievement which enables one to apply the finite volume scheme in the aggregation case as well. The formulation was later extended to breakage process by Kumar [44].

Most of the above existing numerical methods were derived for a particular particulate process. These methods are either less accurate or have inconsistency problem with the moments. Moreover, some methods are not efficient because of their way of formulation. They can not be effectively applied to solve combined processes and multidimensional PBEs. Hence, the motivation of this work is to find an accurate, easily implementing, and computationally efficient numerical schemes for solving PBEs which can effectively model all particulate processes simultaneously. Most of the physical problems are naturally multidimensional, hence the schemes must be easily extendable to the multidimensional problems. We are also interested to study the stability and consistency of the proposed schemes and to study the existence and uniqueness of the solution for simplified models. Additionally, our objectives are to further improve the numerical accuracy and reduce the overall computational time of the schemes by investigating regular, irregular and adaptive meshes in one and two-dimensional cases.

The separation of chiral compounds is of large interest because most of the (bio-)organic molecules are chiral and usually only one of the enantiomers exhibits the desired properties with regards to therapeutic activities or metabolism, whereas the other enantiomer may be inactive or may even cause some undesired effects. The preferential crystallization is an effective and alternative technology for the production of pure enantiomers and has got considerable academic attention in recent years with emphasis on its chemistry and on its application to separate special chiral systems, see [4, 19]. Hence, the motivation of this work is to derive suitable preferential crystallization models for enantiomers with and without fines dissolution. Further objective is to elaborate the model by considering isothermal and non-isothermal conditions. Finally, the aim is to solve the resultant models with our proposed numerical schemes and to analyze their numerical accuracy and errors in the mass balances.

1.3 New Results

This work focuses on the numerical approximations and modeling of population balance equations (PBEs) for the simulation of different processes in chemical engineering. Semi-discrete high resolution finite volume schemes [40, 57, 58] and a method of characteristics (MOC) [49, 61] are proposed for the numerical solutions of the resulting models. In this study nucleation, growth, aggregation and breakage phenomena are considered.

The one and two-dimensional batch crystallization models are investigated here. In crystallization process the crystal size is the most important property variable. The dynamics of crystallization plants can only be understood with crystal size distribution (CSD) which highly influence the product quality and processability. For modeling crystallization process, it is therefore important to use a PBM in terms of the number density which uses size (length) as internal property variable. In case of one-dimensional batch crystallization model we also study the local existence and uniqueness of the solution. With the help of inverse Laplace transformation, we derive a new method which can be used to solve the given Batch crystallization model. Moreover, the semi-discrete high resolution schemes are proposed for the numerical solutions of the resulting one and two-dimensional batch crystallization models. The nucleation and growth processes are considered in this study while aggregation and breakage processes are neglected. The schemes are discrete in property coordinates but continuous in time. The resulting ordinary differential equations can be solved by any standard ODE solver. In this work an adaptive RK45 method is used, which is an embedded Runge-Kutta method of order four and five. In case of one-dimensional schemes we also discuss the issue of positivity (monotonicity), consistency, stability and convergence.

To improve the numerical accuracy further the high resolution schemes can be easily combined with an adaptive mesh refinement technique. Adaptive mesh refinement methods are important in a variety of physical and engineering areas such as fluid dynamics, combustion, heat transfer, material science, and so on. For solving multidimensional PBEs, development of effective and robust adaptive grid methods becomes necessary because uniform grids can be very expensive and may result in loss of accuracy. The resulting numerical solutions may be far away from the real physical phenomena. Successful implementation of the adaptive grid strategy can increase the accuracy of the numerical approximations and can also decrease the overall computational cost. In the past two decades, several moving mesh methods have been proposed for partial differential equations, see [114, 115] and references therein. In this thesis a moving mesh technique of H. Tang and T. Tang [114] is considered in the case of one and two-dimensional PBEs which model batch crystallization processes. The current moving mesh technique is independent of the numerical scheme, hence can be applied to any numerical scheme.

In the present work, a model is derived for batch preferential crystallization of enantiomers with fines dissolution unit. The model is further elaborated by considering the isothermal and non-isothermal conditions. In this model, the crystallization of the preferred enantiomers is assumed to take place in a single crystallizer with a fines dissolution loop. The extracted solution is screened by filters and assumed to be free of larger crystals. Therefore, only small particles are withdrawn to the fines dissolution loop. In order to assure a crystal-free liquid exchange, the withdrawn liquid in the fines dissolution loop is heated, so that the liquid becomes undersaturated and the withdrawn small particles dissolve. Before re-entering into the crystallizer, this liquid is assumed to be cooled again. The attrition,

breakage and agglomeration processes are not considered in this study. Shortly, we also discuss the local existence and uniqueness of the solution for the model without fines dissolution. The model has been further extended for a coupled batch preferential crystallization process with isothermal and non-isothermal conditions. In this setup, the crystallization of two enantiomers is assumed to take place in two separate crystallizers, coupled by their fines dissolution loops. There are two main advantages of considering two coupled crystallizers which are interconnected by two fines dissolution units. The first one is that one gets both enantiomers at the same time in separate crystallizers. Secondly, because of the fines dissolution, the amount of small particles reduces which further enhances the particle growth. Both high resolution schemes and the method of characteristics are implemented for solving the models under consideration. These methods are used for the first time to model such processes.

In this thesis we have also extended the conservative finite volume scheme for one-component pure aggregation [23] to two-component aggregation problems. For this purpose the integro-ordinary differential equation for two-component aggregation process is reformulated to a partial differential equation (PDE) which is coupled with integral equations. The resulting PDE is then solved by a semi-discrete finite volume scheme which also employs the geometric grid discretization technique [31, 33, 34] for internal property variables. In case of reformulated PBE, our numerical method calculates the volume (mass) density instead of the number density. However, one can easily recover back the number density at the end of simulation. The semi-discrete formulation enables one to use any standard adaptive ODE solver. Moreover, the use of a geometric grid discretization shows the efficient application of the finite volume scheme for this specific problem. It proves the versatility, generality and effectiveness of finite volume scheme as well as their ability to accommodate the special techniques which were only introduced for the specific methods used for aggregation process. The current extended finite volume scheme for two-component aggregation uses the basic ideas of the finite volume scheme for one-component aggregation derived in [23]. Therefore, for the reader's convenience the finite-volume scheme for one-component aggregation is also presented with a slight modification as compared to that in [23]. Even though the scheme in [23] is derived for an arbitrary grid, the authors have used a uniform grid in their numerical test problems. We have used geometric grids in our numerical test problems. Additionally, the scheme in [23] is derived in fully discrete form, whereas we have presented the scheme in semi-discrete formulation. The semi-discrete formulation enables one to use an adaptive ODE-solver. A similar procedure is also used to solve pure one-component breakage process with the finite volume scheme. Once again a reformulated PBE is used. We also discuss consistency, stability and convergence of the scheme for both one-component aggregation and breakage problems.

The proposed numerical schemes are further investigated by solving population balance equations with simultaneous nucleation, growth, aggregation and breakage processes. For that purpose once again a reformulated PBE is used where numerical methods calculate the volume (mass) density instead of the number density. However, as stated above one can

easily recover the discrete values of the number density at the end of the simulation. Two methods are proposed for this purpose. In the first method, a method of characteristics (MOC) is used for growth process [49] while a finite volume scheme for aggregation and breakage processes [23, 44] is considered. In the second method, semi-discrete finite volume schemes (FVS) are used for all processes. Note that, in both methods the aggregation and breakage kinetics are solved with the same finite volume formulations. Various combinations of nucleation, growth, aggregation and breakage processes for different choices of nucleation, growth, aggregation and breakage rates are considered. A geometric grid discretization technique has been used in all test problems presented here. The main difference in both methods is the way they calculate the growth term, for example in the MOC the mesh is moved with the characteristic speed, whereby the linear advection is treated exactly. However, the second method uses a finite volume scheme to discretize the advection term. The efficiency and accuracy of the resulting methods are analyzed by comparing their numerical results with each other and with available analytical solutions. For handling the nucleation term in the first scheme, the MOC is combined with a procedure of adding a cell of nuclei size at each time level. The same procedure was also used in [49]. A standard ODE solver can be used to solve the resultant ODEs. There are two main differences between the first method and the one used in [47, 49]. In our current method the aggregation and breakage terms are treated with a finite volume scheme, while in [47, 49] the authors have used the fixed pivot technique for this purpose. Secondly, our numerical method uses a reformulated PBE instead of the original one. This reformulation is necessary in order to apply the finite volume schemes.

1.4 Outline of the Thesis

The contents of the thesis are organized as follows:

In Chapter 2, we present the mathematical formulation of a general population balance model (PBM) for modeling different particulate and dispersed phase processes. Further, we introduce reduced models for pure aggregation, pure breakage, growth and nucleation, as well as simultaneous nucleation, growth, aggregation and breakage processes. Finally a PBM in term of the length property coordinate is introduced. All the models, except the reduced PBM for growth and nucleation processes, are reformulated in order to implement finite volume schemes for their numerical solutions in the following chapters. In reformulated models the volume density instead of the number density is the basic unknown. However, we apply the finite volume schemes directly to the reduced PBMs modeling growth and nucleation processes without any reformulation.

Chapter 3 is concerned with batch crystallization processes. After explaining the fundamentals of crystallization and batch crystallization, we give the one-dimensional batch crystallization model. Then we discuss the local existence and uniqueness of the solution of this model. For this purpose Fourier transformation of the number density is used as

a basic tool. With the help of inverse Laplace transformation, we derive a new method which can be used to solve the given Batch crystallization model. Afterwards, we give the two-dimensional batch crystallization model. For the numerical solutions of resulting models, the one and two-dimensional semi-discrete high resolution schemes of Koren [40] and the one by LeVeque [58] are derived here. Note that in [58] the last scheme is presented in fully discrete form which we have modified to a semi-discrete formulation. We also discuss the issue of positivity (monotonicity), consistency, stability and convergence of the high resolution scheme of Koren. In order to improve the accuracy of the proposed high resolution schemes, a moving mesh technique of H. Tang and T. Tang [114] is introduced. Finally, we give several one and two-dimensional test problems. The results of the proposed schemes are compared with each other and with available analytical solutions.

Chapter 4 introduces preferential batch crystallization for enantiomers. We give a brief introduction of enantiomers, preferential crystallization process and ternary phase diagram. A model for the simulation of preferential crystallization in a single crystallizer with and without fines dissolution is derived. The model is further elaborated by considering isothermal and non-isothermal conditions. We also discuss the existence and uniqueness of the solution for the model without fines dissolution. Afterwards, we extend the model to a coupled batch preferential crystallization process. For both models the same high resolution schemes discussed in Chapter 3 are used. Apart from these schemes, we also introduce the method of characteristics for the numerical solutions of current models. Finally, we give several test problems for the preferential batch crystallization processes. The numerical results of the proposed schemes are compared with each other. Furthermore, numerical errors in mass balances and CPU time for the proposed schemes are also presented.

In Chapter 5 a conservative finite volume approach, originally proposed by Filbet and Laurençot [23] for the one-dimensional aggregation, is extended to simulate two-component aggregation process. We start with the introduction of a population balance equation for pure two component aggregation processes and provide a brief overview of the previous methods derived for the numerical solutions of one and two-component aggregation problems. We derive the finite volume scheme for the numerical approximation of one component aggregation model. Afterwards, the scheme is extended to two-component aggregation process. We also consider pure one-component breakage problem and derive a finite volume for the numerical simulation of this model. We also study the consistency, stability and convergence of the numerical scheme for both one-component aggregation and breakage processes. Finally, several numerical test problems for the one and two-component aggregation processes as well as one-component breakage process are considered. The numerical results of the schemes for different aggregation and breakage kernels as well as different initial distributions are compared with the available analytical solutions.

Chapter 6 focuses on the numerical solutions of population balance models (PBMs) for simultaneous processes. We also give a short overview of the previous method used for the simulation of simultaneous processes. Two numerical methods are proposed here. The

first method combines the method of characteristics (MOC) for the growth process with a finite volume scheme (FVS) for aggregation and breakage processes. For handling nucleation terms, a cell of nuclei size is added at a given time level. The second method purely uses the semi-discrete finite volume scheme for all processes. The proposed techniques are tested for different combinations of processes. Especially those combinations are considered for which analytical solutions are available. The numerical results of both schemes are compared with each other with the available analytical solutions. Chapter 7 concludes the thesis and describes the potential areas of future research work.

Most of the contents of this thesis are already accepted/published in research Journals.

Chapter 3 appeared as

1. Qamar, S., Elsner, M. P., Angelov, I., Warnecke, G., Seidel-Morgenstern, A., A comparative study of high resolution schemes for solving population balances in crystallization, *Comp. & Chem. Eng.*, **30**, (2006), 1119-1131.

2. Qamar, S., Ashfaq, A., Elsner, M. P., Angelov, I., Warnecke, G., Seidel-Morgenstern, A., Adaptive high resolution schemes for multidimensional population balances in crystallization processes, *Comp. & Chem. Eng.*, **31**, (2007), 1296-1311.

3. Qamar, S., Warnecke, G., Analytical and numerical investigations of a batch crystallization model, accepted in *Comp. Appl. Math.*, doi:10.1016/j.cam.2007.12.012, (2008).

Chapter 4 contains

4. Qamar, S., Angelov, I., Elsner, M. P., Ashfaq, A., Seidel-Morgenstern, A., Warnecke, G., Numerical approximations of a population balance model for coupled batch preferential crystallizers, accepted in the special issue of *Appl. Num. Math.*, (2007).

5. Qamar, S., Ashfaq, A., Angelov, I., Elsner, M. P., Warnecke, G., Seidel-Morgenstern, A., Numerical solutions of population balance models in preferential crystallization, *Chem. Eng. Sci.*, **63**, (2008), 1342-1352.

Parts of Chapter 5 appeared as

6. Qamar, S., Warnecke, G., Solving population balance equations for two-component aggregation by a finite volume scheme, *Chem. Eng. Sci.*, **62**, (2007), 679-693.

Chapter 6 contains the articles

7. Qamar, S., Warnecke, G., Numerical solution of population balance equations for nucleation growth and aggregation processes, *Comp. & Chem. Eng.*, **31**, (2007), 1576-1589.

8. Qamar, S., Warnecke, G., Elsner, M. P., Numerical simulation of population balances for combined particulate processes, submitted for publication, (2007).

Chapter 2

Population Balances

This chapter briefly introduces the mathematical models for different particulate processes. In particular, growth, nucleation, aggregation and breakage processes are considered here. The models are then reformulated in order to implement finite volume schemes in the coming chapters.

2.1 The Population Balance Model

In this study an ideally mixed system is considered where all particles are well mixed throughout the external coordinate region. Hence, the population balance equation (1.1) may be integrated over all points in space. The resulting PBE describes the dynamics of the volume distribution function $f := f(t,x) \geq 0$ of particles of volume $x > 0$ at time $t \geq 0$. A general one-dimensional PBE for a well mixed system is given as [31, 84]

$$\begin{aligned}\frac{\partial f(t,x)}{\partial t} =& \dot{\mathcal{Q}}_{\text{in}}(t,x) - \dot{\mathcal{Q}}_{\text{out}}(t,x) - \frac{\partial[G(t,x)f(t,x)]}{\partial x} \\ &+ \mathcal{Q}^{+}_{\text{nuc}}(t,x) - \mathcal{Q}^{-}_{\text{dis}}(t,x) + \mathcal{Q}^{\pm}_{\text{agg}}(t,x) + \mathcal{Q}^{\pm}_{\text{break}}(t,x)\,, \quad (t,x) \in \mathbb{R}^2_+\,, \end{aligned} \tag{2.1}$$

where $\mathbb{R}_+ :=]0, +\infty[$. The terms will be specified as we go along. The above equation must be supplemented with appropriate initial and boundary conditions. Here $\mathcal{Q}^{\pm}_{\beta}(t,x) := \mathcal{B}_{\beta}(t,x) - \mathcal{D}_{\beta}(t,x)$ with $\beta \in \{\text{agg}, \text{break}\}$ and the letters $\mathcal{B}_{\beta}$ and $\mathcal{D}_{\beta}$ represent the birth and death of particles during a process, respectively. The first two terms $\dot{\mathcal{Q}}_{\text{in}}(t,x)$ and $\dot{\mathcal{Q}}_{\text{out}}(t,x)$ on the right hand side represent the inflow to a and outflow from a given system respectively. The third term is responsible for the particles growth with growth rate $G(t,x)$. The terms nuc, diss, agg, break are abbreviated for nucleation, dissolution, aggregation and breakage respectively.

The inflow and outflow from the system are defined as

$$\dot{\mathcal{Q}}_{\text{in}}(t,x) = \frac{\dot{V}_{\text{in}}}{V} f_{\text{in}}(t,x)\,, \qquad \dot{\mathcal{Q}}_{\text{in}}(t,x) = \frac{\dot{V}_{\text{out}}}{V} f_{\text{out}}(t,x)\,. \tag{2.2}$$

The symbols $\dot{V}_{\text{in}}$ and $\dot{V}_{\text{out}}$ denote the volumetric inlet and outlet flow rates from the system of volume V. Here f_{in} and f_{out} are the number densities of inflow and outflow particles.

Particles (for example crystals) are not stable below a certain volume, usually called critical volume (size). Small particles with negative growth rate will finally become smaller than the critical volume and, hence, disappear from the population. This phenomena is described as

$$\mathcal{Q}^{-}_{\text{dis}}(t,x) = \mathcal{D}_{\text{dis}}\, f(t,x)\,, \tag{2.3}$$

where $\mathcal{D}_{\text{dis}}$ represents the dissolution rate. If the particles are assumed to disappear immediately when reaching the critical size, the dissolution rate has to be infinite.

Generally, batch process has no net inflow or outflow of particles therefore the first two terms on the right hand side of equation (2.1) does not appear in the batch process. In this work we will only deal with the batch processes.

The jth moment $M_j(t)$ of the number density is defined as

$$M_j(t) = \int_0^\infty x^j f(t,x)\, dx\,, \tag{2.4}$$

where the zeroth moment $M_0(t)$ and the first moment $M_1(t)$ represent the total number of particles and the total volume (mass) of particles, respectively.

In the following, we give a brief description of different particulate processes and give their corresponding population balance models. In the coming chapters, these models will be used to simulate different particulate and dispersed phase processes.

2.2 Pure Aggregation Process

The Smoluchowski aggregation equation provides a mean field description of a variety of aggregation phenomena. The underlying phenomenon is the merging of two particles into a single one. A graphical representation of aggregation process is given in Figure 2.1. In case of single-component aggregation process, where each particle is fully identified by its volume, it is given as [35, 99]

$$\frac{\partial f(t,x)}{\partial t} = \mathcal{Q}^{\pm}_{\text{agg}}(t,x)\,, \quad (t,x) \in \mathbb{R}^2_+\,, \tag{2.5}$$

$$f(0,x) = f_0(x)\,, \quad x \in \mathbb{R}_+\,. \tag{2.6}$$

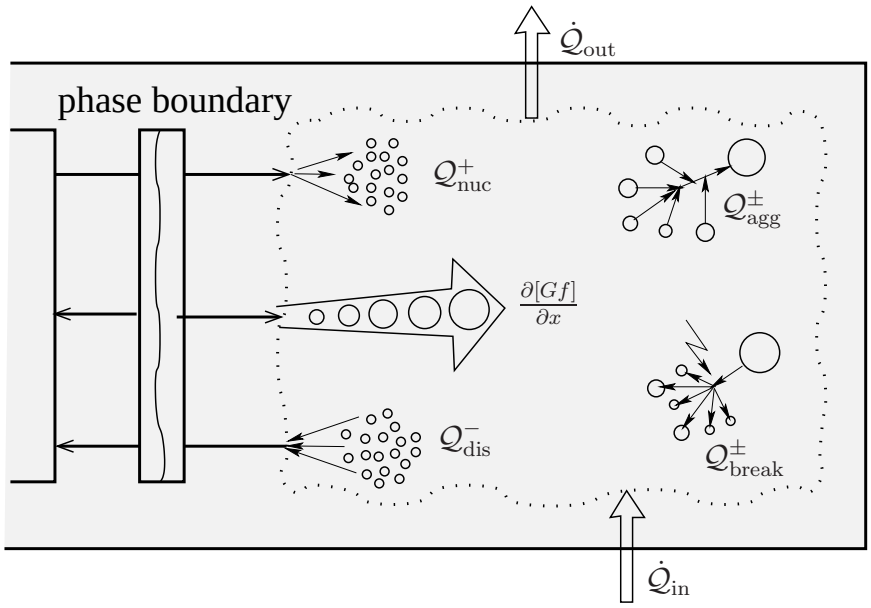

Figure 2.1: A schematic representation of different particulate processes, see [77].

Here $f : \mathbb{R}_{\geq 0} \times \mathbb{R}_{+} \to \mathbb{R}_{\geq 0}$ and $\mathbb{R}_{\geq 0} := [0, +\infty[$. The aggregation reaction term $\mathcal{Q}^{\pm}_{\text{agg}}(t, x)$ is given by

$$\begin{aligned}\mathcal{Q}^{\pm}_{\text{agg}}(t,x) =& \frac{1}{2}\int_0^x \beta(t, x-x', x')\, f(t, x-x')\, f(t, x')\, dx' \\ &- \int_0^\infty \beta(t, x, x')\, f(t, x)\, f(t, x')\, dx' \,. \end{aligned} \tag{2.7}$$

The first integral in $\mathcal{Q}^{\pm}_{\text{agg}}(t, x)$ represents the birth of the particles of volume x resulting from merging of two particles with respective volume x' and $x - x'$, where $x' \in]0, x[$. The second integral in $\mathcal{Q}^{\pm}_{\text{agg}}(t, x)$, also called death term, describes the loss of particles of volumes x by aggregation with other particles of any size. The aggregation coefficient $\beta = \beta(t, x, x')$ is the rate at which the aggregation of two particles with respective volumes x and x' produces a particle of volume $x+x'$. It also represent the properties of the physical medium and is a nonnegative symmetric function,

$$0 \leq \beta(t, x, x') = \beta(t, x', x)\,, \quad (x, x') \in \mathbb{R}^2_{+}\,.$$

Basically it is the probability for such particles to meet and stick together.

Note that, during each aggregation event, the total volume of particles remains conserved while the number of particles decreases. Hence, it can be easily shown that during aggregation process M_0 is a non-increasing function of time. However, for some aggregation kernels β where the frequency of aggregation increases with particle size, the total volume

M_1 may not remain constant throughout simulation time [21, 60]. In this case new forming particles aggregates at faster rate than their parents. As aggregation proceeds, the size of aggregates increases and hence they merge together faster. A runaway growth then takes place, producing particles with *infinite* volume in finite time which are removed from the system. Consequently, M_1 starts to decrease, a phenomenon usually called gelation. It describes a phase change.

The aggregation of liquid droplets is called coagulation. During this process the original droplets become an indistinguishable part of the newly formed droplets, see Gerstlaur [27]. However, in solid particle aggregation or agglomeration the original particles stay intact.

The phenomenon of aggregation appears in a wide range of applications, for example in physics (aggregation of colloidal particles), meteorology (merging of drops in atmospheric clouds, aerosol transport, minerals), chemistry (reacting polymers, soot formation, pharmaceutical industries, fertilizers).

In the literature several numerical methods are available for solving one-component aggregation problems. Among them are the Monte Carlo methods [101], the methods of classes [46, 47, 49, 101, 120], the quadrature method of moments [13, 71, 73], and the method of weighted residuals [101, 122]. In most of these methods instead of regular grids the geometric grids were used, see Hounslow et al. [31, 33, 34] and references therein.

Apart from these methods, Filbet and Laurençot [23] proposed a numerical scheme which is based on a conservative finite volume formulation. To apply the finite volume formulation one can rewrite (2.5) and (2.7) in the form [23]

$$x\frac{\partial f(t,x)}{\partial t} = -\frac{\partial \tilde{\mathcal{F}}_{\text{agg}}(t,x)}{\partial x}\,, \quad (t,x) \in \mathbb{R}^2_+\,, \tag{2.8}$$

where the volume flux is given as

$$\tilde{\mathcal{F}}_{\text{agg}}(t,x) = \int_0^x \int_{x-u}^{\infty} u\,\beta(t,u,v)\,f(t,u)\,f(t,v)\,dvdu\,. \tag{2.9}$$

In Appendix A.1 it is shown that equations (2.5) and (2.7) are equivalent with (2.8) and (2.9). The equations (2.8) and (2.9) can be easily used to apply a finite volume scheme. A brief overview of the finite volume scheme for the current one-component aggregation process is given in Chapter 5. We have also extended the numerical scheme for one-component aggregation problems to two-component aggregation problems in that chapter.

2.3 Pure Breakage Process

Breakage is a process by which particles of bigger sizes break into two or more fragments. The total number of particles in a breakage process increases while the total volume (mass)

remains conserved. A graphical representation of the breakage is shown in Figure 2.1.

Population balances for breakage are widely known in high shear granulation, crystallization, atmospheric science and many other particle related engineering problems. The general form of population balance equation for breakage process is given as [124]

$$\frac{\partial f(t,x)}{\partial t} = \mathcal{Q}^{\pm}_{\text{break}}(t,x)\,, \quad (t,x) \in \mathbb{R}^2_+\,, \tag{2.10}$$

$$f(0,x) = f_0(x)\,, \quad x \in \mathbb{R}_+\,. \tag{2.11}$$

Here, the breakage term $\mathcal{Q}^{\pm}_{\text{break}}(t,x)$ is given by

$$\mathcal{Q}^{\pm}_{\text{break}}(t,x) = \int_x^{\infty} b(t,x,x')\,S(x')\,f(t,x')\,dx' - S(x)\,f(t,x)\,. \tag{2.12}$$

The breakage function $b(t,x,x')$ is the probability density function for the formation of particles of size x from particle of size x'. The selection function $S(x')$ describes the rate at which particles are selected to break. The breakage function has the following properties

$$\int_0^x b(t,x,x')\,dx' = \tilde{N}(x) \quad \text{and} \quad \int_0^x y'\,b(t,y',x)\,dy' = x\,, \tag{2.13}$$

where the function $\tilde{N}(x)$ represents the number of fragments obtained from the breakage of a particle of volume x.

The analytical solutions of PBE (2.10) are only possible for very simple breakage and selection functions, see [10, 123, 124]. Therefore numerical solution techniques are usually needed. Several numerical methods have been used for this purpose. Among them are the Monte Carlo methods [54, 76], the finite differences/discretized population balances [30, 32, 44, 47, 48, 119], the quadrature method of moments [13, 41, 42], and the finite element methods [22].

In order to apply a finite volume scheme one can rewrite (2.10) and (2.12) in the following form [44]

$$x\frac{\partial f(t,x)}{\partial t} = \frac{\partial \tilde{\mathcal{F}}_{\text{break}}(t,x)}{\partial x}\,, \quad (t,x) \in \mathbb{R}^2_+\,, \tag{2.14}$$

where the volume (mass) flux is given as

$$\tilde{\mathcal{F}}_{\text{break}}(t,x) = \int_0^x \int_x^{\infty} y'\,b(t,y',x')\,S(x')\,f(t,x')\,dx'dy'\,. \tag{2.15}$$

The equation (2.14) and (2.15) can be easily used to apply a finite volume scheme. A brief overview of the finite volume scheme for the current one-component breakage process is

given in Chapter 5. In the following we show that one can recover back equation (2.10) and (2.12) from (2.14) and (2.15). Using equation (2.15) in (2.14) we get

$$\begin{aligned} x\frac{\partial f(t,x)}{\partial t} &= \frac{\partial \tilde{\mathcal{F}}_{\text{break}}(t,x)}{\partial x} = \frac{\partial}{\partial x}\int_0^x \int_x^\infty y'\, b(t,y',x')\, S(x')\, f(t,x')\, dx' dy' \\ &= \int_x^\infty x\, b(t,x,x')\, S(x')\, f(t,x')\, dx' - \int_0^x y'\, b(t,y',x)\, S(x)\, f(t,x)\, dy' \\ &= \int_x^\infty x\, b(t,x,x')\, S(x')\, f(t,x')\, dx' - S(x)\, f(t,x) \int_0^x y'\, b(t,y',x)\, dy' \\ &= \int_x^\infty x\, b(t,x,x')\, S(x')\, f(t,x')\, dx' - x\, S(x)\, f(t,x)\,, \end{aligned} \tag{2.16}$$

where according to equation (2.13) $\int_0^x y'\, b(t,y',x)\, dy' = x$. After canceling x from both sides of the equality in (2.16) one get the corresponding equations (2.10) and (2.12).

2.4 Growth and Nucleation Processes

The particles grow when a molecular matter adds to the surface of a particle. During growth process the total number of particles remains the same but the total volume (mass) of particles increases. The size of a particle increases continuously in this process.

Nucleation is a process of new particle formation from a given supersaturated solution. During this process the population of small particles increases. The nuclei are usually considered as the smallest possible particles in the system. In practical applications, such as crystallization, nucleation is assumed to takes place at the minimum particle size due to problems in particle size measurement in this range. Furthermore, in this size range it is not possible to distinguish between nuclei of different sizes due to insufficient resolutions of measuring devices. By growth and agglomeration these particles become visible. A graphical representation of growth and nucleation processes are given in Figure 2.1.

Growth and nucleation processes are very common in a wide range of particulate processes. The crystallization process is one example of such processes. The population balance equation in this case has the form

$$\frac{\partial f(t,x)}{\partial t} = -\frac{\partial [G(t,x) f(t,x)]}{\partial x} + \mathcal{Q}^+_{\text{nuc}}(t,x)\,, \quad (t,x) \in \mathbb{R}^2_+, \tag{2.17}$$

$$f(0,x) = f_0(x)\,, \quad x \in \mathbb{R}_+\,. \tag{2.18}$$

This is a hyperbolic equation with source term. If the nucleation term on the right hand side is zero then the above equation is a homogeneous hyperbolic equation for modeling a pure growth process. The nucleation term is defined as

$$\mathcal{Q}^+_{\text{nuc}} = f_{\text{nuc}}(t,x)\, B_{\text{nuc}}(t)\,, \tag{2.19}$$

where $f_{\text{nuc}} : \mathbb{R}_{\geq 0} \times \mathbb{R}_+ \to \mathbb{R}_{\geq 0}$ represents the number density of nuclei and $B_{\text{nuc}}(t) \in \mathbb{R}_{\geq 0}$ is the nucleation rate.

In the past several numerical techniques were introduced for solving PBE (2.17), see for example Ramkrishna [100] for a review. Discussion on the stability and numerical dispersion of various finite difference approximations can be found in Lapidus and Pinder [52]. An extension of the finite difference-type discretization methods have been proposed by Hounslow et al. [33] and David et al. [15]. However, their numerical results were found to be unsatisfactory, see Kumar and Ramkrishna [49]. A second-order spatial discretization for the growth term on a geometric grid was proposed by Litster et al. [62]. Later on, Muhr, David, and Villermaux [78] used a first-order upwind scheme for the spatial discretization of the growth term. However, due to numerical diffusion a loss in accuracy near steep fronts, peaks, or discontinuities was observed.

In [49] Kumar and Ramkrishna have proposed the method of characteristics (MOC) for the growth term. They found that, in contrast to other numerical techniques, the MOC avoids the numerical dissipation error caused by the growth term discretization. For handling nucleation term, which is usually difficult to treat, the MOC was combined with a procedure of adding a cell of the nuclei size at a given time level. A standard ordinary differential equations (ODEs) solver was used to solve the resultant ODEs.

Apart from these methods, Gunawan et al. [28], Ma et al. [65, 66] and Motz et al. [77] have used fully discrete high resolution schemes for the numerical solution of the PBE (2.17) in case of crystallization process. There are several other high resolution schemes which can be used for the solution of this type of problems, namely the central schemes [50, 79], and those presented in [37, 58, 117], among others.

2.5 Combined Processes

In this section we introduce a population balance equation (PBE) for simultaneous growth, nucleation, aggregation and breakage processes. Afterwards, we reformulate the underlying PBE in a form which can be readily used to implement the proposed finite volume schemes. Consider a PBE of the form

$$\frac{\partial f(t,x)}{\partial t} = -\frac{\partial [G(t,x) f(t,x)]}{\partial x} + \mathcal{Q}^{+}_{\text{nuc}}(t,x) + \mathcal{Q}^{\pm}_{\text{agg}}(t,x) + \mathcal{Q}^{\pm}_{\text{break}}(t,x)\,, \;\; (t,x) \in \mathbb{R}^2_+\,, \quad (2.20)$$

where $f : \mathbb{R}_{\geq 0} \times \mathbb{R}_+ \to \mathbb{R}_{\geq 0}$. Kumar and Ramkrishna [49] have combined their discretization technique on a non-uniform grid for aggregation terms with the method of characteristics (MOC) for growth term in order to solve the above PBEs for simultaneous nucleation, growth and aggregation processes. Apart from that Kumar [44] has used the cell averaged technique, which is an improved version of the fixed pivot technique, to solve different combinations of the above processes.

Lim et al. [61] applied high resolution spatial discretization methods (WENO schemes) and the method of characteristics (MOC) for the dynamic simulations of the batch crystallization including nucleation, growth, aggregation and breakage kinetics. They observed that, steep moving fronts or discontinuities appearing in the solution of the crystallization models were captured well by both methods without any spurious oscillations.

Immanuel et al. [38, 112] have proposed a novel finite volume based decomposition algorithm, called the hierarchical two-tier solution strategy, for the solution of population balance models incorporating simultaneous nucleation, growth, aggregation and breakage processes. The algorithm is based on a two-level discretization where different rate processes are encountered for through different densities and an exchange of information is allowed among the different particle densities to obtain the complete effect of all the processes. In particular, one particle density at the finer level accounts for the cell size sensitive processes of continuous growth and nucleation, while another particle density at the coarser level accounts for less sensitive to the cell width and computationally more intensive processes of aggregation and breakage. This decomposition framework enables efficient computations, and secondly, also naturally accommodates the tailoring the discretizations to suit the accuracy requirements of the various rate processes in an independent manner.

In this work we will combine the method of characteristics (MOC) for growth term with high resolution finite volume schemes for aggregation and breakage processes. Moreover, we will also implement the pure finite volume schemes for all processes. It is therefore convenient to reformulate the underling PBE (2.20) where instead of the number density one calculates the volume (mass) density. Multiplying both sides of equation (2.20) by x, we get

$$x\frac{\partial f(t,x)}{\partial t} = -x\frac{\partial [G(t,x)f(t,x)]}{\partial x} + x\mathcal{Q}^{+}_{\text{nuc}}(t,x) + x\mathcal{Q}^{\pm}_{\text{agg}}(t,x) + x\mathcal{Q}^{\pm}_{\text{break}}(t,x)\,. \tag{2.21}$$

The product rule implies

$$\frac{\partial [xG(t,x)f(t,x)]}{\partial x} = x\frac{\partial [G(t,x)f(t,x)]}{\partial x} + G(t,x)f(t,x)\,. \tag{2.22}$$

Furthermore, the aggregation term $x\mathcal{Q}^{\pm}_{\text{agg}}(t,x)$ and breakage term $x\mathcal{Q}^{\pm}_{\text{break}}(t,x)$ can be rewritten as

$$x\mathcal{Q}^{\pm}_{\text{agg}}(t,x) = -\frac{\partial \tilde{\mathcal{F}}_{\text{agg}}(t,x)}{\partial x}\,, \quad x\mathcal{Q}^{\pm}_{\text{break}}(t,x) = \frac{\partial \tilde{\mathcal{F}}_{\text{break}}(t,x)}{\partial x}\,, \tag{2.23}$$

where $\tilde{\mathcal{F}}_{\text{agg}}(t,x)$ and $\tilde{\mathcal{F}}_{\text{break}}(t,x)$ are given by (2.9) and (2.15), respectively. Let us define $\tilde{f}(t,x) := xf(t,x)$ and $\tilde{\mathcal{Q}}^{+}_{\text{nuc}}(t,x) := x\mathcal{Q}^{+}_{\text{nuc}}(t,x)$. After using equations (2.22) and (2.23) in (2.21), we obtain

$$\begin{aligned}\frac{\partial \tilde{f}(t,x)}{\partial t} =& -\frac{\partial [G(t,x)\tilde{f}(t,x)]}{\partial x} + \frac{G(t,x)\tilde{f}(t,x)}{x} \\ & - \frac{\partial \tilde{\mathcal{F}}_{\text{agg}}(t,x)}{\partial x} + \frac{\partial \tilde{\mathcal{F}}_{\text{break}}(t,x)}{\partial x} + \tilde{\mathcal{Q}}^{+}_{\text{nuc}}(t,x)\,,\end{aligned} \tag{2.24}$$

where $\tilde{f} : \mathbb{R}_{\geq 0} \times \mathbb{R}_+ \to \mathbb{R}_{\geq 0}$. Instead of the original equation (2.20) we will discretize (2.24) to implement the finite volume schemes in Chapter 6. Due to the relation $\tilde{f}(t,x) := xf(t,x)$ one can easily recover back $f(t,x)$.

2.6 Length-Based General PBE

In certain applications, for example crystallization, length is considered as the relevant particle property. It is therefore interesting to rewrite the PBE (2.20) in term of the number density function which uses particle length l as the internal property coordinate. To this end it is necessary to invoke some assumptions about the relationship between particle volume $x \in \mathbb{R}_+$ and particle length $l \in \mathbb{R}_+$. Fore example one can consider the case $x = l^3$. In this case we have the following relationship between the two expressions of the number density function

$$f(t,x)\,dx = f(t,l^3)\,3l^2 dl = n(t,l)\,dl\,, \tag{2.25}$$

where $n(t,l) \geq 0$ is the length based number density and $f(t,x) \geq 0$ is the volume based number density. Moreover, let $G'(t,l)$, $\beta'(t,l,l')$, $b'(l,l')$, $S'(l)$ respectively denote the length based growth rate, aggregation kernel, breakage kernel and selection kernel.

After multiplying equation (2.20) on both sides by $3l^2$, we obtain

$$\frac{\partial n(t,l)}{\partial t} = -\frac{\partial[G'(t,l)n(t,l)]}{\partial l} + \mathcal{K}^+_{\text{nuc}}(t,l) + \mathcal{K}^{\pm}_{\text{agg}}(t,l) + \mathcal{K}^{\pm}_{\text{break}}(t,l)\,, \quad (t,l) \in \mathbb{R}^2_+\,, \tag{2.26}$$

where $G'(t,l) = G(t,x)/3l^2$ and according to derivations in Appendix A.2 we obtain

$$\begin{aligned}\mathcal{K}^{\pm}_{\text{agg}}(t,l) =& \frac{l^2}{2}\int_0^l \frac{\beta'(t,(l^3-l'^3)^{\frac{1}{3}},l')}{(l^3-l'^3)^{\frac{2}{3}}}\, n(t,(l^3-l'^3)^{\frac{1}{3}})\, n(t,l')\,dl' \\ & - \int_0^\infty \beta'(t,l,l')\, n(t,l)\, n(t,l')\,dl', \end{aligned} \tag{2.27}$$

$$\mathcal{K}^{\pm}_{\text{break}}(t,l) = \int_l^\infty b'(t,l,l')\, S'(l')\, n(t,l')\,dl' - S'(l)\, n(t,l)\,, \tag{2.28}$$

$$\mathcal{K}^{+}_{\text{nuc}}(t,l) = n_{\text{nuc}}(t,l)\, B_{\text{nuc}}(t)\,. \tag{2.29}$$

It is interesting to note that $\beta'(t,l,l')$ and $S'(l)$, being intensive properties of the particulate system, can be converted easily from the volume-based to the length based number density functions, whereas $b'(t,l,l')$ results in

$$b'(t,l,l') = 3l^2\, b(t,l^3,l'^3) \quad \text{and} \quad \int_0^l l'^3\, b'(t,l',l)\,dl' = l^3\,. \tag{2.30}$$

In order to apply a finite volume schemes one can rewrite equation (2.26) in the following form

$$l^3\frac{\partial n(t,l)}{\partial t} = -\,l^3\frac{\partial[G'(t,l)n(t,l)]}{\partial l} + l^3\mathcal{K}^+_{\text{nuc}}(t,l) + l^3\mathcal{K}^{\pm}_{\text{agg}}(t,l) + l^3\mathcal{K}^{\pm}_{\text{break}}(t,l)\,. \tag{2.31}$$

Let us define $\tilde{n}(t,l) := l^3\, n(t,l)$ and using the relation

$$\begin{aligned} l^3\, \frac{\partial[G'(t,l)n(t,l)]}{\partial l} &= \frac{\partial[l^3\, G'(t,l)n(t,l)]}{\partial l} - 3l^2\, G'(t,l)n(t,l) \\ &= \frac{\partial[G'(t,l)\tilde{n}(t,l)]}{\partial l} - 3\, \frac{G'(t,l)\tilde{n}(t,l)}{l} \end{aligned} \tag{2.32}$$

in (2.31), we get

$$\begin{aligned} \frac{\partial \tilde{n}(t,l)}{\partial t} =& - \frac{\partial[G'(t,l)\tilde{n}(t,l)]}{\partial l} + 3\, \frac{G'(t,l)\tilde{n}(t,l)}{l} \\ &+ \tilde{\mathcal{K}}^{+}_{\text{nuc}}(t,l) - \frac{\partial \tilde{\mathcal{F}}'_{\text{agg}}(t,l)}{\partial l} + \frac{\partial \tilde{\mathcal{F}}'_{\text{break}}(t,l)}{\partial l}\,, \quad (t,l) \in \mathbb{R}^2_+\,, \end{aligned} \tag{2.33}$$

where $\tilde{n} : \mathbb{R}_{\geq 0} \times \mathbb{R}_+ \to \mathbb{R}_{\geq 0}$. Here $\tilde{\mathcal{K}}^{+}_{\text{nuc}}(t,l) = l^3 \mathcal{K}^{+}_{\text{nuc}}(t,l)$ and

$$\tilde{\mathcal{F}}'_{\text{agg}}(t,l) = \int_0^l \int_{(l^3-u^3)^{\frac{1}{3}}}^{\infty} u^3\, \beta'(t,u,v)\, n(t,u)\, n(t,v)\, dvdu\,, \tag{2.34}$$

$$\tilde{\mathcal{F}}'_{\text{break}}(t,l) = \int_0^l \int_l^{\infty} u^3\, b'(t,u,v)\, S'(v)\, n(t,v)\, dvdu\,. \tag{2.35}$$

If we compare (2.31) and (2.33) it comes out that

$$\mathcal{K}^{\pm}_{\text{agg}} = -\frac{1}{l^3} \frac{\partial \tilde{\mathcal{F}}'_{\text{agg}}}{\partial l}\,, \quad \text{and} \quad \mathcal{K}^{\pm}_{\text{break}} = \frac{1}{l^3} \frac{\partial \tilde{\mathcal{F}}'_{\text{break}}}{\partial l}\,. \tag{2.36}$$

The left hand side relation in (2.36) is verified in Appendix A.3. The proof for the right hand side relation is analogous to (2.16), therefore we skip its proof.

The jth moment $\mu_j(t)$ of this number density is defined as

$$\mu_j(t) = \int_0^{\infty} l^j n(t,l)\; dl\,. \tag{2.37}$$

As mentioned in Chapter 1, in crystallization processes the population balance models are coupled with the mass (mole) balance of the liquid phase which is an ordinary differential equation (ODE) for the solute mass $m(t)$. In that case the growth and nucleation are also functions of $m(t)$. Furthermore, an ODE for the temperature $T(t)$ which can be obtained from the energy balance of the crystallizer may also exist and coupled with the corresponding PBE and mass balance equation of the liquid phase. In Chapter 3 and 4 we will give the detailed models for the batch and preferential crystallization processes.

Note that in case of crystallization processes, Chapters 3 and 4, the crystal length will be considered as the internal property variable. For other particulate processes, Chapters 5 and 6, particle volume will be taken as the internal property variable.

Chapter 3

Batch Crystallization

This chapter starts with a short introduction of crystallization process. Two different operational modes of industrial crystallization plants are briefly explained. We give the one-dimensional population balance models for the simulation of batch crystallization and prove the local existence and uniqueness of the solution of this model. For that purpose Laplace transformation is used as a tool. With the help of inverse Laplace transformation, we derive a new method which can be used to solve numerically the given Batch crystallization model. Afterward, the model is extended to the two-dimensional case. Moreover, the one and two-dimensional semi-discrete finite volume schemes are derived for the numerical solution of the these models. For the one-dimensional schemes the issues of positivity (monotonicity), consistency, stability and convergence are also discussed. To improve the numerical accuracy of the schemes further a moving mesh technique is introduced. Finally, several numerical test problems are considered for the validation of the schemes and are compared with the available analytical solutions.

3.1 Fundamentals of Crystallization

Crystallization is the process of formation of solid crystals from a homogeneous solution and is essentially a solid-liquid separation technique. It is an important separation and purification process used in pharmaceutical, chemical and food industries.

The crystallization concept is very simple and well known. A solution can become supersaturated either by cooling or by evaporation of solvent. The process consists of two major events, nucleation and crystals growth. In case of nucleation, the solute molecules dispersed in the solvent come together to form stable clusters in the nanometer scale under current operating conditions. These stable clusters constitute the nuclei. However when the clusters are not stable, they re-dissolve. Therefore, for stable nuclei the clusters need to achieve a critical size. Such a critical size is dictated by the operating conditions (temperature, supersaturation, etc.). In stable nuclei the atoms are arrange in a defined and periodic manner defining the crystal structure. Note that *crystal structure* is a special

term that refers to the internal arrangement of the atoms, but not the physical external macroscopic properties of the crystal such as size and shape. The crystal growth is the subsequent growth of the nuclei that succeed in achieving the critical cluster size. During nucleation and growth the solute mass transfers from the liquid solution to solid crystals. Consequently, nucleation and growth continue to occur simultaneously as far as the supersaturation exists.

Supersaturation is the driving force of the crystallization, hence the rate of nucleation and growth is driven by the existing supersaturation in the solution. Depending upon the conditions, either nucleation or growth may be predominant over the other. As a result, crystals with different sizes and shapes are obtained. The most significant property of crystals is their size. Crystal size distribution (CSD) is the crucial variable in industrial crystallizers. On the one hand, CSD helps in understanding the dynamics of crystallization plant. On the other hand, CSD is important due to its heavy influence on the product quality and down-stream processability. It influences properties such as filterability, the ability to flow or the dissolution rate of crystalline materials. Industrial crystallization plants can be operated either in *continuous* mode or in *batch* mode.

In case of continuously operated crystallization plant the solution is continuously fed to the crystallizer and product is continuously withdrawn. Continuous processes run for very long period of time and serve for the production of large amounts of bulk materials. They are desired to be operated at a steady state. Hence the product quality is determined by the steady state CSD. This quantity can be influenced by fines dissolution, i.e. the continuous removal and dissolution of small particles. Unfortunately, apart from the desired effect on the CSD this may lead to instability of the steady state. As a result damped oscillations in CSD and supersaturation occur, see [107, 108, 121].

On the other hand, batch cooling crystallization is used for the small scale production of high-value-added fine chemicals and pharmaceuticals. Figure 3.1 shows one of such crystallizers. In this case the product quality is determined by the CSD at the end of the batch, which can be influenced by the cooling profile, i.e. the temperature trajectory during the batch run. In contrast to the continuous crystallization, batch crystallization is a transient process and does not achieve steady state. In batch mode there are, obviously, no feed and product removal streams. Consequently the corresponding terms does not exist in the batch model. In contrast to the continuous crystallization where nucleation, crystal growth and attrition are described by detailed first principle models, in batch mode empirical relations are used to describe nucleation and growth rates. The kinetic parameters involved in these equations have to be determined by parameter identification techniques from experimental data. The parameters summarize dependencies on the chemical system, the crystallizer type, size and geometry and the operating conditions such as temperature range or stirrer speed.

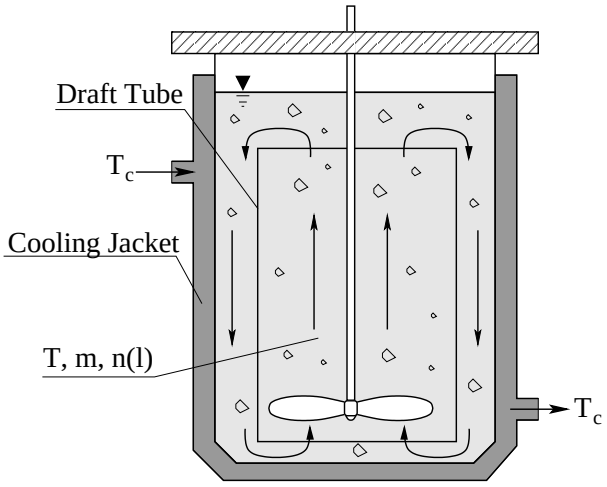

Figure 3.1: Batch crystallizer.

3.2 Model for Batch Crystallization

In the following we introduce relatively simple population balance equations for modeling batch crystallization process. Attrition is not modeled explicitly in these batch crystallization models. Instead, the production of small fragments by attrition is incorporated implicitly in the nucleation rate. Furthermore, breakage and agglomeration of crystals are also neglected. Consequently, the resulting batch models are not expected to be able to predict the effects of, e.g., scale-up or changes in the operating conditions. Nevertheless, they capable to describe the behavior of a given process in the relevant operating range fairly well. In the case of one-dimensional population balance model we also prove the existence and uniqueness of the solution.

3.2.1 One-dimensional batch crystallization model

In the one-dimensional (1D) batch crystallization model, the size of crystals is defined by a characteristic length l (e.g. the edge length in the case of cubic crystals). The crystal size distribution (CSD) is described by the number density function $n(t, l) \geq 0$, which represents the number of crystals per crystal length. Here, a standard model for batch crystallizer is presented and explained. As described above, it is based on a number of simplifying assumptions. Moreover, crystal growth rate can be independent/dependent of crystal size but we assume that nuclei are formed at minimum crystal size. Balancing the number of crystals in an infinitesimal interval of crystal length, a partial differential equation is obtained which, together with appropriate initial and boundary conditions,

describes the temporal evolution of the CSD [75, 103, 121]

$$\frac{\partial n(t,l)}{\partial t} = -\frac{\partial[G(t,l,m)n(t,l)]}{\partial l} + B_0(t,m)\,\delta(l-l_0)\,, \quad (t,l)\in\mathbb{R}_+^2\,, \tag{3.1}$$

$$n(0,l) = n_0(l) \quad l\in\mathbb{R}_+, \tag{3.2}$$

where $\mathbb{R}_+ :=]0,\infty[$. Here, $m := m(t) > 0$ represents the solute mass in the liquid phase, $n_0(l) \in \mathbb{R}_{\geq 0}$ denotes the CSD of seed crystals added at the beginning of the batch, $G(t,l,m) \geq 0$ length based growth rate, $B_0(t,m) \geq 0$ is the nucleation rate at minimum crystal size $l_0 > 0$ and δ is the Dirac delta distribution.

Remark 3.1 *In the last section of Chapter 2 the length based growth is represented by $G'(t,l,m)$. However, to avoid any confusion with the notation in this chapter we simply use $G(t,l,m)$ for the length based Growth.*

Since the number density outside the computational domain is assumed to be zero, the above formulation is equivalent to considering the homogeneous PBE and defining the ratio of nucleation and growth terms as a left boundary condition [121]

$$\frac{\partial n(t,l)}{\partial t} = -\frac{\partial[G(t,l,m)n(t,l)]}{\partial l}\,, \qquad (t,l)\in\mathbb{R}_+^2\,, \tag{3.3}$$

$$n(0,l) = n_0(l)\,, \tag{3.4}$$

$$n(t,l_0) = \frac{B_0(t,m)}{G(t,l_0,m)}\,. \tag{3.5}$$

A mass balance for the liquid phase yields an ordinary differential equation for the solute mass $m(t)$ [75, 103, 121]

$$\frac{\mathrm{d}m(t)}{\mathrm{d}t} = -3\rho_\mathrm{c}\,k_\mathrm{v}\int_0^\infty l^2\,G(t,l,m)\,n(t,l)\;dl \tag{3.6}$$

$$\text{with} \quad m(0) = m_0\,, \tag{3.7}$$

where $\rho_\mathrm{c} > 0$ is the density of crystals and $k_\mathrm{v} > 0$ is the so-called volume shape factor defined such that the volume of a crystal with length l is $k_\mathrm{v}l^3$. The negative sign on the right hand side of (3.6) shows that the solute mass decreases in the solution during crystallization.

Furthermore, an ODE for the temperature $T(t)$ can be obtained from an energy balance of the crystallizer

$$\rho_\mathrm{s}\,V\,c_\mathrm{p}(t)\frac{\mathrm{d}T(t)}{\mathrm{d}t} = -3\Delta H_\mathrm{c}(t)\rho_\mathrm{c}k_\mathrm{v}V\int_0^\infty l^2 G(t,l,m)\,n(t,l)\,\mathrm{d}l - U A_\mathrm{c}\,(T(t)-T_\mathrm{c}(t)) \tag{3.8}$$

$$\text{with} \quad T(0) = T_0\,, \tag{3.9}$$

where $\rho_s > 0$ is the density of the solvent in the crystallizer, V is the volume of crystallizer, U is the overall heat-transfer coefficient, A_c is the total heat transfer and T_c is the jacket temperature. The heat of crystallization $\Delta H_c(t)$ depends on the solute mass. The dependence can be adequately represented by a quadratic fit to empirical data

$$\Delta H_c(t) = A_0 + A_1\, m(t) + A_2\, m^2(t)\,. \tag{3.10}$$

The heat capacity of the solution can be expressed as [121]

$$c_p(t) = C_0 + C_1 \left(\frac{m(t)}{1+m(t)}\right) + C_2 \left(\frac{m(t)}{1+m(t)}\right)^2 . \tag{3.11}$$

The crystal growth depending linearly on size can be defined as [121]

$$G(t,l,m) = k_g\,[S(t,m)]^g\,(a_1 + a_2\, l)\,, \tag{3.12}$$

where $k_g \geq 0$ is growth rate constant, the exponent $g \geq 1$ is a kinetic parameter and a_1, a_2 are some constants so that $a_1 + a_2\, l \geq 0$. The relative supersaturation $S(t,c)$ can be defined as [121]

$$S(t,m) := \frac{m(t) - m_{sat}(t)}{m_{sat}(t)}\,, \tag{3.13}$$

where $m_{sat}(t) > 0$ is the saturation mass which depends on the temperature of the solution. A quadratic fit to the solubility data gives [121]

$$m_{sat}(t) = A_0 + A_1\, T(t) + A_2\, T^2(t)\,. \tag{3.14}$$

Usually, temperature is constant (isothermal case) or a monotonically decreasing function of time (non-isothermal case). Hence $m_{sat}(t)$ either stays constant or decreases with respect to time but remains positive. In this study the attrition is not considered explicitly but the production of small fragments by attrition is contained implicitly in the nucleation rate. The nucleation rate is given as [121]

$$B_0(t,m) = k_b\,[S(t,m)]^b\,\mu_3(t)\,, \tag{3.15}$$

where $\mu_3(t) \geq 0$ is the third moment defined by (2.37), $k_b \geq 0$ is nucleation rate constant and the exponent $b \geq 1$ is a kinetic parameter. Nucleation not only depend on the supersaturation but also on the crystal size distribution (CSD). Both nucleation and growth relation are of empirical nature. The parameters k_g, k_b, g and b have to be determined by parameter identification method [75]. The crystallizer temperature $T(t)$ determines the supersaturation and hence it influences the rates of nucleation $B_0(t,m)$ and growth $G(t,l,m)$ through supersaturation $S(t)$.

Note that in the current work we do not study control of crystallization process, therefore in our numerical studies we are not considering equation (3.8). Instead, the temperature is considered to be either constant or a decreasing function of time. However to check the performance of our proposed schemes, we will give one example where we also consider equation (3.8).

3.2.2 Existence and uniqueness of the solution

In this subsection we focus on the existence and uniqueness of the solution of the one-dimensional batch crystal model described by equations (3.1)-(3.7) and (3.12)-(3.15). For this purpose we use the Laplace transformation of the population balance equation (3.3). For simplicity we assume that the growth term is independent of the crystal size but is a function of time dependent mass $m(t)$ only, i.e. $G(t, m)$. In case of size independent growth the right hand side integral in (3.6) contains the second moment $\mu_2(t)$. Similarly, equation (3.15) depends on the third moment $\mu_3(t)$. Hence, our goal also include the derivation of a system of ordinary differential equations for moments $\mu_i(t)$, $i = 0, 1, 2, 3$ in order to have a closed system.

Let us define the Laplace transformation of $n(t, l)$ by

$$\hat{n}(t, s) := \mathcal{L}[n(t, l); s] = \int_0^\infty e^{-sl}\, n(t, l)\, dl\,, \quad s > 0\,. \tag{3.16}$$

The Laplace transformation of the partial derivative of the number density $n_l(t, l) := \frac{\partial n(t,l)}{\partial l}$ can be similarly defined. The number density $n(t, l)$ is zero outside the computational domain which is a finite crystal size range, hence $n(t, 0) = 0$. We obtain

$$\begin{aligned}
\mathcal{L}[n_l(t, l); s] &= \int_0^\infty e^{-sl}\, n_l(t, l)\, dl \\
&= \left[e^{-sl}\, n(t, l)\right]_0^\infty + s \int_0^\infty e^{-sl} n(t, l)\, dl \\
&= s\, \hat{n}(t, s)\,.
\end{aligned} \tag{3.17}$$

In the light of the above definitions, the Laplace transformation of equation (3.1) gives

$$\int_0^\infty e^{-sl}\, \frac{\partial n(t, l)}{\partial t}\, dl + G(t, m) \int_0^\infty e^{-sl}\, \frac{\partial n(t, l)}{\partial l}\, dl = B_0(t, m) \int_0^\infty e^{-sl}\, \delta(l - l_0)\, dl$$

leading to

$$\frac{d\hat{n}(t, s)}{dt} + s\, G(t, m)\, \hat{n}(t, s) = B_0(t, m)\, e^{-sl_0}\,. \tag{3.18}$$

The initial data for this linear differential equation at $t_0 \geq 0$ are given as

$$\hat{n}(t_0, s) = \int_0^\infty e^{-sl}\, n(t_0, l)\, dl = \hat{n}_0(s)\,. \tag{3.19}$$

Differentiating (3.16) with respect to s we obtain

$$\begin{aligned}
\frac{\partial \hat{n}(t, s)}{\partial s} &= -\int_0^\infty l\, e^{-sl}\, n(t, l)\, dl\,, \\
\frac{\partial^2 \hat{n}(t, s)}{\partial s^2} &= \int_0^\infty l^2\, e^{-sl}\, n(t, l)\, dl\,, \\
\frac{\partial^3 \hat{n}(t, s)}{\partial s^3} &= -\int_0^\infty l^3\, e^{-sl}\, n(t, l)\, dl\,.
\end{aligned}$$

The above derivatives at $s = 0$ give using (2.37)

$$\left.\frac{\partial \hat{n}(t,s)}{\partial s}\right|_{s=0} = -\int_0^\infty l\, n(t,l)\, dl = -\mu_1(t)\,, \tag{3.20}$$

$$\left.\frac{\partial^2 \hat{n}(t,s)}{\partial s^2}\right|_{s=0} = \int_0^\infty l^2\, n(t,l)\, dl = \mu_2(t)\,, \tag{3.21}$$

$$\left.\frac{\partial^3 \hat{n}(t,s)}{\partial s^3}\right|_{s=0} = -\int_0^\infty l^3\, n(t,l)\, dl = -\mu_3(t)\,. \tag{3.22}$$

Moreover, equation (3.16) at $s = 0$ gives

$$\hat{n}(t,0) = \int_0^\infty n(t,l)\, dl = \mu_0(t)\,. \tag{3.23}$$

Then equation (3.18) at $s = 0$ along with (3.23) gives

$$\frac{d\hat{n}(t,0)}{dt} = B_0(t,m) \implies \frac{d\mu_0(t)}{dt} = B_0(t,m)\,. \tag{3.24}$$

Further, the partial derivative of (3.18) at $s = 0$ gives

$$\frac{\partial}{\partial s}\left(\frac{\partial \hat{n}(t,s)}{\partial t}\right)\bigg|_{s=0} + G(t,m)\,\frac{\partial}{\partial s}(s\,\hat{n}(t,s))\bigg|_{s=0} = 0$$

or

$$\frac{\partial}{\partial t}\left(\frac{\partial \hat{n}(t,s)}{\partial s}\right)\bigg|_{s=0} + G(t,m)\;\left[\hat{n}(t,s) + s\,\hat{n}_s(t,s)\right]_{s=0} = 0 \tag{3.25}$$

which implies

$$\frac{d}{dt}\left(\left.\frac{\partial \hat{n}(t,s)}{\partial s}\right|_{s=0}\right) + G(t,m)\,\hat{n}(t,0) = 0\,.$$

Finally we get

$$\frac{d}{dt}\left(\left.\frac{\partial \hat{n}(t,s)}{\partial s}\right|_{s=0}\right) = -G(t,m)\,\hat{n}(t,0)\,. \tag{3.26}$$

Recall equations (3.20) and (3.23), equation (3.26) finally gives

$$\frac{d\mu_1(t)}{dt} = G(t,m)\,\mu_0(t)\,. \tag{3.27}$$

The second derivative of (3.25) at $s = 0$ gives after simplification

$$\frac{\partial}{\partial t}\left(\frac{\partial^2 \hat{n}(t,s)}{\partial s^2}\right)\bigg|_{s=0} + \left[s\,G(t,m)\,\frac{\partial^2 \hat{n}(t,s)}{\partial s^2} + 2\,G(t,m)\,\frac{\partial \hat{n}(t,s)}{\partial s}\right]_{s=0} = 0 \tag{3.28}$$

which implies

$$\frac{d}{dt}\left(\left.\frac{\partial^2 \hat{n}(t,s)}{\partial s^2}\right|_{s=0}\right) + 2\,G(t,m)\left.\frac{\partial \hat{n}(t,s)}{\partial s}\right|_{s=0} = 0\,. \tag{3.29}$$

Now using (3.20) and (3.21) in (3.29), we obtain

$$\frac{d\mu_2(t)}{dt} = 2\,G(t,m)\,\mu_1(t)\,. \tag{3.30}$$

Finally, the third derivative of (3.28) at $s = 0$ gives

$$\frac{d}{dt}\left(\left.\frac{\partial^3 \hat{n}(t,s)}{\partial s^3}\right|_{s=0}\right) + \left[s\,G(t,m)\,\frac{\partial^3 \hat{n}(t,s)}{\partial s^3} + 3\,G(t,m)\,\frac{\partial^2 \hat{n}(t,s)}{\partial s^2}\right]_{s=0} = 0 \tag{3.31}$$

which gives

$$\frac{d}{dt}\left(\left.\frac{\partial^3 \hat{n}(t,s)}{\partial s^3}\right|_{s=0}\right) + 3\,G(t,m)\left.\frac{\partial^2 \hat{n}(t,s)}{\partial s^2}\right|_{s=0} = 0\,. \tag{3.32}$$

After using (3.21) and (3.22) in the above equation we finally obtain

$$\frac{d\mu_3(t)}{dt} = 3\,G(t,m)\,\mu_2(t)\,. \tag{3.33}$$

Using definition (3.21) for $\mu_2(t)$ and keeping in mind that growth rate $G(t,m)$ in the present case is independent of the crystal size, equation (3.6) gives

$$\frac{\mathrm{d}m(t)}{\mathrm{d}t} = -3\rho_\mathrm{c}\,k_\mathrm{v}\,G(t,m)\,\mu_2(t)\,. \tag{3.34}$$

Using equations (3.33) in (3.34) we obtain

$$\frac{\mathrm{d}m(t)}{\mathrm{d}t} = -\rho_\mathrm{c}\,k_\mathrm{v}\,\frac{d\mu_3(t)}{dt}$$

which on integrating over the time interval $[t_0, t]$ gives

$$\int_{t_0}^{t} \frac{\mathrm{d}m(\tau)}{\mathrm{d}\tau}\,\mathrm{d}\tau = -\rho_\mathrm{c}\,k_\mathrm{v}\int_{t_0}^{t} \frac{d\mu_3(\tau)}{d\tau}\,\mathrm{d}\tau\,.$$

Hence, we get the following algebraic equation for the mass balance

$$m(t) + \rho_\mathrm{c}\,k_\mathrm{v}\,\mu_3(t) = m(t_0) + \rho_\mathrm{c}\,k_\mathrm{v}\,\mu_3(t_0)\,. \tag{3.35}$$

In summary, we get a closed system containing four ordinary differential equations for the moments $\mu_i(t),\ i = 0, 1, 2, 3$, coupled with an algebraic equation for the mass $m(t)$. This

system is decoupled from the linear differential equation (3.18).

Knowing the initial number density $n(t_0, l)$ and initial mass $m(t_0)$ one can calculate all the required initial moments, growth and nucleation rates. These initial data are sufficient to calculate $\mu_i(t)$ and $m(t)$ at any time $0 \leq t_0 \leq t$.

This coupled system is obtained from equations (3.24), (3.27), (3.30), (3.33) and (3.35) as follows

$$\frac{d\mu_0(t)}{dt} = B_0(t, m)\,, \tag{3.36}$$

$$\frac{d\mu_i(t)}{dt} = i\,G(t, m)\,\mu_{i-1}(t)\,, \quad i = 1, 2, 3, \tag{3.37}$$

$$m(t) + \rho_{\mathrm{c}}\,k_{\mathrm{v}}\,\mu_3(t) = m(t_0) + \rho_{\mathrm{c}}\,k_{\mathrm{v}}\,\mu_3(t_0) \tag{3.38}$$

with initial data for $t_0 \geq 0$

$$\mu_i(t_0) = \int_0^\infty l^i n(t_0, l)\,dl \geq 0\,, \quad m(t_0) > 0, \quad S(t_0, m) = \left(\frac{m(t_0)}{m_{\mathrm{sat}(t_0)}} - 1\right) > 0\,, \tag{3.39}$$

$$G(t_0, m) = k_{\mathrm{g}}\,S^g(t_0, m) > 0\,, \quad B_0(t_0, m) = k_{\mathrm{b}}\,S^b(t_0, m)\,\mu_3(t_0) > 0\,, \tag{3.40}$$

where $b, g \geq 1$ and $k_{\mathrm{g}}, k_{\mathrm{b}}$ are positive constants. Here $m_{\mathrm{sat}}(t) > 0$ is constant or a monotonically decreasing function of time and is given by relation (3.14). With the help of equations (3.36)-(3.40) we can calculate the growth rate $G(t, m)$ and nucleation rate $B_0(t, m)$ for $0 \leq t_0 \leq t \leq t_{\max}$. After having the growth and nucleation rates we can calculate the transformed number density $\hat{n}(t, s)$ from equations (3.18) and (3.19) in the time interval $0 \leq t_0 \leq t \leq t_{\max}$.

It is clear from equation (3.38) that the mass $m(t)$ is a function of $\mu_3(t)$, i.e. $m(t) = \hat{c}(\mu_3(t))$. Hence, instead of $G(t, m)$ and $B_0(t, m)$ one can also write $G(t, \mu_3)$ and $B_0(t, \mu_3)$.

In order to prove the existence and uniqueness of the solution of the above coupled system of moment equations it is convenient to rewrite the moment system (3.36) and (3.37) in the following form

$$\frac{d\mathbf{u}(t)}{dt} = \mathbf{f}(t, \mathbf{u})\,, \quad \mathbf{u}(t_0) = \mathbf{u}_0\,, \tag{3.41}$$

where

$$\mathbf{u}(t) = \begin{pmatrix} \mu_0(t) \\ \mu_1(t) \\ \mu_2(t) \\ \mu_3(t) \end{pmatrix}\,, \quad \mathbf{f}(t, \mathbf{u}) = \begin{pmatrix} B_0(t, \mu_3) \\ G(t, \mu_3)\,\mu_0 \\ 2\,G(t, \mu_3)\,\mu_1 \\ 3\,G(t, \mu_3)\,\mu_2 \end{pmatrix}\,. \tag{3.42}$$

The Jacobian matrix $\mathbf{J}$ is given by

$$\mathbf{J} := \frac{\partial \mathbf{f}}{\partial \mathbf{u}} = \begin{pmatrix} 0 & 0 & 0 & b\,\alpha(t)\,S^{b-1}(t,\mu_3)\,\mu_3 + k_\mathrm{b}\,S^b(t,\mu_3) \\ G(t,\mu_3) & 0 & 0 & \beta(t)\,S^{g-1}(t,\mu_3)\,\mu_0 \\ 0 & G(t,\mu_3) & 0 & \beta(t)\,S^{g-1}(t,\mu_3)\,\mu_1 \\ 0 & 0 & G(t,\mu_3) & \beta(t)\,S^{g-1}(t,\mu_3)\,\mu_2 \end{pmatrix}, \quad (3.43)$$

where $\alpha(t) := -\frac{b\,\rho_\mathrm{c}\,k_\mathrm{v}\,k_\mathrm{b}}{m_\mathrm{sat}(t)}$ and $\beta(t) := -\frac{g\,\rho_\mathrm{c}\,k_\mathrm{v}\,k_\mathrm{g}}{m_\mathrm{sat}(t)}$.

Proposition 3.1 *Let $\Omega_t \subset \mathbb{R}_{\geq 0}$ and $\Omega \subset \mathbb{R}_{\geq 0}$ are convex. If $\mathbf{f}(t,\mathbf{u})$ is defined on $\Omega_t \times \Omega$ and is continuously differentiable with respect to $\mathbf{u} \in \Omega$, and finally if the Jacobian matrix $\mathbf{J}$ is bounded on $\Omega_t \times \Omega$, i.e,*

$$L := \|\mathbf{J}(t,\mathbf{u})\|_{\Omega_t \times \Omega} < \infty\,. \quad (3.44)$$

Then $\mathbf{f} \in \mathrm{Lip}(\Omega_t \times \Omega)$ with Lipschitz constant L. Here $\|\cdot\|$ is the matrix norm induced by the Euclidean vector norm on $\mathbb{R}^4$.

Proof: The proof of this proposition is given in the text book by Mattheij and Molenaar [72] (Property 1.7 on Page 27).

Now we apply this proposition to the initial value problem (3.41).

Let us assume that for a given initial number density $n(t_0,x) \geq 0$ which is sufficiently smooth, the initial solute mass $m(t_0) > 0$ and the initial saturated mass $m_\mathrm{sat}(t_0) > 0$ the inequalities (3.39) and (3.40) hold. The function $S(t,m)$ is smooth function of time which is initially positive. Hence after a sufficiently small time $0 \leq t_0 < t \ll 1$ this function will still remain non-negative. Moreover, the number density is smooth and non-negative initially hence $\mu_i(t) \geq 0$ for $0 \leq t_0 < t \ll 1$. Since $\mu_3(t) \geq 0$ and m_sat given by (3.14) are chosen so that $0 < m_\mathrm{sat}(t) \leq m_\mathrm{sat}(t_0)$, we get the following inequality from (3.38) and (3.39)

$$\begin{aligned} m(t) &\leq m(t_0) + \rho_\mathrm{c}\,k_\mathrm{v}\,\mu_3(t_0) \\ \implies 0 \leq S(t,m) := \frac{m(t) - m_\mathrm{sat}(t)}{m_\mathrm{sat}(t)} &\leq \frac{m(t_0) - m_\mathrm{sat}(t)}{m_\mathrm{sat}(t)} + \frac{\rho_\mathrm{c}\,k_\mathrm{v}\,\mu_3(t_0)}{m_\mathrm{sat}(t)}\,. \end{aligned} \quad (3.45)$$

Hence, both growth and nucleation, which are functions of $S(t,m)$, are non-negative and bounded. Furthermore, the time we consider is finite and the initial number density is smooth with compact support, i.e, $n_0(l) \geq 0$ for $l \in \Omega_l$, with $\Omega_l \subset R_+$ finite, and zero otherwise. Hence, all the moments of the number density $\mu_i(t)$ at time $0 \leq t_0 < t \ll 1$ are also bounded. Moreover, $g, b \geq 1$.

In the light of the above arguments, it is clear that every term of the Jacobian matrix $\mathbf{J}$ in (3.43) is continuously differentiable and bounded. Hence the norm of the Jacobian matrix

J itself is bounded and the relation (3.44) holds.

The line segment joining two arbitrary points $\mathbf{u}_1, \mathbf{u}_2 \in \Omega$ is given by

$$\mathbf{u}_1 + \lambda\,(\mathbf{u}_2 - \mathbf{u}_1)\,, \quad 0 \le \lambda \le 1\,.$$

For any $t \in \Omega_t$ we may write

$$\mathbf{f}(t, \mathbf{u}_1) - \mathbf{f}(t, \mathbf{u}_2) = -\int_0^1 \frac{d}{d\lambda}\mathbf{f}(t, \mathbf{u}_1 + \lambda\,(\mathbf{u}_2 - \mathbf{u}_1))\,d\lambda \tag{3.46}$$

$$= \int_0^1 \mathbf{J}(t, \mathbf{u}_1 + \lambda\,(\mathbf{u}_2 - \mathbf{u}_1))\,(\mathbf{u}_1 - \mathbf{u}_2)\,d\lambda\,. \tag{3.47}$$

Taking the norm at both sides we obtain the inequality

$$\begin{aligned}\|\mathbf{f}(t, \mathbf{u}_1) - \mathbf{f}(t, \mathbf{u}_2)\| &\le \int_0^1 \|\mathbf{J}(t, \mathbf{u}_1 + \lambda\,(\mathbf{u}_2 - \mathbf{u}_1))\| \cdot \|\mathbf{u}_1 - \mathbf{u}_2\|\,d\lambda \\ &\le L\|\mathbf{u}_1 - \mathbf{u}_2\| \end{aligned} \tag{3.48}$$

with L given by (3.44). Here we have used the boundedness of matrices $\|\mathbf{A}\mathbf{u}\| \le \|\mathbf{A}\|\,\|\mathbf{u}\|$ for any matrix $\mathbf{A} \in \mathbb{R}^{4\times 4}$.

Finally, with the help of Proposition 3.1 we get the following result.

Theorem 3.1 *(Uniqueness). The initial value problem (IVP)* (3.41) *with* $\mathbf{f} \in \mathrm{Lip}(\Omega_t \times \Omega)$ *for some domain* $\Omega_t \times \Omega$ *containing* $(t_0, \mathbf{u}_0)$ *has at most one solution on any time interval for which the solution exists.*

Proof: Suppose that both $\mathbf{u}_1$ and $\mathbf{u}_2$ are solutions of (3.41). The difference $\mathbf{w} = \mathbf{u}_1 - \mathbf{u}_2$ then satisfies the IVP

$$\frac{d\mathbf{w}}{dt} = \mathbf{f}(t, \mathbf{u}_1) - \mathbf{f}(t, \mathbf{u}_2)\,, \quad \mathbf{w}(t_0) = 0\,. \tag{3.49}$$

Multiplying both sides of the ODE by $\mathbf{w}^T$ we find for the left-hand side

$$\mathbf{w}^T\frac{d\mathbf{w}}{dt} = \frac{1}{2}\frac{d}{dt}\left(\mathbf{w}^T(t)\mathbf{w}(t)\right) = \frac{1}{2}\frac{dz(t)}{dt}\,, \tag{3.50}$$

where we introduce the notation

$$z(t) := \mathbf{w}^T(t)\mathbf{w}(t) = \|\mathbf{w}(t)\|^2\,.$$

For the right-hand side we have

$$|\mathbf{w}^T(t)\,(\mathbf{f}(t, \mathbf{u}_1) - \mathbf{f}(t, \mathbf{u}_2))| \le \|\mathbf{w}(t)\|\,\|\mathbf{f}(t, \mathbf{u}_1) - \mathbf{f}(t, \mathbf{u}_2)\| \le L\,z(t)$$

with L the Lipschitz constant of $\mathbf{f}$ given in (3.44). Combining these results we find for the scalar function $z(t)$

$$\frac{dz(t)}{dt} \leq 2Lz\,, \quad z(t_0) = 0\,.$$

Application of the Gronwall lemma (Mattheij and Molenaar [72], Lemma 1.8 on page 28) directly yields $z(t) \leq 0$. Since $z(t) \geq 0$ we conclude that $z(t) = 0$. This proves that $\mathbf{u}_1$ and $\mathbf{u}_2$ are identical for $t \geq t_0 \geq 0$.

□

Theorem 3.2 *(Local existence). The initial value problem* (3.41) *with* $\mathbf{f} \in \mathrm{Lip}(\Omega_t \times \Omega)$ *for some domain* $\Omega_t \times \Omega$ *containing* $(t_0, \mathbf{u}_0)$ *in its interior has a unique solution on a certain interval* $\Omega_t^r = [t_0, t_0 + r]\,, \quad 0 < r \ll 1$.

Proof: The proof of this theorem is already given in Theorem 2.3 of the book by Mattheij and Molenaar [72] on pages 31-33. An essential ingredient of the proof is the Picard iteration, the standard procedure of successive substitutions. It is based on the proposition, see Property I.2.6 of Chapter I in [72], which states that the solution of (3.41) satisfies the integral equation

$$\mathbf{u}(t) = \mathbf{u}_0 + \int_{t_0}^{t} \mathbf{f}(\xi, \mathbf{u}(\xi))\, d\xi\,. \tag{3.51}$$

Every continuous function satisfying (3.51) is automatically differentiable, so the proof of the existence theorem can be formulated in terms of continuous functions. The following recursion yields a series $\mathbf{u}^i(t),\ i = 0, 1, 2, \cdots$, of continuous functions

$$\mathbf{u}(t_0) = \mathbf{u}_0\,, \quad \mathbf{u}^{i+1}(t) = \mathbf{u}_0 + \int_{t_0}^{t} \mathbf{f}(\xi, \mathbf{u}^i(\xi))\, d\xi\,. \tag{3.52}$$

The so called *Picard mapping* P which maps continuous functions on to continuous functions.

After solving the system (3.36) and (3.38), the growth and nucleation rate are available for the whole time interval $[t_0, t]$. Now equations (3.18) and (3.19) can be used to calculate the transformed number density $\hat{n}(t, s)$.

□

In the following we show the existence and uniqueness of the solution of the first order linear differential equation (3.18).

Theorem 3.3 *(Existence and uniqueness) Let* $\Omega_t \subset \mathbb{R}_{\geq 0}$ *and* $\Omega_l \subset \mathbb{R}_+$ *are open intervals and let* $G(t, m)$, $B_0(t, m) \in C(\Omega_t, \Omega_l)$. *Then for every* $(t_0, l_0) \in \Omega_t \times \Omega_l$, *the nonhomogeneous first order linear differential equation*

$$\frac{\partial \hat{n}(t, s)}{\partial t} = -s\, G(t, m)\, \hat{n}(t, s) + B_0(t, m)\, e^{-sl_0}\,, \quad \hat{n}(t_0, s) = \hat{n}_0(s)\,, \tag{3.53}$$

has a unique global solution $\hat{n}(t,s)$. It is given by the formula

$$\hat{n}(t,s) = U(t,t_0,s,m)\,\hat{n}_0(s) \;+\; \int_{t_0}^{t} U(t,\xi,s,m)\,B_0(\xi,m)\,e^{-sl_0}\,d\xi\,, \tag{3.54}$$

$$U(t,\xi,s,m) := \exp\left[-s\int_{\xi}^{t} G(\tau,m)\,d\tau\right].$$

Remark 3.2 *Equation* (3.53) *is depending on $G(t,m)$, $B_0(t,m)$ which are available after solving equations* (3.36)-(3.38). *Hence, according to this theorem equation* (3.53) *has the unique global solution for all times for which the values of $G(t,m)$ and $B_0(t,m)$ are available i.e., for all times for which the solution of the moment system* (3.41) *exists.*

Proof: After calculating $G(t,m)$ and $B_0(t,m)$ from (3.36)-(3.38), equation (3.53) can be easily solved. The derivation of this type of solution is given in the book by H. Amann [5] (page 81, (5.13 b)).

Now suppose that $\hat{m}(t,s) \in C^1(\Omega_t,\Omega_l)$ is some other solution of equation (3.53), that is to say, if

$$\frac{\partial \hat{m}(t,s)}{\partial t} = -s\,G(t,m)\,\hat{m}(t,s) + B_0(t,m)\,e^{-sl_0}\,,\quad \hat{m}(t_0,s) = \hat{m}_0(s)\,,$$

then, by taking the difference, it follows that the function $\hat{u} := \hat{n} - \hat{m} \in C^1(\Omega_t,\Omega_l)$ is a solution of the homogeneous initial value problem

$$\frac{\partial \hat{u}(t,s)}{\partial t} = -s\,G(t,m)\,\hat{u}(t,s)\,,\quad \hat{u}(t_0,s) = 0\,. \tag{3.55}$$

According to Example (5.2 c) on page 72 in the book by Amann [5], equation (3.55) has a unique solution $\hat{u} = 0$. Therefore $\hat{n} = \hat{m}$, i.e., equation (3.53) can be solved uniquely.

□

Finally one can use the inverse Laplace transformation to get back the original number density $n(t,l)$, i.e.

$$n(t,l) = \frac{1}{2\pi i}\int_{\gamma-i\infty}^{\gamma+i\infty} e^{sl}\,\hat{n}(t,s)\,ds\,, \tag{3.56}$$

where γ is a real constant that exceeds the real part of all the singularities of $\hat{n}(t,s)$.

Below we introduce a new technique for solving the given population balance equation (PBE) (3.1). This is the most important step in the derivation of the technique. For this

purpose we use the inverse Laplace transformation (3.56) of equation (3.54) as

$$n(t,l) = \frac{1}{2\pi i}\int_{\gamma-i\infty}^{\gamma+i\infty} \exp\left[s\left(l - \int_{t_0}^{t} G(\tau,m)\,d\tau\right)\right]\,\hat{n}_0(s)\,ds \tag{3.57}$$
$$+ \int_{t_0}^{t} B_0(\xi,m)\,\left[\frac{1}{2\pi i}\int_{\gamma-i\infty}^{\gamma+i\infty} \exp\left[s\left(l - l_0 - \int_{\xi}^{t} G(\tau,m)\,d\tau\right)\right]\,d\xi\right].$$

Let $\tilde{l} := l - l_0$ and using (3.56) we obtain from equation (3.57)

$$n(t,l) = n_0\left(l - \int_{t_0}^{t} G(\tau,m)\,d\tau\right) + \int_{t_0}^{t} B_0(\xi,m)\,\delta\left(\tilde{l} - \int_{\xi}^{t} G(\tau,m)\,d\tau\right)d\xi. \tag{3.58}$$

It is clear from the above equation that $\xi \in [t_0, t]$. Hence the first nucleus which is born initially at $t = t_0$ will grow until $\tilde{l} = \displaystyle\int_{t_0}^{t} G(\tau,m)\,d\tau$. This means that the first nucleus will grow to its maximum possible size. The nuclei born subsequently will have less time to grow because as ξ increases the value of $\displaystyle\int_{\xi}^{t} G(\tau,m)\,d\tau$ decreases.

Note that $G(t,m) \geq 0$ everywhere. In order to further evaluate the second right hand side term in the above equation, we use the substitution

$$v := u(\xi,t) = \int_{\xi}^{t} G(\tau,m)\,d\tau \tag{3.59}$$

with

$$\xi = u^{-1}(v,t)\,, \quad \frac{d\xi}{dv} = \frac{\partial}{\partial v}u^{-1}(v,t)\,. \tag{3.60}$$

Hence, we have

$$\mathcal{J} := \int_{t_0}^{t} B_0(\xi,m)\,\delta\left(\tilde{l} - \int_{\xi}^{t} G(\tau,m)\,d\tau\right)d\xi$$
$$= \int_{u(t_0,t)}^{u(t,t)} B_0(u^{-1}(v,t),m)\,\delta(\tilde{l} - v)\,(u^{-1}(v,t))'\,dv. \tag{3.61}$$

Using (3.59), we obtain

$$\frac{\partial}{\partial v}u^{-1}(v,t) = \frac{1}{\frac{\partial}{\partial \xi}u(u^{-1}(v,t),t)} = \frac{-1}{G(u^{-1}(v,t),m)}\,. \tag{3.62}$$

Moreover, equation (3.59) shows that $u(t,t) = 0$. Hence, (3.61) along with (3.62) gives

$$\mathcal{J} = \int_{0}^{u(t_0,t)} \frac{B_0(u^{-1}(v,t),m)}{G(u^{-1}(v,t),m)}\,\delta(\tilde{l} - v)\,dv = \begin{cases} \frac{B_0(u^{-1}(v,t),m)}{G(u^{-1}(v,t),m)}\,, & \tilde{l} \in]0, u(t_0,t)] \\ 0\,, & \text{otherwise} \end{cases}, \tag{3.63}$$

where $u(t_0,t) = \int_{t_0}^{t} G(\tau,m)\,d\tau$. Using (3.63) in (3.58) and due to (3.60) we finally obtain

$$n(t,l) = n_0\left(l - \int_{t_0}^{t} G(\tau,m)\,d\tau\right) + \begin{cases} \frac{B_0(\xi,m)}{G(\xi,m)}\,, & \tilde{l} \in]0, u(t_0,t)] \\ 0\,, & \text{otherwise} \end{cases}\,. \tag{3.64}$$

The last step is to find ξ in (3.64) needed for any $\tilde{l} \in]0, u(t_0,t)]$. This can be obtained by finding the root of the implicit function $\mathcal{F}(\xi)$ defined as

$$\mathcal{F}(\xi) := \int_{\xi}^{t} G(\tau,m)\,d\tau - \tilde{l}\,, \quad \mathcal{F}'(\xi) := -G(\xi,m) \tag{3.65}$$

with $\tilde{l} := l - l_0$. Then for a given t and $\tilde{l} \in]0, u(t_0,t)]$ one can find ξ by using Newton's formula

$$\xi^{k+1} = \xi^k - \frac{\mathcal{F}^k(\xi)}{\mathcal{F}'^k(\xi)}\,, \tag{3.66}$$

where k represents the number of iteration steps in the Newton's formula. Since in the numerical computations $G(t,m)$ and $B_0(t,m)$ are only available at discrete points in the time domain, we have used a linear interpolation for calculating $G(\xi,m)$ and $B_0(\xi,m)$ with $\xi \in [t_0,t]$.

It is easy to show that $\mathcal{F}(\xi)$ in equation (3.65) has a unique non-negative root $\xi \in [t_0,t]$ if

$$\int_{t_0}^{t} G(\tau,m)\,d\tau \geq \tilde{l}\,, \tag{3.67}$$

i.e. we can find $\xi \in [t_0,t]$ such that $\mathcal{F}(\xi) = 0$ in equation (3.65). Due to (3.67) equation (3.65) implies

$$\mathcal{F}(t_0) > \tilde{l} > \mathcal{F}(t) = 0 \quad \text{and} \quad \mathcal{F}'(\xi) < 0\,. \tag{3.68}$$

Hence the function $\mathcal{F}(\xi)$ is monotonically decreasing. Finally, the strictly monotonicity of the positive growth function $G(t,m) > 0$ implies the uniqueness of ξ. For $\int_{t_0}^{t} G(\tau,m)\,d\tau < \tilde{l}$ there is no solution and we have the lower case, i.e. 0 in the second term on the right hand side, of equation (3.64).

The numerical case studies considered here and in our article [97] show that the Newton's routine needs four to five iterations to get a convergent solution with a tolerance $\epsilon = 10^{-4}$.

Algorithm: In the following we give an algorithm of our technique.

1. Use the initial number density $n_0(l)$ and initial mass m_0 to calculate the required initial moments, growth rate and nucleation rate.

2. After having the initial moments, use equations (3.36)-(3.38) to calculate the discrete values of $\mu_i(t)$ and $m(t)$ in the given time interval $[t_0, t_{\max}]$.

3. To calculate the integral of the growth rate in (3.64) one can use any quadrature formula. Here, we have used the built-in composite trapezoidal rule in the Matlab software.

4. To recover the number density, for example at final simulation time $t = t_{\max}$, first check whether $\tilde{l} \in]0, u(t_0)]$. If yes, use (3.66) to find ξ.

5. Note that $G(t, m)$ and $B_0(t, m)$ are only known at discrete points in the interval $[t_0, t_{\max}]$. Hence to find $G(\xi, m)$ and $B_0(\xi, m)$ at any point of this interval one can use linear interpolation. Here, we have used the built-in Matlab routine in our numerical experiments. After knowing ξ and $G(\xi, m)$ one can re-sort the arrays and can calculate the integral appearing in the equation (3.65) at each iteration step. Stop the iterations when the required tolerance is achieved which is 10^{-4} in our numerical case studies.

6. Finally, use (3.64) to get the required crystal size distribution (CSD).

In this chapter we will consider one numerical test problem for the current method. For further details and more numerical test problems the reader is referred to our article [97].

3.2.3 Two-dimensional batch crystallization model

In general, the number density may have more than one internal coordinate. Let $l_1 := \xi$ and $l_2 := \eta$. The two-dimensional population model for the number density $n := n(t, \xi, \eta) \geq 0$ with the same assumptions as in the one-dimensional case is given as

$$\frac{\partial n}{\partial t} = -\frac{\partial [G_1(t, \xi, m)n]}{\partial \xi} - \frac{\partial [G_2(t, \eta, m)n]}{\partial \eta} + B_0(t, m)\, \delta(\xi - \xi_0, \eta - \eta_0)\,, \tag{3.69}$$

where $t \geq 0$ denotes the time, $\xi \in \mathbb{R}_+$ and $\eta \in \mathbb{R}_+$ are internal coordinates, $m := m(t)$ represents the solute mass in the liquid phase, $G_1(t, \xi, m)$ and $G_2(t, \eta, m)$ are the growth rates along each characteristic length direction, and $B_0(t, m)$ is the nucleation rate which takes place at (ξ_0, η_0).

In the two-dimensional case we are mainly interested in the simulation of the potassium nitrate (KNO_3) crystals. They have particular shape as shown in Figure 3.2. The solute solute mass m(t) in the liquid phase for these particular shaped crystals are given as [14, 28]

$$\frac{\mathrm{d}m(t)}{\mathrm{d}t} = -\rho_{\mathrm{c}} \int_0^\infty \int_0^\infty n(t, \xi, \eta)\, (2\, G_1(t, \xi, m)\, (\xi\eta - \xi^2) + G_2(t, \eta, m)\, \xi^2)\, d\eta\, d\xi\,. \tag{3.70}$$

The solute mass, temperature, supersaturation, growth and nucleation follow similar laws and we will more explicitly present them in the corresponding numerical case studies.

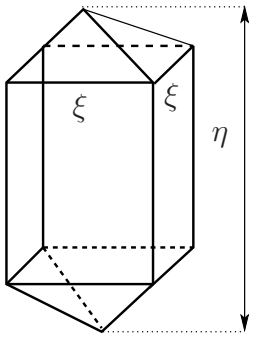

Figure 3.2: KNO_3 crystal

3.3 Numerical Schemes

In this section we drive the high resolution finite volume schemes for the numerical solutions of one and two-dimensional PBE's. We explain the schemes on both uniform and adaptive grids.

3.3.1 One-dimensional high resolution schemes

Here, we briefly review the high resolution semi-discrete finite volume scheme of Koren [40]. We also give another semi-discrete version of the present scheme which in fully discrete form is given by LeVeque [58]. We start with the homogeneous linear hyperbolic equation (3.3) and consider nucleation as a left boundary condition (3.5).

Domain discretization: In order to apply any numerical scheme, the first step is to discretize the computational domain which is the crystal length in the current study. Let N be a large integer, and denote by $(l_{i-\frac{1}{2}})_{i\in\{1,\cdots,N+1\}}$ partitions of interval $[l_0, l_{\max}]$, where l_0 is the minimum and $l_{\max}$ is the maximum crystal length of interest. As shown in Figure 3.3, for each $i = 1, 2, \cdots, N$, Δl represents the cells width, the points l_i refer to the cell centers, and the points $l_{i\pm\frac{1}{2}}$ represent the cell boundaries. We set

$$l_{1/2} = l_0\,, \quad l_{N+1/2} = l_{\max}\,, \quad l_{i+1/2} = l_0 + i\cdot\Delta l\,, \ \text{ for all } i = 1, 2, \cdots N\,. \tag{3.71}$$

Furthermore, we have

$$l_i = (l_{i-1/2} + l_{i+1/2})/2 \quad \text{and} \quad \Delta l = l_{i+1/2} - l_{i-1/2}\,. \tag{3.72}$$

Let $\Omega_i := \left[l_{i-1/2}, l_{i+1/2}\right]$ for $i \geq 1$. We approximate the initial data $n_0(l)$ in each cell by

$$n_i(t_0) = \frac{1}{\Delta l}\int_{\Omega_i} n_0(l)\; dl\,. \tag{3.73}$$

After discretizing the computational domain and assigning the initial data to each grid cell, the next step is to apply the proposed finite volume schemes.

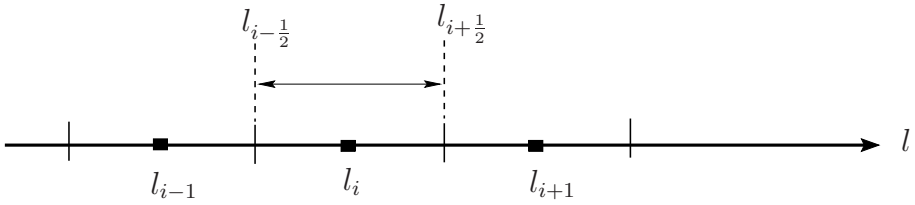

Figure 3.3: Cell centered finite volume grid

Let us define $\mathcal{F}(t,l,m) := G(t,l,m)n(t,l)$. The cell centered finite-volume discretization of (3.3) yields the semi-discrete equation

$$\int_{\Omega_i} \frac{\partial n}{\partial t}\, dl = -\left(\mathcal{F}_{i+\frac{1}{2}} - \mathcal{F}_{i-\frac{1}{2}}\right), \tag{3.74}$$

where $\mathcal{F}_{i\pm\frac{1}{2}} = (Gn)_{i\pm\frac{1}{2}}$ are fluxes at the boundaries of cell Ω_i. Let $n_i(t)$ denote the average value of the number density in each cell Ω_i, i.e.

$$n_i(t) = \frac{1}{\Delta l}\int_{\Omega_i} n(t,l)\, dl\,. \tag{3.75}$$

For the sake of simplicity in the following we will denote $n_i(t)$ by n_i. Therefore equation (3.74) implies

$$\frac{dn_i}{dt} = -\frac{\mathcal{F}_{i+\frac{1}{2}} - \mathcal{F}_{i-\frac{1}{2}}}{\Delta l}, \qquad \text{for } i = 1, 2, \cdots, N, \tag{3.76}$$

where N denotes the total number of cells in the computational domain. The accuracy of finite volume discretization is mainly determined by the way in which the cell-boundary fluxes are computed. Assuming that the flow is in positive l-direction, i.e. $G(t,l) \geq 0$. Then the first order accurate upwind scheme can be obtained by taking the backward differences.

First order upwind scheme:

$$\mathcal{F}_{i+\frac{1}{2}} = \mathcal{F}_i = (Gn)_i\,, \qquad \mathcal{F}_{i-\frac{1}{2}} = \mathcal{F}_{i-1} = (Gn)_{i-1}\,. \tag{3.77}$$

High resolution schemes: High order accuracy can be easily obtained by piecewise polynomial interpolation. One can take for instance

$$\mathcal{F}_{i+\frac{1}{2}} = \mathcal{F}_i + \frac{1+\kappa}{4}\left(\mathcal{F}_{i+1} - \mathcal{F}_i\right) + \frac{1-\kappa}{4}\left(\mathcal{F}_i - \mathcal{F}_{i-1}\right), \quad \kappa \in [-1,1]\,. \tag{3.78}$$

Similarly one can write expression for $\mathcal{F}_{i-\frac{1}{2}}$ as

$$\mathcal{F}_{i-\frac{1}{2}} = \mathcal{F}_{i-1} + \frac{1+\kappa}{4}\left(\mathcal{F}_i - \mathcal{F}_{i-1}\right) + \frac{1-\kappa}{4}\left(\mathcal{F}_{i-1} - \mathcal{F}_{i-2}\right), \quad \kappa \in [-1,1]\,. \tag{3.79}$$

Here κ is a parameter that has to be chosen from the indicated range. For $\kappa = -1$, one gets the second order accurate fully one-sided upwind scheme, and for $\kappa = 1$, the standard second order accurate central scheme. For all other values of $\kappa \in [-1,1]$, a weighted blend is obtained between the central scheme and the fully one-sided upwind scheme. The κ-interpolation is originally introduced by van Leer [55] for application to the nonlinear Euler equations.

Spatial truncation error: In order to calculate the truncation error (consistency order) we use the following definitions.

Definition 3.1 *The spatial truncation error in the cell Ω_i is defined by the residual left by substituting the exact solution n_i into equation* (3.76) *as*

$$\tau_i(t) := \frac{dn_i}{dt} + \frac{\mathcal{F}_{i+\frac{1}{2}} - \mathcal{F}_{i-\frac{1}{2}}}{\Delta l}, \quad i = 1, 2, \cdots, N\,. \tag{3.80}$$

Let $\tau(t) := [\tau_1(t), \tau_2(t), \cdots, \tau_N(t)]^T$. The scheme (3.76) *is called consistent of order p if, for $\Delta l \to 0$,*

$$\|\tau(t)\| := \mathcal{O}(\Delta l^p) \tag{3.81}$$

uniformly for all t. Here $\|\cdot\|$ denotes the $\mathbb{R}^n$ norm.

Let $n_t := \frac{\partial n}{\partial t}$, $\mathcal{F}_l := \frac{\partial \mathcal{F}}{\partial l}$ and analogously the high order derivatives. The truncated Taylor-series expressions of equations (3.78) and (3.79) at point l_i gives after simplifications

$$\begin{aligned}
\mathcal{F}(t, l_{i+\frac{1}{2}}, m) =& \mathcal{F}(t, l_i, m) + \frac{\Delta l}{2}(\mathcal{F}_l)(t, l_i, m) + \frac{\kappa\,\Delta l^2}{2\cdot 2!}(\mathcal{F}_{ll})(t, l_i, m) \\
&+ \frac{\Delta l^3}{2\cdot 3!}(\mathcal{F}_{lll})(t, l_i, m) + \mathcal{O}(\Delta l^4)\,, \\
\mathcal{F}(t, l_{i-\frac{1}{2}}, m) =& \mathcal{F}(t, l_i, m) - \frac{\Delta l}{2}(\mathcal{F}_l)(t, l_i, m) + \frac{\kappa\,\Delta l^2}{2\cdot 2!}(\mathcal{F}_{ll})(t, l_i, m) \\
&+ \left(1 - \frac{3}{2}\kappa\right)\frac{\Delta l^3}{3!}(\mathcal{F}_{lll})(t, l_i, m) + \mathcal{O}(\Delta l^4)\,.
\end{aligned}$$

Substituting the above expressions into (3.76), and using (3.3), we get

$$\begin{aligned}
&\frac{dn(t, l_i)}{dt} + \frac{\mathcal{F}(t, l_{i+\frac{1}{2}}, m) - \mathcal{F}(t, l_{i-\frac{1}{2}}, m)}{\Delta l} \\
&\quad = \underbrace{n_t(t, l_i) + \mathcal{F}_l(t, l_i, m)}_{=0} + \left(\frac{3}{2}\kappa - \frac{1}{2}\right)\frac{\Delta l^2}{3!}\mathcal{F}_{lll}(t, l_i, m) + \mathcal{O}(\Delta l^3) \\
&\quad = \left(\frac{3}{2}\kappa - \frac{1}{2}\right)\frac{\Delta l^2}{3!}\mathcal{F}_{lll}(t, l_i, m) + \mathcal{O}(\Delta l^3)\,.
\end{aligned} \tag{3.82}$$

Hence the flux interpolation formulae (3.78) and (3.79) give a second-order accurate discretization of (3.3) under the constraints that $\mathcal{F}(t,l,m) := G(t,l,m)n(t,l)$ and $n(t,l)$ are sufficiently smooth. Also it is clear from equation (3.82) that this interpolation gives a third order accurate scheme for the choice $\kappa = 1/3$. Hence the scheme (3.76) has consistency order 2 for $\kappa = 1, -1$ and order 3 for $\kappa = 1/3$.

Unfortunately, the above κ-schemes suffer from under- and overshoot and lack of positivity in regions of truly strong variations. Hence we need to pay attention to the aspect of monotonicity, i.e. to the possible occurrence of wiggles and their suppression, as well as to the possible occurrence of negative solution values and their suppression. For that purpose, Koren [40] has used Sweby type flux limiter [113] which will be explained below.

Definition 3.2 Positive (monotone) semi-discretization: *The scheme* (3.76) *is called positive (or non-negative), if for any non-negative initial solution* $n_i(t_0)$ $(n_i(t_0) \geq 0 \,\forall\, i)$ *the evolving solution* $n_i(t)$ *remains non-negative for all* $t \geq t_0$. *Obviously, a scheme is positive, if and only if for all* i *and all* $t \geq t_0$,

$$n_i(t) = 0\,, \quad n_j(t) \geq 0\,, \quad \forall\, j \neq i \implies \frac{dn_i(t)}{dt} \geq 0\,. \tag{3.83}$$

Applying the κ-scheme to the discrete advection operator $\mathcal{F}_{i+\frac{1}{2}} - \mathcal{F}_{i-\frac{1}{2}}$, we get the following stencil

$$\left[\frac{1-\kappa}{4}\, n_{i-2} \quad \frac{-5+3\kappa}{4}\, n_{i-1} \quad \frac{3(1-\kappa)}{4}\, n_i \quad \frac{1+\kappa}{4}\, n_{i+1}\right], \quad \kappa \in [-1,1]\,. \tag{3.84}$$

Verify that there is no value $\kappa \in [-1,1]$ for which the positive coefficient rule [81] is satisfied. Schemes which do not obey this rule admit spurious solution oscillations. The worst κ- scheme with respect to the positive coefficients rule is the $\kappa = 1$-scheme: the standard, second order-accurate, central scheme.

Let us rewrite equation (3.78) to the slope-ratio formulation as

$$\mathcal{F}_{i+\frac{1}{2}} = \mathcal{F}_i + \frac{1}{2}\left(\frac{1-\kappa}{2} + \frac{1+\kappa}{2}\, r_{i+\frac{1}{2}}\right)(\mathcal{F}_i - \mathcal{F}_{i-1})\,, \tag{3.85}$$

where $r_{i+\frac{1}{2}}$ is the so-called upwind ratio of two consecutive flux gradients

$$r_{i+\frac{1}{2}} = \frac{\mathcal{F}_{i+1} - \mathcal{F}_i}{\mathcal{F}_i - \mathcal{F}_{i-1}}\,. \tag{3.86}$$

To achieve positivity we apply flux limiting. Hence, the expression $\frac{1-\kappa}{2} + \frac{1+\kappa}{2}\, r_{i+\frac{1}{2}}$ in the bracket of equation (3.85) has to be replaced by limiting function $\Phi(r_{i+\frac{1}{2}})$, we get

$$\mathcal{F}_{i+\frac{1}{2}} = \mathcal{F}_i + \frac{1}{2}\Phi(r_{i+\frac{1}{2}})\,(\mathcal{F}_i - \mathcal{F}_{i-1})\,. \tag{3.87}$$

This limiting function is supposed to define a high order accurate scheme in smooth monotone regions of the solution, where no wiggles will arise, whereas in regions of sharp gradient the limiter must prevent wiggles and thus enforce monotonicity and positivity. This means that $\Phi_{i+\frac{1}{2}} := \Phi(r_{i+\frac{1}{2}})$ has to work as an intelligent nonlinear switch between a high order scheme and a lower order, positive one. Note that for $\Phi_{i+\frac{1}{2}} = 0$ the first order upwind scheme is recovered, which is positive. Following Koren [40], we adopt the limiting procedure that has been proposed by Sweby [113]. For (3.87) scheme (3.76) reads

$$\frac{dn_i}{dt} + \frac{(1 + \frac{1}{2}\Phi_{i+\frac{1}{2}})(\mathcal{F}_i - \mathcal{F}_{i-1}) - \frac{1}{2}\Phi_{i-\frac{1}{2}}(\mathcal{F}_{i-1} - \mathcal{F}_{i-2})}{\Delta l} = 0\,, \tag{3.88}$$

where

$$r_{i-\frac{1}{2}} = \frac{\mathcal{F}_i - \mathcal{F}_{i-1}}{\mathcal{F}_{i-1} - \mathcal{F}_{i-2}}\,. \tag{3.89}$$

Let us assume $\mathcal{F}_i - \mathcal{F}_{i-1} \neq 0$, i.e. $r_{i-\frac{1}{2}} \neq 0$. Then (3.88) is identical to

$$\frac{dn_i}{dt} + \frac{1}{\Delta l}\left[(1 + \frac{1}{2}\Phi_{i+\frac{1}{2}}) - \frac{\frac{1}{2}\Phi_{i-\frac{1}{2}}}{r_{i-\frac{1}{2}}}\right](\mathcal{F}_i - \mathcal{F}_{i-1}) = 0\,. \tag{3.90}$$

Next assume $r_{i-\frac{1}{2}} = 0$. Then (3.88) is identical to (3.90) if we assume, a priori, that $\Phi_{i-\frac{1}{2}} = 0$ if $r_{i-\frac{1}{2}} = 0$. In this case both formulas yield $\frac{\partial n_i}{\partial t} = 0$, which is sensible in this case. If we now apply the positivity rule (3.83) to (3.90), then we immediately conclude that the flux (3.87) will define a positive scheme if the bracketed term in (3.90) is non-negative. This is true if the limiting values $\Phi_{i\pm\frac{1}{2}}$ satisfy the inequality

$$\frac{\Phi_{i-\frac{1}{2}}}{r_{i-\frac{1}{2}}} - \Phi_{i+\frac{1}{2}} \leq 2\,. \tag{3.91}$$

If we replace the above a priori assumption by the stronger assumption $\Phi_{i-\frac{1}{2}} = 0$ if $r_{i-\frac{1}{2}} \leq 0$, and further suppose that always $\Phi_{i-\frac{1}{2}}, \Phi_{i+\frac{1}{2}} \geq 0$, then (3.91) is true if $\Phi_{i-\frac{1}{2}} \leq 2r_{i-\frac{1}{2}}$.

In summary, the numerical flux (3.87) guarantees a positive semi-discrete solution, if the limiting function satisfies the constraints

$$\Phi_{i-\frac{1}{2}} = 0 \quad \text{if} \quad r_{i-\frac{1}{2}} \leq 0\,, \quad 0 \leq \Phi_{i-\frac{1}{2}}, \Phi_{i+\frac{1}{2}} \leq \zeta\,, \quad \Phi_{i-\frac{1}{2}} \leq 2r_{i-\frac{1}{2}} \tag{3.92}$$

for any constant $\zeta > 0$. This constant may serve as a parameter. If we take $\zeta = 2$ and in addition suppose that $\Phi_{i-\frac{1}{2}}$ and $\Phi_{i+\frac{1}{2}}$ can be uniquely expressed as function values of the respective slope ratios $r_{i-\frac{1}{2}}$ and $r_{i+\frac{1}{2}}$, then (3.91) defines a TVD region given in Figure 3.4 of Sweby [113] which he has introduced for Lax-Wendroff and Beam-Warming methods. For semi-discretization alone one is free to choose $\zeta > 0$ for obtaining positivity and by increasing ζ one can obtain more accuracy near peaks, see numerical examples in [36].

However, it was found in [36] that Range-Kutta methods for the time discretization of (3.90) gives good results by choosing $\zeta = 2$. Here, we have also chosen the same value throughout our calculations.

In this thesis, we will use the $\kappa = 1/3$-scheme and $\kappa = -1$-scheme for our numerical computations which are further explained in the following.

HR-$\kappa = 1/3$ scheme: If we take $\kappa = \frac{1}{3}$ equation (3.85) reduces to

$$\mathcal{F}_{i+\frac{1}{2}} = \mathcal{F}_i + \frac{1}{2}\left(\frac{1}{3} + \frac{2}{3}r_{i+\frac{1}{2}}\right)(\mathcal{F}_i - \mathcal{F}_{i-1}) \ . \tag{3.93}$$

The argument $r_{i+\frac{1}{2}}$ of this function is given by

$$r_{i+\frac{1}{2}} = \frac{\mathcal{F}_{i+1} - \mathcal{F}_i + \varepsilon}{\mathcal{F}_i - \mathcal{F}_{i-1} + \varepsilon} \, . \tag{3.94}$$

This expression has to be evaluated with a small parameter, e.g. $\varepsilon = 10^{-10}$, to avoid division by zero. The next step is to limit the expression $\frac{1}{3} + \frac{2}{3}r_{i+\frac{1}{2}}$ in the brackets of (3.93) in such a way that the constraints (3.92) are satisfied for all possible values of the slope ratios, whereas for smooth monotone solutions, where $r_{i+\frac{1}{2}} \approx 1$, the limited and unlimited fluxes takes the same values. This leads to the following expression for $\mathcal{F}_{i+\frac{1}{2}}$

$$\mathcal{F}_{i+\frac{1}{2}} = \mathcal{F}_i + \frac{1}{2}\phi\left(r_{i+\frac{1}{2}}\right)(\mathcal{F}_i - \mathcal{F}_{i-1}) \ , \tag{3.95}$$

where the flux limiting function ϕ according to Koren [40] is defined as

$$\phi(r_{i+\frac{1}{2}}) = \max\left(0, \min\left(2r_{i+\frac{1}{2}}, \min\left(\frac{1}{3} + \frac{2}{3}r_{i+\frac{1}{2}}, \zeta\right)\right)\right) \ . \tag{3.96}$$

Here we have chosen $\zeta = 2$. By comparing the unlimited second order approximation in (3.93) with the limited one in (3.95) together with (3.96), one can see that for $r_{i+\frac{1}{2}} \in [\frac{1}{4}, \frac{5}{2}]$ both approximations are the same, whereas the limiter function ϕ is bounded for $r_{i+\frac{1}{2}} < \frac{1}{4}$ and $r_{i+\frac{1}{2}} > \frac{5}{2}$ by $2r_{i+\frac{1}{2}}$ and 2, respectively. These limitations of ϕ are in accordance with the boundaries of the monotonicity domain for limiter functions introduced by Sweby [113] which is shown in Figure 3.4.

The motivation of the above limiting function is to use, as much as possible, the original high order scheme and to limit the scheme only when really needed. However, as for as we know, a unique best choice for all sorts of solution profiles does not exist. There are several other limiting functions proposed in the literature, namely, minmod, superbee and MC limiters etc. Each of these limiters leeds to a different high resolution scheme, see LeVeque [58].

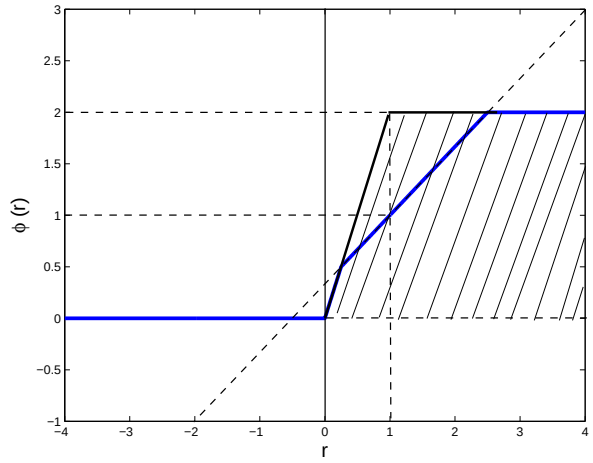

Figure 3.4: Limiter $\phi(r) = \max\left(0, \min\left(2r_{i+\frac{1}{2}}, \min\left(\frac{1}{3} + \frac{2}{3}r_{i+\frac{1}{2}}, 2\right)\right)\right)$ and Sweby's monotonicity domain.

Treatment of boundary cells: A disadvantage of the piecewise polynomial interpolations of the types (3.78) and (3.95) is that they can not be applied straightforward to include boundaries. First we consider the left boundary as shown in Figure 3.5a with inflow boundary condition. Here the cell face $l_{\frac{1}{2}}$ coincides with the inflow boundary. The flux across the inflow boundary $l_{\frac{1}{2}}$ does not need to be approximated as it is known exactly through the boundary condition. At the first inner cell face $l_{\frac{3}{2}}$, one gets an inconsistency problem. Since l_{-1} does not exist, as we refrain from introducing any dummy cells at boundaries, equations (3.78) and (3.95) can not be applied at $l_{\frac{3}{2}}$ for all $\kappa \in [-1, 1)$. In order to avoid this problem we use the first order approximation (3.77) at both boundaries of the first cell $\Omega_1 := [l_{\frac{1}{2}}, l_{\frac{3}{2}}]$, at left boundary of the cell $\Omega_2 := [l_{\frac{3}{2}}, l_{\frac{5}{2}}]$ and at both boundaries of the cell $\Omega_N := [l_{N-\frac{1}{2}}, l_{N+\frac{1}{2}}]$. Let $\mathcal{F}_{in}$ denotes the inflow flux then we have

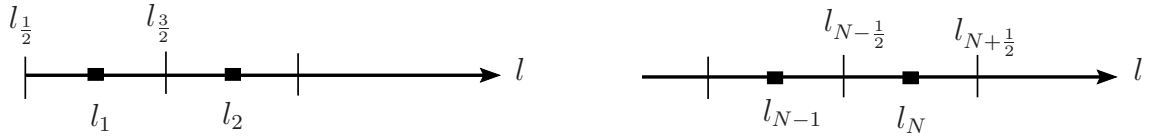

a. At inflow. b. At outflow.

Figure 3.5: Cell centered finite volumes near boundaries

$$\mathcal{F}_{\frac{1}{2}} = \mathcal{F}_{in}\,, \quad \mathcal{F}_{\frac{3}{2}} = \mathcal{F}_1, \quad \mathcal{F}_{N-\frac{1}{2}} = \mathcal{F}_{N-1}\,, \quad \mathcal{F}_{N+\frac{1}{2}} = \mathcal{F}_N\,. \tag{3.97}$$

Note that, we calculate $\mathcal{F}_{N-\frac{1}{2}}$ for the cell Ω_{N-1} by second order approximation (3.95). We have used first order approximation of $\mathcal{F}_{N-\frac{1}{2}}$ in the last cell Ω_N in order to guarantee the

positivity and stability of the scheme discussed below. The fluxes at all other interior cell faces can be calculated by using (3.95). Hence, at the boundary cells the scheme has first order accuracy. However this reduction in accuracy at the boundary cells will not reduce the global accuracy measured in L^1-norm. In case of the negative growth, i.e. $G < 0$, the discretization points (3.78)-(3.97) have to be mirrored at the considered volume boundaries $l_{i+\frac{1}{2}}$ for $i = 1, 2, \cdots N$.

Summary of the limited $\kappa = \frac{1}{3}$ scheme: if $G_{i+\frac{1}{2}} \geq 0$:

$$\begin{aligned}
&\text{if } i = 0 : && \mathcal{F}_{\frac{1}{2}} = \mathcal{F}_{in} \,, \\
&\text{if } i = 1, N-1, N : && \mathcal{F}_{i+\frac{1}{2}} = \mathcal{F}_i \,, \\
&\textit{else} : && \mathcal{F}_{i+\frac{1}{2}} = \mathcal{F}_i + \frac{1}{2}\phi\left(r_{i+\frac{1}{2}}\right)\left(\mathcal{F}_i - \mathcal{F}_{i-1}\right) \,, \\
& && r_{i+\frac{1}{2}} = \frac{\mathcal{F}_{i+1} - \mathcal{F}_i + \varepsilon}{\mathcal{F}_i - \mathcal{F}_{i-1} + \varepsilon} \,,
\end{aligned}$$

else:

$$\begin{aligned}
&\text{if } i = 0, 1, N-1 : && \mathcal{F}_{i+\frac{1}{2}} = \mathcal{F}_{i+1} \,, \\
&\text{if } i = N : && \mathcal{F}_{N+\frac{1}{2}} = \mathcal{F}_{in} \,, \\
&\text{else} : && \mathcal{F}_{i+\frac{1}{2}} = \mathcal{F}_{i+1} + \frac{1}{2}\phi\left(r_{i+\frac{1}{2}}\right)\left(\mathcal{F}_{i+1} - \mathcal{F}_{i+2}\right) \,, \\
& && r_{i+\frac{1}{2}} = \frac{\mathcal{F}_i - \mathcal{F}_{i+1} + \varepsilon}{\mathcal{F}_{i+1} - \mathcal{F}_{i+2} + \varepsilon} \,.
\end{aligned}$$

This algorithm gives a complete HR-$\kappa = 1/3$ scheme for homogeneous population balance equations (PBEs) which can be used for both positive and negative growth rates. The effect on the number density distribution due to nucleation is introduced as a left boundary condition, which is given as

$$n(t, l_0) = \frac{B_0(t, m)}{G_{\frac{1}{2}}(t, m)} \,. \tag{3.98}$$

Stability and convergence of the scheme: In oder to show the stability and convergence of the scheme we use the following definitions and theorems.

Definition 3.3 *The* **logarithmic norm** *of a matrix $A \in \mathbb{R}^{N\times N}$ corresponding to the L^1-norm is defined as, see Hundsdorfer and Verwer [37],*

$$\tilde{\nu}_1(A) = \max_j \left(Re(a_{jj}) + \sum_{i\neq j} |a_{ij}| \right) \,, \tag{3.99}$$

where $Re(z)$ denotes the real part of a complex number z.

The following theorem is useful for calculating the norm of the exponential of a matrix. The proof of this theorem is given in Hundsdorfer and Verwer [37].

Theorem 3.4 *If $A \in \mathbb{R}^{N\times N}$ and $\tilde{\alpha} \in \mathbb{R}$ then we have*

$$\tilde{\nu}_1(A) \le \tilde{\alpha} \iff \|e^{tA}\| \le e^{t\tilde{\alpha}}\,, \text{ for all } t \ge 0\,. \tag{3.100}$$

Proof. See Hundsdorfer and Verwer [37], Chapter 1, Theorem 2.4. □

Let us define

$$\mathcal{D}_i := \frac{1}{\Delta l}\left[(1+\frac{1}{2}\phi(r_{i+\frac{1}{2}})) - \frac{\frac{1}{2}\phi(r_{i-\frac{1}{2}})}{r_{i-\frac{1}{2}}}\right] \ge 0,\;\; \tilde{\mathcal{D}}_2 := \frac{1}{\Delta l}(1+\frac{1}{2}\phi(r_{\frac{5}{2}})) \ge 0\,. \tag{3.101}$$

The semi-discrete scheme (3.90) for the case $\kappa = 1/3$ and cells $\Omega_i,\;\; i = 1, 2, \cdots, N$ can be rewritten as

$$\frac{d\mathbf{n}(t)}{dt} = A\,\mathbf{n}(t) + \mathbf{b}(t,m)\,, \tag{3.102}$$

where $\mathbf{n} = [n_1, n_2, \cdots, n_N]^T$, $\mathbf{b} = [B_0(t,m)/\Delta l, 0, \cdots, 0]^T$,

$$A = \begin{pmatrix} -\frac{G_1}{\Delta l} & 0 & 0 & 0 & \cdots & \cdots & 0 \\ G_1\tilde{\mathcal{D}}_2 & -G_2\tilde{\mathcal{D}}_2 & 0 & 0 & \cdots & \cdots & 0 \\ 0 & G_2\mathcal{D}_3 & -G_3\mathcal{D}_3 & 0 & 0 & \cdots & 0 \\ 0 & 0 & G_3\mathcal{D}_4 & -G_4\mathcal{D}_4 & 0 & \cdots & 0 \\ \vdots & \vdots & \cdots & \vdots & \cdots & \vdots & \vdots \\ 0 & 0 & \cdots & 0 & G_{N-2}\mathcal{D}_{N-1} & -G_{N-1}\mathcal{D}_{N-1} & 0 \\ 0 & 0 & \cdots & 0 & 0 & \frac{G_{N-1}}{\Delta l} & -\frac{G_N}{\Delta l} \end{pmatrix}. \tag{3.103}$$

Since the HR-$\kappa = 1/3$ scheme can not be applied on the boundary cells, we have used the first order upwind scheme (3.77) on the cells $\Omega_1, \Omega_2, \Omega_N$. Now we include a useful definitions and theorem for stability and convergence from [37].

Definition 3.4 *Let $\mathbf{n}(t)$ and $\hat{\mathbf{n}}(t)$ be the vectors of numerical and exact solutions, respectively. The global discretization error is defined by $\epsilon(t) = \hat{\mathbf{n}}(t) - \mathbf{n}(t)$. The scheme is called convergent of order p if, for $\Delta l \to 0$,*

$$\|\epsilon(t)\| = \mathcal{O}(\Delta l^p)\,, \quad \text{uniformly for all } t\,. \tag{3.104}$$

Definition 3.5 *The semi-discrete system* (3.102) *is called stable if we have on all grids*

$$\|e^{tA}\| \leq K e^{t\tilde{\alpha}}\,,\ \textit{for}\ 0 \leq t \leq t_{\max}\,, \tag{3.105}$$

with some constant $k \geq 1$ *and* $\tilde{\alpha} \in \mathbb{R}$ *both independent of* Δl.

Theorem 3.5 *Consider the linear semi-discrete system* (3.102) *and assume the stability condition* (3.105) *is valid. Suppose further that* $\|\tau(t)\| \leq C\,\Delta l^q$ *for* $0 \leq t \leq t_{\max}$ *(consistency of order q) and* $\|\epsilon(0)\| \leq C_0\,\Delta l^q$ *with constant* $C, C_0 > 0$. *Then we have convergence of order* $p = q$ *with error bounds*

$$\|\epsilon(t)\| \leq K C_0\, e^{t\tilde{\alpha}} \Delta l^q + \frac{KC}{\tilde{\alpha}}(e^{t\tilde{\alpha}} - 1)\Delta l^q \ \ \textit{if}\ \tilde{\alpha} \neq 0,\ 0 \leq t \leq t_{\max}\,, \tag{3.106}$$

and

$$\|\epsilon(t)\| \leq K C_0\, \Delta l^q + KC\, t\, \Delta l^q \ \ \textit{if}\ \tilde{\alpha} = 0,\ 0 \leq t \leq t_{\max}\,. \tag{3.107}$$

Proof. See Hundsdorfer and Verwer [37], Chapter 1, Theorem 4.1 for the basic procedure. We just have to show the assumptions need to apply their results.

Since all the elements of the sparse matrix (3.103) are real and the non-diagonal elements are non-negative, the logarithmic norm (3.99) takes the following form

$$\tilde{\nu}_1 = \max_j \left(\sum_i a_{ij} \right)\,. \tag{3.108}$$

Since $\mathcal{D}_i \geq 0$ in (3.103) and according to equation (3.12) the growth term depends linearly on the crystal size l such that $0 \leq G_{i-1} \leq G_i$, we get

$$\sum_i a_{ij} = \mathcal{D}_i\,(G_{i-1} - G_i) \leq 0\,, \quad i = 3, 4, \cdots, N-1 \tag{3.109}$$

and

$$\sum a_{1j} = -\frac{G_1}{\Delta l} \leq 0\,,\ \sum_i a_{2j} = \tilde{\mathcal{D}}_2(G_1 - G_2) \leq 0\,,\ \sum_i a_{Nj} = \frac{G_{N-1} - G_N}{\Delta l} \leq 0\,. \tag{3.110}$$

Hence

$$\tilde{\nu}_1(A) \leq 0\,, \Longrightarrow\ \tilde{\alpha} = 0\,. \tag{3.111}$$

Consequently, Theorem 3.4 can be used to get

$$\|e^{tA}\| \leq 1 \tag{3.112}$$

which ensures the stability of the scheme. The error bound can be obtained by using Theorem 3.5 as

$$\|\epsilon(t)\| = C_0 \Delta l^q + C\, t\, \Delta l^q\,, \quad ,0 \leq t \leq t_{\max} \tag{3.113}$$

with $q = 2$ for $\kappa = -1, 1$ schemes and $q = 3$ for $\kappa = 1/3$-scheme and C_0, C_1 are constants. □

HR-$\kappa = -1$ scheme: In this scheme the expression for the numerical flux can be obtained from equation (3.78) by taking $\kappa = -1$. The scheme is given as [58]

$$\begin{aligned} \frac{dn_i}{dt} &= -\frac{1}{\Delta l}\left(\mathcal{F}_{i+\frac{1}{2}} - \mathcal{F}_{i-\frac{1}{2}}\right)\,, \\ \mathcal{F}_{i+\frac{1}{2}} &= n_i + \frac{1}{2}\varphi\left(\theta_{i+\frac{1}{2}}\right)\left(\mathcal{F}_{i+1} - \mathcal{F}_i\right)\,, \end{aligned} \tag{3.114}$$

where

$$\theta_{i+\frac{1}{2}} = \frac{\mathcal{F}_i - \mathcal{F}_{i-1} + \epsilon}{\mathcal{F}_{i+1} - \mathcal{F}_i + \epsilon}\,. \tag{3.115}$$

Here the limiting function φ uses the van Leer flux limiter [55]

$$\varphi(\theta_{i+\frac{1}{2}}) = \frac{|\theta_{i+\frac{1}{2}}| + \theta_{i+\frac{1}{2}}}{1 + |\theta_{i+\frac{1}{2}}|} \tag{3.116}$$

with the same boundary condition as given by (3.98). Moreover, one can also do a similar stability analysis for the the current HR-$\kappa = -1$ scheme as well.

3.3.2 1-D moving mesh technique

In this section we will explain the numerical procedure for solving the underlying one-dimensional PBE on the moving grid.

Initial mesh discretization: We start with same initial mesh as explained in (3.71)-(3.73). After having a discretized computational domain and assigning the initial data to each grid cell, the next step is to redistribute the mesh and solve the given PBE by using a finite volume scheme.

Note that, the mesh redistribution and the solution of PBE are two independent procedures which are discussed as follows.

Moving mesh technique: In the following, we give a brief overview of the moving mesh technique of Tang et al. [114, 115].

Let us consider, we have an initial partition $l^{[0]}_{i+\frac{1}{2}} = l_{i+\frac{1}{2}}$ of the computation domain $[l_0, l_{\max}]$ by the above mentioned procedure. To obtain a new mesh, move the grid point $l^{[v]}_{i+\frac{1}{2}}$ to $l^{[v+1]}_{i+\frac{1}{2}}$ according to the following Gauss-Seidel iterations

$$\omega\left(n^{[v]}_{i+1}\right)\left(l^{[v]}_{i+\frac{3}{2}} - l^{[v+1]}_{i+\frac{1}{2}}\right) - \omega\left(n^{[v]}_{i}\right)\left(l^{[v+1]}_{i+\frac{1}{2}} - l^{[v+1]}_{i-\frac{1}{2}}\right) = 0\,, \tag{3.117}$$

where ω is a positive weight function e.g. $\omega = \sqrt{1+\alpha_1|n|^2+\alpha_2|\nabla n|^2}$, called monitor function. Here α_1 and α_2 are some non-negative constants. The choice of monitor function ω is based on the properties of the physical solution. Therefore, it can be different for various physical problems. A good choice of monitor function can minimize the number of iteration needed to gain the better control of the grid-distribution near regions where solution $n_i(t)$ has large gradients. Note that, the new mesh $l^{[v+1]}$ generated by (3.117) keeps the monotonicity order of $l^{[v]}$. Repeat the procedure for a fixed number of iterations until $\left\|l^{[v+1]} - l^{[v]}\right\| < \epsilon$, where ϵ is some fixed given tolerance. The updated solution at the centroid of the new grid, i.e. $l^{[v+1]}_i$, is given by

$$n^{[v+1]}_i = \beta^{[v]}_{i+\frac{1}{2}} n^{[v]}_i - \gamma^{[v]}_{i+\frac{1}{2}}\left(\widehat{cn}^{[v]}_{i+\frac{1}{2}} - \widehat{cn}^{[v]}_{i-\frac{1}{2}}\right)\,, \tag{3.118}$$

where

$$\gamma^{[v]}_{i+\frac{1}{2}} = \left(l^{[v+1]}_{i+\frac{1}{2}} - l^{[v+1]}_{i-\frac{1}{2}}\right)^{-1}\,, \quad \beta^{[v]}_{i+\frac{1}{2}} = \gamma^{[v]}_{i+\frac{1}{2}} \cdot \left(l^{[v]}_{i+\frac{1}{2}} - l^{[v]}_{i-\frac{1}{2}}\right) \tag{3.119}$$

and numerical fluxes $\widehat{cn}^{[v]}_{i+\frac{1}{2}}$ are defined as

$$\widehat{cn}^{[v]}_{i+\frac{1}{2}} = \frac{c^{[v]}_{i+\frac{1}{2}}}{2}\left(n^{[v],+}_{i+\frac{1}{2}} + n^{[v],-}_{i+\frac{1}{2}}\right) - \frac{|c^{[v]}_{i+\frac{1}{2}}|}{2}\left(n^{[v],+}_{i+\frac{1}{2}} - n^{[v],-}_{i+\frac{1}{2}}\right)\,, \tag{3.120}$$

where the speed $c^{[v]}_{i+\frac{1}{2}}$ is defined as

$$c^{[v]}_{i+\frac{1}{2}} = l^{[v]}_{i+\frac{1}{2}} - l^{[v+1]}_{i+\frac{1}{2}} \tag{3.121}$$

and $n^{[v],+}_{i+\frac{1}{2}}$ and $n^{[v],-}_{i+\frac{1}{2}}$ are given by

$$n^{[v],+}_{i+\frac{1}{2}} = n^{[v]}_{i+1} + \frac{1}{2}\left(l^{[v+1]}_{i+\frac{1}{2}} - l^{[v+1]}_{i+\frac{3}{2}}\right)\mathcal{S}^{[v]}_{i+1}\,, \tag{3.122}$$

$$n^{[v],-}_{i+\frac{1}{2}} = n^{[v]}_{i} + \frac{1}{2}\left(l^{[v+1]}_{i+\frac{1}{2}} - l^{[v+1]}_{i-\frac{1}{2}}\right)\mathcal{S}^{[v]}_{i}\,. \tag{3.123}$$

Here $\mathcal{S}^{[v]}_i$ is the approximation of the slope $\frac{\partial n^{[v]}}{\partial l}$ at l_i and is defined as

$$\mathcal{S}^{[v]}_i = \left[\text{sign}(\mathcal{S}^{[v],+}_i) + \text{sign}(\mathcal{S}^{[v],-}_i)\right]\frac{\left|\mathcal{S}^{[v],+}_i \mathcal{S}^{[v],-}_i\right|}{\left|\mathcal{S}^{[v],+}_i\right| + \left|\mathcal{S}^{[v],-}_i\right|} \tag{3.124}$$

with

$$\mathcal{S}_i^{[v],+} = \frac{n_{i+1}^{[v]} - n_i^{[v]}}{l_{i+1}^{[v+1]} - l_i^{[v+1]}}, \qquad \mathcal{S}_i^{[v],-} = \frac{n_i^{[v]} - n_{i-1}^{[v]}}{l_i^{[v+1]} - l_{i-1}^{[v+1]}}.$$

In practice it is common to use some temporal or spatial smoothing on the monitor function ω to obtain smoother meshes. One of the reasons for using smoothing is to avoid singular meshes and large approximation errors around the stiff solution area. In this work, we have used a low pass filter for smoothing the monitor function [114, 115]

$$\omega_i \longleftarrow \frac{1}{4}\left(\omega_{i+1} + 2\omega_i + \omega_{i-1}\right), \tag{3.125}$$

where $\omega_i = \omega\left(n_i\right)$. This completes the moving mesh procedure. The next step is to solve the population balance equation on the new adaptive grid.

There are slight differences among the numerical schemes of the previous subsection for the fixed uniform grid and those on the moving mesh. However, for better explanation and for the sack of completeness we again present them in detail on the moving grid.

Semi-discrete high resolution schemes: We evaluate the underlying PBE by using high-resolution finite volume schemes on the new mesh points $\tilde{l}_i$, which are obtained after moving the grid points, to obtain approximation of the number density at next time level. This part is independent of the moving mesh procedure. As a result, one can use any efficient modern numerical technique for solving the PBEs under consideration. In the following we consider the same high resolution schemes presented in the previous subsection. Integration of (3.3) over the control volume $\tilde{\Omega}_i = \left[\tilde{l}_{i-\frac{1}{2}}, \tilde{l}_{i+\frac{1}{2}}\right]$ leads to the following semi-discrete equation

$$\frac{dn_i}{dt} = -\frac{1}{\Delta\tilde{l}_i}\left(\mathcal{F}_{i+\frac{1}{2}} - \mathcal{F}_{i-\frac{1}{2}}\right), \quad \forall\ i = 1, ..., N\,. \tag{3.126}$$

Here $\mathcal{F}_{i\pm\frac{1}{2}} = (Gn)_{i\pm\frac{1}{2}}$ and $n_i = n_i(t)$ denotes the average value of the number density in each cell $\tilde{\Omega}_i$, i.e.

$$n_i = \frac{1}{\Delta\tilde{l}_i}\int_{\tilde{\Omega}_i} n(t,l)\, dl, \tag{3.127}$$

where $\Delta\tilde{l}_i = \tilde{l}_{i+\frac{1}{2}} - \tilde{l}_{i-\frac{1}{2}}$.

First order upwind scheme: In this case the fluxes are exactly the same as given by (3.77).

High order accuracy: High order accuracy can be easily obtained by piecewise polynomial interpolation. One can take for instance [40]

$$\mathcal{F}_{i+\frac{1}{2}} = \mathcal{F}_i + \frac{(1+\kappa)}{4}\cdot\frac{\Delta\tilde{l}_i\left(\mathcal{F}_{i+1} - \mathcal{F}_i\right)}{\Delta\tilde{l}_{i+\frac{1}{2}}} + \frac{1-\kappa}{4}\cdot\frac{\Delta\tilde{l}_i\left(\mathcal{F}_i - \mathcal{F}_{i-1}\right)}{\Delta\tilde{l}_{i-\frac{1}{2}}}, \tag{3.128}$$

where $\Delta\tilde{l}_{i\pm\frac{1}{2}} = \pm(\tilde{l}_{i\pm1} - \tilde{l}_i)$ and $\kappa \in [-1, 1]$. Similarly one can write expression for $\mathcal{F}_{i-\frac{1}{2}}$.

HR-$\kappa = 1/3$ scheme: As given in (3.95), in this scheme the flux $\mathcal{F}_{i+\frac{1}{2}}$ at the right boundary of the control volume $\tilde{\Omega}_i$ is calculated according to the following limited formulation

$$\mathcal{F}_{i+\frac{1}{2}} = \mathcal{F}_i + \frac{1}{2}\phi\left(r_{i+\frac{1}{2}}\right)(\mathcal{F}_i - \mathcal{F}_{i-1}) \,, \tag{3.129}$$

where the flux limited function Φ in this case is defined as

$$\phi(r_{i+\frac{1}{2}}) = \max\left(0, \min\left(2r_{i+\frac{1}{2}}, \min\left(\frac{1}{3}\frac{\Delta\tilde{l}_i}{\Delta\tilde{l}_{i-\frac{1}{2}}} + \frac{2r_{i+\frac{1}{2}}}{3}\frac{\Delta\tilde{l}_i}{\Delta\tilde{l}_{i+\frac{1}{2}}}, 2\right)\right)\right) \tag{3.130}$$

and the argument $r_{i+\frac{1}{2}}$ of the function ϕ is the so-called upwind ratio of two consecutive solution gradients as given by (3.94). Analogously one can formulate the flux $\mathcal{F}_{i-\frac{1}{2}}$ at the left boundary of the control volume $\tilde{\Omega}_i$.

As explained in Section 3.3, the current scheme can not be applied up to and including boundaries. Hence, one has to use the first order upwind scheme (3.77) in the boundary cells.

HR-$\kappa = -1$ scheme: In this scheme the expression for the numerical flux can be obtained from equation (3.128) by taking $\kappa = -1$. In this case the flux $\mathcal{F}_{i+\frac{1}{2}}$ in limited form is given as

$$\mathcal{F}_{i+\frac{1}{2}} = \mathcal{F}_i + \frac{\Delta\tilde{l}_i}{2\Delta\tilde{l}_{i-\frac{1}{2}}}\varphi\left(\theta_{i+\frac{1}{2}}\right)(\mathcal{F}_{i+1} - \mathcal{F}_i) \,, \tag{3.131}$$

$$\text{where} \qquad \theta_{i+\frac{1}{2}} = \frac{\mathcal{F}_i - \mathcal{F}_{i-1} + \varepsilon}{\mathcal{F}_{i+1} - \mathcal{F}_i + \varepsilon} \,.$$

Here the limiting function φ is given by (3.116). Analogously one can also formulate the flux $\mathcal{F}_{i-\frac{1}{2}}$.

ODE-solver: The semi-discrete equations (3.76) and (3.126) results in the system of ordinary differential equations (ODEs). To get the grid values of the number density at next time step the system of ODEs has to be solved by using an ODE-solver. In [36] it was showed theoretically and numerically that Range-Kutta methods guarantee the positive time discretization of the above schemes if one takes the time step Δt according to

$$\Delta t = \frac{\Delta l}{(1 + \zeta/2)\max\limits_i |G_i(t)|} \,. \tag{3.132}$$

However, in this thesis we use an adaptive RK45 method which is an embedded Runge-Kutta methods of order four and five. The method works very well for our selected numerical test problems. All the computations are performed in the programming language

C/C++.

In the following we give an algorithm for the solving the one-dimensional homogeneous PBE by using the above formulation.

Algorithm:

1. Given initial uniform partition $l_{i+\frac{1}{2}}^{[0]} = l_{i+\frac{1}{2}}$ of the computation domain $\Omega_c = [l_0, l_{\max}]$ and the grid values $n_i^{[0]}$ based on the cell average for the initial data $n(0, l)$.

2. Move the grid point $l_{i+\frac{1}{2}}^{[v]}$ to $l_{i+\frac{1}{2}}^{[v+1]}$ according to equation (3.117) and compute $n_i^{[v+1]}$ by using the equations (3.118)-(3.124) for $v \geq 0$. Repeat the updating procedure until $\|l_{i+\frac{1}{2}}^{[v+1]} - l_{i+\frac{1}{2}}^{[v]}\| \leq \epsilon$.

3. Evaluate the underlying PBE by using one of the above mentioned high resolution finite volume schemes on the mesh $l_{i+\frac{1}{2}}^{[v+1]}$ to obtain the numerical approximation at the next time level, say $t^{m+1},\ m \geq 0$.

4. If $t^{m+1} \leq t_{\max}$ then $n_i^{[0]} = n_i^{m+1}$, $l_{i+\frac{1}{2}}^{[0]} = l_{i+\frac{1}{2}}^{[v+1]}$ and *go to step nr. 2.* By n_i^{m+1} we mean the updated grid values of the number density at the next time level, say t^{m+1}, and $t_{\max}$ is the final simulation time.

Note that in case of uniform mesh the step 2 is simply skipped.

3.4 2-D Moving Mesh Technique

In this case we are interested to solve the two-dimensional PBE of the form (3.69).

Mesh discretization: Let N_ξ and N_η be large integers in the ξ and $\eta-$directions, respectively. We assume a Cartesian grid with a rectangular domain $[\xi_0, \xi_{\max}] \times [\eta_0, \eta_{\max}]$ which is covered by cells $C_{ij} \equiv \left[\xi_{i-\frac{1}{2}}, \xi_{i+\frac{1}{2}}\right] \times \left[\eta_{j-\frac{1}{2}}, \eta_{j+\frac{1}{2}}\right]$ for $1 \leq i \leq N_\xi$ and $1 \leq j \leq N_\eta$. The representative coordinates of the population in cell C_{ij} are denoted by (ξ_i, η_j). Here

$$(\xi_{1/2}, \eta_{1/2}) = (\xi_0, \eta_0),\ \ \xi_i = (\xi_{i-1/2} + \xi_{i+1/2})/2,\ \ \eta_j = (\eta_{j-1/2} + \eta_{j+1/2})/2 \tag{3.133}$$

and

$$\Delta\xi_i = \xi_{i+1/2} - \xi_{i-1/2}\,, \quad \Delta\eta_j = \eta_{j+1/2} - \eta_{j-1/2}\,. \tag{3.134}$$

The cell averaged values $n_{i,j}(t_0)$ of the initial data $n_0(\xi,\eta) = n(t_0,\xi,\eta)$ are given as

$$n_{i,j}(t_0) = \frac{1}{\Delta\xi_i \Delta\eta_j} \int_{C_{ij}} n_0(\xi,\eta)\, d\eta d\xi \,. \tag{3.135}$$

Like in the one-dimensional case the next steps are to redistribute the mesh and solve the underlying PBE. As before, both procedures are independent of each other.

Moving mesh technique: The moving mesh procedure for the two-dimensional case follow the same lines as in the one-dimensional case. We refer the reader to the article of Tang et al. [114, 115] where they have explained the procedure in detail. Here, we skip the derivation of current moving mesh technique in two-dimensional case.

High resolution schemes: After moving the grid, the next task is to solve the PBE. The solution of two-dimensional PBE (3.69) by high resolution schemes involves two steps as follows:

Step 1: The first step consists of applying the high resolution scheme to the homogeneous equation of the form

$$\frac{\partial n(t,\xi,\eta)}{\partial t} = -\frac{\partial[G_1(t,\xi,m)n(t,\xi,\eta)]}{\partial \xi} - \frac{\partial[G_2(t,\eta,m)n(t,\xi,\eta)]}{\partial \eta} \,. \tag{3.136}$$

Integration of equation (3.136) over the control volume $\tilde{C}_{ij}$ of the new grid, which is obtained after moving the grid points, gives us the following semi-discrete formulation of finite volume schemes

$$\frac{dn_{i,j}}{dt} = -\frac{\left(\mathcal{F}_{i+\frac{1}{2},j} - \mathcal{F}_{i-\frac{1}{2},j}\right)}{\Delta\tilde{\xi}_i} - \frac{\left(\mathcal{G}_{i,j+\frac{1}{2}} - \mathcal{G}_{i,j-\frac{1}{2}}\right)}{\Delta\tilde{\eta}_j} \,. \tag{3.137}$$

Here $\mathcal{F}_{i\pm\frac{1}{2},j} = (G_1 n)_{i\pm\frac{1}{2},j}$ and $\mathcal{G}_{i,j\pm\frac{1}{2}} = (G_2 n)_{i,j\pm\frac{1}{2}}$. Similar to the one-dimensional case, different approximations of the cell interface fluxes lead to different schemes. Let us assume that $G_1, G_2 > 0$, then we have the following schemes:

First order upwind scheme: In this case the first order accurate upwind scheme is obtained by taking the backward differences

$$\mathcal{F}_{i+\frac{1}{2},j} = \mathcal{F}_{i,j} \,, \quad \mathcal{F}_{i-\frac{1}{2},j} = \mathcal{F}_{i-1,j} \,, \tag{3.138}$$

$$\mathcal{G}_{i,j+\frac{1}{2}} = \mathcal{G}_{i,j} \,, \quad \mathcal{G}_{i,j-\frac{1}{2}} = \mathcal{G}_{i,j-1} \,. \tag{3.139}$$

Where $\mathcal{F}_{i,j} = (G_1 n)_{i,j}$ and $\mathcal{G}_{i,j} = (G_2 n)_{i,j}$.

HR-$\kappa = 1/3$ scheme: In this scheme the flux is calculated according to following limited formulation

$$\mathcal{F}_{i+\frac{1}{2},j} = \mathcal{F}_{i,j} + \frac{1}{2}\phi\left(\mu_{i+\frac{1}{2},j}\right)\left(\mathcal{F}_{i,j} - \mathcal{F}_{i-1,j}\right), \tag{3.140}$$

$$\mathcal{G}_{i,j+\frac{1}{2}} = \mathcal{G}_{i,j} + \frac{1}{2}\phi\left(\nu_{i,j+\frac{1}{2}}\right)\left(\mathcal{G}_{i,j} - \mathcal{G}_{i,j-1}\right), \tag{3.141}$$

where the flux limited function ϕ according to Koren [40] is defined as

$$\phi(\mu_{i+\frac{1}{2},j}) = \max\left(0, \min\left(2\mu_{i+\frac{1}{2},j}, \min\left(\frac{1}{3}\frac{\Delta\tilde{\xi}_i}{\Delta\tilde{\xi}_{i-\frac{1}{2}}} + \frac{2\mu_{i+\frac{1}{2},j}}{3}\frac{\Delta\tilde{\xi}_i}{\Delta\tilde{\xi}_{i+\frac{1}{2}}}, 2\right)\right)\right), \tag{3.142}$$

$$\phi(\nu_{i,j+\frac{1}{2}}) = \max\left(0, \min\left(2\nu_{i,j+\frac{1}{2}}, \min\left(\frac{1}{3}\frac{\Delta\tilde{\eta}_j}{\Delta\tilde{\eta}_{j-\frac{1}{2}}} + \frac{2\nu_{i,j+\frac{1}{2}}}{3}\frac{\Delta\tilde{\eta}_j}{\Delta\tilde{\eta}_{j+\frac{1}{2}}}, 2\right)\right)\right) \tag{3.143}$$

and the arguments $\mu_{i,j+\frac{1}{2}}$ and $\nu_{i,j+\frac{1}{2}}$ of the function ϕ are the so-called upwind ratio of two consecutive flux gradients

$$\mu_{i+\frac{1}{2},j} = \frac{\mathcal{F}_{i+1,j} - \mathcal{F}_{i,j} + \varepsilon}{\mathcal{F}_{i,j} - \mathcal{F}_{i-1,j} + \varepsilon}, \qquad \nu_{i,j+\frac{1}{2}} = \frac{G_{i,j+1} - G_{i,j} + \varepsilon}{G_{i,j} - G_{i,j-1} + \varepsilon}. \tag{3.144}$$

Again $\varepsilon = 10^{-10}$ in order to avoid division by zero. Similarly, one can calculate the fluxes $\mathcal{F}_{i-\frac{1}{2},j}$ and $\mathcal{G}_{i,j-\frac{1}{2}}$.

HR-$\kappa = -1$ scheme: In this case we have

$$\mathcal{F}_{i+\frac{1}{2},j} = \mathcal{F}_{i,j} + \frac{\Delta\tilde{\xi}_i}{2\Delta\tilde{\xi}_{i-\frac{1}{2}}}\varphi(\theta^{\xi}_{i+\frac{1}{2},j})(\mathcal{F}_{i,j} - \mathcal{F}_{i-1,j}), \tag{3.145}$$

$$\mathcal{G}_{i,j+\frac{1}{2}} = \mathcal{G}_{i,j} + \frac{\Delta\tilde{\eta}_j}{2\Delta\tilde{\eta}_{j-\frac{1}{2}}}\varphi(\theta^{\eta}_{i,j+\frac{1}{2}})(\mathcal{G}_{i,j} - \mathcal{G}_{i,j-1}), \tag{3.146}$$

where

$$\theta^{\xi}_{i+\frac{1}{2},j} = \frac{\mathcal{F}_{i,j} - \mathcal{F}_{i-1,j} + \varepsilon}{\mathcal{F}_{i+1,j} - \mathcal{F}_{i,j} + \varepsilon}, \qquad \theta^{\eta}_{i,j+\frac{1}{2}} = \frac{\mathcal{G}_{i,j} - \mathcal{G}_{i,j-1} + \varepsilon}{\mathcal{G}_{i,j+1} - \mathcal{G}_{i,j} + \varepsilon}. \tag{3.147}$$

In a similar manner one can calculate the fluxes $\mathcal{F}_{i-\frac{1}{2},j}$ and $\mathcal{G}_{i,j-\frac{1}{2}}$. Here the limiting function φ is the same as given by (3.116). It has already been shown that these high resolution schemes are also second order accurate, see [40, 58, 59]. The above schemes on the non-uniform grid reduces to the schemes on fixed uniform grid when $\Delta\tilde{\xi}_i = \Delta\tilde{\xi}_{i\pm\frac{1}{2}} = \Delta\xi$ and $\Delta\tilde{\eta}_j = \Delta\tilde{\eta}_{j\pm\frac{1}{2}} = \Delta\eta$.

Step 2: After solving the above homogeneous PBE by a high resolution scheme, the second step is to add the non-homogeneous term, given on the right hand side of (3.69), to the

updated grid values of the distribution function $n_{i,j}(t)$. This technique is usually called Godunov splitting and is repeated at each time step. This method is second order accurate for the first and last time step. It provides accuracy indistinguishable from Strang splitting which is formally second-order accurate for all time steps, for details see LeVeque et al. [59]. Note that, in case of nucleation at minimum crystal size, the non-homogeneous term which includes only the nucleation term, is only added to the updated number density at the first updating cell, i.e. $n_{0,0}(t)$ in this case. Furthermore, in the one-dimensional case instead of using nucleation as a boundary condition one can also use the same Godunov splitting procedure. One can easily see that in this particular case both procedures are the same.

3.5 Numerical Test Problems

In order to validate the current high resolution schemes and moving mesh technique, several numerical test problems for the one and two-dimensional batch crystallization processes are considered. The results of the proposed numerical schemes are compared with each other and available analytical solutions. In order to demonstrate the importance of the moving mesh technique, the numerical solutions on both uniform and adaptive grids are also compared with each other. In some test cases, we also give the total/relative errors. As mentioned before, the choice of monitor function is mainly based on the properties of the physical solution. The selected monitor functions in the following test problems give minimum number of iterations to control the grid-distribution in the vicinity of the large gradients in the solution. However currently, we have no such empirical relation which can be used for the choice of monitor function. Therefore, all the monitor functions used in the following problems are somehow chosen intuitively.

3.5.1 One-dimensional problems

Here, we present several one-dimensional test problems of batch crystallization processes.

Test problem 1:

The previous discussions about requirements on numerical schemes show that, the dynamic behavior of particulate processes can be better approximated if the hyperbolic part of the population balance equation is computed more accurately. Therefore, the aim of this simple problem is to demonstrate the importance of high resolution schemes for the correct numerical approximation of the hyperbolic part of the population balance equation with sharp discontinuities in the solution. Although most of the initial particles distributions in the real processes are of Gaussian-type, these distributions can be very sharp. An additional reason of discontinuity can be the processes operation. For example, injection of seeds in an initially supersaturated solution will result in a burst of nearly zero sized particles due to secondary nucleation. Hence the present hard test case may help in choosing the right

numerical method. This problem was also considered in [77]. We start with a simple homogeneous population balance equation (3.3) and take the growth rate $G = 1.0\,\mu m/s$. The initial data for the number density are given by [77]:

$$n(0,l) = \begin{cases} 1 \times 10^{10}\,\#/\mu m & \text{if } 10\,\mu m < l < 20\,\mu m\,, \\ 0 & \text{elsewhere}\,. \end{cases} \tag{3.148}$$

Here the unit $\#/\mu m$ denotes number per micrometer. The crystal size range $0 \leq l \leq 100\,\mu m$ is discretized into 100 mesh elements. The analytical solution of this problem with initial profile $n(0,l) = n_0(l)$ is simply the initial profile which is translated by a distance Gt, i.e.

$$n(t,l) = n_0(l - Gt)\,.$$

The monitor function ω is taken as

$$\omega = \sqrt{1 + \alpha_1 \left(\frac{n_l}{\max|n|}\right)^2 + \alpha_2 \left(\frac{n}{\max|n|}\right)^2}\,. \tag{3.149}$$

Here, we take $\alpha_1 = \alpha_2 = 4 \times 10^3$ and approximate the derivative n_l of the number density n by central difference formula. The averaged number density after 60 seconds is shown in Figure 3.6. The comparison of numerical results at moving grid with those at uniform grid shows that moving mesh technique further improved the results. The $HR-\kappa = 1/3$ scheme has better results as compared to the first order upwind scheme and $HR-\kappa = -1$ scheme. In Figure 3.7 the numerical results of the current schemes are also compared with the CE/SE method of Chang [11] and the commercial software PARSIVAL [122]. The results show that the CE/SE method resolve the density profile very well. However, one can see a small overshoot in the PARSIVAL results on the left corner of the step function. This does not appear in the results of finite volume schemes. From the figure it is clear that PARSIVAL has also resolved the discontinuous profiles quite well. The CE/SE method results are better than all other schemes. Table 3.1 gives the total L^1 and L^2-errors in the current numerical schemes at uniform and adaptive grids which are normalized with the total sum of the absolute values of the exact solution, i.e.

$$L^1 - error = \frac{\sum_{i=1}^{N} |n_i^e - n_i| \Delta l_i}{\sum_{i=1}^{N} |n_i^e| \Delta l_i}\,, \quad L^2 - error = \frac{\sqrt{\sum_{i=1}^{N} (n_i^e - n_i)^2 \Delta l_i}}{\sum_{i=1}^{N} |n_i^e| \Delta l_i}\,. \tag{3.150}$$

Here $n_i^e,\ n_i$ represent the exact and numerical solutions in cell Ω_i, respectively. One can clearly see that $HR - \kappa = 1/3$ provides less errors. For all schemes the total error reduces at adaptive grid.

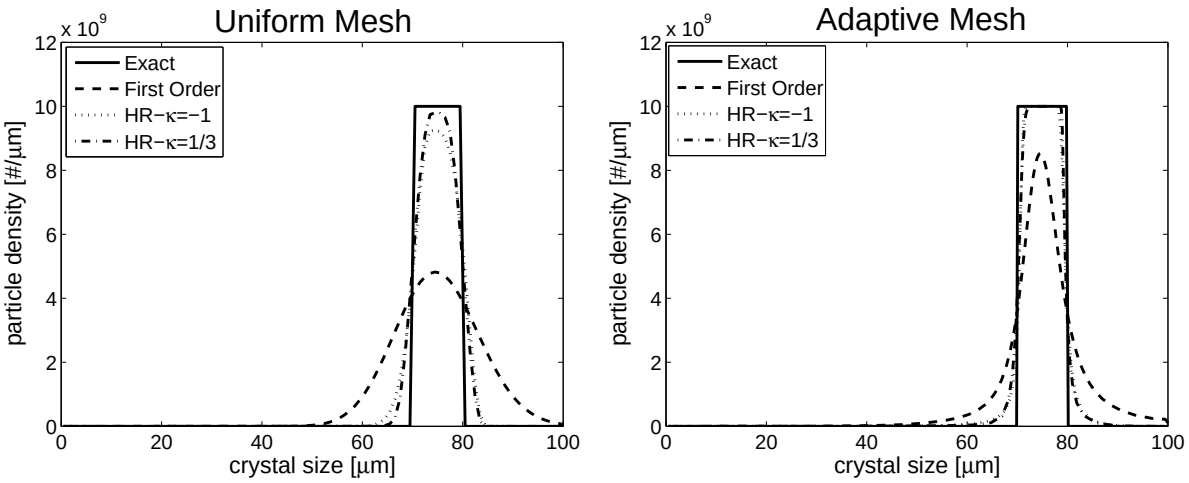

Figure 3.6: Test problem 1: Uniform and adaptive mesh results for $N = 100$ at $t = 60\,s$.

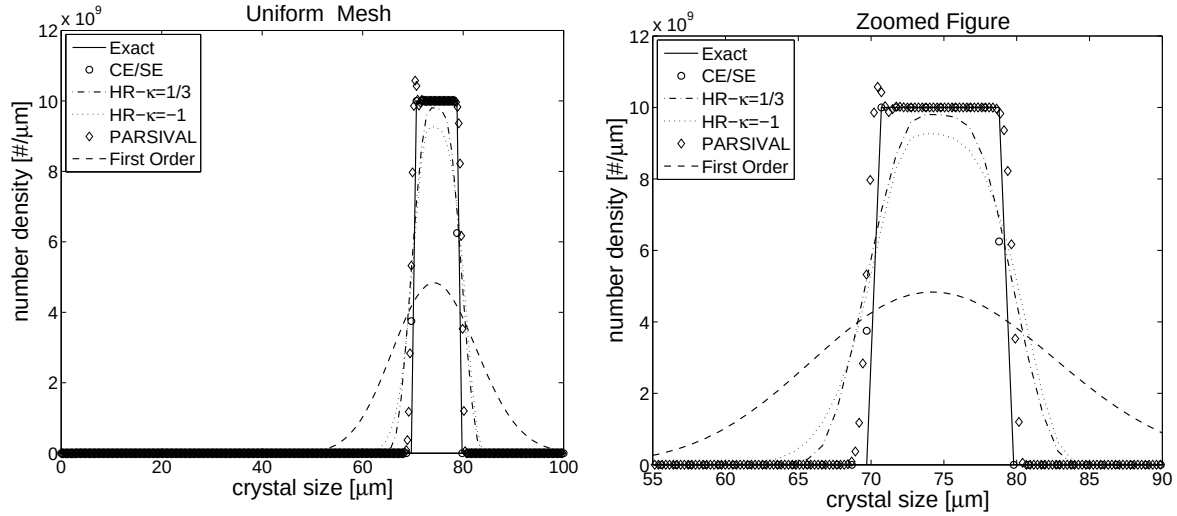

Figure 3.7: Test problem 1: Comparison of different schemes on uniform mesh.

Table 3.1: Total errors in the schemes for the Test problem 1

Method	*Uniform*		*Adaptive*	
	L^1-*error*	L^2-*error*	L^1-*error*	L^2-*error*
First order scheme	1.022	0.190	0.628	0.127
HR-$\kappa = -1$ scheme	0.341	0.094	0.199	0.073
HR-$\kappa = 1/3$ scheme	0.270	0.085	0.195	0.071

Test problem 2:

In order to further analyze the performance of above numerical schemes and moving mesh technique, we consider the numerical example of Leonard and Niknafs [56] with slight modifications. We start again with a homogeneous population balance equation of the type (3.3) with constant growth rate $G = 1.0\,\mu m/s$. The analytical solution of this problem for the initial profile $n(0,l) = n_0(l)$ is given as

$$n(t,l) = n_0(l - Gt)\,.$$

In order to perform a clear comparison of the schemes we divide the crystal length $l_{max} = 20\,\mu m$ into 100 equal subintervals. The initial data for the number density are given by

$$n(0,l) = \begin{cases} \frac{1}{\sqrt{0.32\pi}} e^{-500(0.1l-0.3)^2}\ \#/\mu m & \text{if } 2\,\mu m < l \le 4\,\mu m\,, \\ 1\,\#/\mu m & \text{if } 6\,\mu m < l \le 8\,\mu m\,, \\ 1 - |l-11|\,\#/\mu m & \text{if } 10\,\mu m < l \le 12\,\mu m\,, \\ \sqrt{1 - 100(0.1l-1.5)^2}\,\#/\mu m & \text{if } 14\,\mu m < l \le 16\,\mu m\,, \\ 0 & \text{elsewhere}\,. \end{cases} \tag{3.151}$$

Here the monitor function is the same as in (3.149) with $\alpha_1 = 9 \times 10^3$ and $\alpha_2 = 2 \times 10^2$. Figure 3.8 gives the comparison of different schemes. Again the results with moving mesh technique have better resolution and $HR - \kappa = 1/3$ is superior than others. In Figure 3.9 the numerical results of the current schemes are also compared with the CE/SE method of Chang [11] and the commercial software PARSIVAL [122]. Once again the CE/SE method has better results than other schemes. Again a small overshoot is visible in the PARSIVAL results.

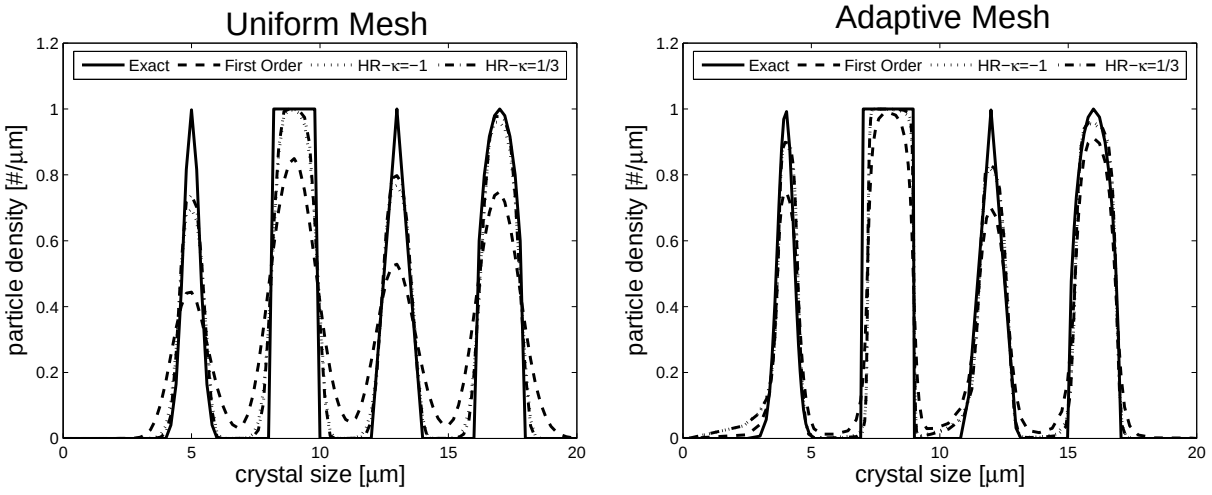

Figure 3.8: Test problem 2: Uniform and adaptive mesh results for $N = 100$ at $t = 1\,s$.

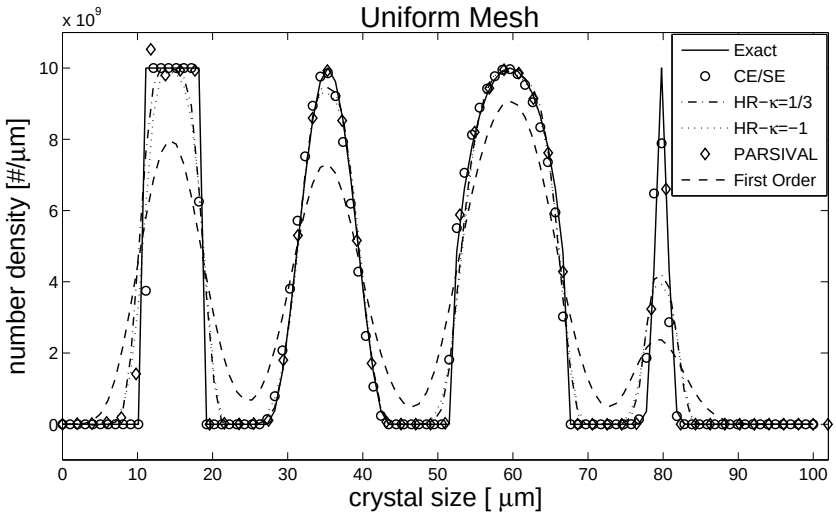

Figure 3.9: Test problem 2: Comparison of different schemes on uniform mesh.

Test problem 3:

This problem was considered by Lim et al. [61]. Suppose that the stiff nucleation takes place at a minimum crystal size ($l_0 = 0$) as a function of time

$$n(t, 0) = 100 + 10^6 \exp(-10^4 (t - 0.215)^2)\, \#/\mu m. \tag{3.152}$$

Hence, we consider the PBE (3.3) with nucleation as a left boundary condition. The crystal size and time ranges are $0 \leq l \leq 2.0\,\mu m$ and $0 \leq t \leq 0.5\,s$, respectively. The square step initial condition for the number density is given as

$$n(0, l) = \begin{cases} 100\,\#/\mu m & \text{for } 0.4\,\mu m \leq l \leq 0.6\,\mu m\,, \\ 0.01\,\#/\mu m & \text{elsewhere}\,. \end{cases} \tag{3.153}$$

Here we consider constant growth rate with $G = 1.0\,\mu m$. The analytical solution is given as [61]

$$n(t, l) = \begin{cases} 100 + 10^6 \exp(-10^4((Gt - l) - 0.215)^2)\,\#/\mu m & \text{for } 0.0 \leq l \leq Gt\,\mu m\,, \\ 100\,\#/\mu m & \text{for } 0.4\,\mu m \leq l - Gt \leq 0.6\,\mu m\,, \\ 0.01\,\#/\mu m & \text{elsewhere}\,. \end{cases} \tag{3.154}$$

In the solution, a square step discontinuous shock and a narrow wave which is originated from nucleation move along the propagation path-line, $l = l_0 + Gt$. The numerical test is carried out on 200 grid points. The results are shown in Figures 3.10. One can see that the first order upwind scheme is very diffusive, while the high resolution scheme resolves all the profiles of the solution quite well. The stiff nucleation at the left boundary, which produces a sharp peak and a second step profile, makes this problem much harder than the previous problems.

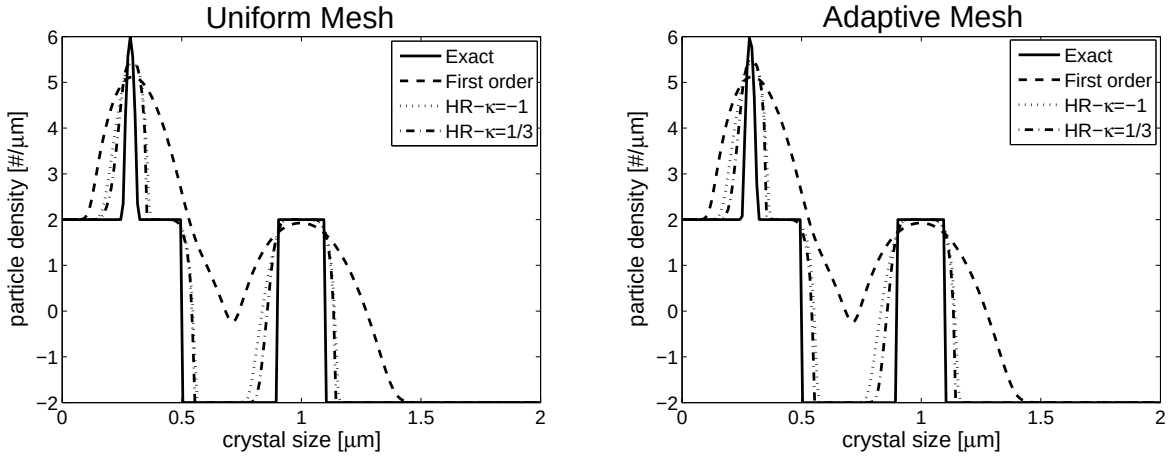

Figure 3.10: Test problem 3: Uniform and adaptive mesh results for $N = 100$ at $t = 60\,s$.

Test problem 4:

This problem is taken from [65, 66]. Here the nucleation rate term is a function of time-dependent solute mass and growth rate term is a function of both mass and crystal size. We select this problem in oder to show the accuracy and efficiency of the HR-schemes for real batch process. In the present case, the growth rate is given by equation (3.12) with $a_1 = 1$ and $a_2 = 0.1$, nucleation rate is given by (3.15), and the mass balance of the solute in the liquid phase is given by (3.6).

The kinetic parameters reported for the crystallization of potassium nitrate (KNO_3) crystals were used, see Table 3.2. The saturated mass is given as

$$m_{\text{sat}}(t)\left[\frac{g}{g \text{ of water}}\right] = 1.721 \times 10^{-4}T^2(t) - 5.88 \times 10^{-3}T(t) + 0.1286\,. \tag{3.155}$$

The simulation used an exponentially decaying temperature trajectory

$$T(t)[^oC] = 32 - 4(1 - e^{-\frac{t}{18600}})\,. \tag{3.156}$$

The initial data are given as

$$n(0,l) = \begin{cases} -3.48 \times 10^{-4}l^2 + 0.136l - 13.3\,\#/m & \text{if } 180.5 \le l \le 210.5\,, \\ 0 & \text{elsewhere.} \end{cases} \tag{3.157}$$

In this problem we take the monitor function of the form $\omega = 1/\sqrt{1 + \alpha|n|^2}$ with $\alpha = 90$. The results at uniform and adaptive grids are shown in Figure 3.11. The results on the moving mesh technique again show the signs of improvement.

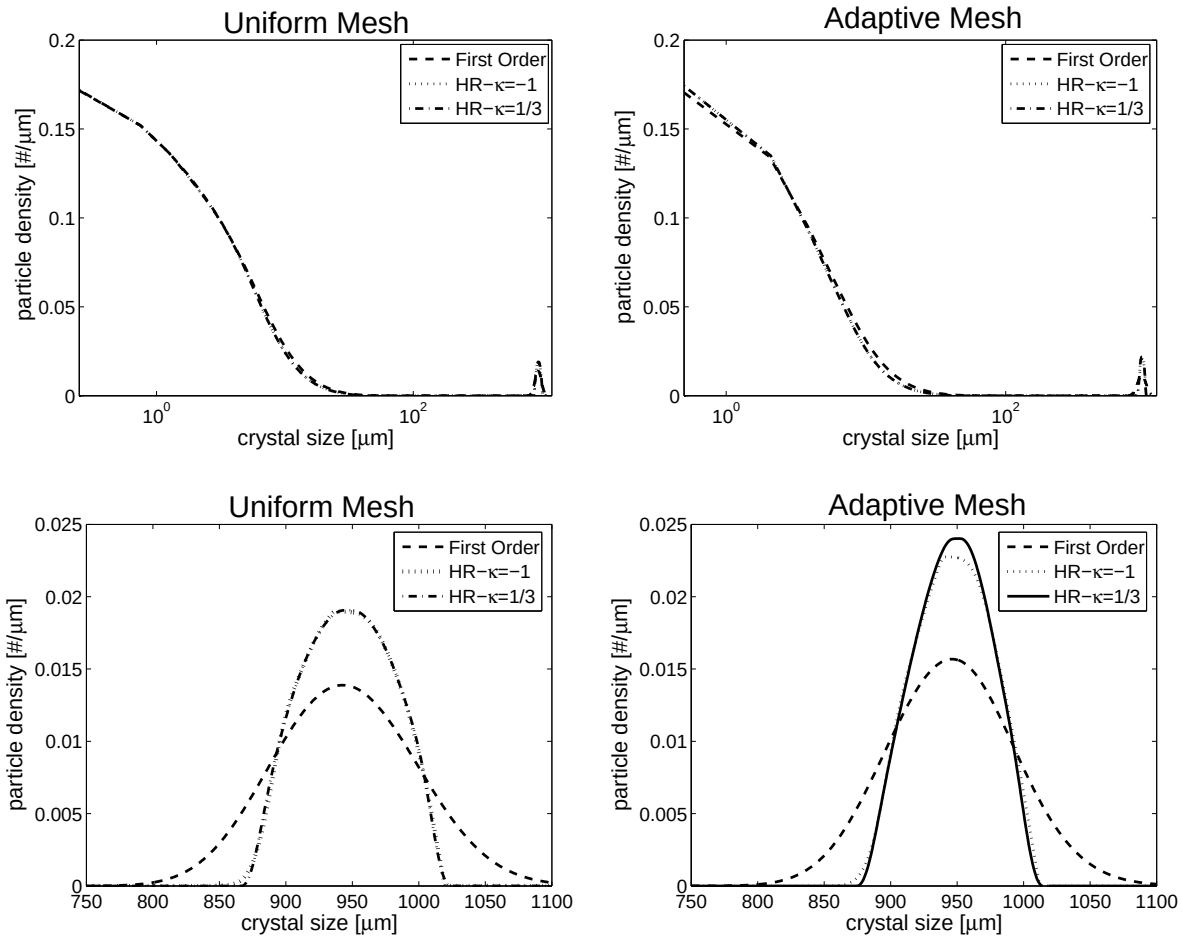

Figure 3.11: Test problem 4: Comparison of uniform and adaptive mesh results.

Table 3.2: Parameters for the Test problem 4

Description	*Symbol*	*Value*	*Unit*
Maximum crystal size	$l_{\max}$	1100	μm
Mesh size	Δl	0.5	μm
Simulation time	t	1000	s
Number of grid points	N	2200	–
Growth rate constant	k_{g}	$1.16 \cdot 10^2$	$\frac{\mu m}{s}$
Growth rate exponent	g	1.32	–
Nucleation rate constant	k_{b}	$4.64 \cdot 10^{-7}$	$\frac{1}{\mu m^3 s}$
Nucleation rate exponent	b	1.78	–
Volume shape factor	k_{v}	1.0	–
Initial mass	$m(0)$	0.493	$\frac{g}{g \text{ of water}}$
Density of crystals	ρ_{c}	$2.11 \cdot 10^{-12}$	$\frac{g}{\mu m^3}$

Test problem 5:

Here we present a numerical test problem in order to test our new method derived in Subsection 3.2.2. The initial data as a bimodel (Gaussian) function are given as

$$n(t,l) = \frac{m_{\text{seeds}}}{k_{\text{v}}\,\rho_{\text{c}}\,\mu_3(0)\sqrt{2\pi}}\left[\frac{1}{\sqrt{\sigma_1}}\exp\left(\frac{l-\bar{l}_1}{\sqrt{2}\sigma_1}\right)^2 + \frac{1}{\sqrt{\sigma_2}}\exp\left(\frac{l-\bar{l}_2}{\sqrt{2}\sigma_2}\right)^2\right]. \tag{3.158}$$

Here $\sigma_1 = 1.667 \cdot 10^{-4}\,m$, $\sigma_2 = 2.5 \cdot 10^{-4}\,m$, $\bar{l}_1 = 8 \cdot 10^{-4}\,m$ and $\bar{l}_2 = 1.6 \cdot 10^{-3}\,m$. The maximum crystal size to be considered is $l_{\max} = 0.005\,m$. The interval $[0, l_{\max}]$ is subdivided into 300 equidistant grid points. The final time for the simulation was taken as 900 minutes. The kinetic parameters and other constants considered in this problem are given in Table 3.3. The crystallizer was kept at an isothermal temperature $33\,^oC$.

Table 3.3: Parameters for the Test problem 5

Description	*Symbols*	*Value*	*Unit*
Growth rate constant	k_{g}	$1.37 \cdot 10^{-5}$	$\frac{m}{min}$
Growth rate exponent	g	1.0	$-$
Nucleation rate constant	k_{b}	$3.42 \cdot 10^{7}$	$\frac{1}{m^3\,min}$
Nucleation rate exponent	b	2.624	$-$
Density of crystals	ρ_{c}	1250	$\frac{kg}{m^3}$
Volume shape factor	k_{v}	0.0288	$-$
Initial mass	$m(0)$	0.09901	kg
Saturated mass	m_{sat}	0.0918	kg
Mass of seeds	m_{seeds}	$2.5 \cdot 10^{-3}$	kg

The left hand side of Figure 3.12 represents the distribution of the initial seeds. The right hand side plots presents the numerical solution of the PBE by using the HR-$\kappa = 1/3$ scheme of Koren [40] and our new method (cf. equations (3.36)-(3.38) and (3.64)-(3.66)). It is clear from the plots that HR-$\kappa = 1/3$ scheme resolves the resulting final distribution quite well. The sharp edge, resulting from burst of nuclei when the seeds are added in the supersaturated solution, is well preserved. Figure 3.13 shows the temporal evolution of the mass and first four moments. The symbols represent the moments obtained from the HR-$\kappa = 1/3$ scheme, while the plots with lines are obtained by solving the reduced moments model. The results show that mass and moments plots of the HR-$\kappa = 1/3$ scheme and reduced moments model agrees very well. Finally, Figure 3.14 shows the temporal evolution of the number density during the simulation time obtained from the HR-$\kappa = 1/3$ scheme. The errors in mass balances for the HR-$\kappa = 1/3$ and moments model are given in Table 3.4. This is an important measure of the quality of the approximations. A comparison shows that HR-$\kappa = 1/3$ scheme has larger errors than the moments model.

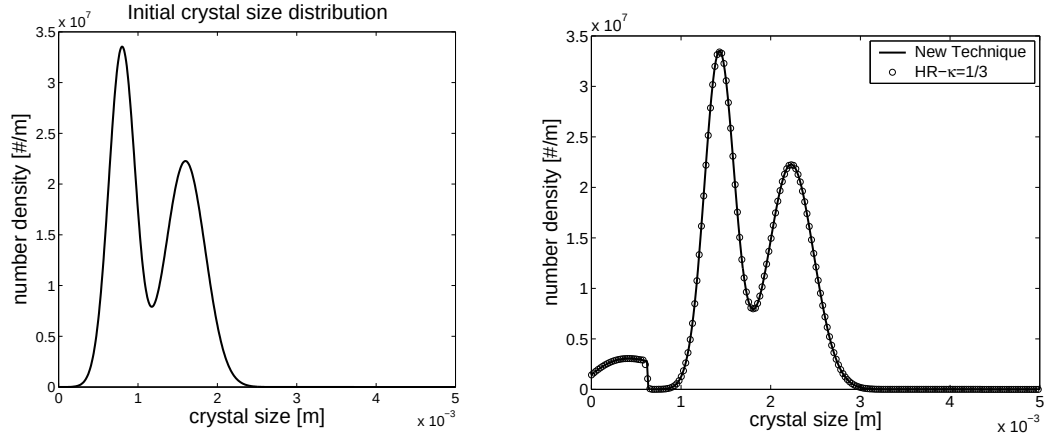

Figure 3.12: Test problem 5: Initial number density on the left and number density at $t = 900$ minutes on the right.

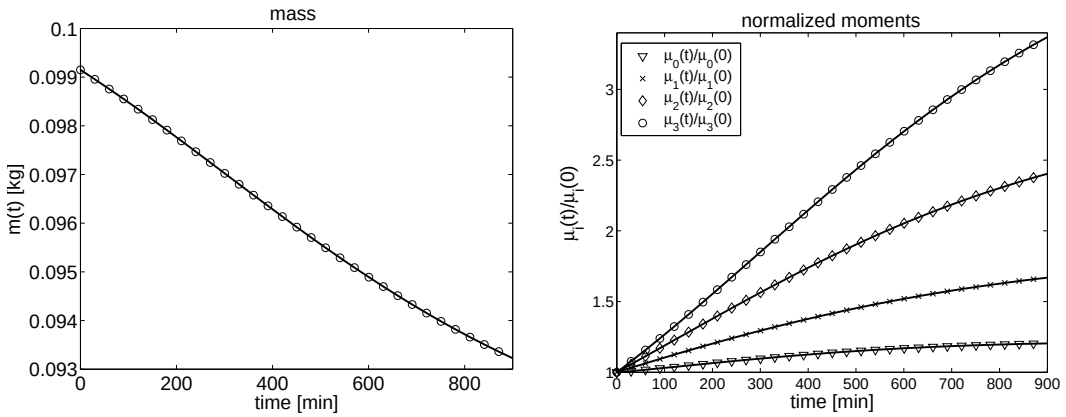

Figure 3.13: Test problem 5: Plots of mass and moments normalized with initial values.

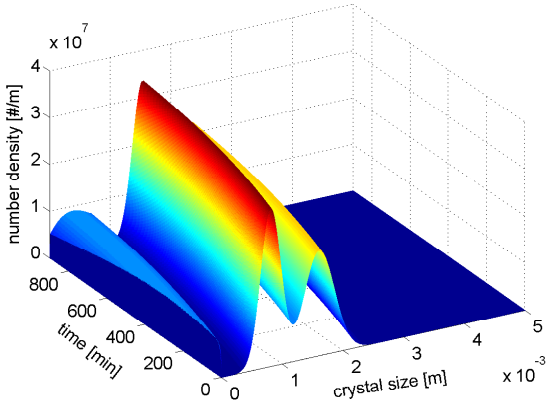

Figure 3.14: Test problem 5: Evolution of crystal size distribution in time

Table 3.4: Errors in mass balances for the Test Problem 5

Description	*HR-$\kappa = 1/3$ scheme*	*Moments model*
Absolute error	2.06×10^{-8}	6.94×10^{-17}
Relative error	2.08×10^{-7}	6.83×10^{-16}

Test problem 6:

As mentioned at the end of Subsection 3.2.1, we are not considering the control of crystallization process. However, to analyze the performance of our numerical schemes, we consider this example in which PBM is coupled with ODEs for mass balance and temperature. This problem was studied by Rawlings et al. [103, 104] and Shi et al. [107] which produces potassium sulfate crystals. Here we have to solve equations (3.3)-(3.9). In [107] the authors have calculated $n(t,l)/\rho_s$, therefore we also calculate the same quantity. The growth and nucleation rates are by

$$G(t,m) = k_b \, \exp(-E_g/RT) \left(\frac{m(t) - m_{sat}(t)}{m_{sat}(t)} \right)^g , \tag{3.159}$$

$$B_0(t,m) = k_b \, \exp(-E_b/RT) \left(\frac{m(t) - m_{sat}(t)}{m_{sat}(t)} \right)^b \mu_3(t) , \tag{3.160}$$

where E_g is the growth activation energy and E_b is the nucleation activation energy. The values of the process parameters are given in Table 3.5. The equations for saturation mass m_{sat} and metastable mass c_{mat} are given as

$$m_{sat}(t) = 6.29 \times 10^{-2} + 2.46 \times 10^{-3} T(t) - 7.14 \times 6 \times 10^{-6} T^2(t) , \tag{3.161}$$

$$m_{mat}(t) = 7.76 \times 10^{-2} + 2.46 \times 10^{-3} T(t) - 8.10 \times 6 \times 10^{-6} T^2(t) . \tag{3.162}$$

These two masses represent the constraints on the solute mass in the liquid phase, i.e., $m_{sat} \leq m \leq m_{mat}$ that must hold during the whole batch run. The initial seed distribution of the seeded batch crystallizer is assumed to be a parabolic distribution, from 250 to $300\,\mu m$, and the maximum density of initial seed distribution, which is $2/\mu m\, g$ solvent, occurs at $275\,\mu m$, i.e.,

$$n(0,l) = \begin{cases} 0.0032\,(300 - l)\,(l - 250) & 250\,\mu m \leq l \leq 300\,\mu m , \\ 0 & \text{otherwise} . \end{cases} \tag{3.163}$$

We have used our proposed high resolution schemes for the numerical solution of this model with 1200 mesh points. Figure 3.15 shows the the evolution of the reactor temperature $T(t)$, the solution mass $m(t)$, and PSD under a linear cooling strategy (where the jacket temperature, T_c, is cooled down linearly from 50 to $30\,^oC$). From the third moments plot it is clear that there is a gap between the crystals formed by nucleation and those growing from seeds during the whole reaction period. In the figures the superscript 's' stands for seeds and 'n' for nucleation.

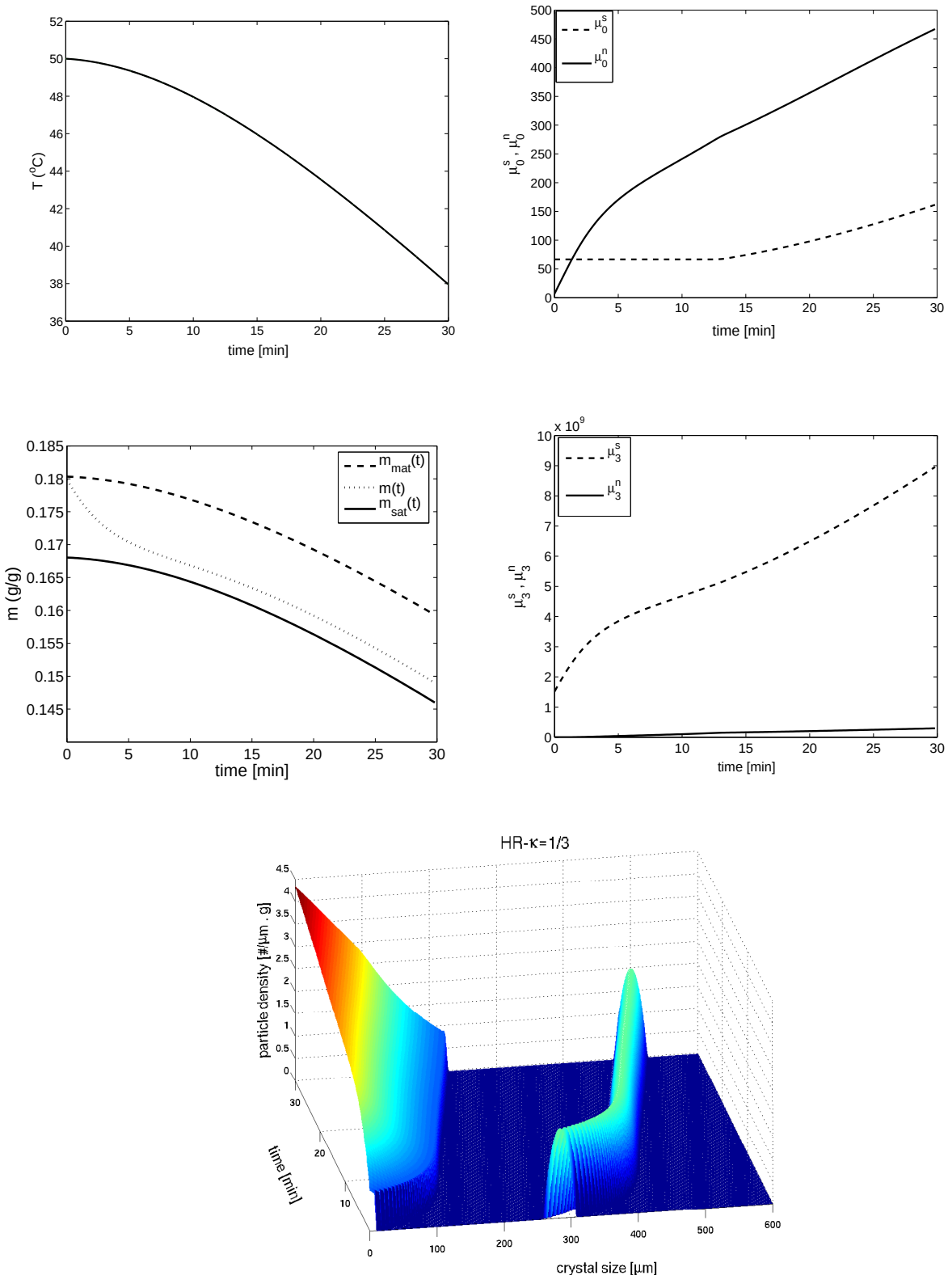

Figure 3.15: Test problem 6: Simulation results for $N = 1200$ at $t = 30$ minutes.

Table 3.5: Parameter values for the Test problem 6

$b = 1.45$	$g = 1.5$
$k_{\rm b} = 285.0\, 1/(s\,\mu m^3)$	$k_{\rm g} = 1.44 \cdot 10^8\, \mu m/s$
$E_{\rm b}/R = 7517.0\, K$	$E_{\rm g}/R = 4859.0\, K$
$U = 1800\, kJ/m^2\, h\, K$	$A_{\rm c} = 0.25\, m^2$
$\Delta H = 44.5\, KJ/kg\, h\, K$	$c_{\rm p} = 3.8\, kJ/K\, kg$
$\rho_{\rm s} V = 27.0\, kg$	$\rho_{\rm c} = 2.66 \cdot 10^{-12} g/\mu m^3$
$k_{\rm v} = 1.5$	$t_{\max} = 30\, min$
$N = 1200$	$l_{\max} = 600\, \mu m$

3.5.2 Two-dimensional problems

Here, we present test problems for the two-dimensional batch crystallization process.

Test problem 7:

The initial data considered here is a two-dimensional cylinder with a circular base and can be described as follows

$$n(0,\xi,\eta) = \begin{cases} 1 \times 10^{10}\, \#/\mu m & \text{if } r \le 5\,, \\ 0 & \text{elsewhere}\,. \end{cases} \tag{3.164}$$

Here $r = \sqrt{(\xi-15)^2 + (\eta-15)^2}$. The computational domain is taken as $[0, 100\,\mu m] \times [0, 100\,\mu m]$ which is discretized by 200×200 mesh points and we consider constant growth rates $G_1 = G_2 = 1 \mu m/s$. The monitor function ω used is

$$\omega = \sqrt{1 + \alpha_1 \left(\frac{n_\xi^2 + n_\eta^2}{\max |n|^2} \right) + \alpha_2 \left(\frac{n}{\max |n|} \right)^2}\,. \tag{3.165}$$

Here we take $\alpha_1 = 5 \times 10^3$ and $\alpha_2 = 0$. We approximate the ξ and $\eta-$derivatives of the number density n by central difference formula. The final simulation time is 60 seconds. Figure 3.16 shows the comparison of different numerical schemes on uniform and adaptive mesh along the mesh diagonal, and it clearly shows that achievement of cylindrical shape is much more better with adaptive mesh. Figures 3.17 show the three-dimensional plots of the number densities which show that $HR - \kappa = 1/3$ scheme results are better than the other schemes. Table 3.6 gives the total L^1 and L^2-errors in the numerical schemes at uniform and adaptive grids which are normalized with the total sum of absolute values of the exact solution, i.e., for a uniform grid they can be defined as

$$L^1 - error = \frac{\sum_{j=1}^{N_\eta} \sum_{i=1}^{N_\xi} |n_{i,j}^e - n_{i,j}| \Delta\xi_i \Delta\eta_j}{\sum_{j=1}^{N_\eta} \sum_{i=1}^{N_\xi} |n_{i,j}^e| \Delta\xi_i \Delta\eta_j}, \quad L^2 - error = \frac{\sqrt{\sum_{j=1}^{N_\eta} \sum_{i=1}^{N_\xi} (n_{i,j}^e - n_{i,j})^2 \Delta\xi_i \Delta\eta_j}}{\sum_{j=1}^{N_\eta} \sum_{i=1}^{N_\xi} |n_{i,j}^e| \Delta\xi_i \Delta\eta_j}\,. \tag{3.166}$$

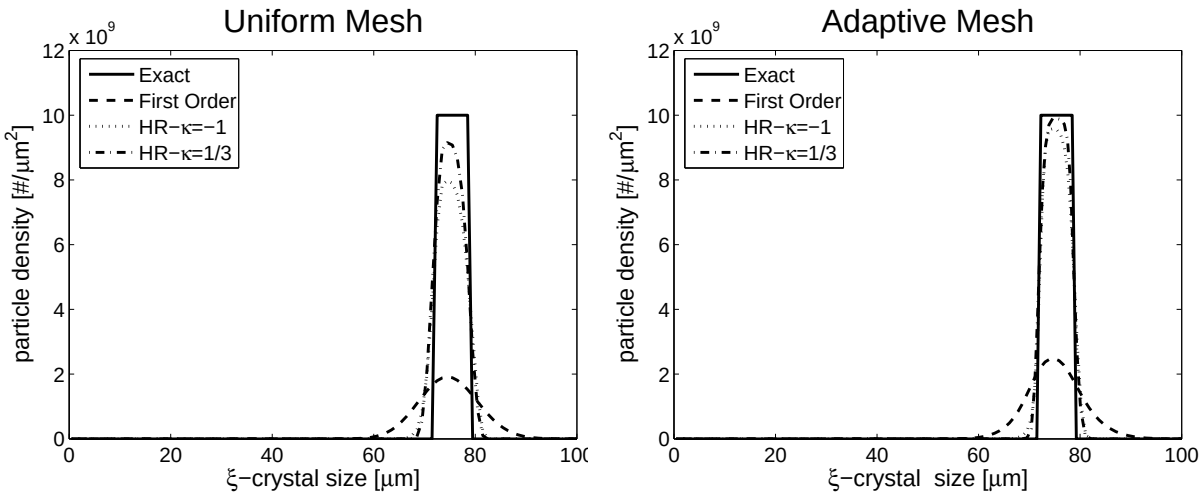

Figure 3.16: Test problem 7: Uniform and adaptive mesh results along $\xi = \eta$.

Here $n^e_{i,j}$, $n_{i,j}$ represent the exact and numerical solutions in cell i, respectively. One can clearly see that $HR-\kappa = 1/3$ produces less errors. For all schemes the total error reduces at adaptive grid.

Table 3.6: Total errors in the schemes for the Test problem 7

Method	*Uniform*		*Adaptive*	
	L^1-*error*	L^2-*error*	L^1-*error*	L^2-*error*
First order scheme	0.886	$8.984 \cdot 10^{-4}$	0.882	$8.914 \cdot 10^{-4}$
HR-$\kappa = -1$ scheme	0.212	$3.280 \cdot 10^{-4}$	0.201	$3.007 \cdot 10^{-4}$
HR-$\kappa = 1/3$ scheme	0.167	$3.131 \cdot 10^{-4}$	0.150	$2.646 \cdot 10^{-4}$

Test problem 8:

The initial data is two-dimensional Gaussian-distribution function of the form

$$n(0,\xi,\eta) = \begin{cases} \frac{1}{\sqrt{2\pi}\,\sigma} e^{-500[(0.02\xi-\mu)^2+(0.02\eta-\mu)^2]}\,\#/\mu m & \text{if } r \le 6\,, \\ 0 & \text{elsewhere}\,. \end{cases} \tag{3.167}$$

Here $r = \sqrt{(\xi-15)^2+(\eta-15)^2}$, $\sigma = 0.4\,\mu m$ and $\mu = 0.2875\,\mu m$. The computational domain is taken as $[0, 100\,\mu m] \times [0, 100\,\mu m]$ which is discretized by 200×200 mesh points and we consider constant growth rates $G_1 = G_2 = 1\mu m/s$. The monitor function ω used is (3.165). Here we take $\alpha_1 = 5 \times 10^3$ and $\alpha_2 = 0$. We approximate the $\xi-$ and $\eta-$derivatives of the number density n by central difference formula. The final simulation time is 60 seconds. Figure 3.18 shows the results along the mesh diagonal, while the three-dimensional plots are given in Figure 3.19. The left hand side results are obtained on

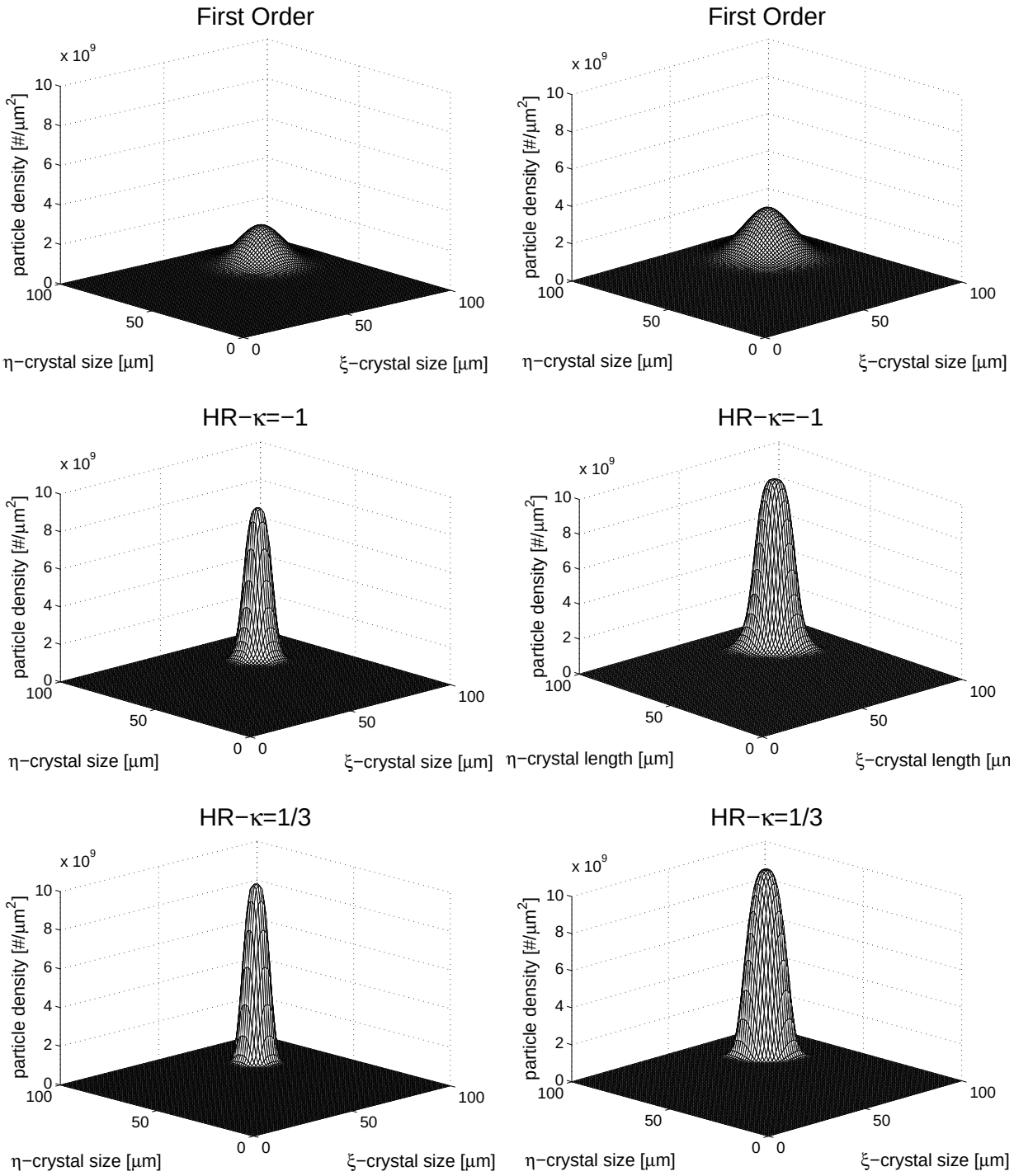

Figure 3.17: Test problem 7: Uniform (left column) and adaptive (right column) mesh results for $N_\xi = 200$ and $N_\eta = 200$ at $t = 60\,s$.

uniform grid, while the right hand side results are obtained on adaptive grid. The results on the moving mesh technique again show improvements. Table 3.7 give the total L^1 and L^2-errors (3.166) in the schemes which are normalized with total sum of the exact solution. One can see that $HR-\kappa = 1/3$ has less error and further reduces with the moving mesh technique.

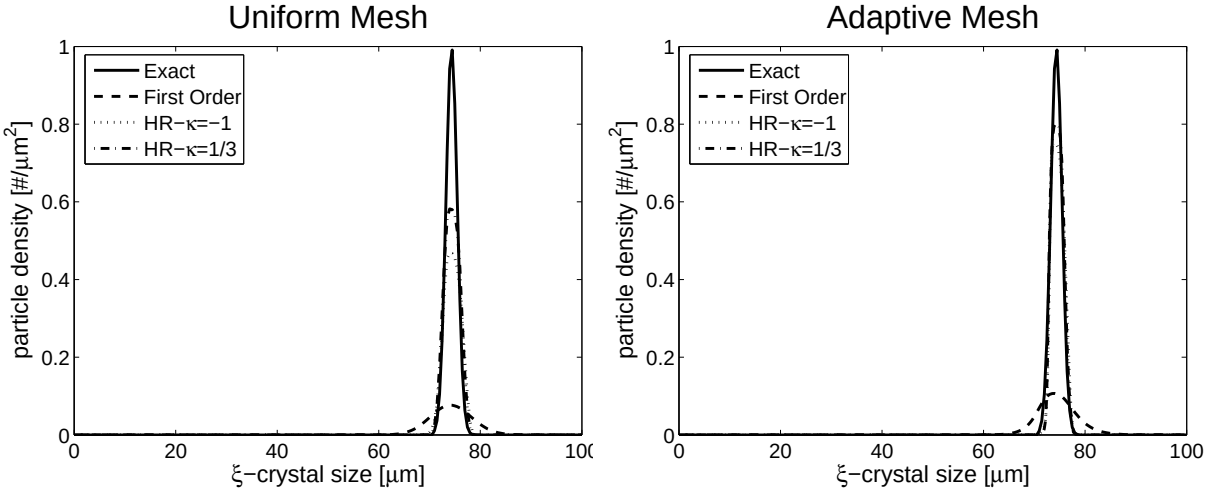

Figure 3.18: Test problem 8: Uniform and adaptive mesh results along $\xi = \eta$.

Table 3.7: Total errors in the schemes for the Test problem 8

Method	*Uniform*		*Adaptive*	
	L^1-*error*	L^2-*error*	L^1-*error*	L^2-*error*
First order scheme	0.971	$1.556 \cdot 10^{-3}$	0.969	$1.472 \cdot 10^{-3}$
HR-$\kappa = -1$ scheme	0.446	$7.845 \cdot 10^{-4}$	0.409	$4.977 \cdot 10^{-4}$
HR-$\kappa = 1/3$ scheme	0.336	$5.905 \cdot 10^{-4}$	0.288	$3.458 \cdot 10^{-4}$

Test problem 9:

This problem is taken from [14]. The initial data are

$$n(0,\xi,\eta) = \begin{cases} -3.48 \times 10^{-4}(\xi^2+\eta^2) + 0.136(\xi+\eta) - 26.6 & \text{if } 180.05 \le \xi,\eta \le 210.05\,, \\ 0 & \text{elsewhere}\,. \end{cases} \tag{3.168}$$

The nucleation rate is given by

$$B_0(t,m) = k_{\rm b}\left(\frac{m(t)-m_{\rm sat}(t)}{m_{\rm sat}(t)}\right)^b \left(\mu_{2,1}(t) - \frac{2}{3}\mu_{3,0}(t)\right)\,, \tag{3.169}$$

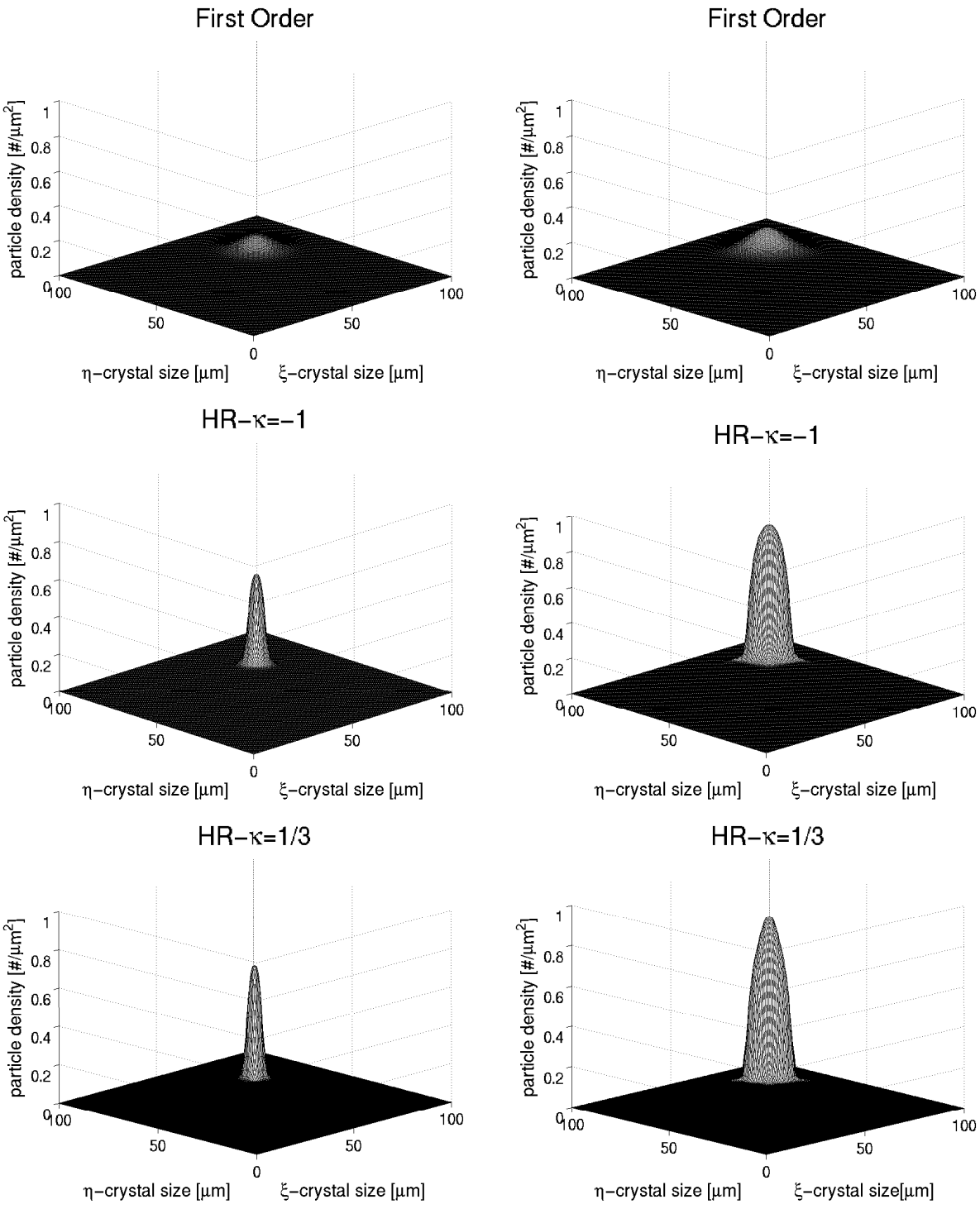

Figure 3.19: Test problem 8: Uniform (left column) and adaptive (right column) mesh results for $N_\xi = 200$ and $N_\eta = 200$ at $t = 60\,s$.

where the moments $\mu_{i,j}$ are calculated as

$$\mu_{i,j}(t) = \int_0^\infty \int_0^\infty \xi^i \eta^j n(t,\xi,\eta)\, d\eta\, d\xi\,. \tag{3.170}$$

The size independent growth rates G_1 and G_2 are given as

$$G_1(t,\xi,m) = k_{\mathrm{g1}} \left(\frac{m(t) - m_{\mathrm{sat}}(t)}{m_{\mathrm{sat}}(t)} \right)^{g1}, \tag{3.171}$$

$$G_2(t,\eta,m) = k_{\mathrm{g2}} \left(\frac{m(t) - m_{\mathrm{sat}}(t)}{m_{\mathrm{sat}}(t)} \right)^{g2}. \tag{3.172}$$

Here, k_{g1}, k_{g2}, g_1 and g_2 are the kinetic parameters. The kinetic parameters reported for the crystallization of potassium nitrate (KNO_3) crystals were used, see Table 3.8. The solute mass in the liquid phase for the $KMNO_3$ crystal is given by (3.70). The shape of the crystal is shown in Figure 3.2. The initial mass is taken as $m(0) = 0.307\, \frac{g}{g \text{ of water}}$.

Table 3.8: Parameter values for the Test problem 9

Description	*Symbol*	*Value*	*Unit*
Maximum crystal size in ξ-direction	$\xi_{\max}$	400	μm
Maximum crystal size in η-direction	$\eta_{\max}$	900	μm
Simulation time	t	600	s
Number of grid points	N_ξ	400	–
Number of grid points	N_η	900	–
x-Growth rate constant	k_{g1}	12.21	$\frac{\mu m}{s}$
y-Growth rate constant	k_{g2}	100.75	$\frac{\mu m}{s}$
x-Growth rate exponent	g_1	1.48	–
y-Growth rate exponent	g_2	1.74	–
Nucleation rate constant	k_{b}	$7.49 \cdot 10^{-8}$	$\frac{1}{\mu m^3 s}$
Nucleation rate exponent	b	2.04	–
density of crystals	ρ_{c}	$2.338 \cdot 10^{-12}$	$\frac{g}{\mu m^3}$

The saturated solute mass obeys [116]

$$m_{\mathrm{sat}}(t) \left[\frac{g}{g \text{ of water}} \right] = 9.3027 \times 10^{-5} T^2(t) + 9.7629 \times 10^{-5} T(t) + 0.2087\,. \tag{3.173}$$

The temperature trajectory T(t) follows an exponential decaying profile

$$T(t)[^oC] = 32 - 4(1 - e^{-\frac{t}{310}})\,. \tag{3.174}$$

Here the monitor function is the same as given in (3.165) with $\alpha_1 = 2 \times 10^4$ and $\alpha_2 = 0$. The results are shown in Figure 3.20. The left hand side results are obtained on uniform grid, while the right hand side results are obtained on adaptive grid.

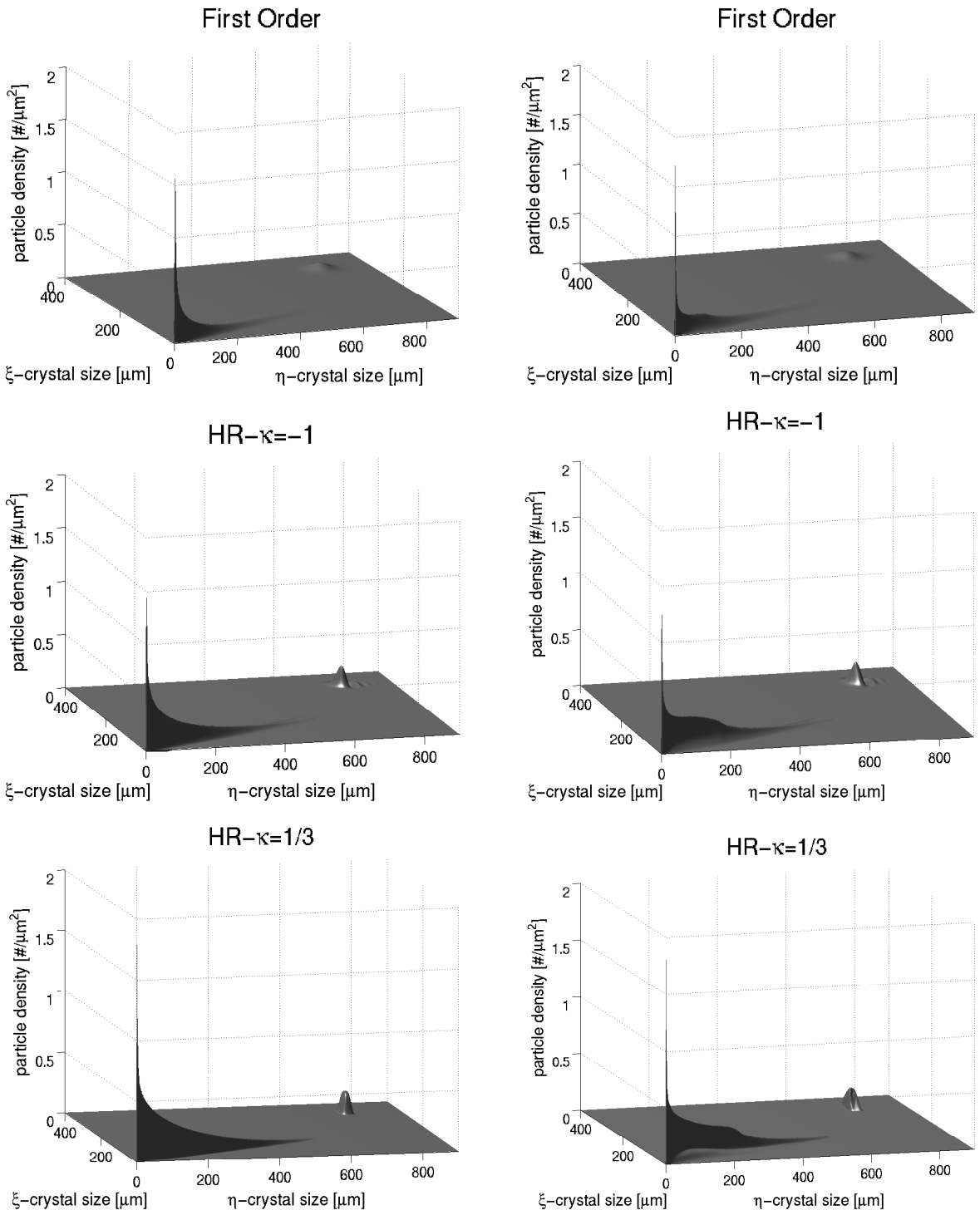

Figure 3.20: Test problem 9: Uniform (left column) and adaptive (right column) mesh results for 400×900 grid at $t = 600\,s$.

Test problem 10:

This problem is also taken from [28]. In this problem nucleation rate is mass dependent, while growth rate is a function of both mass and crystal size. The nucleation rate is given by (3.169). The growth rates G_1 and G_2 are given as

$$G_1(t,\xi,m) = k_{g1}\left(\frac{m(t)-m_{sat}(t)}{m_{sat}(t)}\right)^{g1} 0.1(1+0.6\xi)\,, \tag{3.175}$$

$$G_2(t,\eta,m) = k_{g2}\left(\frac{m(t)-m_{sat}(t)}{m_{sat}(t)}\right)^{g2} 0.1(1+0.6\eta)\,, \tag{3.176}$$

where ξ and η are the characteristic crystal length as shown in Figure 3.2. Here, k_{g1}, k_{g2}, g_1 and g_2 are the kinetic parameters. The kinetic parameters reported for the crystallization of potassium nitrate (KNO_3) crystals were used. The kinetic parameters determined from experimental data, see Gunawan et al. [29], are reported in Table 3.9. The mass of solute and corresponding saturated solute mass are again given by (3.70) and (3.173), while temperature trajectory T(t) is given by (3.174). The initial data are given as

$$n(0,\xi,\eta) = \begin{cases} -3.48\times10^{-2}(\xi^2+\eta^2)+1.36(\xi+\eta)-26.6 & \text{if } 18.05 \le \xi,\eta \le 21.05\,, \\ 0 & \text{elsewhere}\,. \end{cases} \tag{3.177}$$

Table 3.9: Parameter values for the Test problem 10

Description	*Symbol*	*Value*	*Unit*
Maximum crystal size in ξ-direction	ξ_{max}	40	μm
Maximum crystal size in η-direction	η_{max}	80	μm
Simulation time	t	80	s
Number of grid points	N_ξ	100	–
Number of grid points	N_η	200	–
ξ-Growth rate constant	k_{g1}	12.21	$\frac{\mu m}{s}$
η-Growth rate constant	k_{g2}	100.75	$\frac{\mu m}{s}$
ξ-Growth rate exponent	g_1	1.48	–
η-Growth rate exponent	g_2	1.74	–
Nucleation rate constant	k_b	$7.49\cdot10^{-8}$	$\frac{1}{\mu m^3 s}$
Nucleation rate exponent	b	2.04	–
Density of crystals	ρ_c	$2.338\cdot10^{-12}$	$\frac{g}{\mu m^3}$

Here the monitor function is the same as given in (3.165) with $\alpha_1 = 2\times10^4$ and $\alpha_2 = 1\times10^3$. The results are shown in Figure 3.21. The left hand side results are obtained on uniform grid, while the right hand side results are obtained on adaptive grid. Since the solution profiles in this problem are not very sharp, the high resolution schemes on the uniform mesh resolve the physical solution very well. Hence, the moving mesh technique has no

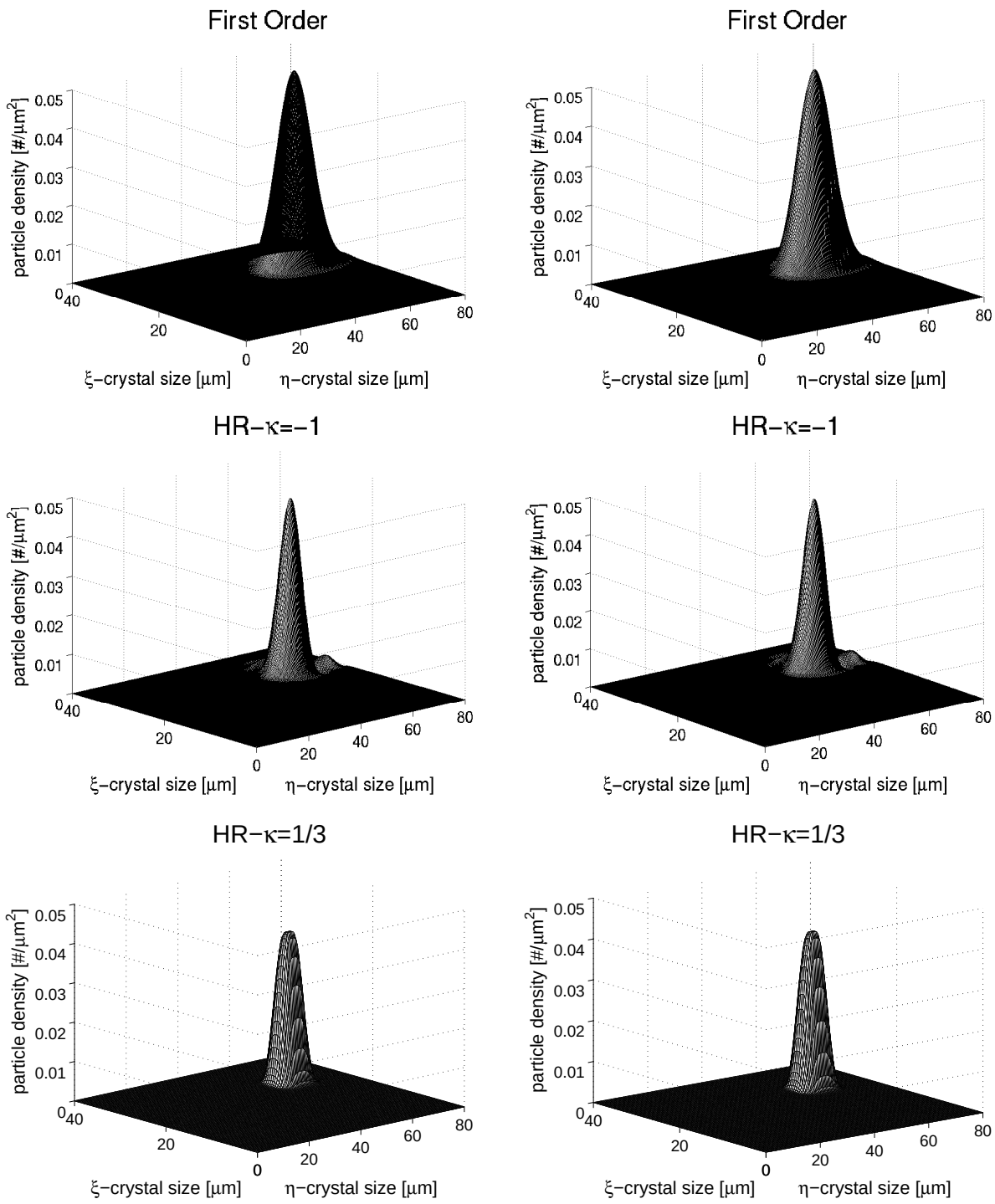

Figure 3.21: Test problem 10: Uniform (left column) and adaptive (right column) mesh results for $N_\xi = 100$ and $N_\eta = 200$ at $t = 80\,s$.

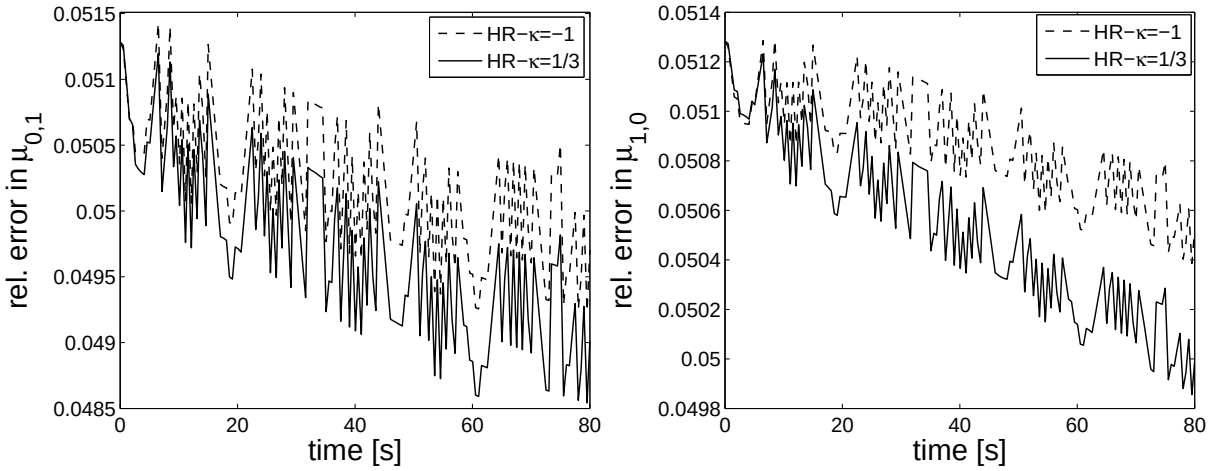

Figure 3.22: Test problem 10: Relative errors in moments on uniform mesh for $N_\xi = 100$ and $N_\eta = 200$

considerable effect on the solution. The plots in Figure 3.22 show the errors in the moments $\mu_{i,j}(t)$ of the particle density on uniform grid. Due to the above mentioned reason the errors in the moments on uniform and adaptive grids are the same for this problem.

Chapter 4

Preferential Crystallization

This chapter explains the basic concepts of preferential crystallization for enantiomers and introduces the mathematical models for the simulation of such processes. Two different setups for the preferential crystallization of the enantiomers are considered here. In the first setup a single crystallizer with a fines dissolution unit is considered which preferentially crystallizes one enantiomer. In the second setup two coupled preferential crystallizers are considered which are interconnected with two fines dissolution pipes. In the coupled case both enantiomers are crystallized in separate crystallizers simultaneously. The models are then further elaborated for isothermal and non-isothermal conditions. Apart from the semi-discrete high resolution finite volume scheme which were introduced in the last chapter, the method of characteristics (MOC) is introduced here. Afterwards, the numerical results of the schemes are compared with each other for the test problems of single and coupled crystallizers.

4.1 Enantiomers

In chemistry, two stereoisomers are said to be enantiomers if they are mirror images of each other (chiral compounds). Much as a left and right hand are different but one is the mirror image of the other, enantiomers are stereoisomers whose molecules are non-superimposable mirror images of each other. Figure 4.1 gives the illustration of amino acid enantiomers as an example.

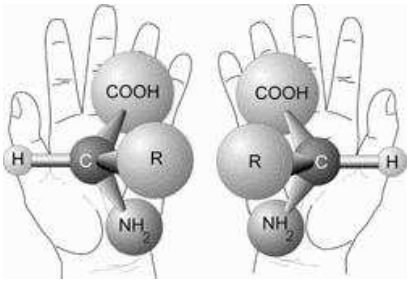

Figure 4.1: Amino acid enantiomers

Enantiomers are symmetric organic molecules with identical chemical and physical properties but with different properties regarding metabolism as well as their ability to rotate plane-polarized light by equal amounts but in opposite directions.

A solution of equal parts of an optically-active isomer and its enantiomer is known as a racemic solution for which the net rotation of plane-polarized light is equal to zero.

4.1.1 Fundamentals of preferential crystallization

Separation of chiral molecules is an important question in industry as many (bio-)organic molecules are chiral. Usually, one of the enantiomers shows the desired properties for therapeutic activities or metabolism, whereas the other enantiomer may be inactive or may even cause some undesired effects. Complementing the most commonly used classical resolution via formation of diastereomers, direct crystallization methods have become increasingly important in recent years. An attractive process is based on enantioselective preferential crystallization. This concept is usually applied to the so-called conglomerates, which form physical mixture of crystals where each crystal is enantiomerically pure. In solution such systems tend to reach an equilibrium state in which the liquid phase will have racemic (50/50) composition and the solid phase will consist of a mixture of crystals of both enantiomers. However, before approaching this state, it is possible to preferentially produce crystals of just one of the enantiomers after seeding with the corresponding homochiral crystals. The process is essentially based on the different crystal surface areas of both enantiomers provided initially.

It is worth noting that preferential crystallization is used up to now only for a few substances on industrial scale. However, this technique has recently got a considerable academic attention with emphasis on its chemistry and on its application to separate special chiral systems. It is an effective and comparatively cheap technology for enantioseparation at different scales.

4.1.2 Ternary phase diagram

The principle of preferential crystallization processes can be illustrated in a ternary phase diagram, see Figure 4.2. A saturated solution at temperature $T_{cryst} + \Delta T$ is cooled down to T_{cryst}, where the cooled liquid should be in the metastable zone, i.e. zone in which any particle-free supersaturated solution will stay clear for a finite time, that means no spontaneous (primary) nucleation takes place. In Figure 4.2 point A represents an initial mixture of two enantiomers and a solvent (e.g.: L-threonine, D-threonine and water). An enantiomeric excess (as depicted) is beneficial for the separation process, but not strictly necessary. At this point the crystallizer is seeded with crystals of enantiomer E_1. As the solution is supersaturated, the seeds will grow and secondary nucleation will occur. If hypothetically there would no primary nucleation of enantiomer E_2, the crystallization process would end at point M, which is the equilibrium point for E_1 only. But experimental results show that after some time primary nucleation of E_2 is induced and therefore, after sufficiently long time, the trajectory is attracted by the common equilibrium point for E_1 and E_2, i.e. point E. At this last moment the crystallization of both enantiomers takes places at the same time, but for the counter-enantiomer with a higher rate (the desired

enantiomer has already been almost crystallized).

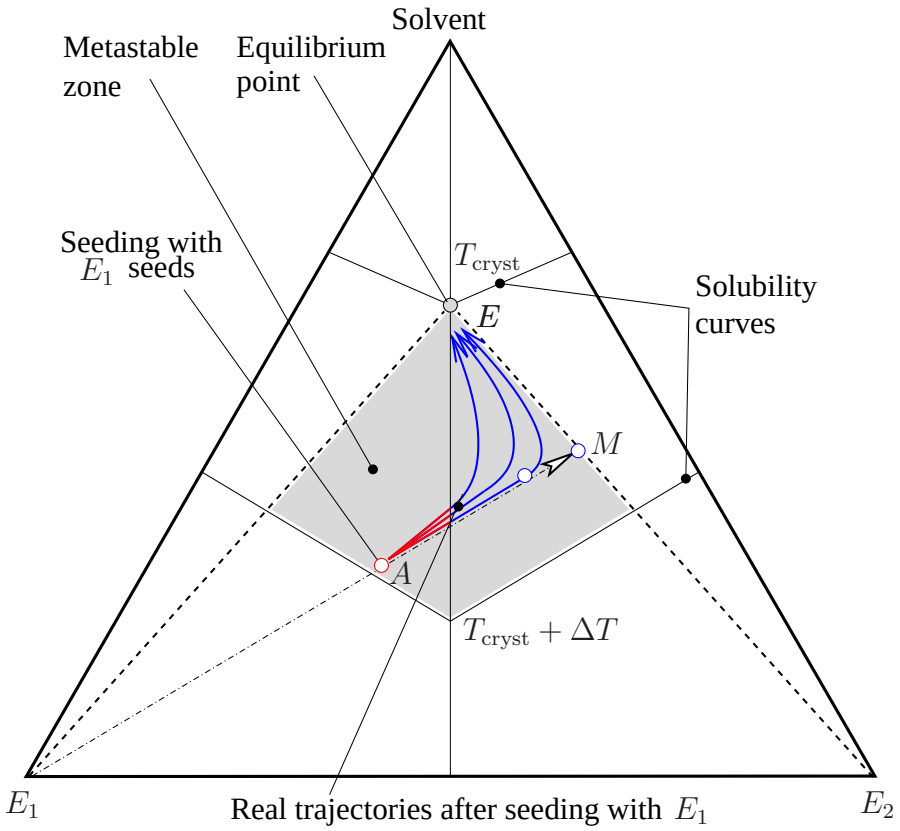

Figure 4.2: Principle of preferential crystallization illustrated in ternary phase diagram.

The course of the crystallization can be followed by the means of the analytical setup in batch crystallizer. A polarimeter is used for an on-line measuring of the concentration differences between both enantiomers due to different deviation of the polarized light of the two components. A density meter indicates the overall concentration of the two enantiomers. With those two variables, the temporal concentration development of the two enantiomers can be calculated. The polarimetric signal Figure 4.3 is used to follow the course of the process. It starts with zero or a negative value if there is an excess of the desired enantiomer at the beginning. The polarimetric signal is increasing during the crystallization of preferred (seeded) enantiomer. Before the maximum is achieved, the gradient of the curve is going up because of the increasing surface area of the crystals and also because of the occurrence of nuclei which offer additional surface area. Later on the gradient is decreasing, because the supersaturation is being consumed. The maximum of the curve is a consequence of the slower crystallization of the seeded enantiomer, and also because of the start of the crystallization of the counter-enantiomer. After reaching the maximum, both enantiomer are crystallizing together, but at this moment the crystallization rate of

the counter enantiomer is higher. The measured optical rotation angle decreases up to a value of zero where steady state is reached at the end of process. These $\alpha-$curves are used as experimental results for the comparison with the obtained simulation results. It can be also taken as reference for the estimation of some model parameters. The shape of crystals investigated during experiments are shown in Figure 4.4.

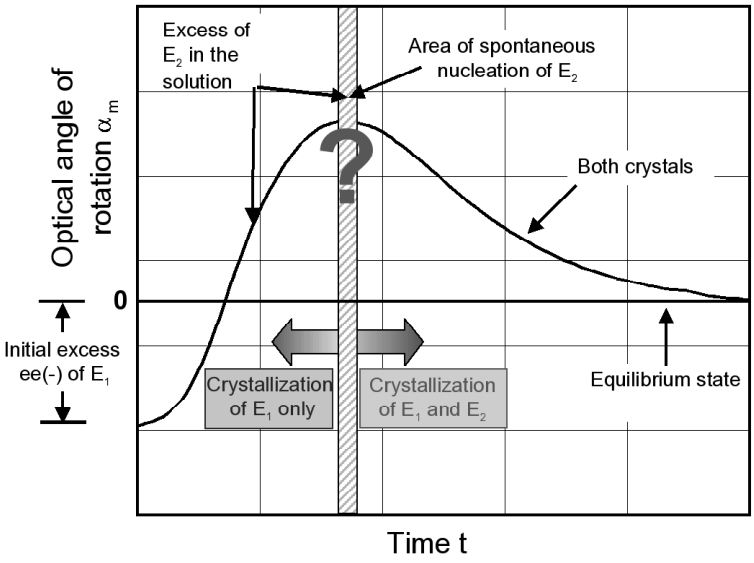

Figure 4.3: Typical polarimetric signal providing qualitative information about crystallization process by entrainment.

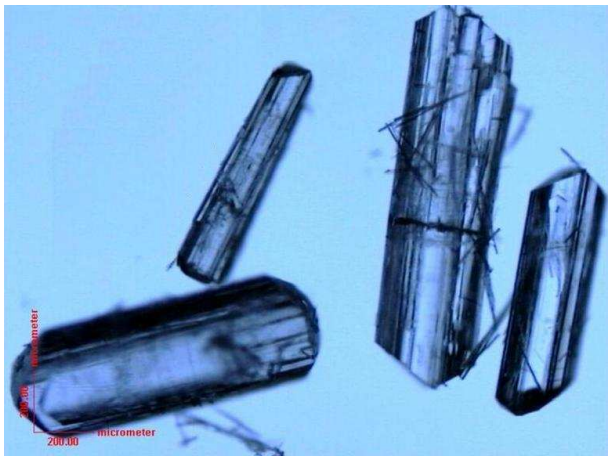

Figure 4.4: Illustration of typical shapes of the investigated crystals of theorine.

4.2 Single Preferential Crystallizer Model

In this section, a mathematical model is provided for the simulation of preferential crystallization of enantiomer in a single batch crystallizer connected with a fines dissolution unit. Fines dissolution might lead to bigger crystals and more narrow distributions. This can fulfill special requirements regarding the product quality and simplifies downstream processes like filtration. A simplified dynamic model of an ideally mixed batch crystallizer for isothermal and non-isothermal conditions is supplied. Here we are considering the simplest case, in which a recycle pipe is attached to the crystallizer and we assume that fines dissolve completely at the end of the pipe. Before entering in the opposite crystallizer, this liquid is assumed to be cooled again. This ensures that there will be no negative effect on the particles in the crystallizer due to warm liquid flux. The attrition, agglomeration and breakage processes are not considered in the current study. Figure 4.5 shows the schematic diagram of the single preferential crystallizer with a pipe for fines dissolution.

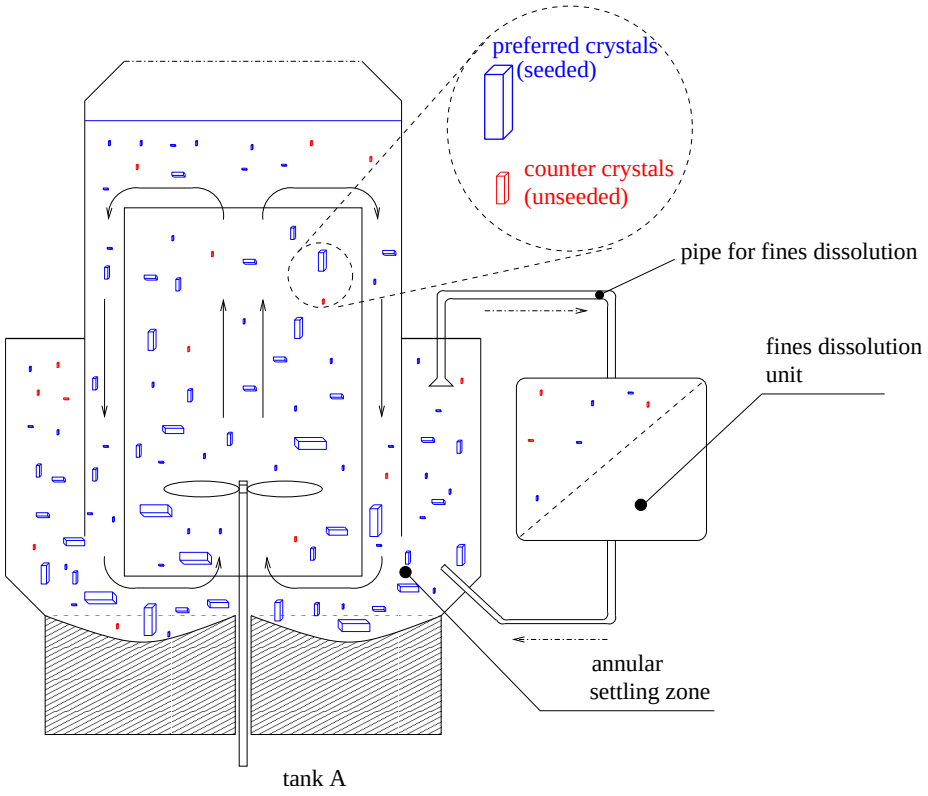

Figure 4.5: Single-batch process setup with fines dissolution

The population balance for the solid phase is as follows

$$\frac{\partial n^{(k)}(t,l)}{\partial t} = -G^{(k)}(t, m^{(p)}, m^{(c)}) \frac{\partial n^{(k)}(t,l)}{\partial l} - \frac{1}{\tau_1} h(l) n^{(k)}(t,l)\,, \quad k \in \{p, c\}\,, \tag{4.1}$$

where $(t, l) \in \mathbb{R}^2_+$, '$p$' stands for preferred enantiomer and 'c' for counter enantiomer. Here $n^{(k)}(t, l) \geq 0$ and $G^{(k)}(t) \geq 0$ represent the number density and size independent growth rate of the corresponding enantiomer of size $l > 0$ at time $t \geq 0$, respectively. In equation(4.1) τ_1 is the residence time for the crystallizer. It is defined as

$$\tau_1 = \frac{V}{\dot{V}}\,, \tag{4.2}$$

where V is the the volume of the crystallizer and $\dot{V}$ is the volumetric flow rate. Again in equation (4.1), $h(l)$ is a death function, which describes the dissolution of particles below some critical size. It can be defined as a step (Heaviside) function. Figure 4.6 presents such a function with $l_{\text{crit}} = 2 \cdot 10^{-4}\ m$.

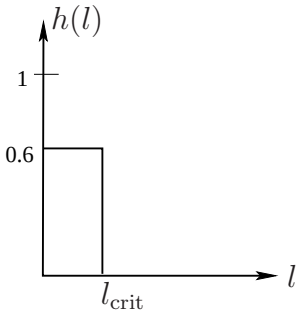

Figure 4.6: Death function $h(l)$

The $j-$th moment of the number density $n^{(k)}(t, l)$ is defined as

$$\mu_j^{(k)}(t) := \int_0^\infty l^j n^{(k)}(t, l)\, dl\,. \tag{4.3}$$

The mass balance for the liquid phase in the crystallizer is given by

$$\frac{dm^{(k)}(t)}{dt} = \dot{m}_{\text{in}}^{(k)}(t) - \dot{m}_{\text{out}}^{(k)}(t) - 3\rho_{\text{c}} k_{\text{v}} G^{(k)}(t, m^{(p)}, m^{(c)})\, \mu_2^{(k)}(t)\,, \quad t \in \mathbb{R}_{\geq 0}. \tag{4.4}$$

Here, $\mu_2^{(k)}(t)$ is the second moments, $k_{\text{v}} > 0$ is the volumetric factor and $\rho_{\text{c}} > 0$ is the crystal density.

Because of the fines dissolution this equation has two mass fluxes. The first one $\dot{m}_{\text{out}}^{(k)}(t)$ is the mass flux in the liquid phase which is being taken out from the crystallizer due to outgoing liquid. The second one $\dot{m}_{\text{in}}^{(k)}(t)$ is the incoming mass flux in the crystallizer from the dissolution pipe. They are defined as

$$\dot{m}_{\text{out}}^{(k)}(t) = w^{(k)}(t, m^{(p)}, m^{(c)}) \rho_{\text{liq}}(T) \dot{V}\,, \tag{4.5}$$

$$\dot{m}_{\text{in}}^{(k)}(t) = \dot{m}_{\text{out}}^{(k)}(t - \tau_2) + \frac{k_{\text{v}} \rho_{\text{c}}}{\tau_1} \int_0^\infty l^3 h(l) n^{(k)}(l, t - \tau_2)\, dl\,. \tag{4.6}$$

Here $w^{(k)}$ represent mass fractions and τ_2 is the residence time of the dissolution unit (the pipe) which is defined as

$$\tau_2 = \frac{\pi r^2 L}{\dot{V}}\,, \tag{4.7}$$

where r is the radius and L is the length of the pipe.

The birth of new particles (nucleation) is incorporated in this model as a left boundary condition for the PBE at minimum crystal size $l = l_0$, i.e.,

$$n^{(k)}(t, l_0) = \frac{B_0^{(k)}(t, m^{(p)}, m^{(c)})}{G^{(k)}(t, m^{(p)}, m^{(c)})}\,, \quad k \in \{p, c\}\,. \tag{4.8}$$

The assumption behind this substitution is that if $B_0 \geq 0$ is rate of appearance of near zero-sized particles, then

$$B_0(t, m^{(p)}, m^{(c)}) = \left.\frac{dN}{dt}\right|_{t,l\to l_0} = \left[\frac{dN}{dl}\cdot\frac{dl}{dt}\right]_{t,l\to l_0} = n(t, l_0)G(t, m^{(p)}, m^{(c)})\,. \tag{4.9}$$

Here N is the number of crystals. The given model covers the case of isothermal operation, i.e. the temperature is considered to be constant during the whole batch process. A natural extension of the process idea is to vary the temperature during the batch process according to a specified and meaningful temperature profile.

The growth rate kinetics are described as [19, 20]

$$G^{(k)}(t, m^{(p)}, m^{(c)}) = k_{\mathrm{g}}\left(S^{(k)}(t, m^{(p)}, m^{(c)})\right)^g\,, \tag{4.10}$$

where $k_{\mathrm{g}} > 0$ and $g \geq 1$. Here $S^{(k)}$ denotes the relative supersaturation for the preferred and counter enantiomers

$$S^{(k)}(t, m^{(p)}, m^{(c)}) = \frac{w^{(k)}(t, m^{(p)}, m^{(c)})}{w_{\mathrm{eq}}^{(k)}(t, m^{(p)}, m^{(c)})} - 1, \qquad k \in \{p, c\}. \tag{4.11}$$

In equation (4.11), $w^{(p)}$ is the mass fraction of the dissolved preferred enantiomer, $w^{(c)}$ is the mass fraction of the dissolved counter enantiomer, $w_{\mathrm{eq}}^{(p)}$ is equilibrium mass fraction for the preferred enantiomer and $w_{\mathrm{eq}}^{(c)}$ is equilibrium mass fraction for the counter enantiomer.

The mass fractions are defined as

$$w^{(k)}(t, m^{(p)}, m^{(c)}) := \frac{m^{(k)}(t)}{m^{(p)(t)} + m^{(c)}(t) + m_{\mathrm{solv}}(t)}, \quad k \in \{p, c\}\,, \tag{4.12}$$

where $m_{\mathrm{solv}}(t)$ is the mass of solvent (water here). The nucleation rate kinetics are described as [19, 20]

$$B_0^{(p)}(t, m^{(p)}, m^{(c)}) = k_{\mathrm{b}}^{(p)}\left(S^{(p)}(t, m^{(p)}, m^{(c)})\right)^{b^{(p)}}\mu_3^{(p)}(t)\,, \tag{4.13}$$

$$B_0^{(c)}(t, m^{(p)}, m^{(c)}) = k_{\mathrm{b}}^{(c)} e^{-\frac{b^{(c)}}{ln\left(S^{(c)}(t, m^{(p)}, m^{(c)})+1\right)^2}}\,, \tag{4.14}$$

where $b^{(k)} \geq 1$ and $k_{\mathrm{b}}^{(k)} > 0$. Note that the above model reduces to the case of no fines dissolution when the last term on the right hand side of (4.1) and the first two terms on the right hand side of (4.4) are zero. Then equations (4.5) and (4.6) are not needed. Hence, for without fines dissolution case the model reduces to

$$\frac{\partial n^{(k)}(t,l)}{\partial t} = -G^{(k)}(t, m^{(p)}, m^{(c)}) \frac{\partial n^{(k)}(t,l)}{\partial l}\,, \tag{4.15}$$

$$\frac{dm^{(k)}(t)}{dt} = -3\rho_{\mathrm{c}} k_{\mathrm{v}} G^{(k)}(t, m^{(p)}, m^{(c)})\, \mu_2^{(k)}(t). \tag{4.16}$$

4.2.1 Existence and uniqueness of the solution for without fines dissolutions model

The existence and uniqueness of the solution follow similar procedure as presented in Section 3.2.2 of Chapter 3. For this purpose we use again the Laplace transformation of the population balance equation (4.15). The mass balances (4.16) and the nucleation rates (4.13) and (4.14) are functions of moments. Hence, our goal also include the derivation of a system of ordinary differential equations for moments $\mu_i^{(k)}(t)$, $i = 0, 1, 2, 3$ in order to have a closed system. Let us define the Laplace transformation of $n^{(k)}(t,l)$ by

$$\hat{n}^{(k)}(t,s) = \mathcal{L}[n^{(k)}(t,l); s] = \int_0^\infty e^{-sl}\, n^{(k)}(t,l)\, dl\,, \quad s > 0 \tag{4.17}$$

and following similar procedure as in Section 3.2.2, we obtain

$$\frac{\partial \hat{n}^{(k)}(t,s)}{\partial t} + s\, G^{(k)}(t, m^{(p)}, m^{(c)})\, \hat{n}^{(k)}(t,s) = B_0^{(k)}(t, m^{(p)}, m^{(c)})\, e^{-sl_0}\,, \quad k \in \{p, c\}\,, \tag{4.18}$$

where the initial data for this linear differential equation at $t_0 \geq 0$ are given as

$$\hat{n}^{(k)}(t_0,s) = \int_0^\infty e^{-sl}\, n^{(k)}(t_0,l)\, dl = n_0^{(k)}(s)\,. \tag{4.19}$$

The coupled moment system and algebraic equations for mass balances are given by

$$\frac{d\mu_0^{(k)}(t)}{dt} = B_0^{(k)}(t, m^{(p)}, m^{(c)})\,, \tag{4.20}$$

$$\frac{d\mu_i^{(k)}(t)}{dt} = i\, G^{(k)}(t, m^{(p)}, m^{(c)})\, \mu_{i-1}^{(k)}(t)\,, \quad i = 1, 2, 3, \tag{4.21}$$

$$m^{(k)}(t) + \rho_{\mathrm{c}}\, k_{\mathrm{v}}\, \mu_3^{(k)}(t) = m^{(k)}(t_0) + \rho_{\mathrm{c}}\, k_{\mathrm{v}}\, \mu_3^{(k)}(t_0) \tag{4.22}$$

with initial data for $t_0 \geq 0$

$$\mu_i^{(k)}(t_0) = \int_0^\infty l^i n^{(k)}(t_0, l)\, dl \geq 0\,, \quad m^{(k)}(t_0) = m_0^{(k)} > 0\,. \tag{4.23}$$

Here $w_{\text{eq}}^{(k)}(t) > 0$ are constants or monotonically decreasing functions of time as given by relations (4.54) and (4.55). With the help of equations (4.20)-(4.23) we can calculate the growth rates $G^{(k)}(t, m^{(p)}, m^{(c)})$ and nucleation rates $B_0^{(k)}(t, m^{(p)}, m^{(c)})$ for $0 \leq t_0 \leq t \leq t_{\max}$. After having the growth and nucleation rates we can calculate the transformed number density $\hat{n}(t, s)$ from equations (4.18) and (4.19).

The proof of local existence and uniqueness of the solution of equations (4.20) and (4.21) are exactly the same as given in Section 3.2.2 by using Proposition 3.1, Theorem 3.1 and Theorem 3.2.

One can prove the existence and uniqueness of the solution of current model (4.18) by using similar arguments as discussed in Section 3.2.2 of Chapter 3. The solution of equations (4.18) and (4.19) is given by

$$\begin{aligned} \hat{n}^{(k)}(t, s) =& U^{(k)}(t, t_0, s, m^{(p)}, m^{(c)}) \hat{n}_0^{(k)}(s) \\ &+ \int_{t_0}^t U^{(k)}(t, \xi, s, m^{(p)}, m^{(c)}) B_0^{(k)}(\xi, m^{(p)}, m^{(c)}) e^{-sl_0}\, d\xi\,, \qquad (4.24) \\ U^{(k)}(t, \xi, s, m^{(p)}, m^{(c)}) :=& \exp\left[-s \int_\xi^t G^{(k)}(\tau, m^{(p)}, m^{(c)})\, d\tau\right], \quad \forall\, \xi, t \in \Omega_t\,. \end{aligned}$$

The uniqueness of the solution can be proved by using Theorem 3.3. □

4.3 Coupled Preferential Crystallizers Model

This section gives a mathematical model for the simulation of preferential crystallization of enantiomers in two batch preferential crystallizers which are interconnected with fines dissolution pipes. A simplified dynamic model of ideally mixed batch crystallizers for isothermal and non-isothermal conditions is simulated. Here, we are considering the simplest case, in which inflow and outflow pipes are attached to the crystallizers and we assume that fines dissolves completely at the end of the pipe. Furthermore, we are assuming the same volume and residence time for both crystallizers. Similar assumptions hold for the two dissolution pipes as their volume and residence time are identical. The function of the pipes (heat exchanger) is to provide sufficient heat to the fines so that they can dissolve completely. Figure 4.7 shows the schematic diagram of the coupled preferential crystallizers. In vessel A the L- threonine is preferred enantiomer while D- threonine is counter and in vessel B vice versa. Both enantiomers crystallizes simultaneously in separate crystallizers.

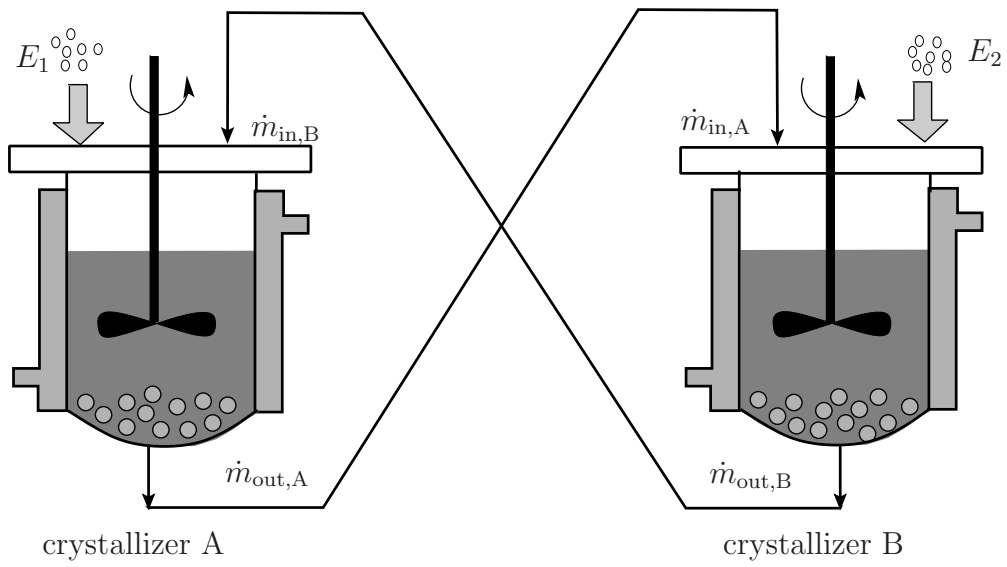

Figure 4.7: Coupled batch process setup

The balance laws for the solid phase are as follows

$$\frac{\partial n_\alpha^{(k)}(t,l)}{\partial t} = -G_\alpha^{(k)}(t, m_\alpha^{(p)}, m_\alpha^{(c)}) \frac{\partial n_\alpha^{(k)}(t,l)}{\partial l} - \frac{1}{\tau_{1,\alpha}} h_\alpha(l) n_\alpha^{(k)}(t,l)\,, \quad (t,l) \in \mathbb{R}_+^2\,, \tag{4.25}$$

where $\mathbb{R}_+ :=]0, \infty[$, $k \in \{p, c\}$ and $\alpha \in \{\text{A}, \text{B}\}$. The notation k stands for preferred or counter enantiomers and α for crystallizers A and B. In equation (4.25) $\tau_{1,\alpha}$ is the residence time in the corresponding crystallizer. It is defined as

$$\tau_{1,\alpha} = \frac{V_\alpha}{\dot{V}_\alpha}\,, \tag{4.26}$$

where V_α is the the volume of each crystallizer and $\dot{V}_\alpha$ is the corresponding volumetric flux rate. Again in equation (4.25), $h_\alpha(l)$ is a death function, which describes the dissolution of particles below some critical size, see Figure 4.6.

The mass balance for the liquid phase in the crystallizer is given by

$$\frac{dm_{\text{A}}^{(k)}(t)}{dt} = \dot{m}_{\text{in,B}}^{(k)}(t) - \dot{m}_{\text{out,A}}^{(k)}(t) - 3\rho_{\text{c}} k_{\text{v}} G_{\text{A}}^{(k)}(t, m_{\text{A}}^{(p)}, m_{\text{A}}^{(c)})\, \mu_{2,\text{A}}^{(k)}(t)\,, \tag{4.27}$$

$$\frac{dm_{\text{B}}^{(k)}(t)}{dt} = \dot{m}_{\text{in,A}}^{(k)}(t) - \dot{m}_{\text{out,B}}^{(k)}(t) - 3\rho_{\text{c}} k_{\text{v}} G_{\text{B}}^{(k)}(t, m_{\text{B}}^{(p)}, m_{\text{B}}^{(c)})\, \mu_{2,\text{B}}^{(k)}(t)\,. \tag{4.28}$$

Here, $\mu_{2,\alpha}^{(k)}(t)$ represents the second moment of the number density $n_\alpha^{(k)}(t,l)$. Because of the fines dissolution these equations have four mass fluxes in (4.27) and (4.28). The first one $\dot{m}_{\text{in,A}}^{(k)}(t)$ is the mass flux in the liquid phase which is going into the crystallizer B. The

second one $\dot{m}^{(k)}_{\mathrm{out,A}}(t)$ is the outgoing mass flux of crystallizer A going into the dissolution pipe. The mass flux $\dot{m}^{(k)}_{\mathrm{in,B}}(t)$ is the incoming mass flux for crystallizer A and $\dot{m}^{(k)}_{\mathrm{out,B}}(t)$ is the outgoing flux from crystallizer B. They are defined as follow

$$\dot{m}^{(k)}_{\mathrm{out},\alpha}(t) = w^{(k)}_{\alpha}(t, m^{(p)}_{\alpha}, m^{(c)}_{\alpha})\, \rho_{\mathrm{liq}}(T)\dot{V}_{\alpha}\,, \quad k \in \{p, c\}\,, \;\; \alpha \in \{\mathrm{A}, \mathrm{B}\}\,, \tag{4.29}$$

$$\dot{m}^{(k)}_{\mathrm{in},\alpha}(t) = \dot{m}^{(k)}_{\mathrm{out},\alpha}(t - \tau_{2,\alpha}) + \frac{k_{\mathrm{v}}\rho}{\tau_{1,\alpha}} \int_0^{\infty} l^3 h_{\alpha}(l) n^{(k)}_{\alpha}(t - \tau_{2,\alpha}, l)\, dl\,, \tag{4.30}$$

where $w^{(k)}_{\alpha}$ are the mass fractions. Here $\tau_{2,\alpha}$ is the residence time of the dissolution unit (the pipe) interconnecting both crystallizers. It is defined as

$$\tau_{2,\alpha} = \frac{\pi r^2_{\alpha} L_{\alpha}}{\dot{V}_{\alpha}}\,, \tag{4.31}$$

where r_{α} and L_{α} are the radius and length of each pipe, respectively.

The birth of new particles (nucleation) is incorporated in this model as a left boundary condition for the PBE at minimum crystal size $l = l_0$.

$$n^{(k)}_{\alpha}(t, l_0) = \frac{B^{(k)}_{\alpha}(t, m^{(p)}_{\alpha}, m^{(c)}_{\alpha})}{G^{(k)}_{\alpha}(t, m^{(p)}_{\alpha}, m^{(c)}_{\alpha})}\,. \tag{4.32}$$

The growth rate kinetics are described as

$$G^{(k)}_{\alpha}(t) = k_{\mathrm{g}} \left(S^{(k)}_{\alpha}(t, m^{(p)}_{\alpha}, m^{(c)}_{\alpha})\right)^{g}\,. \tag{4.33}$$

Here $S^{(k)}_{\alpha}$ denotes the relative supersaturation for the corresponding enantiomer defined as

$$S^{(k)}_{\alpha}(t) = \frac{w^{(k)}_{\alpha}(t, m^{(p)}_{\alpha}, m^{(c)}_{\alpha})}{w^{(k)}_{\mathrm{eq},\alpha}(t, m^{(p)}_{\alpha}, m^{(c)}_{\alpha})} - 1. \tag{4.34}$$

Here $w^{(k)}_{\alpha}$ is mass fraction of the dissolved enantiomer, while $w^{(k)}_{\mathrm{eq},\alpha}$ is equilibrium mass fraction for the corresponding enantiomer. The mass fraction is defined as

$$w^{(k)}_{\alpha}(t, m^{(p)}_{\alpha}, m^{(c)}_{\alpha}) = \frac{m^{(k)}_{\alpha}(t)}{m^{(p)}_{\alpha}(t) + m^{(c)}_{\alpha}(t) + m_{\mathrm{solv}}(t)}, \tag{4.35}$$

where m_W is the mass of solvent (here water). The nucleation rates are described as

$$B^{(p)}_{\alpha}(t, m^{(p)}_{\alpha}, m^{(c)}_{\alpha}) = k^{(p)}_{\mathrm{b}} \left(S^{(p)}_{\alpha}(t, m^{(p)}_{\alpha}, m^{(c)}_{\alpha})\right)^{b^{(p)}} \mu^{(p)}_{3,\alpha}(t)\,, \tag{4.36}$$

$$B^{(c)}_{\alpha}(t, m^{(p)}_{\alpha}, m^{(c)}_{\alpha}) = k^{(c)}_{\mathrm{b}} e^{-\frac{b^{(c)}}{ln\left(S^{(c)}_{\alpha}(t, m^{(p)}_{\alpha}, m^{(c)}_{\alpha})+1\right)^2}}\,. \tag{4.37}$$

The given model covers the case of isothermal operation, i.e. the temperature is kept constant during the batch process. A natural extension of the process would be to vary the temperature during the batch process according to a specified temperature profile.

4.4 Numerical Schemes

In order to solve the above models for preferential crystallization of enantiomers, we use the same numerical schemes which are presented in the last chapter. Alternatively, we are also interested to apply the method of characteristics (MOC) for the solution of the above models. In the following we give a brief overview of the method.

4.4.1 Method of characteristics (MOC)

For the derivation and explanation of the numerical scheme, it is convenient to consider a single population balance equation (PBE). The application of the scheme to the desired models of preferential crystallization is then straightforward. We consider a PBE of the form

$$\frac{\partial n(t,l)}{\partial t} = -\frac{\partial [G(t,l)n(t,l)]}{\partial l} + \mathcal{Q}(t,l)\,, \quad (t,l) \in \mathbb{R}^2_+\,, \tag{4.38}$$

where $\mathbb{R}_+ :=]0,\infty[$, $G(t,l) \geq 0$ is the length based growth and $\mathcal{Q}(t,l)$ is any source term. For a scalar linear conservation law, for example PBE (4.38) in the present case, there exist characteristic curves along which information propagates. The mesh is moved with the characteristic speed, whereby the linear advection is treated exactly. This drastically reduces numerical diffusion in the solution of the scheme in comparison to other schemes which use some discretization techniques for approximating the advection term.

For the MOC we use the same initial discretization at time $t = 0$ as given by (3.71)-(3.73) in the previous chapter for the finite volume schemes and consider a moving mesh along the characteristics with mesh points $l_{i+1/2}(t)$ for $i = 0, 1, 2, \cdots N$.

Let us substitute the growth rate $G(t,l)$ by

$$\frac{dl}{dt} := G(t,l)\,. \tag{4.39}$$

Then equation (4.38) leads to

$$\frac{\partial n(t,l)}{\partial t} + \frac{\partial}{\partial l}\left(\frac{dl}{dt}\cdot n(t,l)\right) = \mathcal{Q}(t,l)\,. \tag{4.40}$$

Integration over the control volume $\Omega_i(t) = \left[l_{i-\frac{1}{2}}(t), l_{i+\frac{1}{2}}(t)\right]$ gives

$$\int\limits_{\Omega_i(t)} \frac{\partial n(t,l)}{\partial t}\, dl + \left(\frac{dl}{dt}\cdot n(t,l)\right)\Bigg|_{l_{i-\frac{1}{2}}(t)}^{l_{i+\frac{1}{2}}(t)} = \int\limits_{\Omega_i(t)} \mathcal{Q}(t,l)\, dl\,. \tag{4.41}$$

The Leibniz formula [1] on the left hand side of (4.41) gives

$$\frac{d}{dt}\int\limits_{\Omega_i(t)} n(t,l)\; dl = \int\limits_{\Omega_i(t)} \mathcal{Q}(t,l)\; dl\,. \tag{4.42}$$

Let $n_i := n_i(t)$ and $\mathcal{Q}_i := \mathcal{Q}_i(t)$ denote, respectively, the average values of the number density and source term in each cell Ω_i. Like equation (3.75), they are defined as

$$n_i := \frac{1}{\Delta l_i(t)}\int\limits_{\Omega_i} n(t,l)\, dl\,, \qquad \mathcal{Q}_i := \frac{1}{\Delta l_i(t)}\int\limits_{\Omega_i} \mathcal{Q}(t,l)\, dl\,, \tag{4.43}$$

where $\Delta l_i(t) = l_{i+\frac{1}{2}}(t) - l_{i-\frac{1}{2}}(t)$. After using the above definitions, equation (4.42) implies

$$\frac{d}{dt}\left[\left(l_{i+\frac{1}{2}}(t) - l_{i-\frac{1}{2}}(t)\right) n_i\right] = \Delta l_i(t)\, \mathcal{Q}_i\,. \tag{4.44}$$

By using the product rule and (4.39), the left hand side of (4.44) gives

$$\begin{aligned}\frac{d}{dt}\left[\left(l_{i+\frac{1}{2}}(t) - l_{i-\frac{1}{2}}(t)\right) n_i\right] &= \Delta l_i(t)\,\frac{dn_i}{dt} + \left(\frac{dl_{i+\frac{1}{2}}}{dt} - \frac{dl_{i-\frac{1}{2}}}{dt}\right) n_i \\ &= \Delta l_i(t)\,\frac{dn_i}{dt} + \left(G_{i+\frac{1}{2}} - G_{i-\frac{1}{2}}\right) n_i\,. \end{aligned} \tag{4.45}$$

After replacing the left hand side of (4.44) with (4.45) and dividing the resulting equation by $\Delta l_i(t)$, one gets

$$\frac{dn_i}{dt} = -\left(G_{i+\frac{1}{2}} - G_{i-\frac{1}{2}}\right)\frac{n_i}{\Delta l_i(t)} + \mathcal{Q}_i\,. \tag{4.46}$$

In summary to use the MOC, we have to solve the following set of equations

$$\frac{dn_i}{dt} = -\left(G_{i+\frac{1}{2}} - G_{i-\frac{1}{2}}\right)\frac{n_i}{\Delta l_i(t)} + \mathcal{Q}_i\,, \tag{4.47}$$

$$\frac{dl_{i+\frac{1}{2}}}{dt} = G_{i+\frac{1}{2}}\,, \qquad \forall\; i = 1, 2, \cdots, N \tag{4.48}$$

with initial data

$$n(0, l_i) = n_0(l_i)\,. \tag{4.49}$$

Note that, in case of size independent growth the first term on the right hand side of (4.47) is zero.

Treatment of nucleation term: In order to incorporate nucleation into the algorithm, a new cell of nuclei size is added at a given time level. The total number of mesh points can be kept constant by deleting the last cell at the same time level. Hence, all the variables such as $n_i(t)$ and $l_i(t)$ are initiated at these time levels and the time integrator restarts. In this case the boundary condition is again the same as given by (3.98). The above system of ordinary differential equations can be solved by any standard ODE solver.

4.5 Numerical Test Problems

In order to validate our numerical schemes for the considered models of preferential crystallization with fines dissolution, we solve three numerical test problems. In all test problems we have taken the minimum crystal size $l_0 = 10^{-8}m$.

4.5.1 Single crystallizer

Here, we consider two test problems for this model with and without fines dissolution and isothermal and non-isothermal conditions.

Test problem 1:

The idea behind choosing this problem is its practical considerations, see [19, 20] and references therein. The initial number density function of the seeds of preferred enantiomer is given as

$$n^{(p)}(0,l) = \frac{1}{\sqrt{2\pi}\sigma I_{\mathrm{a}}} \cdot \frac{1}{l} \cdot \exp\left[-\frac{1}{2} \cdot \left(\frac{ln(l) - \overline{\mu}}{\sigma}\right)^2\right], \quad I_{\mathrm{a}} = \frac{k_{\mathrm{v}} \cdot \rho_{\mathrm{c}}}{m_{\mathrm{seeds}}} \mu_3^{(p)}(0)\,. \tag{4.50}$$

Crystals of the counter enantiomer are initially not present, i.e.

$$n^{(c)}(0,l) = \quad 0\,. \tag{4.51}$$

Here we assume $\sigma = 0.3947\,m$, $\overline{\mu} = -6.8263\,m$, while m_{seeds} is the mass of initial seeds. The maximum crystal size that was expected is $l_{\max} = 0.005\,m$ which is subdivided into 500 grid points. The final simulation time was taken as 600 minutes.

The kinetic parameters considered in this problem are given in Table 4.1. They are capable to describe the crystallization of the enantiomers of the amino acid threonine in water.

The temperature trajectory used for the simulation is as follows

$$T(t)[^oC] = -1.24074 \times 10^{-7}\,t^3 + 4.50926 \times 10^{-5}\,t^2 - 4.05556 \times 10^{-3}\,t + 33\,. \tag{4.52}$$

Here the time is taken in minutes. While considering this temperature trajectory, the constants k_{g} and $k_{\mathrm{b}}^{(k)}$ will become functions of temperature as given below.

$$k_{\mathrm{g}}(t) = k_{\mathrm{g},0} \cdot e^{-\frac{E_{\mathrm{A,g}}}{R(T(t)+273.15)}}, \quad k_{\mathrm{b}}^{(k)}(t) = k_{\mathrm{b},0}^{(k)} \cdot e^{-\frac{E_{\mathrm{A,b}}}{R(T(t)+273.15)}}. \tag{4.53}$$

Here $k_{\mathrm{g},0}$, $E_{\mathrm{A,g}}$, $k_{\mathrm{b},0}^{(k)}$, $E_{\mathrm{A,b}}$ and R are constants given in Table 4.1. The equilibrium mass fraction of one enantiomer depends on the mass fraction of the other enantiomer and on

temperature. They are given as

$$w_{\text{eq}}^{(p)}(t, m_\alpha^{(p)}, m_\alpha^{(c)}) = \sum_{j=0}^{2} T^j(t) \left(A_j + B_j \, w^{(c)}(t, m_\alpha^{(p)}, m_\alpha^{(c)}) \right) , \tag{4.54}$$

$$w_{\text{eq}}^{(c)}(t, m_\alpha^{(p)}, m_\alpha^{(c)}) = \sum_{j=0}^{2} T^j(t) \left(C_j + D_j \, w^{(p)}(t, m_\alpha^{(p)}, m_\alpha^{(c)}) \right) . \tag{4.55}$$

The constants in above two equations are also given in Table 4.1. Note that the same equations (4.54) and (4.55) are also used in the isothermal case, where the temperature remains constant.

Figures 4.8 and 4.9 show the number density plots for preferred enantiomer for isothermal condition at 33^oC and for the non-isothermal case (temperature follows equation (4.52)). In these figures the number densities for with and without fines dissolution are given. Each figure compares the different numerical methods used to solve the population balance model. In the isothermal case with fines dissolution, the peak of number density resulting from nucleation is smaller in comparison to the peak of number density without fines dissolution. It is due to the fact that fines are taken out from the crystallizer, heated in recycled pipe, thus dissolved and sent back to the crystallizer. This increases the supersaturation of the solution in the crystallizer which consequently reduces the secondary nucleation. Hence the number density resulting from nucleation is also reduced. The number density resulting from initial seed distribution will increase in the case of fines dissolution because the supersaturation of solution in the crystallizer increases which will allow the nuclei to grow more in comparison to the case without fines dissolution.

In the non-isothermal case, the temperature is a time-dependent polynomial. As temperature is reduced the nucleation rate increases which in turn increases the number density resulting from nucleation. Hence in the non-isothermal case, where the temperature is reducing with time, the number density increases in comparison to the isothermal case. The number of peaks in the crystal size distribution depends on the temperature profile. The number density in non-isothermal case with fines dissolution is better because the crystal size is larger than in the other cases. Figures 4.10 and 4.11 show the three dimensional plots of number density along t and l.

Figure 4.12 shows the mass fraction plots for preferred (p-) and counter (c-) enantiomer with and without fines dissolution. In isothermal case, mass fraction of p-enantiomer decreases sharply because we seeded p-enantiomer and it crystallizes out. While c-enantiomer mass fraction stays constant at the beginning and then decreases later because of spontaneous primary nucleation. At some time, both curves will join which is the point where both enantiomer have similar equilibrium levels. The curve for each enantiomer with fines dissolution is above compared to without fines dissolution due to the fact that solubility increases in case of fines dissolution. In non-isothermal case, mass fractions are completely

controlled by the temperature profile.

Figure 4.13 shows the supersaturation plots for both enantiomers. Their behavior is entirely dependent on temperature which is clear from equations (4.54) and (4.55). Figures 4.14, 4.15 and 4.16 show the growth rate, nucleation rate and third moment plots for $HR - \kappa = -1$ scheme and are the same for other schemes. At the beginning, growth rate and nucleation rate for the p-enantiomer reduces significantly because of sharp changes in mass fraction and supersaturation. In the non-isothermal case, the nucleation rate for the c-enantiomer with fines dissolution achieves a very high nucleation rate value because primary nucleation requires high level of supersaturation.

The third moment plots in the isothermal case for p-enantiomer stays constant at the end of the process, because of no further change in mass fraction and supersaturation. For the non-isothermal case, the behavior results from mass fraction, supersaturation and temperature profile. Generally, for all plots in the non-isothermal case, the trends of the plots will vary with a different temperature profiles and initial crystal size distribution.

Tables 4.2 and 4.3 show the percentage errors in mass preservation for the cases without and with fines dissolution under isothermal and non-isothermal conditions, respectively. Both tables show that in the case of finite volume schemes, there are negligible changes in the percentage errors when we increase the number of mesh points from $N = 500$ to $N = 1000$. However, with the method of characteristics (MOC) the percentage errors decreases as we increase the number of mesh points. The finite volume schemes have large percentage errors as compared to the MOC. In these tables we have also given the computational time for all schemes. It is clear from the tables that MOC requires less computational time as compared to the finite volume schemes. However, for all schemes the computational times are less than eight seconds with $N = 1000$ mesh points. In Tables 4.2 and 4.3 we have only presented the computational time for the isothermal case and was found to be the same for the non-isothermal case. All the computations were performed on computer with 1.73 GHz processor and 2 GB RAM. The programs are written in C programming language and were compiled with gcc 3.3.5 compiler using Suse Linux version 9.3 operating system.

Finally, Figure 4.17 compares the numerical and experimental results for the alpha-curve. The experimental results were obtained by Elsner et al. [19, 20]. Since the curve is not sharp, the results of the first and second order schemes are almost the same. The results show an excellent agreement among experimental and numerical results.

Table 4.1: Parameters for Test problems 1,2 and 3

Description	*Symbol*	*Value*	*Unit*
Growth rate constant	$k_{\mathrm{g},0}$	$4.62 \cdot 10^8$	$\frac{m}{min}$
Growth rate exponent	g	1.0	$-$
Activation energy	$E_{\mathrm{A,g}}$	$75.6 \cdot 10^3$	kJ/mol
Nucleation rate constant (seeded)	$k_{\mathrm{b},0}^{(p)}$	$3.24 \cdot 10^{25}$	$\frac{1}{m^3\, min}$
Nucleation rate exponent (seeded)	$b^{(p)}$	4.0	$-$
Activation energy	$E_{\mathrm{A,b}}$	$78.7 \cdot 10^3$	kJ/mol
Nucleation rate constant (unseeded)	$k_{\mathrm{b},0}^{(c)}$	$3.84 \cdot 10^6$	$\frac{1}{min}$
Nucleation rate exponent (unseeded)	$b^{(c)}$	$6.0 \cdot 10^{-2}$	$-$
Universal gas constant	R	8.314	$J/mol \cdot K$
Density of crystals	ρ_{c}	1250	$\frac{kg}{m^3}$
Density of liquid	ρ_{liq}	1000	$\frac{kg}{m^3}$
Volume shape factor	k_{v}	0.0248	$-$
Initial mass of p-enantiomer	$m^p(0)$	0.100224	kg
Initial mass of c-enantiomer	$m^c(0)$	0.100224	kg
Mass of solvent	m_{solv}	0.799552	kg
Mass of seeds	m_{seeds}	$2.5 \cdot 10^{-3}$	kg
Residence time in crystallizer	τ_1	60	min
Volume of crystallizer	V_1	$1.0 \cdot 10^{-3}$	m^3
Residence time in pipe	τ_2	10	min
Radius of pipe	r	$1.0 \cdot 10^{-2}$	m
Length of pipe	L	$5.3 \cdot 10^{-1}$	m
Constant (seeded)	A_0	0.056157	$-$
Constant (seeded)	A_1	0.00143838	$-$
Constant (seeded)	A_2	$-3.41777 \cdot 10^{-6}$	$-$
Constant (seeded)	B_0	0.00624436	$-$
Constant (seeded)	B_1	-0.0039185	$-$
Constant (seeded)	B_2	$4.4174 \cdot 10^{-5}$	$-$
Constant (unseeded)	C_0	0.0574049	$-$
Constant (unseeded)	C_1	0.0013584	$-$
Constant (unseeded)	C_2	$-2.3638 \cdot 10^{-6}$	$-$
Constant (unseeded)	D_0	0.0071391	$-$
Constant (unseeded)	D_1	-0.00383673	$-$
Constant (unseeded)	D_2	$4.2345 \cdot 10^{-5}$	$-$

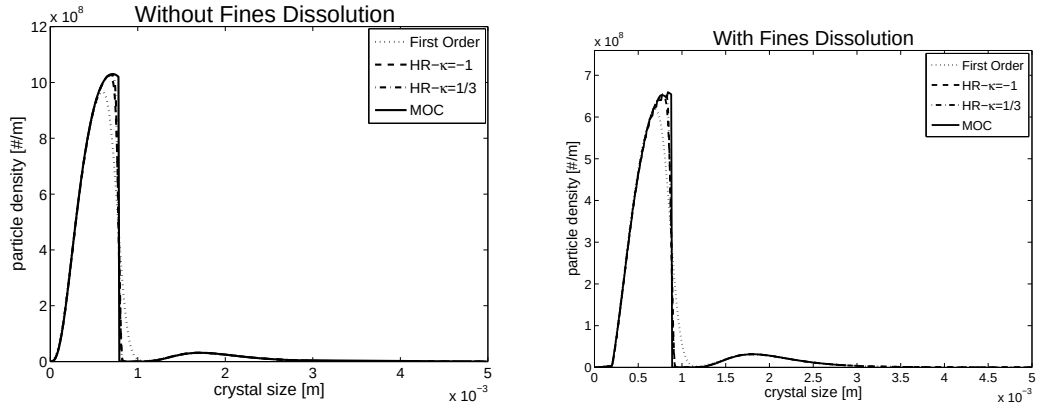

Figure 4.8: Test problem 1: Comparison of the preferred enantiomer number density for different numerical methods and isothermal case at 600 minutes.

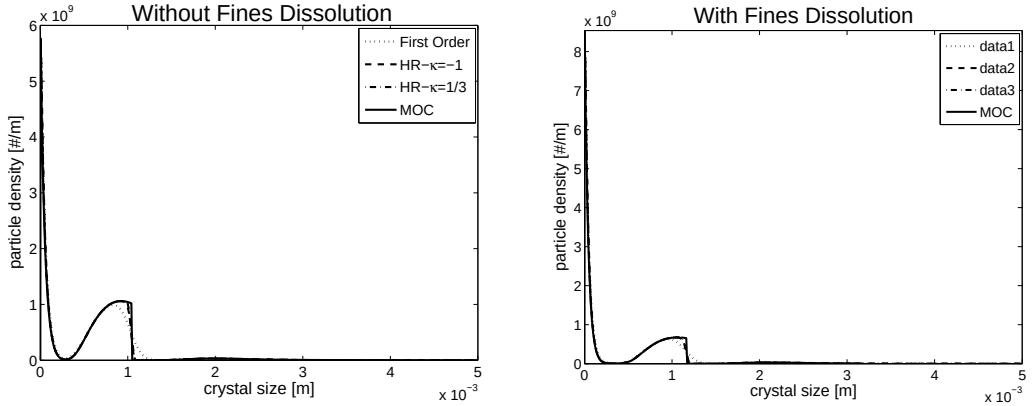

Figure 4.9: Test problem 1: Comparison of the preferred enantiomer number density for different methods and non-isothermal case at 600 minutes.

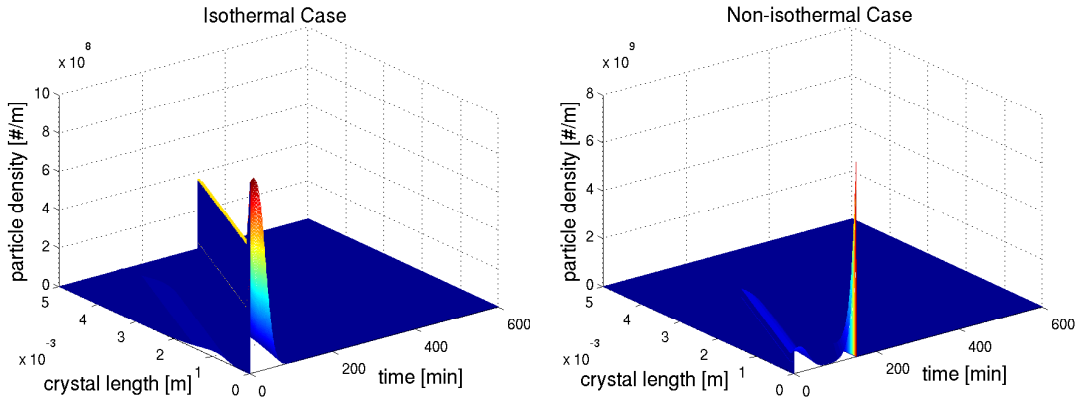

Figure 4.10: Test problem 1: Comparison of number density for the preferred enantiomer with fines dissolution using MOC.

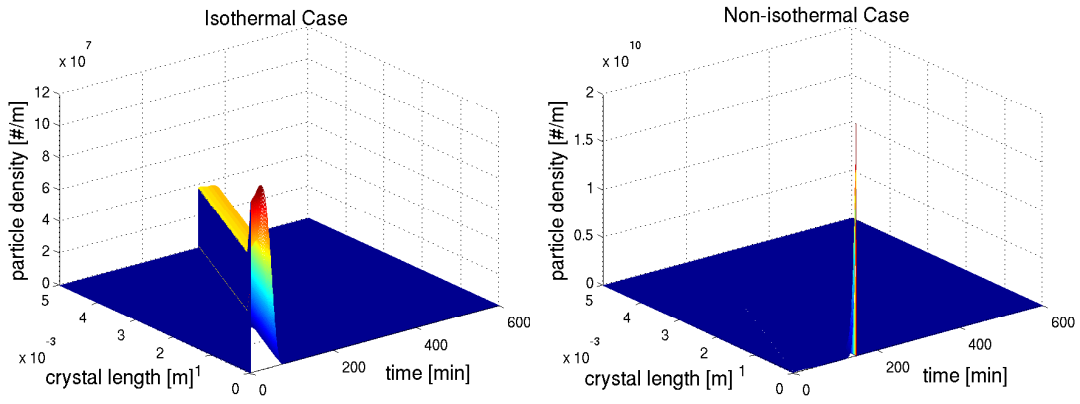

Figure 4.11: Test problem 1: Comparison of the number density for the counter enantiomer with fines dissolution using MOC.

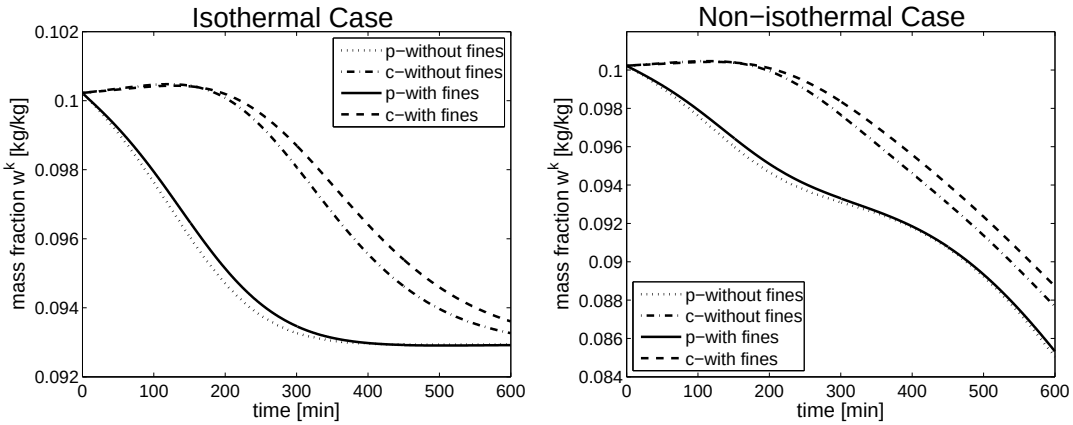

Figure 4.12: Test problem 1: Comparison of mass fractions in the liquid phase for the preferred (p-) and counter (c-) enantiomer.

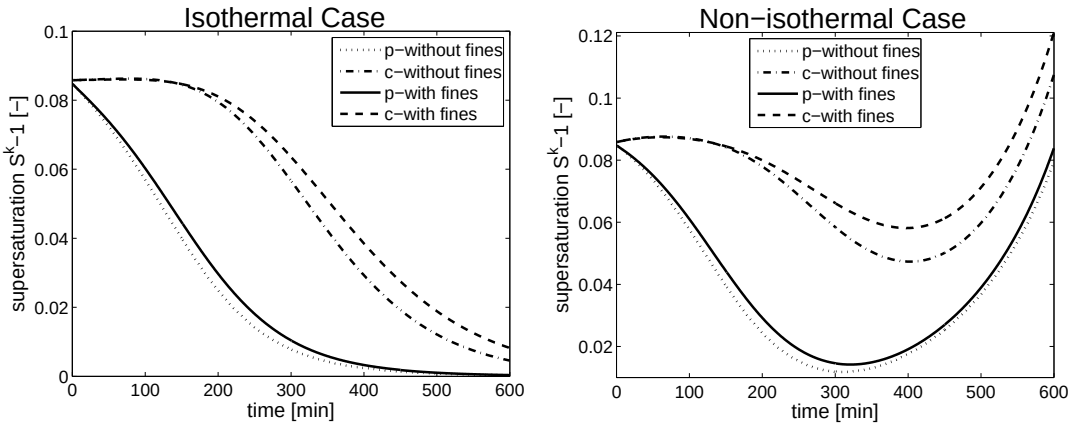

Figure 4.13: Test problem 1: Comparison of supersaturations for the preferred (p-) and counter (c-) enantiomer.

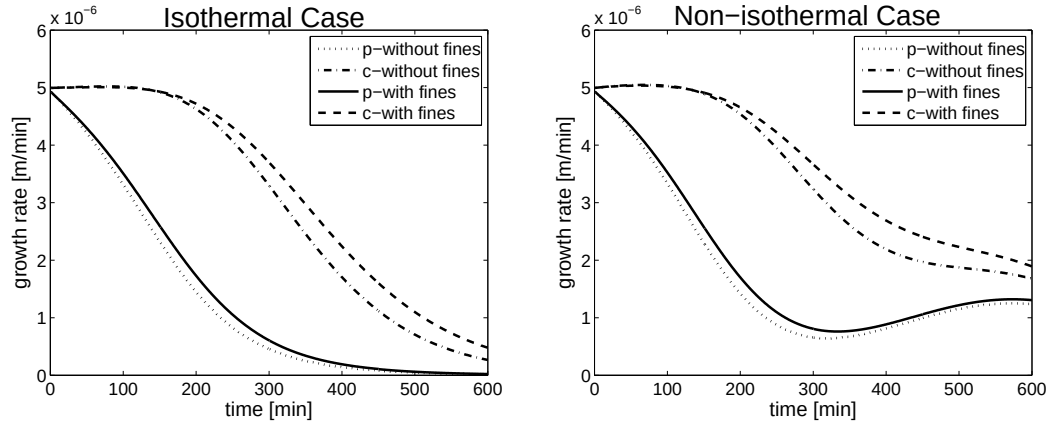

Figure 4.14: Test problem 1: Comparison of growth rates for the preferred (p-) and counter (c-) enantiomer.

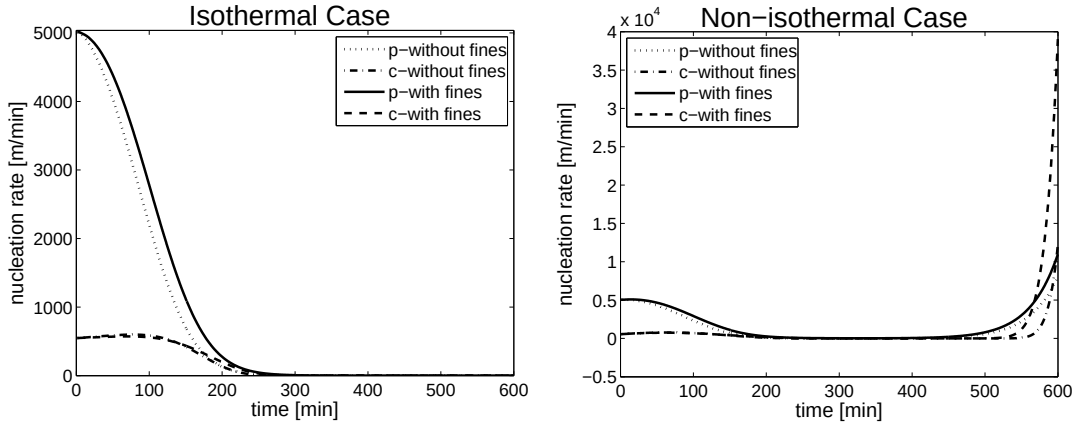

Figure 4.15: Test problem 1: Comparison of nucleation rates for the preferred (p-) and counter (c-) enantiomer.

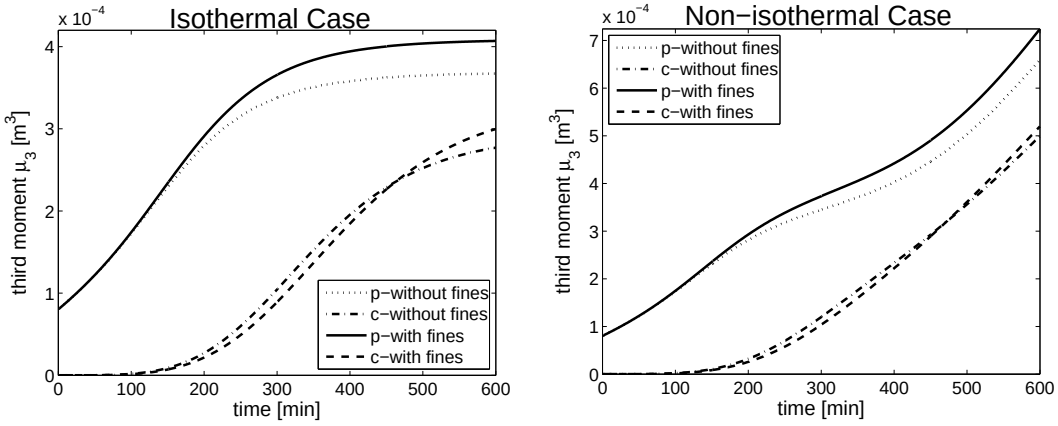

Figure 4.16: Test problem 1: Comparison of third moments for the preferred (p-) and counter (c-) enantiomer.

Table 4.2: Test problem 1: Percentage errors in mass balance (without fines dissolution).

Method	*Isothermal*		*Non-isothermal*		*CPU time (s) (isothermal)*	
	N=500	*N=1000*	*N=500*	*N=1000*	*N=500*	*N=1000*
First order scheme	3.737	3.775	4.460	4.669	1.5	3.1
HR-$\kappa = -1$ scheme	3.811	3.813	4.733	4.736	2.2	4.4
HR-$\kappa = 1/3$ scheme	3.813	3.814	4.736	4.737	2.3	4.6
MOC	2.604	1.844	3.792	2.917	0.34	0.41

Table 4.3: Test problem 1: Percentage errors in masses balance (with fines dissolution).

Method	*Isothermal*		*Non-isothermal*		*CPU time (s) (isothermal)*	
	N=500	*N=1000*	*N=500*	*N=1000*	*N=500*	*N=1000*
First order scheme	2.801	2.838	2.841	2.904	2.3	5.5
HR-$\kappa = -1$ scheme	2.873	2.875	2.962	2.965	3.1	7.5
HR-$\kappa = 1/3$ scheme	2.875	2.876	2.965	2.967	3.5	7.7
MOC	1.823	1.30	2.055	1.086	0.39	0.71

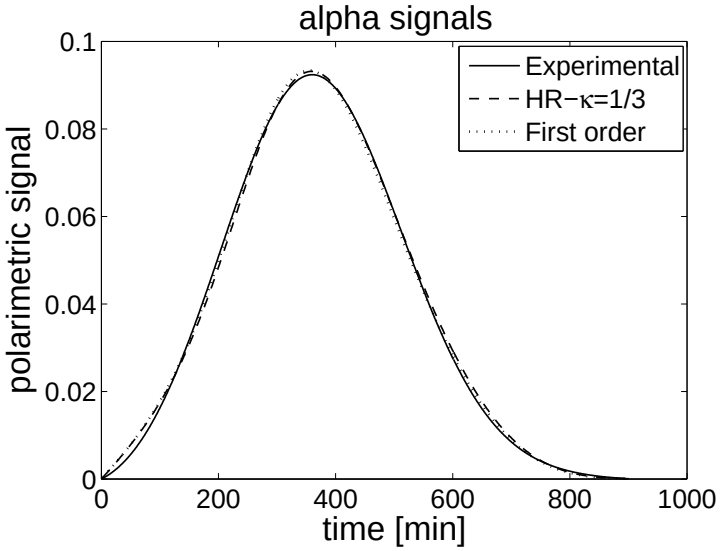

Figure 4.17: Test problem 1: Comparison of experimental and numerical results.

Test problem 2:

The parameters of this problem has also been used in the experiments, see [19, 20] and references therein. The initial number density for the seeds is

$$n^{(p)}(0,l) = \frac{10^7}{\sigma I_{\mathrm{a}}\sqrt{2\pi}} \exp\left(\frac{l-\overline{l}}{\sigma\sqrt{2}}\right)^2 \quad \text{with } I_{\mathrm{a}} = \frac{k_V \cdot \rho_c}{m_{\mathrm{seeds}}}\, \mu_3^{(p)}(0)\,, \tag{4.56}$$

$$n^{(c)}(0,l) = \quad 0\,. \tag{4.57}$$

Here m_{seeds} is the mass of initial seeds, $\overline{l} = 4 \cdot 10^{-4}\, m$ and $\sigma = \overline{l}/15$. The maximum crystal size $l_{\max} = 0.002\, m$ is subdivided into 400 grid points. The final time for the simulation is again 600 minutes. The other parameters considered in this problem are given in Table 4.1.

Figures 4.18 and 4.19 show the number density plots for the preferred enantiomer for isothermal (temperature is constant $= 33^oC$) and non-isothermal case (temperature is time-dependent polynomial, see equation 4.52) with and without fines dissolution.

For the isothermal case, the number density resulting from nucleation is very small and is impossible to see in the current plots. But in case of the non-isothermal we can see it in the small size range of plots. Also, the crystal size increases in the non-isothermal case because of increased supersaturation while with fines the effects are very small. The small effects are due to the chosen temperature profile and the initial crystal size distribution. Figures 4.20 and 4.21 show the three dimensional plots of the number density.

Figures 4.22 and 4.23 show the plots for mass fraction and supersaturation, respectively. Figures 4.24, 4.25 and 4.26 show the growth rate, nucleation rate and third moment plots for both enantiomers in isothermal and non-isothermal cases. These results are obtained from $HR - \kappa = -1$ scheme and are the same for other schemes. The results have similar behavior as in Test problem 1 due to the facts discussed in that problem.

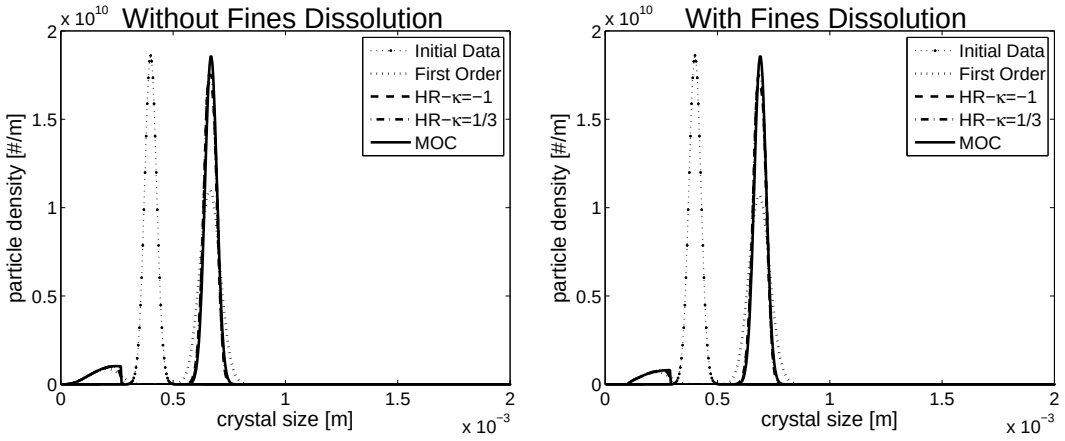

Figure 4.18: Test problem 2: Comparison of the preferred enantiomer number density for different numerical methods and isothermal case. Here both the initial number density and the final number density distribution at 600 minutes are presented.

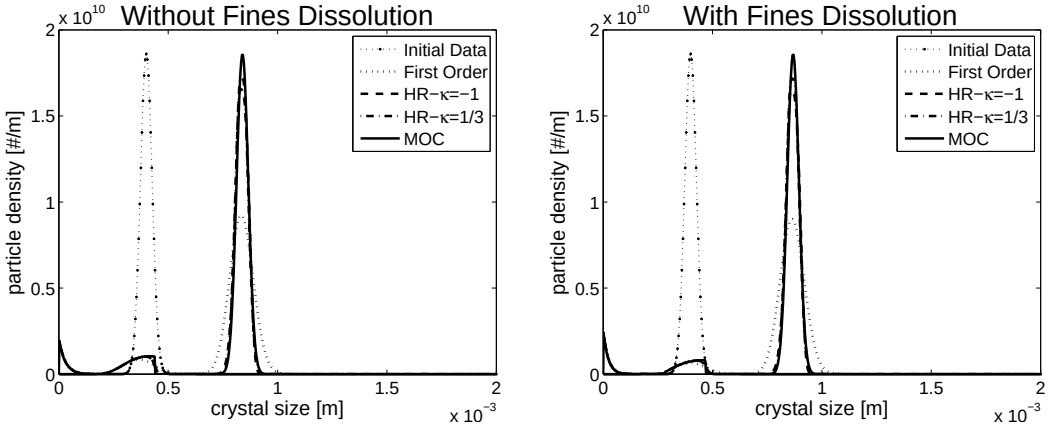

Figure 4.19: Test problem 2: Comparison of number density for different numerical methods for the non-isothermal case.

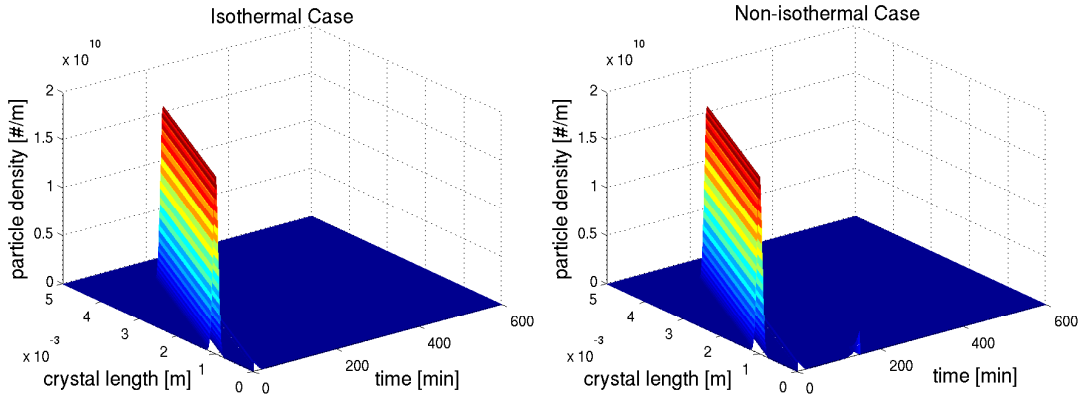

Figure 4.20: Test problem 2: Comparison of number density for the preferred enantiomer with fines dissolution.

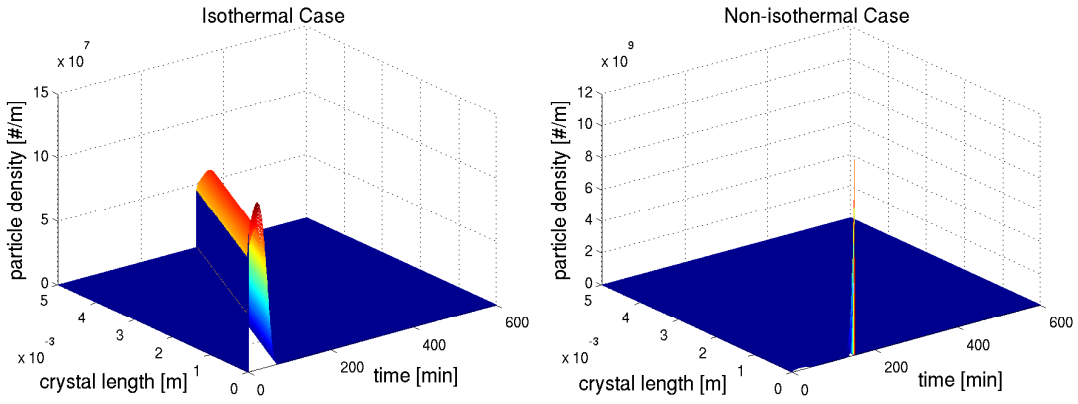

Figure 4.21: Test problem 2: Comparison of number density for the counter enantiomer with fines dissolution.

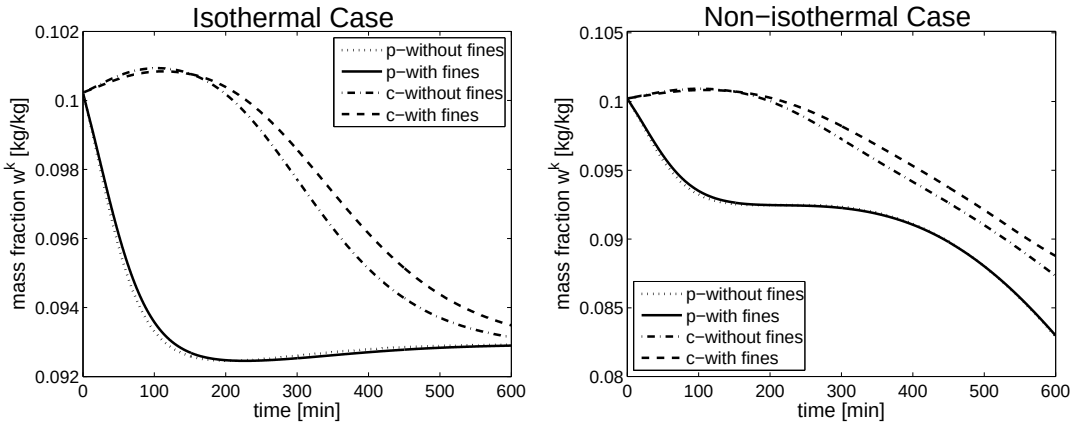

Figure 4.22: Test problem 2: Comparison of mass fractions for the preferred (p-) and counter (c-) enantiomer.

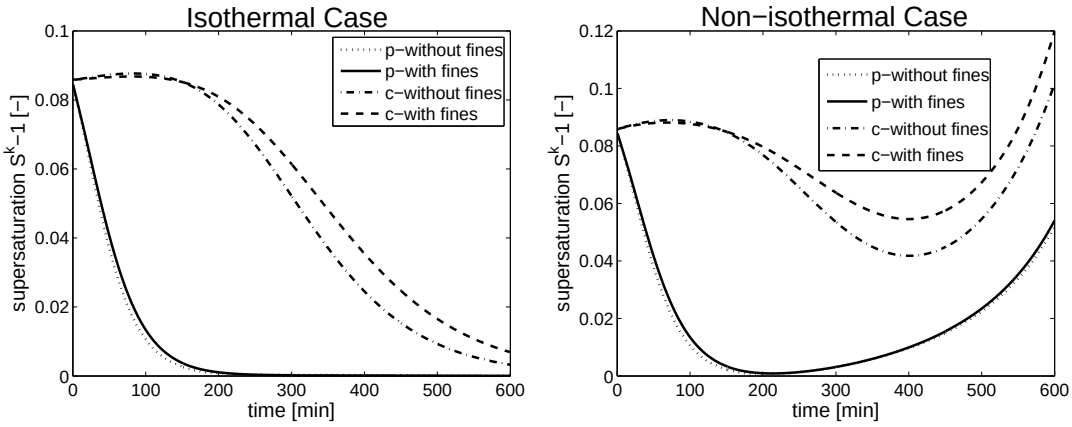

Figure 4.23: Test problem 2: Comparison of supersaturations for the preferred (p-) and counter (c-) enantiomer.

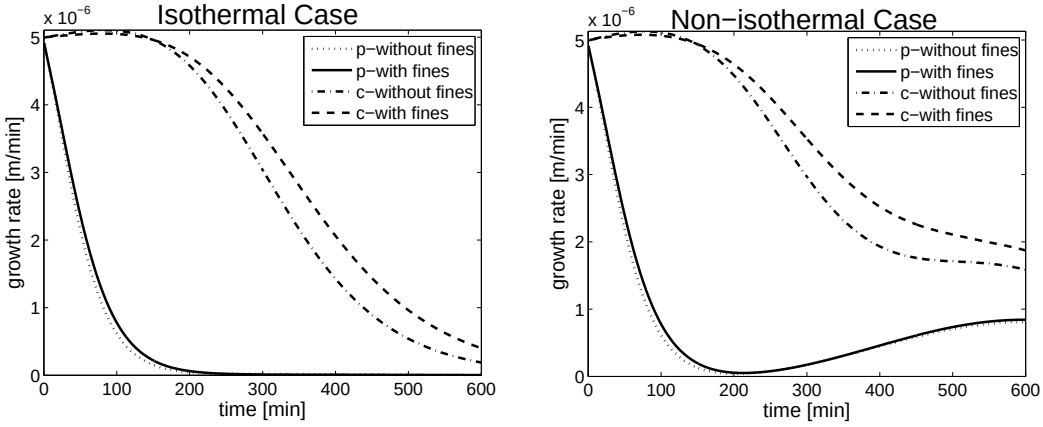

Figure 4.24: Test problem 2: Comparison of growth rates for the preferred (p-) and counter (c-) enantiomer.

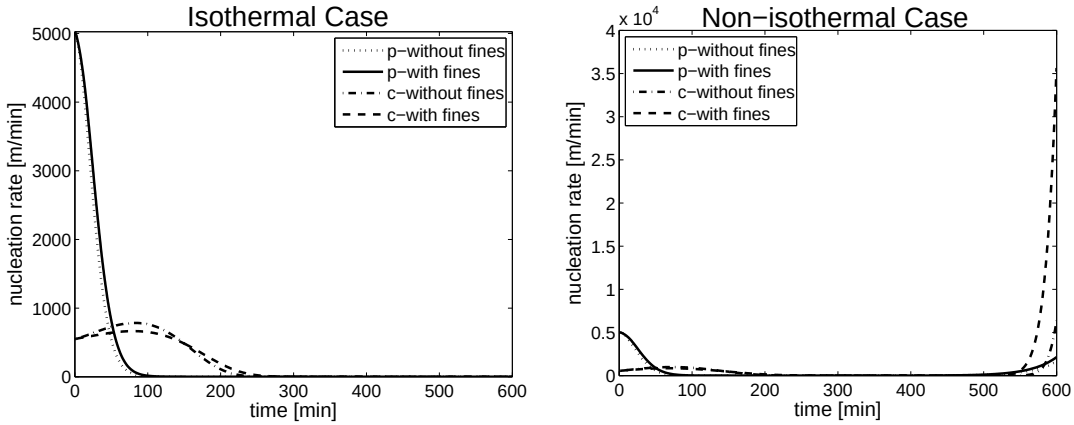

Figure 4.25: Comparison of nucleation rates for the preferred (p-) and counter (c-) enantiomer.

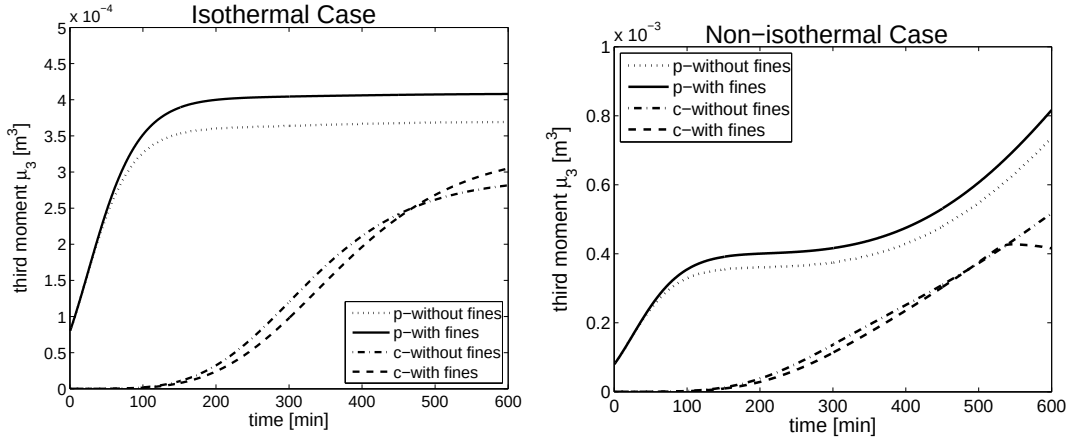

Figure 4.26: Test problem 2: Comparison of third moments for the preferred (p-) and counter (c-) enantiomer.

4.5.2 Coupled crystallizers

Here we give one test problem for the crystallization of enantiomers in coupled crystallizers.

Test problem 3:

In order to validate our numerical schemes for the current model of coupled preferential crystallizers, we consider the following numerical test problem. Again, we have taken the minimum crystal size $l_0 = 0$.

The initial number density of the preferred anantiomer in each crystallizer is given as

$$n_\alpha^{(p)}(0,l) = \frac{1}{\sqrt{2\pi}\sigma I_\alpha} \cdot \frac{1}{l} \cdot \exp\left[-\frac{1}{2} \cdot \left(\frac{ln(l) - \overline{\mu}}{\sigma}\right)^2\right] \tag{4.58}$$

with $I_\alpha = \frac{k_v \cdot \rho_c}{M_{\text{seeds},\alpha}} \mu_{3,\alpha}^{(p)}(0)$. The corresponding number density of the counter enantiomer in each crystallizer is zero, i.e.

$$n_\alpha^{(c)}(0,l) = 0\,. \tag{4.59}$$

Here $\sigma = 0.3947\,m$, $\overline{\mu} = -6.8263\,m$, and $M_{\text{seeds},\alpha}$ is the mass of initial seeds in tank $\alpha \in \{\text{A}, \text{B}\}$. The maximum crystal size is $l_{\max} = 0.005\,m$ which is subdivided into 500 grid points. The final time for the simulation is 600 minutes. The kinetic parameters considered in this problem are given in Table 4.1. Note that enantiomer E_1 is preferred in crystallizer A and enantiomer E_2 is preferred in crystallizer B. The temperature trajectory is the same as given by (4.52). Here the time is taken in minutes. While considering this temperature trajectory, the constants k_g and $k_b^{(k)}$ will become the functions of temperature as given by equation (4.53). The equilibrium mass fraction of one anantiomer depends on the mass fraction of the other enantiomer and on the temperature

$$w_{\text{eq},\alpha}^{(p)}(t, m_\alpha^{(p)}, m_\alpha^{(c)}) = \sum_{i=0}^{2} T^i(t) \left(A_i + B_i w_\alpha^{(c)}(t, m_\alpha^{(p)}, m_\alpha^{(c)})\right), \tag{4.60}$$

$$w_{\text{eq},\alpha}^{(c)}(t, m_\alpha^{(p)}, m_\alpha^{(c)}) = \sum_{i=0}^{2} T^i(t) \left(C_i + D_i w_\alpha^{(p)}(t, m_\alpha^{(p)}, m_\alpha^{(c)})\right). \tag{4.61}$$

The constants in above two equations are given in Table 4.1. Figure 4.27 shows the number density plots in tank A for preferred enantiomer with isothermal case (temperature is constant $= 33^oC$) and non-isothermal case (temperature follows equation (4.52)). Note that, in the current test problem the plots for the enantiomer E_1 in tank A and for the enantiomer E_2 in tank B are the same. In isothermal case, the first large peak in the number density distribution is due to high nucleation rate of preferred enantiomer at the beginning of the process. While the second small number density peak is due to the initial crystals growth.

Table 4.4: Test problem 3: Mass preservation in the schemes for coupled case

Method	*Percentage error Isothermal Case*	*Percentage error Non-isothermal Case*
First order scheme	2.945	2.148
HR-$\kappa = -1$ scheme	3.020	2.301
HR-$\kappa = 1/3$ scheme	3.022	2.302
MOC	1.781	1.996

In non-isothermal case, the temperature is decreasing function of time, hence the peak in the number density generated by nucleation has higher value as compared to isothermal case because of temperature profile. The number of peaks in the number density distribution for non-isothermal case entirely depends on the temperature profile used.

Figures 4.27 compares different numerical methods used for solving the current coupled population balance model in tank A. There is no visible difference between the results of the schemes, so one can not say exactly which one is better. Table 4.4 shows the percentage errors for mass preservation which are minimum in case of the MOC as compared to the finite volume schemes. Furthermore, there is no significant differences in the plots of MOC and finite volume schemes for the mass fraction, supersaturation, growth rate, nucleation rates and third moment. Therefore we have included only plots of MOC results. Figures 4.28 and 4.29 shows the number density in three dimensional for preferred enantiomer and counter enantiomer.

Figure 4.30 shows the mass fraction plots for preferred (p-) and counter (c-) enantiomer. In isothermal case, mass fraction of p-enantiomer decreases sharply because we have seeded p-enantiomer and it crystallizes out. While c-enantiomer mass fraction stays constant at the beginning and decreases later because of spontaneous primary nucleation. After some time both curves will join which is the point of equilibrium level for both enantiomers. In non-isothermal case, mass fraction is completely control by temperature profile.

Figure 4.31 shows the supersaturation plots for both enantiomer in tank A. Their behavior is entirely depending on the temperature as suggested by equations 4.60 and 4.61. Figures 4.32 and 4.33 show the growth rate and nucleation rate plots. At the beginning, growth rate and nucleation rate for p-enantiomer reduces significantly because of sharp changes in the mass fraction and supersaturation. In the non-isothermal case, nucleation rate for the counter enantiomer achieves a larger value because the supersaturation level is higher.

Figure 4.34 shows the trajectories of the third moments. In the isothermal case for the p-enantiomer, at the end of the process, it stays constant because of no further change in mass fraction and supersaturation. In the non-isothermal case the third moment does not approach a steady state because of decreasing temperature in the crystallizer

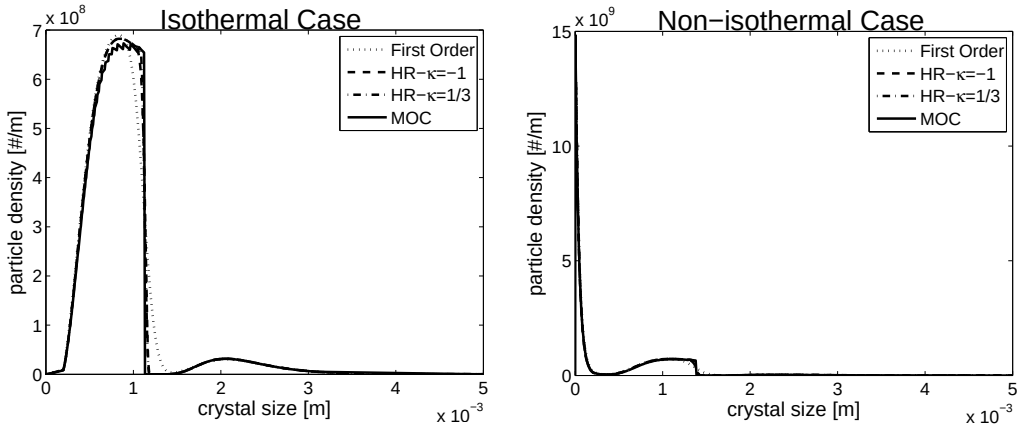

Figure 4.27: Test problem 3: Comparison of the number density for the preferred enantiomer for different operation modes at $t = 600$ minutes.

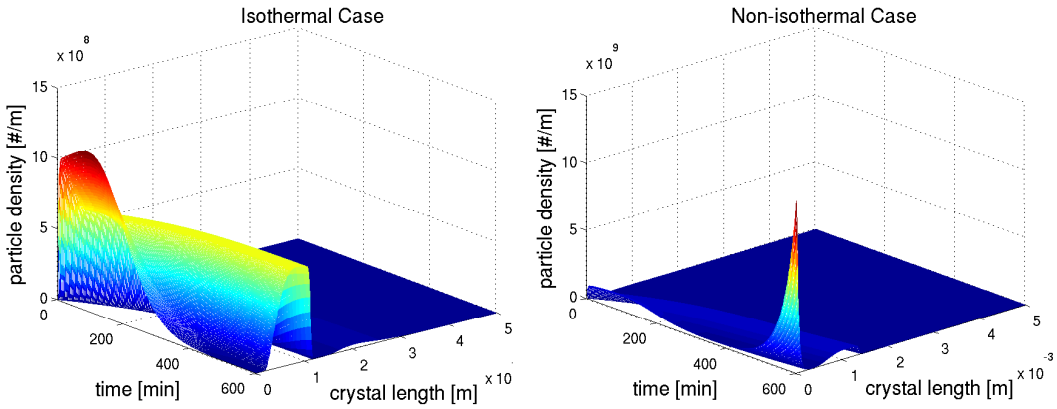

Figure 4.28: Test problem 3: Three dimensional plots of number density for the preferred enantiomer by using MOC.

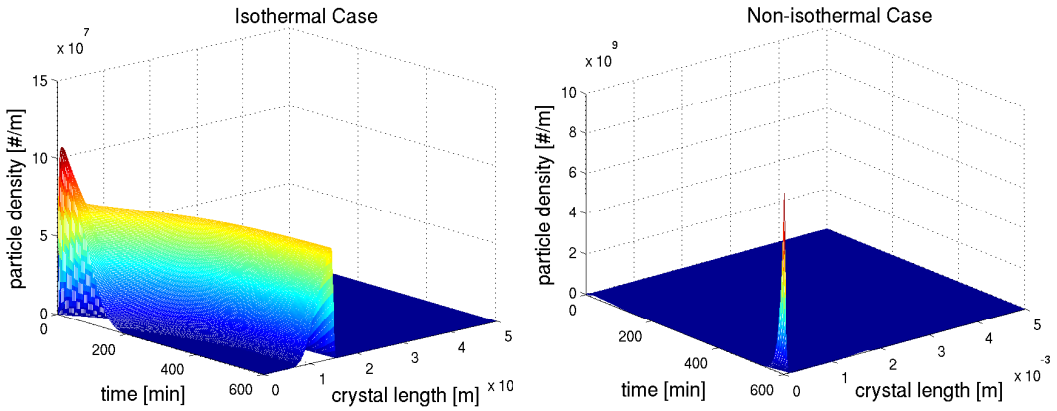

Figure 4.29: Test problem 3: Three dimensional plots of number density for the counter enantiomer using MOC.

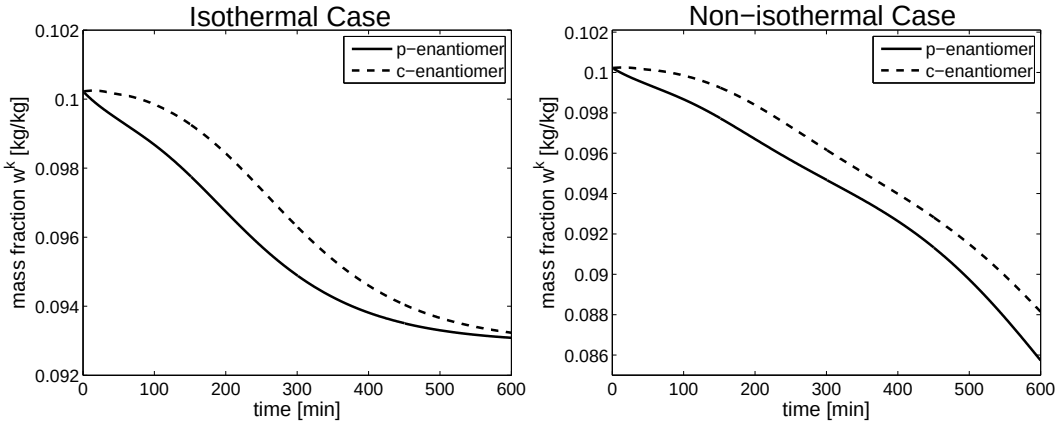

Figure 4.30: Test problem 3: Comparison of the mass fractions for the preferred (p-) and counter (c-) enantiomer using MOC.

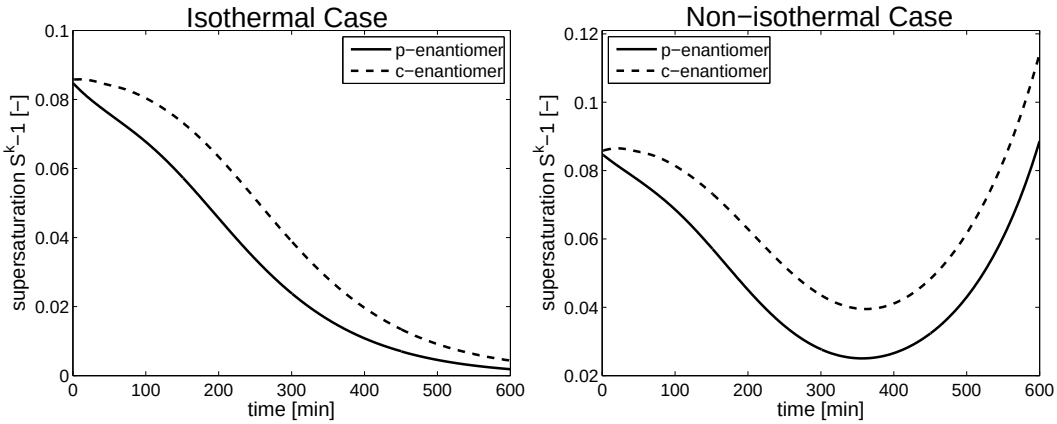

Figure 4.31: Test problem 3: Comparison of the supersaturations for the preferred (p-) and counter (c-) enantiomer using MOC.

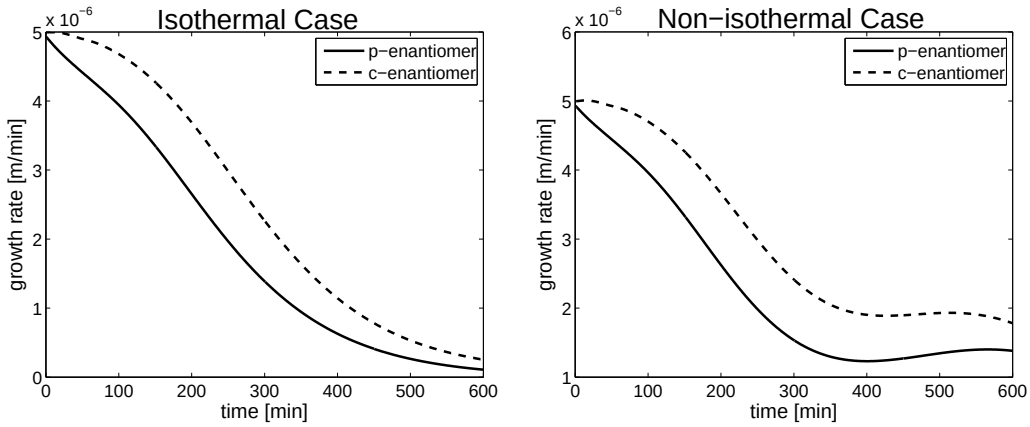

Figure 4.32: Test problem 3: Comparison of growth rates for the preferred (p-) and counter (c-) enantiomer using MOC.

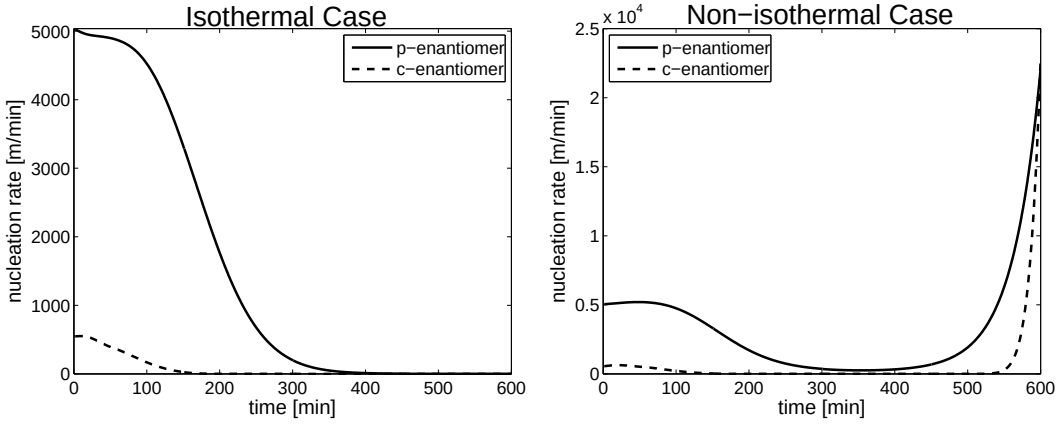

Figure 4.33: Test problem 3: Comparison of nucleation rates for the preferred (p-) and counter (c-) enantiomer using MOC.

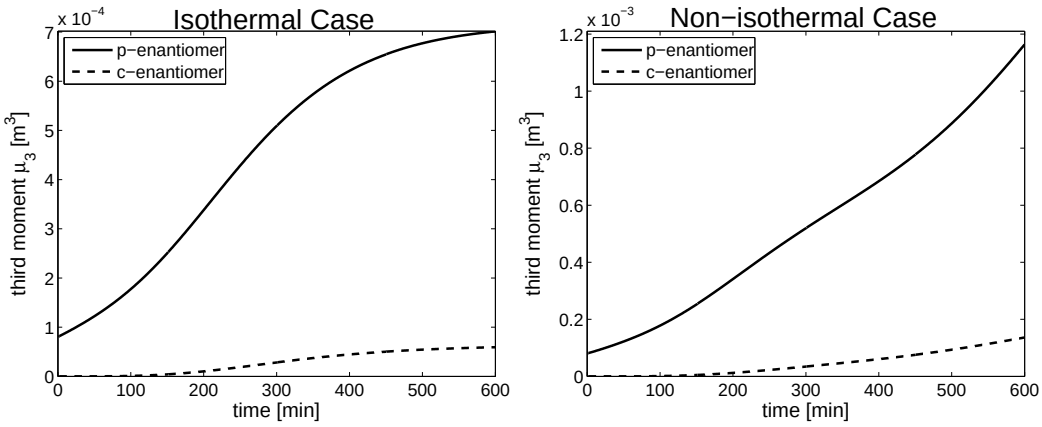

Figure 4.34: Test problem 3: Comparison of third moments for the preferred (p-) and counter (c-) enantiomer using MOC.

Chapter 5

Pure Aggregation and Breakage

This chapter is concerned with binary aggregation and breakage phenomena. We starts with a brief introduction about multicomponent aggregation processes. The reformulated PBE for the one-component aggregation is numerically solved by using a semi-discrete finite volume scheme. We also discuss the consistency and stability of the proposed numerical scheme. The procedure is then extended to the population balance equation for two-component aggregation model and derive a finite volume scheme to numerically solve the underlying model. Further, we consider one-component pure breakage problem and derive a finite volume scheme for the numerical simulation of the underlying model. Moreover, we study the stability, consistency and convergence of the numerical scheme for breakage problem. Finally, numerical test problems for the one and two-component aggregation and one-component breakage processes are presented. The numerical results are validated against the available analytical solutions.

5.1 Multi-Component Aggregation Processes

In many aggregation processes, there are several particle properties variables which influence the particle density distribution. Therefore, a one-dimensional population balance equation (PBE), where the particle size is assumed to be the only variable, is not adequate to simulate such processes. The multi-component aggregation has various applications in many scientific, medical, and industrial research areas. In case of two-component aggregation the population balance equation (PBE), which is an extension of the PBE for the one-component aggregation (see (2.5)-(2.7)), is given as [64]

$$\begin{aligned}\frac{\partial f(t,x,y)}{\partial t} =& \frac{1}{2}\int_0^x\int_0^y \beta(t,x-x',y-y',x',y')f(t,x-x',y-y')f(t,x',y')dx'dy' \\ &- \int_0^\infty\int_0^\infty \beta(t,x,y,x',y')f(t,x,y)f(t,x',y')dx'dy' \,, \end{aligned} \tag{5.1}$$

where $f(t, x, y)$ is the number density function at time $t \geq 0$. The aggregation kernel $\beta(t, x, y, x', y')$ gives the extent of the aggregation processes and represents the properties of the physical medium.

Generally, the solution of multi-component aggregation is very challenging. Under considerable simplifications, Lushnikov [64] solved analytically the underlying PBE (5.1) for two-component aggregation. However, in practical situations numerical procedures are the only tools which can be used to solve the PBE (5.1). In the literature, few numerical methods are available for the simulation of multi-component aggregation phenomena. Kim and Seinfeld [39] proposed a finite element scheme, while Laurenzi et al. [53] used Monte Carlo methods in order to simulate multi-component aggregation processes. Recently, Vale and McKenna [118] extended the fixed pivot techniques of Kumar and Ramkrishna [47] for determining the number density function in two-component aggregation processes. Similar to the one-component case the method looks very impressive. Their results in the two-component aggregation show similar behavior like those obtained in one-component aggregation.

On the other hand, several numerical methods are available for solving one-component aggregation problems. Among them are the Monte Carlo methods [101], the methods of classes [46, 47, 49, 101, 120], the quadrature method of moments [13, 71, 73], and the method of weighted residuals [101, 122]. In most of these methods instead of regular grids the geometric grid discretizations were used, see Hounslow et al. [31, 33, 34] and references therein.

Apart from these methods, Filbet and Laurençot [23] proposed a numerical scheme which is based on a conservative finite volume formulation. The authors showed that, both from a theoretical and numerical point of view, the non-conservative truncation of the Smoluchowski coagulation equation is a good approximation to study the gelation phenomenon, see [24]. They have also performed rigorous mathematical analysis of the scheme and proved that numerical results of the scheme converges to the exact solution, see [9]. The authors have rewritten the population balance equation for aggregation problems in a form which can be readily solved by a finite volume scheme. This special reformulation was a great achievement which enables one to apply the finite volume scheme in the aggregation case as well. Their numerical results show the second order accuracy of the scheme. They have also performed several numerical simulations to check the known conjectured behavior of the solution near the gelation time or as time increases to infinity. In the latter case, they also have checked the validity of the dynamical scaling hypothesis. In all cases, the numerical simulations are in good agreement with physical conjectures. Their work is very important to justify the application of such schemes to population balance equations.

Our main focus is the extension of the above mentioned conservative finite volume approach to two-component aggregation. For this purpose, a reformulation of (5.1) is introduced which converts this integro-ordinary differential equation to a partial differential equation

which is coupled with an integral equation. The resulting equation is then solved by a semi-discrete finite volume scheme which also employs the geometric grid discretization technique for the internal variables. The semi-discrete formulation enables one to use any standard adaptive ODE solver. Moreover, the use of a geometric grid discretization shows the efficient application of the finite volume scheme for this specific problem. It proves the versatility, generality and effectiveness of finite volume scheme as well as their ability to accommodate the special techniques which were only introduced for the specific methods used for aggregation processes. The current extended finite volume scheme for two-component aggregation uses the basic ideas of the finite volume scheme for one-component aggregation derived in [23]. Therefore, the reader should first understand the finite-volume scheme for one-component aggregation process. For the reader convenience, we re-derive the finite-volume scheme for one-component aggregation with a slight modification as compared to that presented in [23]. Even though the scheme in [23] is derived for an arbitrary grid, the authors have used a uniform grid in their numerical test problems. Here, we give further numerical test problems which are solved on geometric grids. Moreover, in contrast to [23] we present the scheme in a semi-discrete form.

5.1.1 One-component aggregation process

The Smoluchowski aggregation equation describes the growth of particle (droplet, etc.) clusters by binary aggregation. The underlying mechanism is the merging of two particles into a single one. In the simple situation where each particle is fully identified by its volume, it describes the dynamics of the volume distribution function $f = f(t,x) \geq 0$ of particles of volume $x > 0$ at time $t \geq 0$ and is given by PBE (2.5)-(2.7) in Section 2.2 of Chapter 2.

To apply the finite volume formulation one needs the reformulation of (2.5)-(2.7) which are given by equations (2.8) and (2.9). This reformulated PBE is restated as

$$x\frac{\partial f(t,x)}{\partial t} = -\frac{\partial \tilde{\mathcal{F}}_{\text{agg}}(t,x)}{\partial x}\,, \quad (t,x) \in \mathbb{R}^2_+\,, \tag{5.2}$$

where the volume flux is given by

$$\tilde{\mathcal{F}}_{\text{agg}}(t,x) = \int_0^x \int_{x-u}^{\infty} u\,\beta(t,u,v)\,f(t,u)\,f(t,v)\,dvdu\,, \quad x \in \mathbb{R}_+\,. \tag{5.3}$$

Taking advantage of this reformulation, we can use the finite volume scheme in order to solve the aggregation equation numerically.

Since the volume variable x ranges in the unbounded interval $\mathbb{R}_+$, the first step is to reduce the computation to a finite interval. Here we truncate the volume variable to some maximal

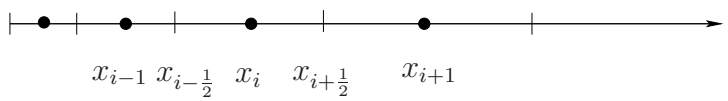

Figure 5.1: A typical 1D grid. The lines denote the cell boundaries and dots are the centroids of the cells.

value R_x, see [23]. In this case $\tilde{\mathcal{F}}_{\text{agg}}(t,x)$ in (5.3) is replaced by

$$\mathcal{F}_{\text{agg}}(t,x) := \int_0^x \int_{x-u}^{R_x} u\beta(t,u,v)f(t,u)f(t,v)dvdu\,, \quad x \in]0,R_x[\,. \tag{5.4}$$

After reducing the computation to a bounded interval, the second step is to introduce the volume discretization. To this end, let N be a large integer, and denote by $(x_{i-\frac{1}{2}})_{i\in\{0,\cdots,N\}}$ the partitions of $]0,R_x[$. Then according to geometric grid discretization we have

$$x_{-1/2} = 0\,, \quad \text{and} \quad x_{i+1/2} = 2^{(i-N)/3}R_x\,, \ \forall\ i = 0,2,\cdots N\,. \tag{5.5}$$

A typical one-dimensional geometric grid is given in Figure 5.1. Furthermore, we set

$$x_i = (x_{i-1/2} + x_{i+1/2})/2\,, \quad \Delta x_i = x_{i+1/2} - x_{i-1/2} \tag{5.6}$$

and $\Omega_i = \left[x_{i-1/2}, x_{i+1/2}\right]$ for $i \geq 0$. As can be seen from (5.2), it is natural to compute $\tilde{f}(t,x) := xf(t,x)$ instead of $f(t,x)$. We then define the approximation $\tilde{f}_i(0)$ of the initial data $\tilde{f}(0,x) = xf(0,x)$ by

$$\tilde{f}_i(0) = \frac{1}{\Delta x_i}\int_{\Omega_i} \tilde{f}(0,x)dx\,. \tag{5.7}$$

After integrating (5.2) over the control volume Ω_i, we get the following upwind numerical scheme in a semi-discrete form

$$\frac{d\tilde{f}_i}{dt} = -\frac{(\mathcal{F}_{\text{agg}})_{i+1/2} - (\mathcal{F}_{\text{agg}})_{i-1/2}}{\Delta x_i}\,, \quad 0 \leq i \leq N\,, \tag{5.8}$$

where $\tilde{f}_i := \tilde{f}_i(t)$ and according to [23]

$$(\mathcal{F}_{\text{agg}})_{i+1/2} = \sum_{k=0}^{i} \Delta x_k \tilde{f}_k \left\{ \sum_{j=\alpha_{i,k}}^{N} \int_{\Omega_j} \frac{\beta(x',x_k)}{x'}dx'\tilde{f}_j + \int_{x_{i+1/2}-x_k}^{\alpha_{i,k}-1/2} \frac{\beta(x',x_k)}{x'}dx'\tilde{f}_{\alpha_{i,k}-1} \right\} + \mathcal{O}(\Delta x_i^3)\,. \tag{5.9}$$

The integer $\alpha_{i,k}$ corresponds to the index of the cell such that $x_{i+1/2} - x_k \in \Omega_{\alpha_{i,k}-1}$. Notice that the approximate flux $(\mathcal{F}_{\text{agg}})_{i+1/2}$ is an approximation for $-1 \leq i \leq N$ of

$$\begin{aligned}\mathcal{F}_{\text{agg}}(x_{i+1/2}) &= \int_0^{x_{i+1/2}} \int_{x_{i+1/2}-x^*}^{R_x} \beta(x', x^*) x^* f(x^*) f(x') dx' dx^* \\ &= \sum_{k=0}^{i} \int_{\Omega_k} x^* f(x^*) \int_{x_{i+1/2}-x^*}^{R_x} \beta(x', x^*) f(x') dx' dx^* \,. \end{aligned} \tag{5.10}$$

For all values of the aggregation kernel β which are considered in the test problems, the integrals appearing in (5.9) can be solved analytically. However, in general these integral terms can not be computed analytically. Therefore keeping in view the more complex nature of aggregation kernel β, in this work we have approximated them by a mid-point quadrature formula which is second order accurate. Since the current finite volume scheme is explicit, all the terms appearing on the right hand side of equation (5.8) can be calculated from the values of the variables at previous time step. Therefore, the performance of the mid point rule for the approximation of the integral terms will not be affected if β evolves with time.

The last step is to solve the resultant ODEs system (5.8) by using an adaptive ODE solver. For this purpose, we use RK45 method which is an embedded Runge-Kutta methods of order four and five.

This completes the derivation of the finite volume scheme for one-component aggregation. In the next subsection we extend the scheme to the case of two-component aggregation. Before going to the derivation of the finite volume scheme for two-component aggregation processes, it is very important to understand the numerical procedure for the one-component aggregation process given in this subsection. The later is a building block for the extension of the finite volume scheme to two-component aggregation process.

Before going to the derivation of two dimensional scheme, let us investigate some basic properties of the scheme (5.8).

In the following we briefly discuss some linear theoretical results on positivity of the numerical scheme for one-component aggregation, see also see [23]. Let Δt be the time step in the numerical scheme and $t^n = n\Delta t$ for $n = 1, 2, \cdots, N_t$, where N_t represents the total number of time discretizations.

Proposition 5.1 *Under the stability condition on the time step Δt such that*

$$\Delta t \sup_{i,n} \left(\int_{\delta_h}^{R_x} \frac{\beta(x_i, x')}{x'} \tilde{f}(t^n, x') dx' \right) < 1, \tag{5.11}$$

where $\delta_h = \min\{\Delta x_i/2;\, i = 0, 1, \cdots, N\}$*, the function* $\tilde{f}$ *is nonnegative and its total volume is a non-increasing function of time, that is,*

$$\frac{d}{dt}\left(\sum_{i=0}^{N} \Delta x_i\, \tilde{f}_i\right) \leq 0\,. \tag{5.12}$$

Moreover, if $\varphi : [0, +\infty) \to [0, \infty)$ *is non-increasing function, then*

$$\frac{d}{dt}\left(\sum_{i=0}^{N} \Delta x_i\, \varphi(x_i)\, \tilde{f}_i\right) \leq 0\,. \tag{5.13}$$

Proof. This proposition is also given in [23]. For $(i, j) \in \{0, 1, \cdots, N\}$, let us introduce the notations

$$\mathcal{A}_{i,j} = \int_{\Omega_i} \frac{\beta(x', x_j)}{x'} dx'\,, \qquad \mathcal{B}_{i,j} = \int_{x_{i+1/2}-x_j}^{\alpha_{i,j}-1/2} \frac{\beta(x', x_j)}{x'} dx'\,. \tag{5.14}$$

Then equation (5.9) implies

$$\begin{aligned}
(\mathcal{F}_{\text{agg}})_{i+1/2} =& \sum_{k=0}^{i} \Delta x_k \tilde{f}_k \left[\sum_{j=\alpha_{i,k}}^{N} \mathcal{A}_{j,k}\tilde{f}_j + \mathcal{B}_{i,k}\tilde{f}_{\alpha_{i,k}-1}\right] \\
=& \Delta x_i \tilde{f}_i \left[\sum_{j=\alpha_{i,i}}^{N} \mathcal{A}_{j,i}\tilde{f}_j + \mathcal{B}_{i,i}\tilde{f}_{\alpha_{i,i}-1}\right] + \sum_{k=0}^{i-1} \Delta x_k \tilde{f}_k \sum_{j=\alpha_{i-1,k}}^{N} \mathcal{A}_{j,k}\tilde{f}_j \\
& - \sum_{k=0}^{i-1} \Delta x_k \tilde{f}_k \sum_{j=\alpha_{i-1,k}}^{\alpha_{i,k-1}} \mathcal{A}_{j,k}\tilde{f}_j + \sum_{k=0}^{i-1} \Delta x_k \tilde{f}_k \mathcal{B}_{i,k}\tilde{f}_{\alpha_{i,k}-1}\,.
\end{aligned}$$

If $\alpha_{i,k} = \alpha_{i-1,k}$, we have $\mathcal{B}_{i,k} \leq \mathcal{B}_{i-1,k}$ and

$$\begin{aligned}
(\mathcal{F}_{\text{agg}})_{i+1/2} \leq& \Delta x_i \tilde{f}_i \left[\sum_{j=\alpha_{i,i}}^{N} \mathcal{A}_{j,i}\tilde{f}_j + \mathcal{B}_{i,i}\tilde{f}_{\alpha_{i,i}-1}\right] \\
& + \sum_{k=0}^{i-1} \Delta x_k \tilde{f}_k \sum_{j=\alpha_{i-1,k}}^{N} \mathcal{A}_{j,k}\tilde{f}_j + \sum_{k=0}^{i-1} \Delta x_k \tilde{f}_k \mathcal{B}_{i-1,k}\tilde{f}_{\alpha_{i,k}-1} \\
\leq& \Delta x_i \tilde{f}_i \left[\sum_{j=\alpha_{i,i}}^{N} \mathcal{A}_{j,i}\tilde{f}_j + \mathcal{B}_{i,i}\tilde{f}_{\alpha_{i,i}-1}\right] + (\mathcal{F}_{\text{agg}})_{i-1/2}\,.
\end{aligned}$$

If $\alpha_{i,k} \neq \alpha_{i-1,k}$, we have $\alpha_{i,k} > \alpha_{i-1,k}$ and

$$\begin{aligned}(\mathcal{F}_{\text{agg}})_{i+1/2} \leq & \Delta x_i \tilde{f}_i \left[\sum_{j=\alpha_{i,i}}^{N} \mathcal{A}_{j,i} \tilde{f}_j + \mathcal{B}_{i,i} \tilde{f}_{\alpha_{i,i}-1} \right] \\ & + (\mathcal{F}_{\text{agg}})_{i-1/2} - \sum_{k=0}^{i-1} \Delta x_k \tilde{f}_k \mathcal{A}_{\alpha_{i,k}-1,k} \tilde{f}_{\alpha_{i,k}-1} + \sum_{k=0}^{i-1} \Delta x_k \tilde{f}_k \mathcal{B}_{i,k} \tilde{f}_{\alpha_{i,k}-1} \\ \leq & \Delta x_i \tilde{f}_i \left[\sum_{j=\alpha_{i,i}}^{N} \mathcal{A}_{j,i} \tilde{f}_j + \mathcal{B}_{i,i} \tilde{f}_{\alpha_{i,i}-1} \right] + (\mathcal{F}_{\text{agg}})_{i-1/2} \,,\end{aligned}$$

since $\mathcal{B}_{i,k} \leq \mathcal{A}_{\alpha_{i,k}-1,k}$. Hence in both cases it follows from (5.8)

$$\frac{d\tilde{f}_i}{dt} \geq - \left[\sum_{j=\alpha_{i,i}}^{N} \mathcal{A}_{j,i} \tilde{f}_j + \mathcal{B}_{i,i} \tilde{f}_{\alpha_{i,i}-1} \right] \tilde{f}_i \,. \tag{5.15}$$

Let

$$\gamma_i(\tilde{f}) = \sum_{j=\alpha_{i,i}}^{N} \mathcal{A}_{j,i} \tilde{f}_j + \mathcal{B}_{i,i} \tilde{f}_{\alpha_{i,i}-1} \geq 0 \,. \tag{5.16}$$

Then (5.15) can be rewritten as

$$\frac{d\tilde{f}_i}{dt} \geq -\gamma_i(\tilde{f})\, \tilde{f}_i \,. \tag{5.17}$$

Applying the forward Euler method (RK1) to the system (5.17) gives

$$\tilde{f}_i^{n+1} = \tilde{f}_i^n - \Delta t\, \gamma_i(\tilde{f}^n)\, \tilde{f}_i^n \,. \tag{5.18}$$

It follows directly from the above equation that for

$$\Delta t \leq \Delta t_0 = \frac{1}{\sup\limits_i \gamma_i(\tilde{f}^n)} \tag{5.19}$$

the positivity is guaranteed i.e., $\tilde{f}_i^{n+1} \geq 0$.

Let us assume that $\gamma_i(\tilde{f})$ in (5.17) remains almost the same over all stages s of the Runge-Kutta schemes. Therefore, we are considering the system with "frozen coefficient"

$$\frac{d\tilde{f}_i}{dt} \geq -\gamma_i(\tilde{f}^n)\, \tilde{f}_i \tag{5.20}$$

for $t^{n-1} \le t \le t^n$. On this system we can apply the linear theory of Bolly and Crouzeix [8]. From their Theorem 2 it can be deduced that we will have positivity for (5.20) under the condition $\Delta t \le \Delta t_0/C$, where Δt_0 is the threshold for Euler's method and C is the largest nonnegative number such that the stability function and all its derivatives are nonnegative on the interval $[-C, 0]$. In Theorem 2.2 of [43] it was shown that $C = 1$ for any Runge-Kutta method having order $p = s$, where s are the stages of the Runge-Kutta methods. Hence, for Runge-Kutta methods of order $p \ge 2$ one can also use the same condition for "linear positivity", namely

$$\Delta t \ \sup_i \gamma_i(\tilde{f}^n) = \Delta t \ \sup_i \left(\sum_{j=\alpha_{i,i}}^{N} \mathcal{A}_{j,i} \tilde{f}_j^n + \mathcal{B}_{i,i} \tilde{f}_{\alpha_{i,i}-1}^n \right) \le 1 \,. \tag{5.21}$$

Next, the time monotonicity (5.12) of the total volume of $\tilde{f}$ follows at once from the non-negativity of $\tilde{f}$ by summing (5.8) with respect to i.

Finally, let $\varphi : [0, +\infty) \to [0, +\infty)$ be a non-increasing function. It follows from (5.8)

$$\frac{d}{dt}(\varphi(x_i)\tilde{f}_i) = -\varphi(x_i)\frac{(\mathcal{F}_{\text{agg}})_{i+1/2} - (\mathcal{F}_{\text{agg}})_{i-1/2}}{\Delta x_i} \,. \tag{5.22}$$

Multiplying both sides of the equality in above equation with Δx_i and summing the resulting identities over i, we obtain

$$\frac{d}{dt}\left(\sum_{i=0}^{N} \Delta x_i \, \varphi(x_i)\tilde{f}_i \right) \le \sum_{i=1}^{N} \underbrace{(\mathcal{F}_{\text{agg}})_{i-1/2}}_{\ge 0} \underbrace{(\varphi(x_i) - \varphi(x_{i-1}))}_{\le 0} \le 0 \,. \tag{5.23}$$

This proves inequality (5.13). □

Proposition 5.2 *Assume the time step Δt satisfies* (5.11). *Then for all $t \in [0, t_{\max}]$,*

$$\int_0^{R_x} f(t, x)\, dx \le \|f_{in}\|_{L^1} \,, \tag{5.24}$$

where f_{in} is the initial number density of seeds, see [24].

Proof. Here we will proceed with induction. Let us assume that $f_0(x) \ge 0$ and $f_0 \in L^1(0, R_x)$. Next, assume that the function $f(t^n, x)$ is non-negative and

$$\int_0^{R_x} f(t^n, x)\, dx \le \|f_{in}\|_{L^1} \,. \tag{5.25}$$

Now we have to prove that $f(t^{n+1}) \le \|f_{in}\|_{L^1}$.

Since $\tilde{f} = x\, f$, equation (5.8) after summing over i gives

$$\frac{d}{dt}\left(\sum_{i=0}^{N} \Delta x_i\, f_i\right) = -\sum_{i=0}^{N} \frac{(\mathcal{F}_{\text{agg}})_{i+1/2} - (\mathcal{F}_{\text{agg}})_{i-1/2}}{x_i}\,. \tag{5.26}$$

Of course with the aggregation term the number of particles decreases ($(\mathcal{F}_{\text{agg}})_{i+1/2} \geq 0$, $\forall\, i$) and assume that $x_i \leq x_{i+1}$, then

$$-\sum_{i=0}^{N} \frac{(\mathcal{F}_{\text{agg}})_{i+1/2} - (\mathcal{F}_{\text{agg}})_{i-1/2}}{x_i} \leq -\sum_{i=0}^{N} (\mathcal{F}_{\text{agg}})_{i+1/2} \left(\frac{1}{x_i} - \frac{1}{x_{i+1}}\right) \leq 0\,. \tag{5.27}$$

Hence equation (5.26) gives

$$\frac{d}{dt}\left(\sum_{i=0}^{N} \Delta x_i\, f_i\right) \leq 0\,. \tag{5.28}$$

Now using equation (5.25) we obtain

$$\sum_{i=0}^{N} \Delta x_i\, f_i^{n+1} \leq \sum_{i=0}^{N} \Delta x_i\, f_i^{n} \leq \|f_{in}\|_{L^1}\,. \tag{5.29}$$

We remark that $f_0(x)$ is an approximation of $f_{in}(x)$, with strong convergence in $L^1(0, R_x)$. □

5.1.2 Two-components aggregation process

This subsection focuses at the extension of one-component aggregation processes to two-component aggregation. For a spatially homogeneous system equation (5.1) can be restated as

$$\partial_t f(t,x,y) = \mathcal{J}^{\pm}_{\text{agg}}(t,x,y)\,, \quad (t,x,y) \in \mathbb{R}^3_+\,, \tag{5.30}$$

$$f(0,x,y) = f_0(x,y)\,, \quad x,y \in \mathbb{R}^2_+\,, \tag{5.31}$$

where $\mathbb{R}^2_+ :=]0,+\infty[\times]0,+\infty[$ and the aggregation term $\mathcal{J}^{\pm}_{\text{agg}}(t,x,y)$ is given by

$$\begin{aligned}\mathcal{J}^{\pm}_{\text{agg}}(t,x,y) =& \frac{1}{2}\int_0^x \int_0^y \beta(t,x-x',y-y',x',y') f(t,x-x',y-y') f(t,x',y')\,dx'dy' \\ &- \int_0^\infty \int_0^\infty \beta(t,x,y,x',y') f(t,x,y) f(t,x',y')\,dx'dy'\,,\end{aligned} \tag{5.32}$$

where $f(t,x,y)dxdy$ is the number of particles of state (x,y) per unit volume at time t and $\beta(t,x,y,x',y')$ is the aggregation rate coefficient. The internal coordinates x and y

denote the amount of each component in the particle, which can be mass, moisture content, volume, etc. Again, the first integral in $\mathcal{J}^{\pm}_{\text{agg}}(t,x,y)$ accounts for the formation of particles with property (x,y) resulting from the merging of two particles with respective properties (x',y') and $(x-x',y-y')$, $[x',y'] \in]0,x[\times]0,y[$. The second integral in $\mathcal{J}^{\pm}_{\text{agg}}(t,x,y)$ describes the loss of particles with property (x,y) by aggregation with other particles. Similar to the one-component case, the aggregation coefficient $\beta(t,x,y,x',y')$ characterizes the rate at which the aggregation of two particles with respective properties (x,y) and (x',y') produces a particle of property $(x+x',y+y')$ and is a nonnegative symmetric function,

$$0 \le \beta(t,x,y,x',y') = \beta(t,x',y',x,y)\,, \quad (x,y,x',y') \in \mathbb{R}^4_+\,.$$

During each aggregation event, the total volume of particles is conserved, while the number of particles decreases. The moments $M_{i,j}$ of the number density $f = f(t,x,y) \ge 0$ are defined as

$$M_{i,j}(t) = \int_0^\infty \int_0^\infty x^i y^j f(t,x,y)dxdy. \tag{5.33}$$

In order apply the finite volume scheme we need a reformulation of the two-component aggregation equation (5.30) which results in hyperbolic-type PDE of the form

$$(x+y)\frac{\partial f}{\partial t} = -\frac{\partial \tilde{\mathcal{F}}_{\text{agg}}}{\partial x}(t,x,y) - \frac{\partial \tilde{\mathcal{G}}_{\text{agg}}}{\partial y}(t,x,y) + \frac{\partial^2 \tilde{\mathcal{H}}_{\text{agg}}}{\partial x \partial y}(t,x,y)\,, \tag{5.34}$$

where

$$\tilde{\mathcal{F}}_{\text{agg}}(t,x,y) = \int_0^x \int_{x-u}^\infty \int_0^\infty (u+y)\,\beta(t,u,y,v,w)\,f(t,u,y)\,f(t,v,w)\,dwdvdu\,, \tag{5.35}$$

$$\tilde{\mathcal{G}}_{\text{agg}}(t,x,y) = \int_0^y \int_{y-v}^\infty \int_0^\infty (x+v)\,\beta(t,x,v,u,w)\,f(t,x,v)\,f(t,u,w)\,dwdudv\,, \tag{5.36}$$

$$\tilde{\mathcal{H}}_{\text{agg}}(t,x,y) = \int_0^x \int_0^y \int_{x-u}^\infty \int_{y-v}^\infty (u+v)\,\beta(t,u,v,w,z)\,f(t,u,v)\,f(t,w,z)\,dzdwdvdu\,. \tag{5.37}$$

It has been shown in Appendix A.4 that one can recover equations (5.30) and (5.32) from (5.34)-(5.37). We take advantage of the reformulation (5.34) and propose a conservative finite volume scheme for the numerical solution of this model.

Since $(x,y) \in \mathbb{R}^2_+$, like in the one-component case the first step is to reduce the computation to a finite interval. For that purpose, we truncate the variables (x,y) to some maximal

values (R_x, R_y). This leads equations (5.35)-(5.37) to the following form

$$\mathcal{F}_{\text{agg}}(t,x,y) = \int_0^x \int_{x-u}^{R_x} \int_0^{R_y} (u+y)\,\beta(t,u,y,v,w)\,f(t,u,y)\,f(t,v,w)\,dwdvdu\,, \tag{5.38}$$

$$\mathcal{G}_{\text{agg}}(t,x,y) = \int_0^y \int_{y-v}^{R_y} \int_0^{R_x} (x+v)\,\beta(t,x,v,u,w)\,f(t,x,v)\,f(t,u,w)\,dwdudv\,, \tag{5.39}$$

$$\mathcal{H}_{\text{agg}}(t,x,y) = \int_0^x \int_0^y \int_{x-u}^{R_x} \int_{y-v}^{R_y} (u+v)\,\beta(t,u,v,w,z)\,f(t,u,v)\,f(t,w,z)\,dzdwdvdu\,. \tag{5.40}$$

Having reduced the computation to a bounded interval, the next step is to introduce volume discretization. To this end, let N_x and N_y be large integers. We assume a Cartesian grid on the rectangular domain $[0,R_x]\times[0,R_y]$ which is covered by cells $C_{i,j} \equiv \left[x_{i-\frac{1}{2}}, x_{i+\frac{1}{2}}\right] \times \left[y_{j-\frac{1}{2}}, y_{j+\frac{1}{2}}\right]$ for $0 \le i \le N_x$ and $0 \le j \le N_y$. The representative coordinates of the population in cell $C_{i,j}$ are denoted by (x_i, y_j). For the sake of clarity a typical two-dimensional grid is given in Figure 5.2. The geometric grid discretization technique gives us

$$(x_{-1/2}, y_{-1/2}) = (0,0)\,, \quad \left(x_{i+1/2}, y_{j+1/2}\right) = \left(2^{(i-N_x)/3}R_x, 2^{(j-N_y)/3}R_y\right)\,, \tag{5.41}$$

for $0 \le i \le N_x, 0 \le j \le N_y$. Here we choose

$$x_i = (x_{i-1/2} + x_{i+1/2})/2\,, \quad y_j = (y_{j-1/2} + y_{j+1/2})/2 \tag{5.42}$$

and set

$$\Delta x_i = x_{i+1/2} - x_{i-1/2}\,, \quad \Delta y_j = y_{j+1/2} - y_{j-1/2}\,. \tag{5.43}$$

From (5.34) it seems natural to compute $\tilde{f}(t,x) := (x+y)f(t,x,y)$ rather than $f(t,x,y)$. We then define the approximation $\tilde{f}_{i,j}(0)$ of the initial data $\tilde{f}_0(x,y) = (x+y)f_0(x,y)$ by

$$\tilde{f}_{i,j}(0) = \frac{1}{\Delta x_i \Delta y_j} \int_{C_{i,j}} \tilde{f}_0(x,y)dydx\,. \tag{5.44}$$

Integration of equation (5.34) over the control volume $C_{i,j}$ gives us the following semi-discrete formulation of the finite volume scheme

$$\begin{aligned}\frac{d\tilde{f}_{i,j}}{dt} = &-\frac{(\mathcal{F}_{\text{agg}})_{i+1/2,j} - (\mathcal{F}_{\text{agg}})_{i-1/2,j}}{\Delta x_i} - \frac{(\mathcal{G}_{\text{agg}})_{i,j+1/2} - (\mathcal{G}_{\text{agg}})_{i,j-1/2}}{\Delta y_j} \\ &+ \frac{(\mathcal{H}_{\text{agg}})_{i+1/2,j+1/2} - (\mathcal{H}_{\text{agg}})_{i+1/2,j-1/2} - (\mathcal{H}_{\text{agg}})_{i-1/2,j+1/2} + (\mathcal{H}_{\text{agg}})_{i-1/2,j-1/2}}{\Delta x_i \Delta y_j}\,,\end{aligned} \tag{5.45}$$

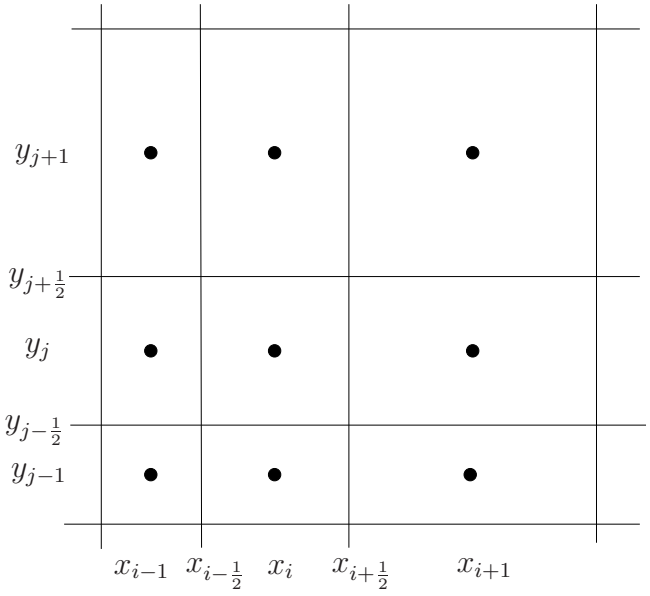

Figure 5.2: A typical Cartesian grid on which one can use the proposed scheme. The lines denote the cell boundaries and dots are the centroids of the cells.

where $0 \leq i \leq N_x$, $0 \leq j \leq N_y$. The approximation of equations (5.38)-(5.40) gives (see Appendix A.5)

$$(\mathcal{F}_{\text{agg}})_{i+1/2,j} = \sum_{k=0}^{i} \Delta x_k \tilde{f}_{k,j} \sum_{m=0}^{N_y} \Delta y_m \left\{ \sum_{l=\alpha_{i,k}}^{N_x} \int_{C_{l,j}} \frac{\beta(x', y_j, x_k, y_m)}{x' + y_j} dx' \tilde{f}_{l,m} + \int_{x_{i+1/2}-x_k}^{\alpha_{i,k}-1/2} \frac{\beta(x', y_j, x_k, y_m)}{x' + y_j} dx' \tilde{f}_{\alpha_{i,k}-1,m} \right\}, \tag{5.46}$$

where the integer $\alpha_{i,k}$ corresponds to the index of the cell such that $x_{i+1/2} - x_k \in C_{\alpha_{i,k}-1,j}$. For more explanation about the approximation (5.46) of (5.38) the reader is referred to Appendix A.5. Similarly

$$(\mathcal{G}_{\text{agg}})_{i,j+1/2} = \sum_{k=0}^{j} \Delta y_k \tilde{f}_{i,k} \sum_{m=0}^{N_x} \Delta x_m \left\{ \sum_{l=\alpha_{j,k}}^{N_y} \int_{C_{i,l}} \frac{\beta(x_i, y', x_m, y_k)}{x_i + y'} dy' \tilde{f}_{m,l} + \int_{y_{j+1/2}-y_k}^{\alpha_{j,k}-1/2} \frac{\beta(x_i, y', x_m, y_k)}{x_i + y'} dy' \tilde{f}_{m,\alpha_{j,k}-1} \right\}. \tag{5.47}$$

Here the integer $\alpha_{j,k}$ corresponds to the index of the cell such that $y_{j+1/2} - y_k \in C_{i,\alpha_{j,k}-1}$.

Finally

$$
\begin{aligned}
(\mathcal{H}_{\text{agg}})_{i+1/2,j+1/2} = \sum_{k=0}^{i}\sum_{m=0}^{j}\Delta x_k \Delta y_m \tilde{f}_{k,m} \Bigg\{ & \sum_{l=\alpha_{i,k}}^{N_x}\sum_{n=\alpha_{j,m}}^{N_y}\int\limits_{C_{l,n}} \frac{\beta(x',y',x_k,y_m)}{x'+y'} dy'dx' \tilde{f}_{l,n} \\
& + \sum_{n=\alpha_{j,m}}^{N_y} \int\limits_{x_{i+1/2}-x_k}^{\alpha_{i,k}-1/2} \frac{\beta(x',y_n,x_k,y_m)}{x'+y_n} dx' \tilde{f}_{\alpha_{i,k}-1,n} \\
& + \sum_{l=\alpha_{i,k}}^{N_x} \int\limits_{y_{j+1/2}-y_k}^{\alpha_{j,m}-1/2} \frac{\beta(x_l,y',x_k,y_m)}{x_l+y'} dy' \tilde{f}_{l,\alpha_{j,m}-1} \\
& + \int\limits_{x_{i+1/2}-x_k}^{\alpha_{i,k}-1/2}\int\limits_{y_{j+1/2}-y_k}^{\alpha_{j,m}-1/2} \frac{\beta(x',y',x_k,y_m)}{x'+y'} dy'dx' \, \tilde{f}_{\alpha_{i,k}-1,\alpha_{j,m}-1} \Bigg\} .
\end{aligned} \tag{5.48}
$$

Once again a second order accurate mid-point quadrature formula is used for the approximation of integral terms appearing in equations (5.46)-(5.48).

Similar to the one-component case the last step is to solve the resultant ODEs system (5.45) by a standard ODE solver. This completes the formulation of the finite volume scheme for the two-component aggregation.

5.2 Pure Breakage

In this section we focuses on the pure one-component breakage process. Breakage is a process by which particles of bigger sizes break into two or more fragments. The total number of particles in a breakage process increases while the total volume (mass) remains conserved.

Population balances for breakage are widely known in high shear granulation, crystallization, atmospheric science and many other particle related engineering problems. The general form of population balance equation for breakage process is already given by equations (2.10) and (2.12) in Section 2.3 of Chapter 2.

In Section 2.3, a reformulation of (2.10) and (2.12) are given by (2.14) and (2.15). A similar reformulation was also introduced in [44]. In equation (2.16) it has been verified that both formulations are equivalent. Here we restate the reformulated PBE as

$$
x\frac{\partial f}{\partial t} = \frac{\partial \tilde{\mathcal{F}}_{\text{break}}(t,x)}{\partial x}, \quad (t,x) \in \mathbb{R}^2_+ , \tag{5.49}
$$

where the volume (mass) flux is given as

$$\tilde{\mathcal{F}}_{\text{break}}(t,x) = \int_0^x \int_x^\infty y'\, b(t,y',x')\, S(x')\, f(t,x')\, dx' dy' \,. \tag{5.50}$$

This reformulation of the original PBE for breakage process is suitable to implement the finite volume scheme. Since the volume variable x ranges in the unbounded interval $\mathbb{R}_+$, the first step is to reduce the computation to a finite interval. Once again we truncate the volume variable to some maximal value R_x. In this case $\tilde{\mathcal{F}}_{\text{break}}(t,x)$ in (5.50) is replaced by

$$\mathcal{F}_{\text{break}}(t,x) := \int_0^x \int_x^{R_x} y'\, b(t,y',x')\, S(x')\, f(t,x')\, dx' dy' \,. \tag{5.51}$$

After reducing the computation to a bounded interval, the second step is to introduce the volume discretization. To this end, we use the same discretization as given by (5.5) and (5.6). Similar to the case of aggregation, it is natural to compute $\tilde{f}(t,x) = xf(t,x)$ instead of $f(t,x)$. We then define the approximation $\tilde{f}(0,x)$ of the initial data by (5.7). After integrating (5.49) over the control volume $\Omega_i := \left[x_{i-1/2}, x_{i+1/2}\right]$, we get the following upwind numerical scheme in a semi-discrete form

$$\frac{d\tilde{f}_i}{dt} = \frac{(\mathcal{F}_{\text{break}})_{i+1/2} - (\mathcal{F}_{\text{break}})_{i-1/2}}{\Delta x_i} \,, \quad 0 \le i \le N \,, \tag{5.52}$$

where $\tilde{f}_i := \tilde{f}_i(t)$ and

$$(\mathcal{F}_{\text{break}})_{i+1/2} = \int_0^{x_{i+\frac{1}{2}}} x^* \int_{x_{i+1/2}}^{R_x} b(x^*,x')\, S(x')\, f(x') dx' dx^* \tag{5.53}$$

$$= \sum_{k=0}^{i} \int_{\Omega_k} x^* \left(\sum_{j=i+1}^{N} \tilde{f}_j \int_{\Omega_j} b(x^*,x')\, \frac{S(x')}{x'}\, dx' \right) dx^* + \mathcal{O}(\Delta x^3) \,. \tag{5.54}$$

In matrix form (5.52) can be written as

$$\frac{d\tilde{\mathbf{f}}(t)}{dt} = A\, \tilde{\mathbf{f}}(t) \tag{5.55}$$

where the vector $\tilde{\mathbf{f}} = [\tilde{f}_1, \tilde{f}_2, \cdots, \tilde{f}_N]^T$ and the matrix

$$A = \begin{pmatrix} \frac{1}{\Delta x_1}(\mathcal{C}_{\frac{1}{2},1}) & \frac{1}{\Delta x_1}(\mathcal{C}_{\frac{3}{2},2} - \mathcal{C}_{\frac{1}{2},2}) & \cdots & \frac{1}{\Delta x_1}(\mathcal{C}_{\frac{3}{2},N_x} - \mathcal{C}_{\frac{1}{2},N_x}) \\ 0 & \frac{1}{\Delta x_2}(\mathcal{C}_{\frac{3}{2},2} - \mathcal{C}_{\frac{1}{2},2}) & \cdots & \frac{1}{\Delta x_2}(\mathcal{C}_{\frac{5}{2},N_x} - \mathcal{C}_{\frac{3}{2},N_x}) \\ \vdots & & & \vdots \\ 0 & \cdots & 0 & \frac{1}{\Delta x_{N_x}}(\mathcal{C}_{N_x+\frac{1}{2},N_x} - \mathcal{C}_{N_x-\frac{1}{2},N_x}) \end{pmatrix} . \tag{5.56}$$

For convenience we use $\mathcal{C}_{i+\frac{1}{2},j} := \int_0^{x_{i+\frac{1}{2}}} x^* \left(\int_{\Omega_j} b(x^*, x') \, \frac{S(x')}{x'} \, dx' \right) dx^* \geq 0.$

For all values of $b(x^*, x')$ and $S(x')$ which are considered in the test problems, the integral appearing in (5.54) can be solved analytically. However, in general the integral term may not be computed analytically. In that case one my use a second order quadrature formula. The last step is to solve the resulting ODEs system (5.52) by using a standard ODE solver. This completes the derivation of finite volume scheme for one-component breakage model.

Proposition 5.3 *Under the stability condition on the time step*

$$\Delta t \, \sup_i \left(\frac{S(x_i)}{x_i} \int_0^{x_{i+\frac{1}{2}}} x' \, b(x', x_i) \, dx' \right) < 1, \tag{5.57}$$

the function $\tilde{f}$ is nonnegative and its total volume is a non-decreasing function of time,

$$\frac{d}{dt}(\sum_{i=0}^{N} \Delta x_i \, \tilde{f}_i) \geq 0 \, . \tag{5.58}$$

Moreover, if $\varphi : [0, +\infty) \to [0, \infty)$ is non-increasing function, then

$$\frac{d}{dt}(\sum_{i=0}^{N} \Delta x_i \, \varphi(x_i) \, \tilde{f}_i) \geq 0 \, . \tag{5.59}$$

Proof. Equation (5.54) implies

$$\begin{aligned}
(\mathcal{F}_{\text{break}})_{i+1/2} &= \sum_{k=0}^{i} x_k \, \Delta x_k \sum_{j=i+1}^{N} b(x_k, x_j) \, \frac{S(x_j)}{x_j} \, \Delta x_j \, f_j \\
&= \sum_{k=0}^{i} x_k \, \Delta x_k \sum_{j=i}^{N} b(x_k, x_j) \, \frac{S(x_j)}{x_j} \, \Delta x_j \, f_j - \sum_{k=0}^{i} x_k \, \Delta x_k \, b(x_k, x_i) \, \frac{S(x_i)}{x_i} \, \Delta x_i \, f_i \\
&= \sum_{k=0}^{i-1} x_k \, \Delta x_k \sum_{j=i}^{N} b(x_k, x_j) \, \frac{S(x_j)}{x_j} \, \Delta x_j \, f_j - \sum_{k=0}^{i} x_k \, \Delta x_k \, b(x_k, x_i) \, \frac{S(x_i)}{x_i} \, \Delta x_i \, f_i \\
&\quad + x_i \, \Delta x_i \left(\sum_{j=i}^{N} b(x_k, x_j) \, \frac{S(x_j)}{x_j} \, \Delta x_j \, f_j \right) \\
&\geq (\mathcal{F}_{\text{break}})_{i-1/2} - \sum_{k=0}^{i} x_k \, \Delta x_k \, b(x_k, x_i) \, \frac{S(x_i)}{x_i} \, \Delta x_i \, f_i \, .
\end{aligned}$$

Hence it follows from (5.52)

$$\frac{d\tilde{f}_i}{dt} \geq -\left[\sum_{k=0}^{i} x_k\,\Delta x_k\,b(x_k,x_i)\,\frac{S(x_i)}{x_i}\right]\tilde{f}_i\,. \tag{5.60}$$

Let

$$\tilde{\gamma}_i := \left(\sum_{k=0}^{i} x_k\,\Delta x_k\,b(x_k,x_i)\,\frac{S(x_i)}{x_i}\right) \geq 0\,. \tag{5.61}$$

Then (5.60) can be rewritten as

$$\frac{d\tilde{f}_i}{dt} \geq -\tilde{\gamma}_i\,\tilde{f}_i\,. \tag{5.62}$$

Applying the forward Euler method (RK1) to the system (5.63) gives

$$\tilde{f}_i^{n+1} = \tilde{f}_i^{n} - \Delta t\,\tilde{\gamma}_i\,\tilde{f}_i^{n}\,. \tag{5.63}$$

It follows directly from the above equation that for

$$\Delta t \leq \Delta t_0 = \frac{1}{\sup\limits_i \tilde{\gamma}_i} \tag{5.64}$$

the positivity is guaranteed i.e., $\tilde{f}_i^{n+1} \geq 0$. Using the same arguments as discussed in Proposition 5.1 one can show that for all Runge-Kutta methods of order $p \geq 2$ the same condition (5.64) can be used for preserving the positivity of the scheme.

Next, the time monotonicity (5.58) of the total volume of $\tilde{f}$ follows at once from the non-negativity of $\tilde{f}$ by summing (5.52) with respect to i.

Finally, let $\varphi : [0,+\infty) \to [0,+\infty)$ be a non-increasing function. It follows from (5.52)

$$\frac{d}{dt}(\varphi(x_i)\tilde{f}_i) = \varphi(x_i)\frac{(\mathcal{F}_{\text{break}})_{i+1/2} - (\mathcal{F}_{\text{break}})_{i-1/2}}{\Delta x_i}\,. \tag{5.65}$$

Multiplying both sides of the equality in above equation with Δx_i and summing the resulting identities over i, gives

$$\frac{d}{dt}(\sum_{i=0}^{N}\Delta x_i\,\varphi(x_i)\tilde{f}_i) \geq \sum_{i=1}^{N}\underbrace{(\mathcal{F}_{\text{agg}})_{i-1/2}}_{\geq 0}\,\underbrace{(\varphi(x_{i-1}) - \varphi(x_i))}_{\geq 0} \geq 0\,. \tag{5.66}$$

This proves inequality (5.59). □

Proposition 5.4 *Assume the time step Δt satisfies* (5.57). *Then for all $t \in [0, t_{\max}]$,*

$$\int_0^{R_x} f(t,x)\,dx \le \|f_{in}\|_{L^1}\,. \tag{5.67}$$

Proof. Here we will proceed with induction. Let us assume that $f_0(x) \ge 0$ and $f_0 \in L^1(0, R_x)$. Next, assume that the function $f(t^n, x)$ is non-negative and

$$\int_0^{R_x} f(t^n,x)\,dx \le \|f_{in}\|_{L^1}\,. \tag{5.68}$$

Now we have to prove that $f(t^{n+1}) \le \|f_{in}\|_{L^1}$.

Using the forward difference formula, equation (5.52) gives

$$\tilde{f}_i^{n+1} = \tilde{f}_i^n + \frac{\Delta t}{\Delta x_i}\left((\mathcal{F}_{\text{break}})_{i+1/2} - (\mathcal{F}_{\text{break}})_{i-1/2}\right)\,, \quad 0 \le i \le N\,. \tag{5.69}$$

Since $\tilde{f} = x\,f$, the above equation after summing over i gives

$$\sum_{i=0}^{N} \Delta x_i\, f_i^{n+1} = \sum_{i=0}^{N} \Delta x_i\, f_i^n + \Delta t \sum_{i=0}^{N} \frac{(\mathcal{F}_{\text{break}})_{i+1/2} - (\mathcal{F}_{\text{break}})_{i-1/2}}{x_i}\,. \tag{5.70}$$

Of course with the break term the number of particles increases ($(\mathcal{F}_{\text{break}})_{i-1/2} \ge 0,\ \ \forall\, i$) and assume that $x_{i-1} \le x_i$, then

$$\sum_{i=0}^{N} \frac{(\mathcal{F}_{\text{break}})_{i+1/2} - (\mathcal{F}_{\text{break}})_{i-1/2}}{x_i} \le \sum_{i=0}^{N} (\mathcal{F}_{\text{agg}})_{i-1/2}\left(\frac{1}{x_i} - \frac{1}{x_{i-1}}\right) \le 0\,. \tag{5.71}$$

Using (5.68) and (5.71) in equation (5.70) we finally get

$$\sum_{i=0}^{N} \Delta x_i\, f_i^{n+1} \le \sum_{i=0}^{N} \Delta x_i\, f_i^n \le \|f_{in}\|_{L^1}\,. \tag{5.72}$$

We remark that $f_0(x)$ is an approximation of $f_{in}(x)$, with strong convergence in $L^1(0, R_x)$. □

5.2.1 Consistency, stability and convergence in semi-discrete form

One can easily verify the consistency of the semi-discrete scheme (5.52) from the equation (5.54). It comes out that the numerical flux is second order accurate. Subsequently, we obtain for the spatial truncation error defined by (3.80) and (3.81)

$$\|\tau(t)\| = \mathcal{O}(\Delta x^2)\,, \quad \text{uniformly for all } t\,. \tag{5.73}$$

In order to show the stability of the scheme we compute the logarithmic norm (3.99) of the matrix A in (5.56) as

$$\tilde{\nu}_1(A) = \max_j \left(Re(a_{jj}) + \sum_{i \neq j} |a_{ij}| \right) . \tag{5.74}$$

Since all the elements of matrix A are real and all the non-diagonal elements are non-negative, the above logarithmic norm takes the following form

$$\tilde{\nu}_1(A) = \max_j \left(\sum_i a_{ij} \right) . \tag{5.75}$$

Then (5.56) gives

$$\sum_i a_{ij} = \sum_{i=1}^{j} \mathcal{C}_{i-\frac{1}{2},j} \left(\frac{1}{\Delta x_j} - \frac{1}{\Delta x_{j-1}} \right) \leq 0 . \tag{5.76}$$

Hence

$$\tilde{\nu}_1(A) \leq 0 . \tag{5.77}$$

Consequently, Theorem 3.4 can be used to get

$$\|e^{tA}\| \leq 1 , \tag{5.78}$$

which ensures the stability of the scheme. The error bound can be obtained by using Theorem 3.5 as

$$\|\epsilon(t)\| = C_0 \, x^2 + C \, t \, x^2 , \quad 0 \leq t \leq t_{\max} \tag{5.79}$$

with constants C_0 and C.

5.3 Numerical Test Problems

In order to test our schemes, we start with the test problems for the one-component aggregation and then go to the test problems for the two-component aggregation. Here, the two-component test problems are somehow extensions of the test problems for one-component aggregation case. It is therefore interesting to see the performance of the scheme in both cases. This enables one to see the affect on the performance of the scheme when we go from one-component aggregation case to two-component aggregation. Afterwards, we give four test cases for the one-component breakage process.

Since our finite volume schemes (5.8), (5.45) and (5.52) have semi-discrete formulation, the resultant system of ODEs are then solved by RK45 method, which is an embedded Runge-Kutta method of order four and five. The value tol= 10^{-6} was used for the error control

tolerance. Note that, the performance of the schemes is not restricted to this particular ODE-solver, one may use any standard ODE-solver for this purpose.

All computations were performed on computer with a 1.73 GHz processor and 2 GB RAM. The programs are written in C programming language and were compiled under Linux operating system. Moreover, the quantities considered in the test problems are dimensionless.

5.3.1 Test problems for one-component aggregation

Scott [105] has presented analytical solutions for one-component aggregation with three kind of kernels (constant, sum and product) and with different initial conditions. Here, we compare our results with the analytical solutions for all three kernels and the exponential initial size distribution. Furthermore, we also give one test problem for the sum kernel and the Gaussian-type initial size distribution.

Test problem 1: As a first step towards the validation of the current scheme, we consider the constant kernel $\beta(x, x') = \beta_0$ and the exponential initial particle size distribution (PSD) as

$$f(0, x) = \frac{N_0}{x_0} \exp(-x/x_0)\,. \tag{5.80}$$

The analytical solution in terms of the number density is given as [105]

$$f(t, x) = \frac{4N_0}{x_0(\tau + 2)^2} \exp\left(\frac{-2x'}{\tau + 2}\right)\,, \tag{5.81}$$

where $\tau = N_0\beta_0 t$ and $x' = x/x_0$. The values $M_0(0) := N_0$ and x_0 are the initial number of particles per unit volume and the initial mean volume of the particles, respectively. In the numerical study we take the constants x_0 and N_0 equal to one. The exact values of the first three moments are given in Table 5.1 where t_{gel} represents the gelling time. All the results are obtained on a geometric grid of the form $x_{i+1} = 2^{1/3}x_i$. Figure 5.3 show average number density at $\tau = 5, 20, 100$ and the corresponding moments until $\tau = 100$. The three time instants correspond to a degree of aggregation I_{agg} of 71, 91, and 98%. For batch systems, it is defined according to Hounslow [31] as

$$I_{agg} = 1 - \frac{M_0(t)}{M_0(0)}\,,$$

where $M_0(t)$ is the zeroth moment at time t. The numerical results are in good agreement with the analytical results. Nevertheless, there is an observable mismatch in the right region of the moving front, which does not seem to be increasing in time. In fact, what we observe is that the front is somehow smeared with respect to the actual solution. The front smearing behavior was also observed in the other schemes, see [46, 47]. In [46], the authors have given a qualitative comparison of their scheme with analytical solutions

Table 5.1: Moments in one-component aggregation for Test problems 1,2,3.

$M_j(t)$	$\beta = \beta_0$	$\beta = \beta_0(x + x')$	$\beta = \beta_0 x x'$
$j = 0$	$\frac{2M_0(0)}{2+\beta_0 M_0 t},\ \forall\, t$	$M_0(0)\exp(-\beta_0 M_1 t),\ \forall\, t$	$M_0(0) - \frac{1}{2}\beta_0 M_1^2 t,\ 0 < t < t_{gel}$
$j = 1$	$M_1(0),\ \forall\, t$	$M_1(0),\ \forall\, t$	$M_1(0), \quad 0 < t < t_{gel}$
$j = 2$	$M_2(0) + \beta_0 M_1^2 t,\ \forall\, t$	$M_2(0)\exp(2\beta_0 M_1 t),\ \forall\, t$	$\frac{M_2(0)}{1-\beta_0 M_2(0) t},\ 0 < t < t_{gel}$

and the solutions of the scheme in [47]. If we compare the current scheme results with those schemes, it is clear that the current scheme has better accuracy like the improved scheme in [46]. However, our results looks far better than the results of the scheme in [47]. The computational time of the current scheme at $t = 100$ is 0.99 seconds which is almost equivalent to the CPU times of schemes in [46, 47].

Furthermore, one can see that all the first four moments are in very good agreement with their corresponding analytical solutions. If we compare the moment plots of the current schemes with those in [46], it seems that our results are better than both schemes. Note that in [46] the authors have only given the first two moments, while here we have presented four moments in order to clearly see the performance of the scheme for the higher moments. For this problem, it has already been shown in [23] that the current scheme is second order accurate numerically. As expected we also found that the numerical error is proportional to Δx^2, where as Δx represents the mesh cell size.

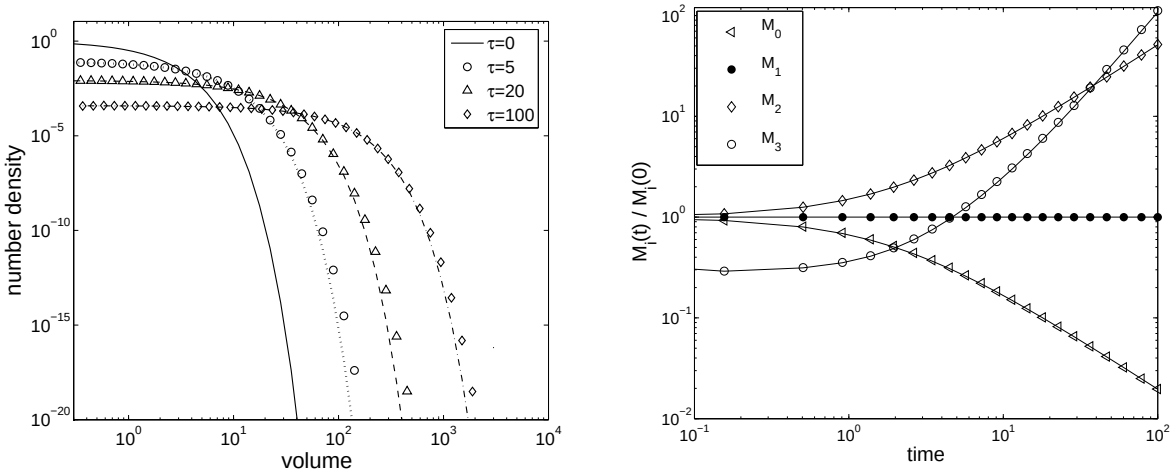

Figure 5.3: Test problem 1: One-component aggregation for constant kernel and $N = 40$.

Test problem 2: Here we consider the sum kernel $\beta(t, x, x') = \beta_0(x + x')$ with initial data as given in (5.80). The analytical solution is given as [105]

$$f(t, x) = \frac{N_0(1-\alpha)}{x_0 x' \sqrt{\alpha}} \exp(-(1+\alpha)x) I_1(2x'\sqrt{\alpha}) \,, \tag{5.82}$$

where $\tau = N_0\beta_0 x_0 t$, $x' = x/x_0$, $\alpha = 1 - exp(-x_0\tau)$ and I_1 is the modified Bessel function of first kind of order one. The exact values of the first three moments are given in Table 5.1. Figure 5.4 show the average number density at $\tau = 0.4, 1, 1.8$ and the moments until $\tau = 1.8$. The three time instants correspond to a degree of aggregation of 33, 63, and 83%. The numerical results are again in good agreement with the analytical results. Nevertheless, there is an observable under estimation in the front region. Again this behavior can also be observed in the other schemes, see [46, 47]. If we compare the current results with those in [46], it seems that the current scheme results are in good agreement with the improved scheme results of [46]. However, the results looks far better than the scheme in [47]. All of the first four moments are in very good agreement with their corresponding analytical solutions. However, there is an observable mismatch in the third moment M_3 after a long time. The CPU time of the current scheme at $t = 1.8$ is 1.16 seconds which is again equivalent to the CPU times of the schemes in [46, 47].

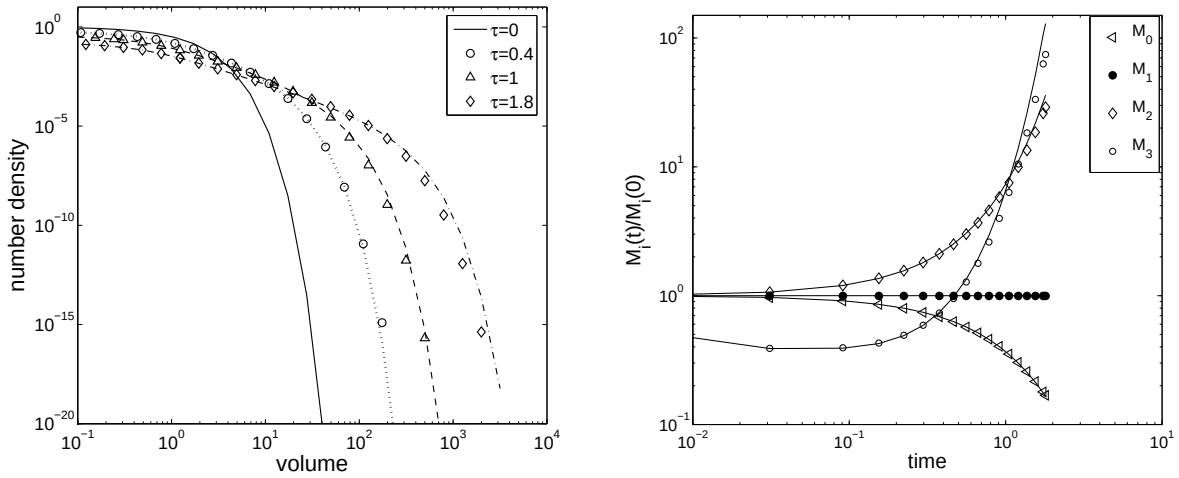

Figure 5.4: Test problem 2: One-component aggregation for sum kernel and $N = 40$.

Test problem 3: The third test corresponds to the multiplicative aggregation kernel $\beta(x, x') = \beta_0 x x'$. The initial data is the same as given in (5.80). The analytical solution is given as [105]

$$f(t, x) = \frac{N_0}{x_0} \exp(-x'(\tau + 1)) \sum_{k=0}^{\infty} \frac{T^k x'^{3k}}{(k+1)!\,\Gamma(2k+2)} \,, \tag{5.83}$$

where $\tau = N_0\beta_0 x_0^2 t$, $x' = x/x_0$ and Γ is the gamma function. Note that product kernel is a gelling kernel for any arbitrary initial distribution, see Smit et al. [110]. However, our simulation results are obtained before the gelling time arrives. The exact values of moments are given in Table 5.1. Figure 5.5 give the average number density at $\tau = 0.1, 0.25, 0.45$ and the moments until $\tau = 0.45$. The numerical results are again in good agreement with the analytical results. Again, there is an observable under estimation in the front region, which seems to be increasing with the degree of aggregation. Comparison of the current results with those in [46] show that, the current scheme has better results as compared to improved scheme in [46] and the scheme in [47]. The first three moments looks comparable to the corresponding analytical solutions. The three time instants correspond to a degree of aggregation of 5, 13, and 22%. The CPU time of the current scheme at $t = 0.45$ is 0.71 seconds. In case of product kernel, it has already been shown in [23] that the current scheme is second order accurate numerically. We have also found that the scheme preserves the second order accuracy.

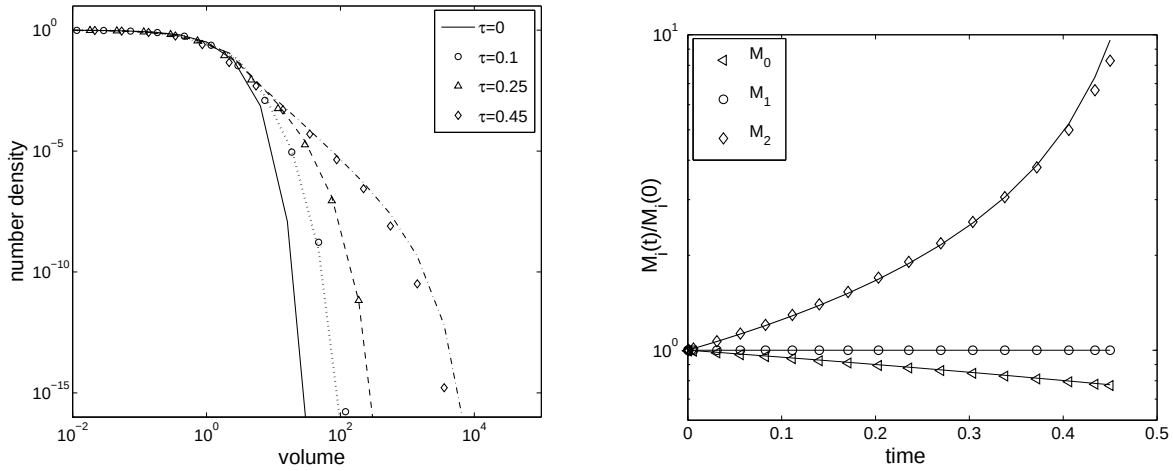

Figure 5.5: Test problem 3: One-component aggregation for product kernel and $N = 200$.

Test problem 4: In order to demonstrate further the effectiveness of the current scheme, we consider the following Gaussian-type initial distribution

$$f(0, x) = \frac{4N_0\, x'}{x_0} \exp\left(-x'\right) \tag{5.84}$$

with $x' = x/x_0$ and the sum kernel $\beta(x, x') = \beta_0(x + x')$. For this case Scott [105] has provided the following analytical solution

$$f(t, x) = \frac{N_0}{x_0}(1 - \alpha) \exp(-(2 + \alpha)x') \sum_{k=0}^{\infty} \frac{\alpha^k (x')^{3k+1} 2^{2k+2}}{(k + 1)!\, \Gamma(2k + 2)}\,, \tag{5.85}$$

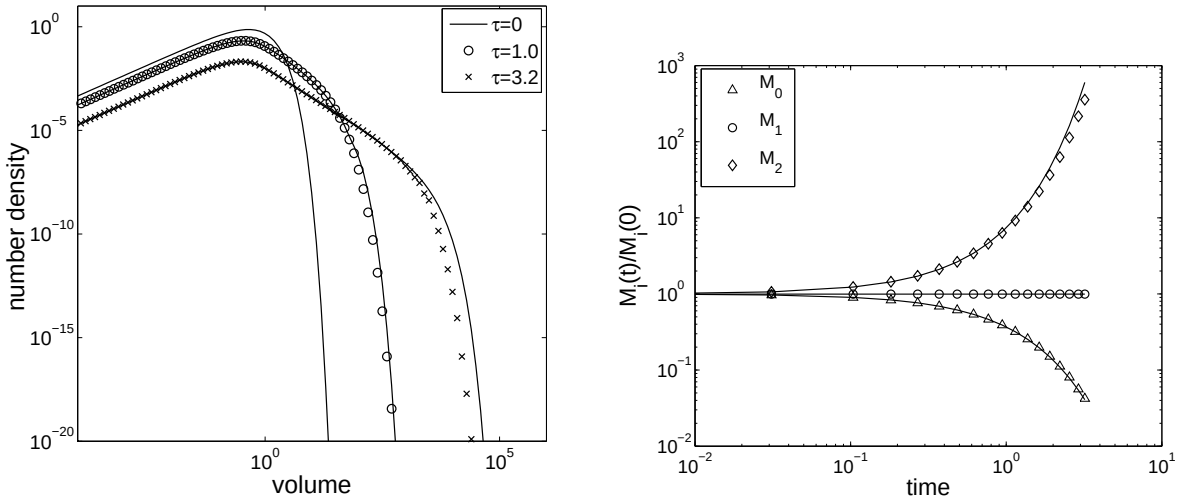

Figure 5.6: Test problem 4: One-component aggregation with Gaussian-type initial distribution for $N = 200$.

where $\tau = N_0\beta_0 x_0 t$, and $\alpha = 1 - \exp(-x_0\tau)$. The exact values of moments are given in Table 5.1. Figure 5.6 give the average number density at $\tau = 0, 1.0, 3.2$ and the moments until $\tau = 3.2$. The numerical results are again in good agreement with the analytical results. Nevertheless, there is an observable under estimation in the front region of the solution at $\tau = 3.2$. The two time instants correspond to a degree of aggregation of 63% and 96%. If we compare the results of the current scheme with those in [46], the current scheme give comparable results to the improved scheme in [46] and better than the scheme in [47]. The first three numerical moments are also comparable to the analytical ones.

5.3.2 Two-component aggregation

In the case of two-component aggregation analytical solutions are only available for the constant kernel. Hence, the numerical results are only compared against analytical solutions for constant aggregation kernel $\beta = \beta_0$. In all numerical results we take a square mesh of 40×40 mesh points.

Test problem 5: The initial data are

$$f(0, x, y) = \frac{N_0}{x_0 y_0} \exp\left(-\frac{x}{x_0} - \frac{y}{y_0}\right) \tag{5.86}$$

and the analytical solution is given as [64]

$$f(t, x, y) = \frac{4N_0}{(\tau+2)^2 x_0 y_0} \exp\left(-\frac{x}{x_0} - \frac{y}{y_0}\right) I_0(\theta)\,, \quad \text{with} \quad \theta = \left(\frac{4\tau x y}{(\tau+2)x_0 y_0}\right)^{\frac{1}{2}}. \tag{5.87}$$

Here $\tau = \beta_0 N_0 t$ and I_0 is the modified Bessel function of first kind of order zero. For this solution, we have the analytical solution for the following moments

$$M_{0,0}(\tau) = 2N_0/(2+\tau)\,, \quad M_{1,0}(\tau) = x_0\, N_0\,, \quad M_{1,1}(\tau) = x_0 y_0 N_0\,(1+\tau)\,. \tag{5.88}$$

For the numerical calculations we take $N_0 = 1,\ x_0 = 1$ and $y_0 = 1$. The numerical results are shown in Figure 5.7. The first plot show the comparison of analytical and numerical results which are plotted along the diagonal for three dimensionless times $\tau = 5, 20, 100$. The three time instants correspond to a degree of aggregation of 71, 91, and 98%, respectively. In this log-log plot the abscissa axis represents the variable x. The numerical results are in good agreement with the analytical ones. However, one can see the over estimation in the result of $\tau = 100$. The current test problem is an extension of the Test Problem 1 where one-component aggregation was considered. If we compare the results of Figures 5.3 and 5.7, one can see that in both cases the overall behavior of the results are the same. However, the two-component results seems even better than the one-component case. This shows that, the current finite volume scheme maintains its accuracy when extended to two-component aggregation case. The second plot in Figure 5.7 show that the numerical moments are in excellent agreement with the analytical ones. The last plot is the three-dimensional mesh plot of the number density at $\tau = 100$ which we have obtained from the same finite volume scheme. The CPU time of the current scheme at $t = 100$ is 4.2 minutes. According to our expectations, it was found found that our scheme in two-component aggregation case is also second order accurate and the order of convergence remains around 2.

Test problem 6: The initial data are

$$f(0,x,y) = \frac{16N_0}{x_0 y_0}\left(\frac{x}{x_0}\right)\left(\frac{y}{y_0}\right)\exp\left(-\frac{2x}{x_0} - \frac{2y}{y_0}\right)\,. \tag{5.89}$$

The analytical solution is given as [25]

$$f(t,x,y) = \frac{8N_0}{x_0 y_0\sqrt{\tau(\tau+2)^3}}\exp\left(-\frac{2x}{x_0} - \frac{2y}{y_0}\right)\,\left[I_0(\theta) - J_0(\theta)\right]\,, \tag{5.90}$$

where

$$\theta = 4\left(\frac{xy}{x_0 y_0}\right)^{\frac{1}{2}}\left(\frac{\tau}{\tau+2}\right)^{\frac{1}{4}}\,. \tag{5.91}$$

Here $\tau = \beta_0 N_0 t$ and J_0 and I_0 are, respectively, the Bessel function and the modified Bessel functions of first kind of order zero. For the numerical calculations we take $N_0 = 1,\ x_0 = 1$ and $y_0 = 1$. The exact moments for this problem are given as [118]:

$$M_{0,0}(\tau) = 2N_0/(2+\tau)\,, \quad M_{1,0}(\tau) = x_0\, N_0\,, \quad M_{2,0}(\tau) = \frac{1}{2}x_0^2 N_0\,(3+2\tau)\,, \tag{5.92}$$

$$M_{1,1}(\tau) = x_0 y_0 N_0\,(1+\tau)\,, \quad M_{3,0}(\tau) = \frac{3}{2}x_0^3 N_0\,(1+\tau)(2+\tau)\,, \tag{5.93}$$

$$M_{2,1}(\tau) = \frac{1}{2}x_0^2 y_0 N_0\,(3+7\tau+3\tau^2)\,. \tag{5.94}$$

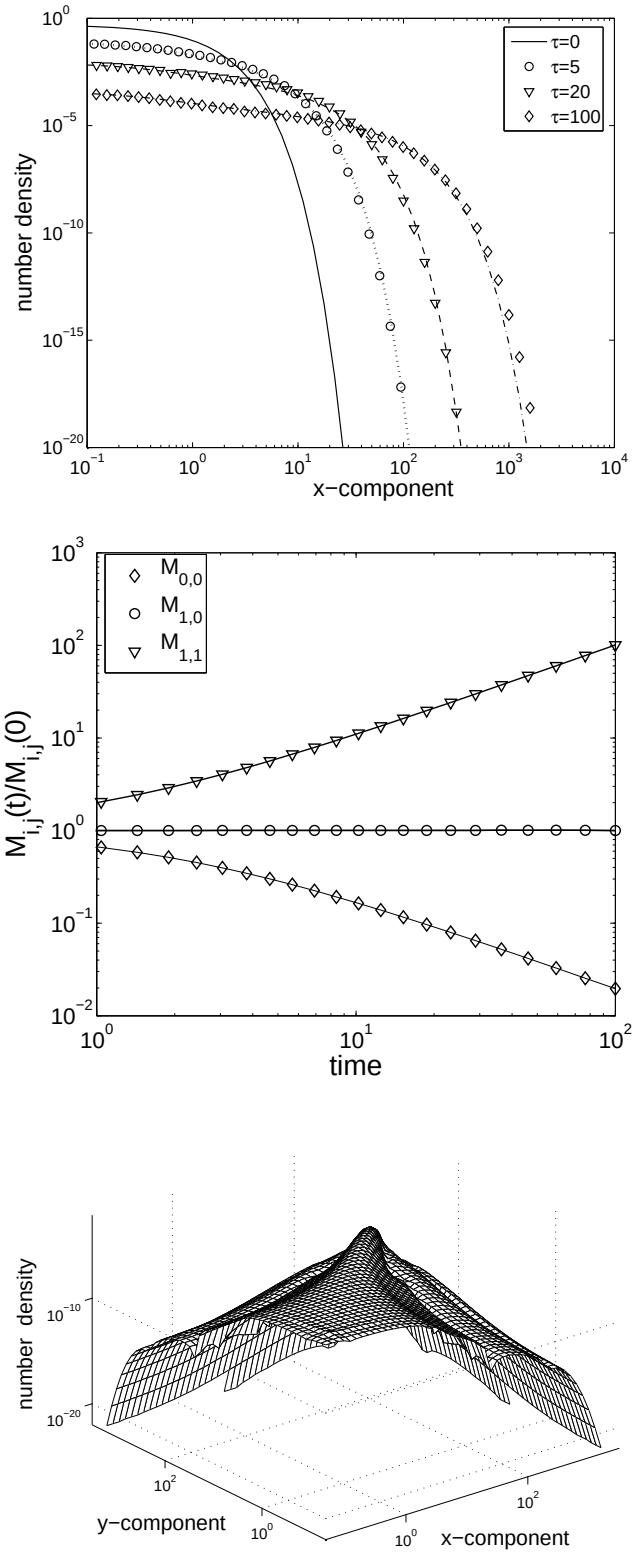

Figure 5.7: Test problem 5: Results of two-component aggregation.

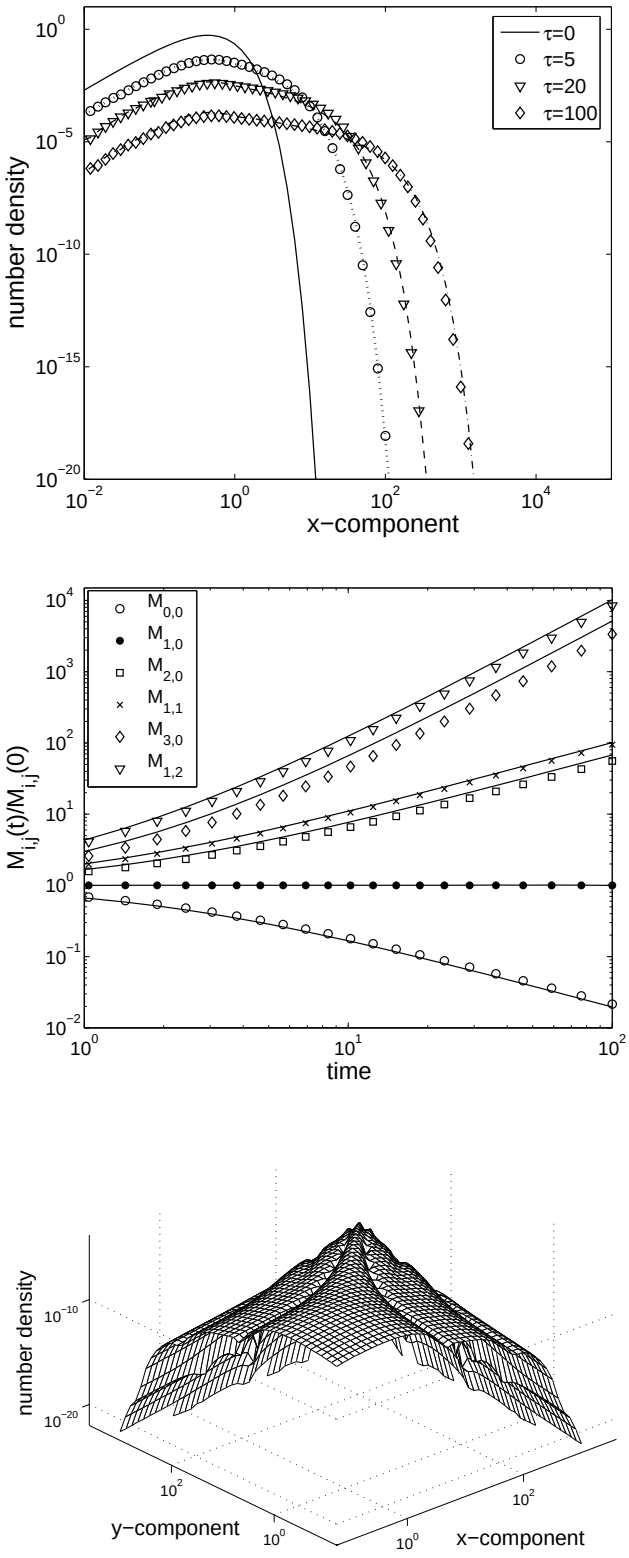

Figure 5.8: Test problem 6: Results of two-component aggregation.

This test problem was considered in [118]. The numerical results are shown in Figure 5.8. The first plot shows the comparison of analytical and numerical results which are plotted along the diagonal for three dimensionless times $\tau = 5, 20, 100$. The three time instants correspond to a degree of aggregation of 71, 91, and 98%, respectively. In this log-log plot the abscissa axis represents the variable x. The numerical results are again comparable with the analytical ones. If we compare our numerical results with those in [118], it is seems that our results are better for simulation times $\tau = 5, 20$. For these simulation times there is a visible over estimation in the results of the scheme in [118], while our results are in excellent agreement with analytical results. Although, there is a very slight under estimation in our result for $\tau = 100$, but this under estimation seems to be less than the over estimation in the results of the scheme in [118] for the same time. The second plot in Figure 5.8 show that the numerical moments are in good agreement with the analytical solutions. However, the moment M_{30} has a visible mismatch with analytical results which is also visible in the results given in [118]. The last plot is the three-dimensional mesh plot of the number density from our scheme at $\tau = 100$. The CPU time of the current scheme at $t = 100$ is 4.5 minutes.

Test problem 7: The initial data are

$$f(0, x, y) = \frac{4N_0}{x_0 y_0} \left(\frac{x}{x_0}\right) \exp\left(-\frac{2x}{x_0} - \frac{y}{y_0}\right). \tag{5.95}$$

The analytical solution is given as [25]

$$f(t, x, y) = \frac{16N_0}{x_0 y_0 (\tau+2)^2} \exp\left(-\frac{2x}{x_0} - \frac{y}{y_0}\right) \sum_{k=0}^{\infty} \frac{\left(\frac{4\tau y}{(\tau+2)y_0}\right)^k \left(\frac{x}{x_0}\right)^{2k+1}}{k!(2k+1)!}. \tag{5.96}$$

Here $\tau = \beta_0 N_0 t$. For the numerical calculations we take $N_0 = 1,\ x_0 = 1$ and $y_0 = 1$. The exact moments for this problem are also the same as given in (5.92)-(5.94).

This test problem was also considered in [118]. The numerical results are shown in Figure 5.9. The first plot show the comparison of analytical and numerical results which are plotted along the diagonal for three dimensionless times $\tau = 5, 20, 100$. The three time instants correspond to a degree of aggregation of 71, 91, and 98%, respectively. In this log-log plot the abscissa axis represents the variable x. The numerical results are again quite comparable with the analytical ones.

The comparison of our numerical results with those in [118] show that, both schemes give comparable solutions for this test problem. However, our results shows a small under estimation while the results in [118] show over estimation and that is the main difference in both results.

The second plot in Figure 5.9 show that the numerical moments are in good agreement with the analytical solutions. The moments plot of our scheme and the scheme in [118]

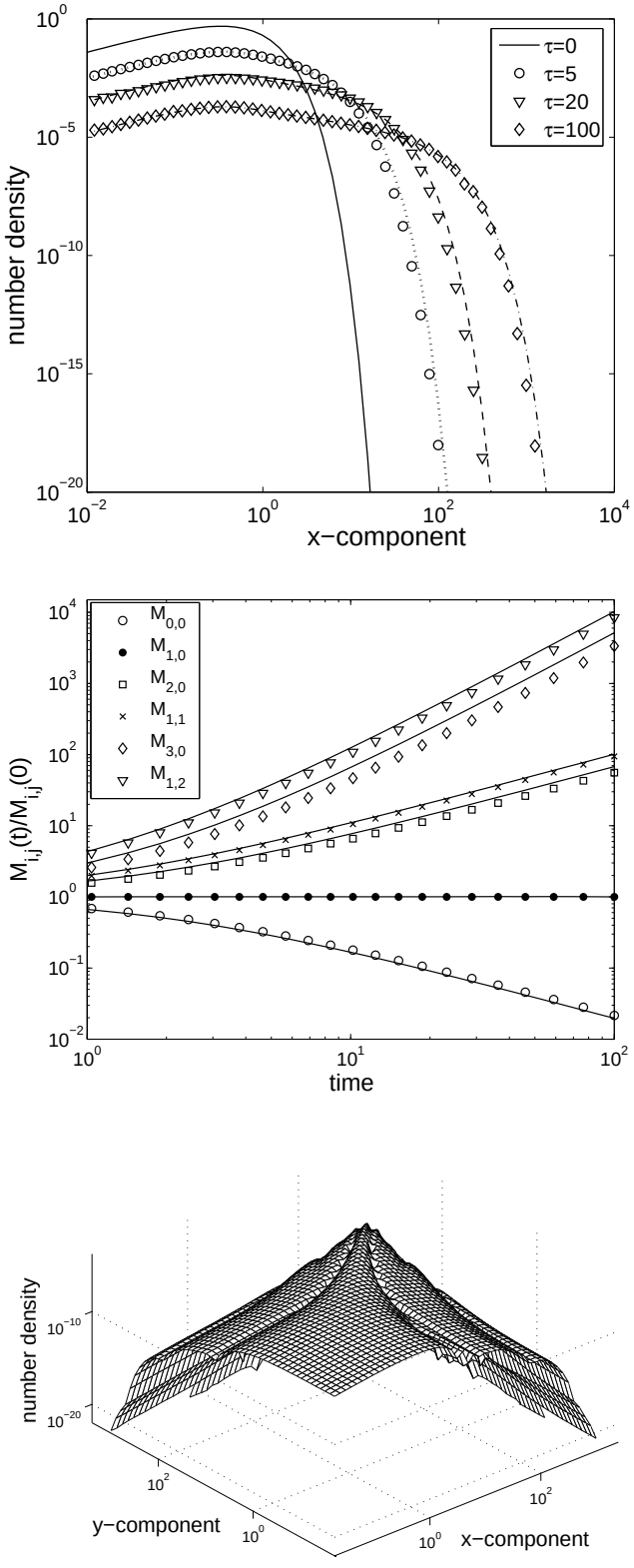

Figure 5.9: Test problem 7: Results of two-component aggregation.

give similar trends. Again, the main difference is the under estimation in our results and over estimation in the results of the scheme in [118]. The last plot is the three-dimensional mesh plot of the number density from our scheme at $\tau = 100$. The CPU time of the current scheme at $t = 100$ is 13.5 minutes.

Test problem 8: The initial data for this problem is the same as in Test problem 5. However instead of the constant kernel, here we consider sum kernel $\beta(t, x, y, x', y') = \beta_0(x + y + x' + y')$. As mentioned before, in the two-component case we have no exact solutions for other than a constant kernel. Here, we want to show that the current scheme can also be used for other kernels as well. The first plot in Figure 5.10 give the average number density from our scheme at $\tau = 0.2, 0.4, 1.0$ which are plotted along the diagonal. The second plot is a three dimensional plot of number density at $t = 1.0$ from our scheme.

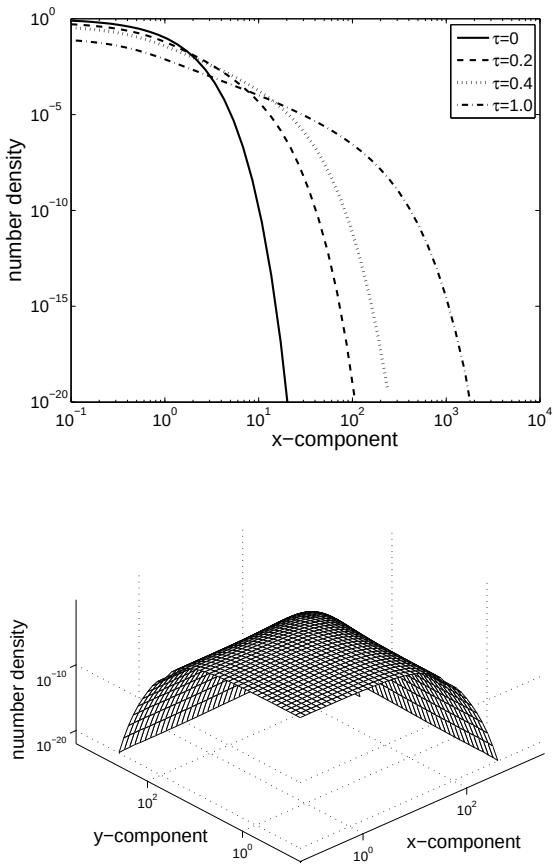

Figure 5.10: Test problem 8: Results of two-component aggregation.

5.3.3 One-component breakage

In this section, the performance of the proposed finite volume scheme is analyzed for one-component breakage process. The particle size distribution (PSD) and its moments are compared with the available analytical solutions.

Test problem 9: Here we consider four test cases that can be solved analytically. The analytical solutions for different initial PSDs and other parameters have been provided by Ziff and McRedy [123]. Two different kinds of initial PSDs, exponential and mono-disperse, are considered here. The analytical solutions and the corresponding initial conditions are given in Table 5.2. In the first two test cases we take the maximum particle size $R_x = 125$ while in the last two test cases $R_x = 1$.

In the first test case, exponential distribution is taken as initial PSD. In Figure 5.11, the analytical and numerical particle size distributions along with their first three moments are compared with each other. The final simulation time is $t = 10$. Here we have used the geometric grid with $q = 3$ and 60 mesh points. The results for the PSD are given on semi-log scales while linear scale is used for the moments plots. Since particles flows towards the small size range in the breakage process, it is very important to see the performance of the scheme there. From the results it is clear that finite volume scheme predict the PSD and the first three moments very well. In the second test case, again the exponential distribution is taken as initial PSD. Figure 5.12 shows the results. The final simulation time is $t = 5$. The numerical results are in very good agreement with analytical solutions. One can not see difference between the analytical and numerical solutions. Again we have used geometric grid with $q = 3$ and 60 mesh points.

In the third test case, a mono-disperse distribution is used as initial PSD. Figure 5.13 shows the comparison of analytical and numerical solutions. The final time of simulation is $t = 1000$. Here we have used the geometric grid with $q = 3$ and 60 mesh points. The number density is plotted on semi-log scale whereas the zero moments is on the linear scale. The numerical results are again in good agreement with the corresponding analytical results. However, a very small underestimation can be seen in the numerical results. The last example also corresponds to the mono-disperse initial distribution. Here we have used the geometric grid with $q = 4$ and 60 mesh points. The results on semi-log scale are shown in Figure 5.14 with simulation time $t = 2000$. Here one can see a visible difference in analytical and numerical results. Once again the method did well in the lower size range, however an underestimation can be seen in the middle of the distribution. Also we have a visible under estimation in the zero moment here which is given on semi-log scale.

Table 5.2: Initial data and analytical solutions for pure breakage process

Case	$S(x)$	$b(x,x')$	$f(0,x)$	Analytical solution, $f(t,x)$
1	x	2/x'	$\exp(-x)$	$\exp(-x(1+t))\,(1+t)^2$
2	x^2	2/x'	$\exp(-x)$	$\exp(-tx^2-x)\,[1+2t(1+x)]$
3	x	2/x'	$\delta(x-R_x)$	$\exp(-tx)\left(\delta(x-R_x)+\left[2t+t^2(R_x-x)\right]\vartheta(R_x-x)\right)$
4	x^2	2/x'	$\delta(x-R_x)$	$\exp(-tx^2)\,(\delta(x-R_x)+2tR_x\,\vartheta(R_x-x))$

In table 5.2 the function ϑ is a step function which is defined as

$$\vartheta(x-R_x)=\begin{cases}1\,, & x<R_x\\ 0\,, & \text{otherwise.}\end{cases} \tag{5.97}$$

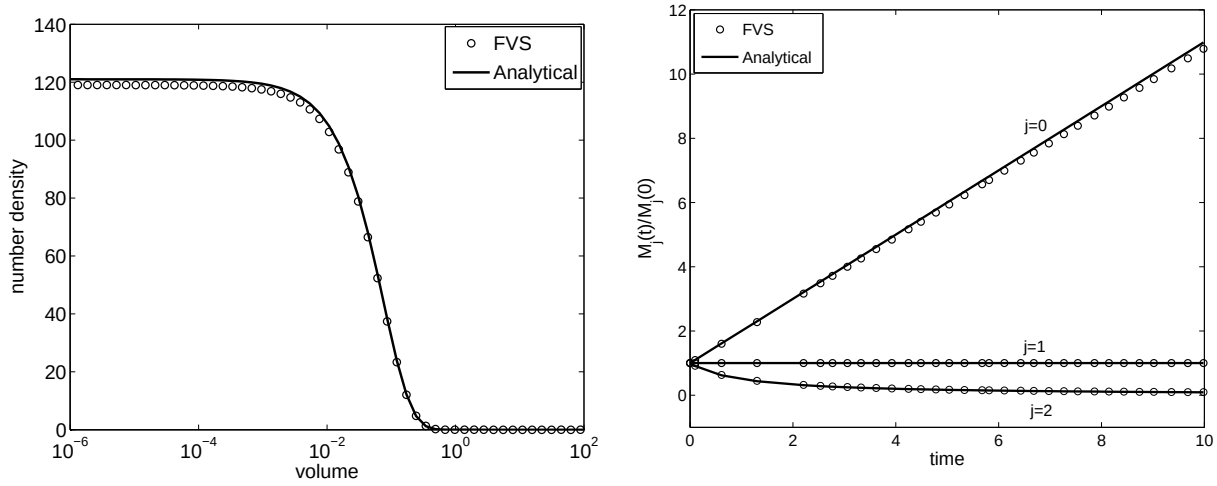

Figure 5.11: Test problem 9: One-component breakage with exponential initial distribution (Case 1 in Tabel 5.2), $q=3$, $N=60$ and $t=10$.

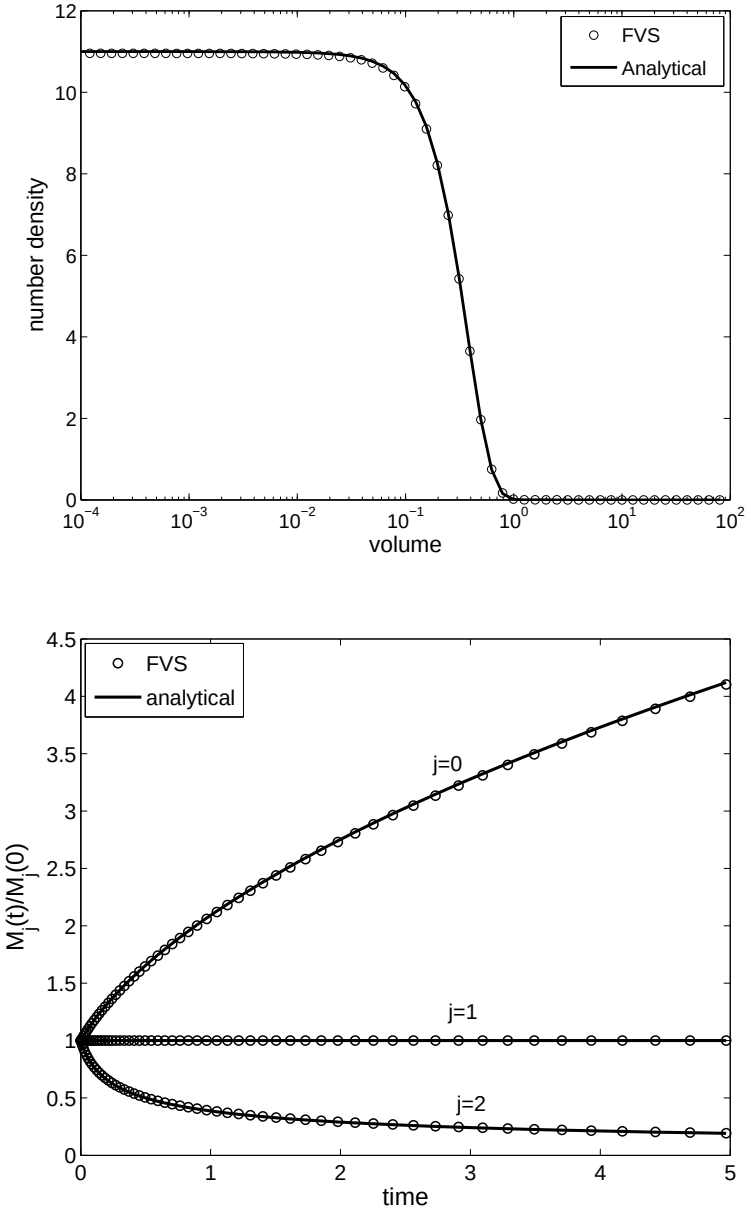

Figure 5.12: Test problem 9: One-component breakage with exponential initial distribution (Case 2 in Tabel 5.2), $q = 3$, $N = 60$ and $t = 5$.

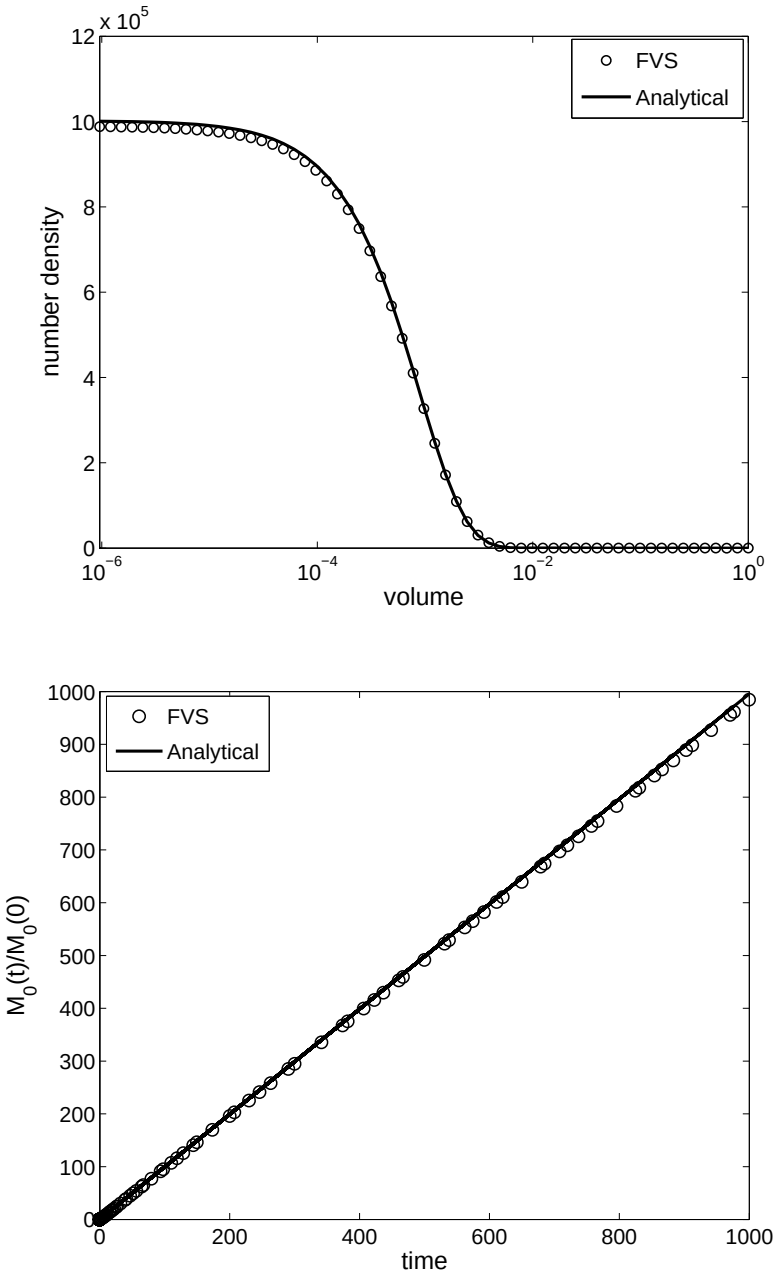

Figure 5.13: Test problem 9: One-component breakage with mono-disperse initial distribution (Case 3 in Tabel 5.2), $q = 3$, $N = 60$ and $t = 1000$.

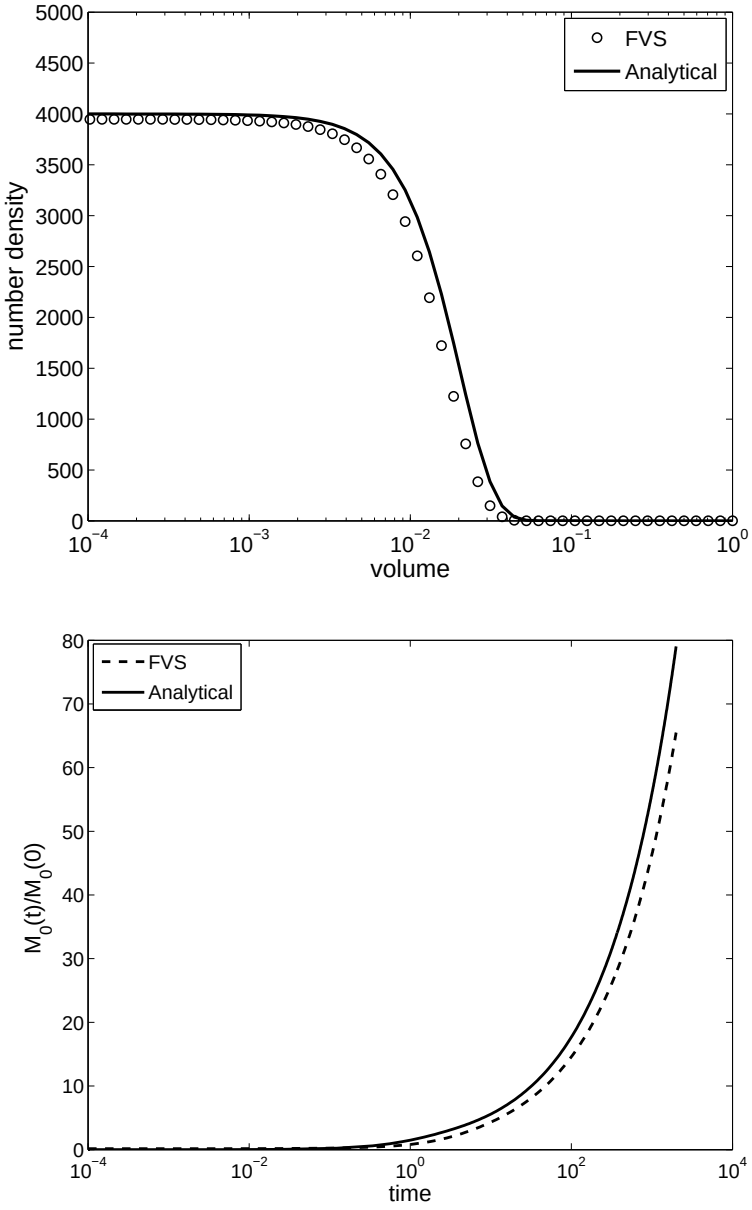

Figure 5.14: Test problem 9: One-component breakage with mono-disperse initial distribution (Case 4 in Tabel 5.2), $q = 4$, $N = 60$ and $t = 2000$.

Chapter 6

Simultaneous Processes

This chapter focuses on the numerical approximations of PBEs with simultaneous nucleation, growth, aggregation and breakage phenomena for modeling particulate processes. Two methods are proposed for this purpose. The first method combines a method of characteristics for growth term [49] with a finite volume scheme for aggregation and breakage terms. In the second method, a semi-discrete finite volume scheme (FVS) is used for all processes. Note that, in both methods the aggregation and breakage kinetics are solved with the same finite volume formulation which were derived in the last chapter. The main difference in both methods is the way they calculate the growth term. In the first method the mesh is moved with the characteristic speed, whereby the linear advection is treated exactly. While the second method uses the same finite volume schemes which have already been used in the previous chapters for the discretization of the advection terms. The efficiency and accuracy of the resulting methods are analyzed by comparing their numerical results with each other and with the available analytical solutions. For handling the nucleation term in the first scheme, the MOC is combined with a procedure of adding a cell of the nuclei size at each time level. The same procedure was also used in [49]. A standard ODE solver can be used to solve the resulting system of ODEs.

There are two main differences between the first method and the one used in [47, 49]. In our current method the aggregation and breakage terms are treated with a finite volume scheme, while in [47, 49] the authors have used the fixed pivot technique for aggregation and breakage processes. Secondly, our numerical method uses a reformulated PBE instead of the original one. This reformulation is necessary in order to apply the finite volume scheme efficiently. In case of reformulated PBE, our numerical methods calculate the volume (mass) density instead of the number density. However, one can easily recover back the number density at the end of simulation.

The chapter is organized as follows. In Section 6.1, starts with the reformulated PBE (2.24) and propose two different grid discretizations. We derive the first method which combines the method of characteristics (MOC) and the finite volume scheme (FVS). Afterwards, as a second method the finite volume scheme is derived for all processes. In Section 6.2,

several numerical results for different combinations of the nucleation, growth, aggregation and breakage processes are presented. The numerical results are also validated against the available analytical solutions.

6.1 The Mathematical Model

The reformulated form of PBE (2.20) has already been derived in Section 2.5 of Chapter 2 and is given by equation (2.24). Let us define $\tilde{f}(t,x) := xf(t,x)$ then (2.24) implies

$$\begin{aligned}\frac{\partial \tilde{f}(t,x)}{\partial t} =& -\frac{\partial[G(t,x)\tilde{f}(t,x)]}{\partial x} + \frac{G(t,x)\tilde{f}(t,x)}{x} \\ & - \frac{\partial \tilde{\mathcal{F}}_{\text{agg}}(t,x)}{\partial x} + \frac{\partial \tilde{\mathcal{F}}_{\text{break}}(t,x)}{\partial x} + \tilde{\mathcal{Q}}^{+}_{\text{nuc}}(t,x), \qquad (6.1)\\ \tilde{f}(0,x) =& \tilde{f}_0(x)\,, \quad x \in \mathbb{R}_+\,, \qquad (6.2)\end{aligned}$$

where according to (5.3), (5.50) and (2.19),

$$\tilde{\mathcal{F}}_{\text{agg}}(t,x) = \int_0^x \int_{x-u}^{\infty} u\,\beta(t,u,v)\,f(t,u)\,f(t,v)\,dvdu\,, \qquad (6.3)$$

$$\tilde{\mathcal{F}}_{\text{break}}(t,x) = \int_0^x \int_x^{\infty} y'\,b(t,y',x')\,S(x')\,f(t,x')\,dx'dy'\,, \qquad (6.4)$$

$$\tilde{\mathcal{Q}}_{\text{nuc}}(t,x)(t,x) := x\mathcal{Q}_{\text{nuc}}(t,x) = x\,f_{\text{nuc}}(t,x)\,B_{\text{nuc}}(t)\,. \qquad (6.5)$$

6.1.1 Domain discretization

In order to apply any numerical scheme, the first step is to discretize the computational domain. Here, we give two types of grid discretization, i.e., regular (or irregular grid) and geometric grid. Both types of discretizations have already been explained in the previous chapters. However, for the sake of completeness we are going to present them once again.

Regular/Irregular grid: Let N be a large integer representing the total number of cells, we denote by $(x_{i-\frac{1}{2}})_{i\in\{1,\cdots,N+1\}}$ a mesh of $[x_{\min}, x_{\max}]$, where $x_{\min}$ is the minimum and $x_{\max}$ is the maximum value of the property variable. We set

$$x_{1/2} = x_{\min}, \quad x_{N+1/2} = x_{\max}, \quad x_{i+1/2} = x_{\min} + i\cdot\Delta x_i\,, \text{ for } i = 1,2,\cdots N-1\,. \qquad (6.6)$$

Furthermore we set

$$x_i = (x_{i-1/2} + x_{i+1/2})/2\,, \quad \Delta x_i = x_{i+1/2} - x_{i-1/2}\,. \qquad (6.7)$$

Geometric grid: In order to capture the initial profile properly, in some test problems it is useful to use a geometric grid. A typical one-dimensional geometric grid is given as:

$$x_{1/2} = x_{\min}\,, \quad x_{i+1/2} = x_{\min} + 2^{(i-N)/q}(x_{\max} - x_{\min})\,, \text{ for } i = 1, 2, \cdots, N \tag{6.8}$$

with x_i and Δx_i as given in (6.7) and the parameter q is any positive integer.

Let $\Omega_i := \left[x_{i-1/2}, x_{i+1/2}\right]$ for $i \geq 0$. We approximate the initial data $\tilde{f}(0,x) := xf(0,x)$ in each grid cell by

$$\tilde{f}_i(0) = \frac{1}{\Delta x_i} \int\limits_{\Omega_i} \tilde{f}(0,x)dx\,. \tag{6.9}$$

After having a discretized computational domain and assigning the initial data to each grid cell, the next step is to solve the given PBE (6.1)-(6.5). In (6.3) and (6.4) the volume variable x ranges in the unbounded interval $\mathbb{R}_+$, hence the first step is to reduce the computations to a finite interval which are already given by equations (5.4) and (5.51). Hence we have to solve the following set of equations

$$\begin{aligned}\frac{\partial \tilde{f}(t,x)}{\partial t} =& -\frac{\partial[G(t,x)\tilde{f}(t,x)]}{\partial x} + \frac{G(t,x)\tilde{f}(t,x)}{x} \\ & - \frac{\partial \mathcal{F}_{\text{agg}}(t,x)}{\partial x} + \frac{\partial \mathcal{F}_{\text{break}}(t,x)}{\partial x} + \tilde{\mathcal{Q}}^{+}_{\text{nuc}}(t,x), \end{aligned} \tag{6.10}$$

$$\tilde{f}(0,x) = \tilde{f}_0(x)\,, \quad x \in \mathbb{R}_+\,, \tag{6.11}$$

where according to (5.4), (5.51) and (2.19),

$$\mathcal{F}_{\text{agg}}(t,x) = \int\limits_0^x \int\limits_{x-u}^{x_{\max}} u\,\beta(t,u,v)\,f(t,u)\,f(t,v)\,dvdu\,, \tag{6.12}$$

$$\mathcal{F}_{\text{break}}(t,x) = \int\limits_0^x \int\limits_{x}^{x_{\max}} y'\,b(t,y',x')\,S(x')\,f(t,x')\,dx'dy'\,, \tag{6.13}$$

$$\tilde{\mathcal{Q}}_{\text{nuc}}(t,x)(t,x) = x\,f_{\text{nuc}}(t,x)\,B_{\text{nuc}}(t)\,. \tag{6.14}$$

In the following we derive two numerical methods for the approximation of above modified population balance equation.

6.1.2 Method I: Combination of FVS and MOC

In this case we are interested to apply the method of characteristics for the growth process and a finite volume scheme for the aggregation process. For a scalar linear conservation law, for example PBE in the present case, there exist unique characteristic curves along which information propagates. If the solution moves along the propagation path-line, the

advection term $\partial(G\tilde{f})/\partial x$ in the current PBE disappears. This drastically reduces numerical diffusion in the solution of the scheme in comparison to other schemes which use some discretization technique for approximating the advection term.

For the MOC we use (6.6) or (6.8) as initial mesh at time $t = 0$ and consider a moving mesh along characteristics with mesh points $x_{i+1/2}(t)$ for $i = 0, 1, 2, \cdots N$.

Let us substitute the growth rate $G(t, x)$ by

$$\frac{dx}{dt} := G(t, x)\,. \tag{6.15}$$

Then equation (6.1) implies

$$\frac{\partial \tilde{f}(t,x)}{\partial t} + \frac{\partial}{\partial x}\left(\frac{dx}{dt}\tilde{f}(t,x)\right) = -\frac{\partial \mathcal{F}_{\text{agg}}(t,x)}{\partial x} + \frac{\partial \mathcal{F}_{\text{break}}(t,x)}{\partial x} + \frac{G(t,x)\tilde{f}(t,x)}{x} + \tilde{\mathcal{Q}}^{+}_{\text{nuc}}(t,x)\,. \tag{6.16}$$

Integration over the control volume $\Omega_i(t) := \left[x_{i-\frac{1}{2}}(t), x_{i+\frac{1}{2}}(t)\right]$ gives

$$\begin{aligned}\int\limits_{\Omega_i(t)} \frac{\partial \tilde{f}(t,x)}{\partial t}\,dx + \left(\frac{dx}{dt}\tilde{f}(t,x)\right)\Bigg|_{x_{i-\frac{1}{2}}(t)}^{x_{i+\frac{1}{2}}(t)} &= -\left[(\mathcal{F}_{\text{agg}})_{i+\frac{1}{2}} - (\mathcal{F}_{\text{agg}})_{i-\frac{1}{2}}\right] \\ &+ \left[(\mathcal{F}_{\text{break}})_{i+\frac{1}{2}} - (\mathcal{F}_{\text{break}})_{i-\frac{1}{2}}\right] + \int\limits_{\Omega_i(t)} \frac{G(t,x)\tilde{f}(t,x)}{x}\,dx + \int\limits_{\Omega_i(t)} \tilde{\mathcal{Q}}^{+}_{\text{nuc}}(t,x)\,dx\,.\end{aligned} \tag{6.17}$$

By using the Leibniz formula [1] backwards on the left hand side of (6.17) we get

$$\begin{aligned}\frac{d}{dt}\int\limits_{\Omega_i(t)} \tilde{f}(t,x)\,dx &= -\left[(\mathcal{F}_{\text{agg}})_{i+\frac{1}{2}} - (\mathcal{F}_{\text{agg}}))_{i-\frac{1}{2}}\right] + \left[(\mathcal{F}_{\text{break}})_{i+\frac{1}{2}} - (\mathcal{F}_{\text{break}})_{i-\frac{1}{2}}\right] \\ &+ \int\limits_{\Omega_i(t)} \frac{G(t,x)\tilde{f}(t,x)}{x}\,dx + \int\limits_{\Omega_i(t)} \tilde{\mathcal{Q}}^{+}_{\text{nuc}}(t,x)\,dx\,.\end{aligned} \tag{6.18}$$

Let $\tilde{f}_i := \tilde{f}_i(t)$ and $(\tilde{\mathcal{Q}}^{+}_{\text{nuc}})_i := (\tilde{\mathcal{Q}}^{+}_{\text{nuc}})_i(t)$ denote, respectively, the average values of the number density and nucleation term in each cell Ω_i. They are defined as

$$\tilde{f}_i := \frac{1}{\Delta x_i(t)}\int\limits_{\Omega_i(t)} \tilde{f}(t,x)\,dx\,, \qquad (\tilde{\mathcal{Q}}^{+}_{\text{nuc}})_i := \frac{1}{\Delta x_i(t)}\int\limits_{\Omega_i(t)} \tilde{\mathcal{Q}}^{+}_{\text{nuc}}(t,x)\,dx\,. \tag{6.19}$$

After using the above definitions, equation (6.18) implies

$$\begin{aligned}\frac{d}{dt}\left[\left(x_{i+\frac{1}{2}}(t) - x_{i-\frac{1}{2}}(t)\right)\tilde{f}_i\right] &= -\left[(\mathcal{F}_{\text{agg}})_{i+\frac{1}{2}} - (\mathcal{F}_{\text{agg}})_{i-\frac{1}{2}}\right] + \left[(\mathcal{F}_{\text{break}})_{i+\frac{1}{2}} - (\mathcal{F}_{\text{break}})_{i-\frac{1}{2}}\right] \\ &+ \Delta x_i(t)\,\frac{G_{i+\frac{1}{2}}\tilde{f}_i}{x_i(t)} + \Delta x_i(t)\,(\tilde{\mathcal{Q}}^{+}_{\text{nuc}})_i\,.\end{aligned} \tag{6.20}$$

By using the product rule and (6.15), the left hand side of (6.20) gives

$$\frac{d}{dt}\left[\left(x_{i+\frac{1}{2}}(t)-x_{i-\frac{1}{2}}(t)\right)\tilde{f}_i\right]=\Delta x_i(t)\,\frac{d\tilde{f}_i}{dt}+\left(\frac{d\tilde{x}_{i+\frac{1}{2}}}{dt}-\frac{d\tilde{x}_{i-\frac{1}{2}}}{dt}\right)\tilde{f}_i$$
$$=\Delta x_i(t)\,\frac{d\tilde{f}_i}{dt}+\left(G_{i+\frac{1}{2}}-G_{i-\frac{1}{2}}\right)\tilde{f}_i\,. \tag{6.21}$$

After replacing the left hand side of (6.20) with (6.21) and dividing the resultant equation by $\Delta x_i(t)$ one gets

$$\frac{d\tilde{f}_i}{dt}=-\frac{1}{\Delta x_i(t)}\left[(\mathcal{F}_{\text{agg}})_{i+\frac{1}{2}}-(\mathcal{F}_{\text{agg}})_{i-\frac{1}{2}}\right]+\frac{1}{\Delta x_i(t)}\left[(\mathcal{F}_{\text{break}})_{i+\frac{1}{2}}-(\mathcal{F}_{\text{break}})_{i-\frac{1}{2}}\right]$$
$$+\frac{G_{i+\frac{1}{2}}\tilde{f}_i}{x_i(t)}-\left(G_{i+\frac{1}{2}}-G_{i-\frac{1}{2}}\right)\frac{\tilde{f}_i}{\Delta x_i(t)}+(\tilde{\mathcal{Q}}^{+}_{\text{nuc}})_i\,, \tag{6.22}$$

where $(\mathcal{F}_{\text{agg}})_{i+1/2}$ is given by (5.9) and $(\mathcal{F}_{\text{break}})_{i+1/2}$ by (5.53) and (5.53). In summary, we have to solve the following set of equations:

$$\frac{d\tilde{f}_i}{dt}=-\frac{1}{\Delta x_i(t)}\left[(\mathcal{F}_{\text{agg}})_{i+\frac{1}{2}}-(\mathcal{F}_{\text{agg}})_{i-\frac{1}{2}}\right]+\frac{1}{\Delta x_i(t)}\left[(\mathcal{F}_{\text{break}})_{i+\frac{1}{2}}-(\mathcal{F}_{\text{break}})_{i-\frac{1}{2}}\right]$$
$$+\frac{G_{i+\frac{1}{2}}\tilde{f}_i}{x_i(t)}-\left(G_{i+\frac{1}{2}}-G_{i-\frac{1}{2}}\right)\frac{\tilde{f}_i}{\Delta x_i(t)}+(\tilde{\mathcal{Q}}^{+}_{\text{nuc}})_i\,, \tag{6.23}$$

$$\frac{d\tilde{x}_{i+\frac{1}{2}}}{dt}=G_{i+\frac{1}{2}}\,,\qquad \forall\ i=1,2,\cdots,N \tag{6.24}$$

with initial condition

$$\tilde{f}(0,x_i)=\tilde{f}_0(x_i)\,. \tag{6.25}$$

As a boundary condition the number density is taken to be zero outside the computational domain. This means that there exist no smaller or bigger particle than our specified size range of particles. The above system of ordinary differential equations can be solved by any standard ODE solver.

Presence of a nucleation term: In order to overcome the nucleation problem a new cell of nuclei size is added at a given time level. The total number of mesh points can be kept constant by deleting the last cell at the same time level. Hence, all the variables such as $\tilde{f}_i(t)$ and $x_i(t)$ are initiated at these time levels and the time integrator restarts.

6.1.3 Method II: Semi-discrete finite volume scheme (FVS)

Alternatively, one can use a semi-discrete finite volume scheme in order to solve the PBE (6.1) without any further modification. Here, we will give only the direct formulations of

the scheme which is already explained in Chapter 3.

Let us define $\mathcal{F}(t,x) = G(t,x)\tilde{f}(t,x)$. Integration of (6.1) over the control volume $\Omega_i := \left[x_{i-\frac{1}{2}}, x_{i+\frac{1}{2}}\right]$ gives

$$\int\limits_{\Omega_i} \frac{\partial \tilde{f}(t,x)}{\partial t}\, dx = -\int\limits_{\Omega_i} \frac{\partial \mathcal{F}(t,x)}{\partial x}\, dx + \int\limits_{\Omega_i} \frac{\mathcal{F}(t,x)}{x}\, dx - \int\limits_{\Omega_i} \frac{\partial \mathcal{F}_{\text{agg}}(t,x)}{\partial x}\, dx + \int\limits_{\Omega_i} \frac{\partial \mathcal{F}_{\text{break}}(t,x)}{\partial x}\, dx\, dx + \int\limits_{\Omega_i} \tilde{\mathcal{Q}}^{+}_{\text{nuc}}(t,x)\, dx\,. \quad (6.26)$$

Let $\tilde{f}_i = \tilde{f}_i(t)$ and $(\tilde{\mathcal{Q}}^{+}_{\text{nuc}})_i = (\tilde{\mathcal{Q}}^{+}_{\text{nuc}})_i(t)$ denote respectively the average value of the number density and the nucleation term as given in (6.19). Then (6.26) becomes

$$\begin{aligned}\frac{d\tilde{f}_i}{dt} =& -\frac{1}{\Delta x_i}\left[\mathcal{F}_{i+\frac{1}{2}} - \mathcal{F}_{i-\frac{1}{2}}\right] + \frac{\mathcal{F}_i}{x_i} - \frac{1}{\Delta x_i}\left[(\mathcal{F}_{\text{agg}})_{i+\frac{1}{2}} - (\mathcal{F}_{\text{agg}})_{i-\frac{1}{2}}\right] \\ &+ \frac{1}{\Delta x_i}\left[(\mathcal{F}_{\text{break}})_{i+\frac{1}{2}} - (\mathcal{F}_{\text{break}})_{i-\frac{1}{2}}\right] + (\tilde{\mathcal{Q}}^{+}_{\text{nuc}})_i\,,\end{aligned} \quad (6.27)$$

where $(\mathcal{F}_{\text{agg}})_{i+1/2}$ is given by (5.9) and $(\mathcal{F}_{\text{break}})_{i+1/2}$ by (5.53). The flux $\mathcal{F}_{i+\frac{1}{2}}$ at the right cell interface flux is according to (3.131)

$$\mathcal{F}_{i+\frac{1}{2}} = \mathcal{F}_i + \frac{\Delta x_i}{2\,\Delta x_{i-\frac{1}{2}}}\varphi\left(r_i^{+}\right)\left(\mathcal{F}_{i+1} - \mathcal{F}_i\right)\,, \quad (6.28)$$

where

$$\Delta x_{i-\frac{1}{2}} = x_i - x_{i-1}\,, \quad \Delta x_i = x_{i+\frac{1}{2}} - x_{i-\frac{1}{2}} \quad (6.29)$$

and the flux limiting function φ is given by (3.116). The argument r_i^{+} of the function φ is the so-called upwind ratio of two consecutive solution gradients

$$r_i^{+} = \frac{\mathcal{F}_i - \mathcal{F}_{i-1} + \varepsilon}{\mathcal{F}_{i+1} - \mathcal{F}_i + \varepsilon}\,. \quad (6.30)$$

Analogously, one can formulate the flux $\mathcal{F}_{i-\frac{1}{2}}$ at the left boundary of the control volume Ω_i. The expression has to be evaluated with a small parameter, e.g. $\varepsilon = 10^{-10}$, in order to avoid division by zero. One can also use $HR - \kappa = 1/3$ scheme for this model which according to the analysis in Chapter 3 is more accurate. However, for the test problems considered in this chapter both the $HR - \kappa = -1$ and the $HR - \kappa = 1/3$ schemes have same accuracy.

Again, the resultant ODEs in (6.23) and (6.27) can be solved with any standard ODEs-solver.

6.2 Numerical Test Problems

The numerical schemes derived in this article can be applied to solve various combinations of nucleation, growth and aggregation processes for different choices of nucleation, growth and aggregation rates. However, to validate the current schemes, it is needed to test the schemes for the test problems where analytical solutions are also available. In the literature, analytical solutions of the PBEs are only available for the following combinations of processes

- Pure growth.
- Simultaneous growth and aggregation.
- Simultaneous aggregation and breakage.
- Simultaneous aggregation and nucleation.
- Simultaneous growth and nucleation.

In this section, we will consider test cases for above combinations of processes. Note that, analytical solutions for pure aggregation and pure breakage also do exist and have already been thoroughly discussed in the last chapter.

In all numerical test problems the lines represent the analytical solutions while symbols are used to represent the numerical solutions.

6.2.1 Pure growth

Constant growth problem: Here we consider constant growth with $G(x) = G_0$ and an exponential initial distribution of the form

$$f(0,x) := f_0(x) = \frac{N_0}{x_0} \exp\left(-\frac{x}{x_0}\right) , \tag{6.31}$$

where N_0 and x_0 are the total number of particles and the mean volume of particles at time $t = 0$, respectively. In both methods we use a geometric grid (6.8) with $q = 3$. The analytical solution is given by

$$f(t,x) = f_0(x - G_0 t) . \tag{6.32}$$

Here, we take $G_0 = 1$, $N_0 = 5$, $x_0 = 0.01$ and 60 mesh points. In Figure 6.1, the numerical results of both methods are compared with the analytical solution. Note that the first plot (top plot) uses a log on both axes so that the solutions are not merely shifted in the graph. The MOC results (top plot) are in excellent agreement with the analytical solution and are hardly distinguishable. The stability and numerical diffusion of the numerical solution which marred the performance of the finite difference techniques are completely absent in

the present scheme. The numerical results of FVS (middle plot) are also in agreement with the analytical solution. However, one can see a clear numerical dissipation on the left hand side discontinuity. A comparison of the MOC and FVS (bottom plot) shows that FVS results are little bit diffusive. Instead of any other scheme which uses some discretization technique for the advection term, the MOC results show a clear advantage where the advection term disappears from the governing equation. The first plot in Figure 6.1 shows that the rapid growth rate results in very rapid growth of small particles, while the large particles stay nearly unchanged.

Linear growth: Here $G(x) = G_0 x$ with exponential initial distribution (6.31). For the numerical simulation we take $G_0 = 1$, $x_0 = 0.01$ and $N_0 = 5$. The analytical solution is given by [49]

$$f(t, x) = f_0 \left(x e^{-G_0 t} \right) e^{-G_0 t} . \tag{6.33}$$

In both methods we use a geometric grid (6.8) with $q = 4$ and 200 mesh points. Figure 6.2 shows the comparison of numerical and analytical results. Once again the numerical results of MOC (top plot) are in excellent agreement with the analytical results. However, one can see a visible numerical dissipation in the results of the FVS (bottom plot) on both left and right ends of the number density profile. The numerical results of the first scheme again justifies the use of MOC for growth term.

6.2.2 Simultaneous growth and aggregation

In this case, five analytical solutions are available from Ramabhadran et al. [98]. The cases represent various combinations of constant and linear growth rates, constant and sum aggregation kernels, as well as exponential and gamma initial distributions. Kumar and Ramkrishna [49] have also considered all these test problems. The specific choices for each case are given in Table 6.1 and their corresponding analytical solutions are given in Appendix B.1. The exact zero and first moments for different growth rates and aggregation kernels are given in Table 6.2. Here we have tested our schemes for all five cases. In each case, we take $N_0 = 5$, $x_0 = 0.01$. A geometric grid with $q = 6$ is chosen to cover the size range of interest at initial time. Simulation results are presented for different simulation times. In both methods we use 100 mesh points for all five test cases. In the following we discuss all these case one by one.

Constant growth and constant aggregation: Here we consider $G(x) = G_0$ and $\beta(x, x') = \beta_0$. The simulation results for cases 1 and 2 of Table 6.1 are shown in Figures 6.3 and 6.4, respectively. Both figures indicate that the numerical results of the first and second methods are in very good agreement with the analytical results and those in [49] across several order of magnitude. Even at very small values the results looks very promising. However, the numerical results of the second method are dissipative at the left

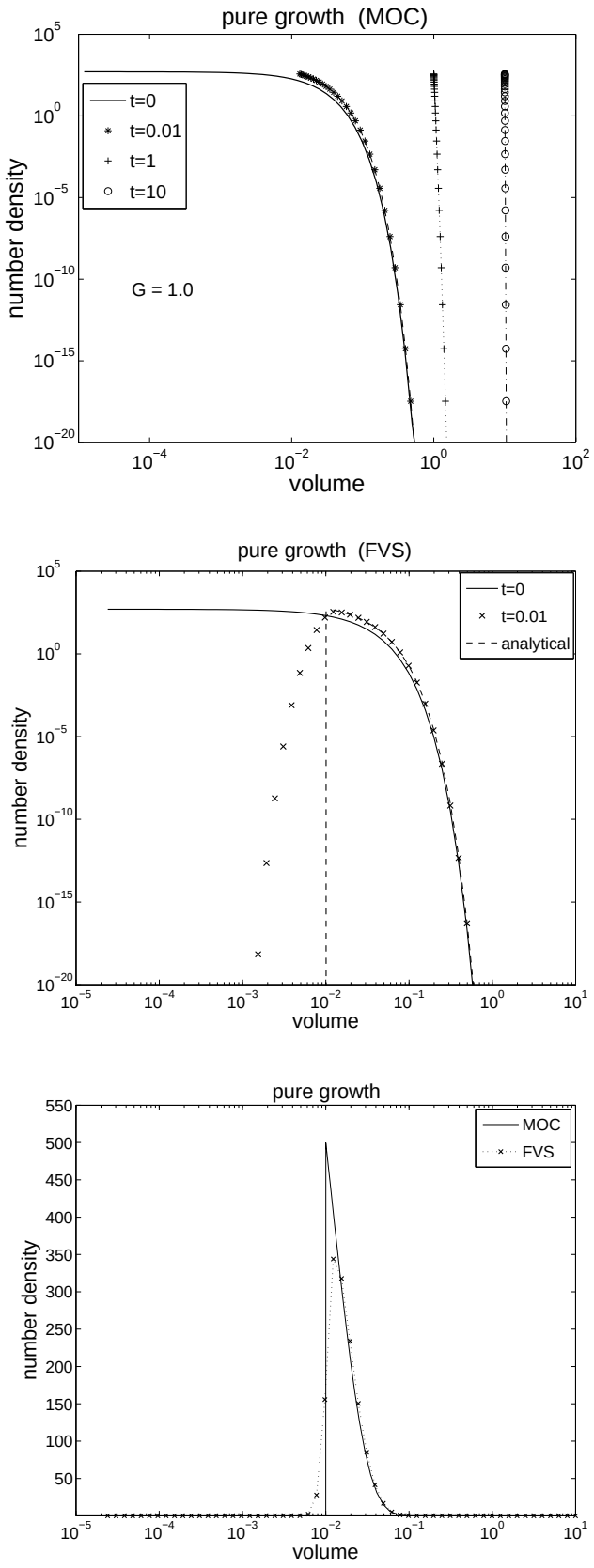

Figure 6.1: Pure growth: The comparison of numerical results (symbols) with analytical solutions (lines) for constant growth problem.

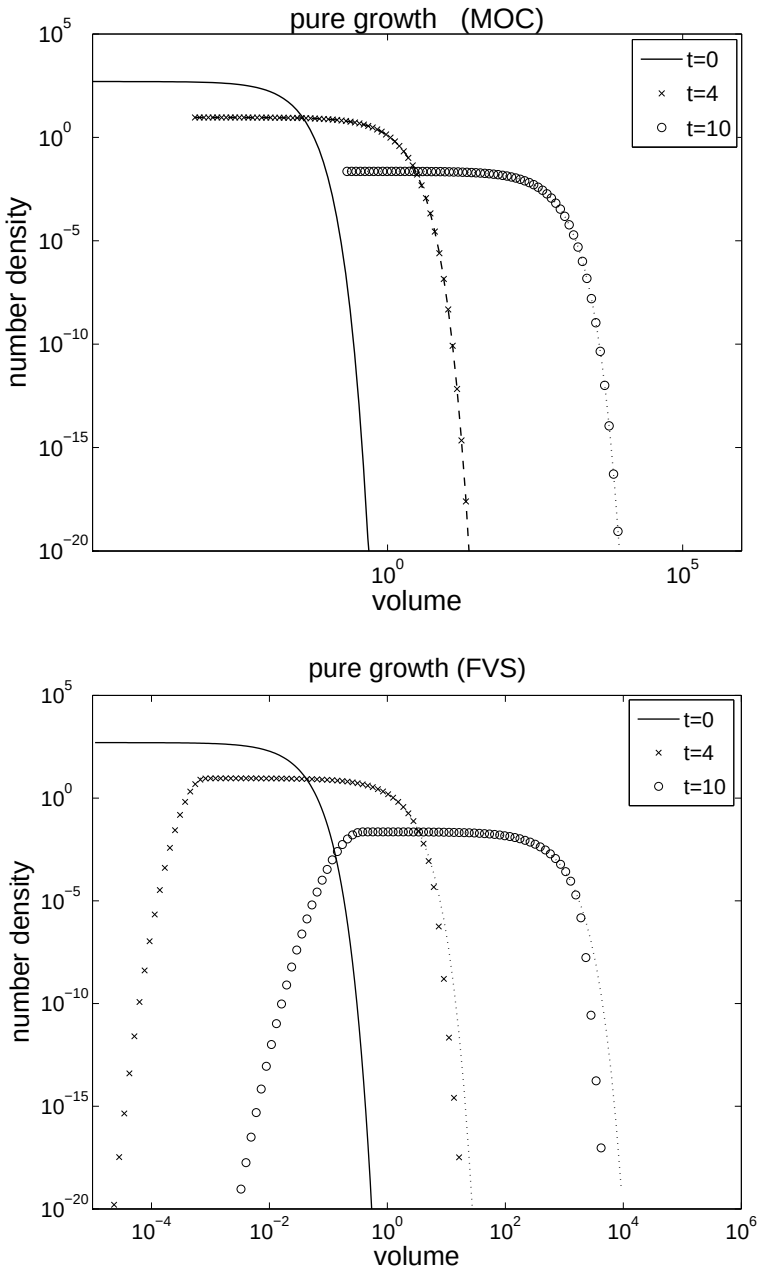

Figure 6.2: Pure growth: The comparison of numerical results (symbols) with analytical solutions (lines) for linear growth problem.

Table 6.1: Simultaneous growth and aggregation: Various combinations of growth function, aggregation kernel and initial conditions

Case	$G(x)$	$\beta(x,x')$	$f_0(x)$
1	1	100	$\frac{N_0}{x_0}\exp\left(-x/x_0\right)$
2	1	100	$\frac{N_0}{x_0}\left(x/x_0\right)\exp\left(-x/x_0\right)$
3	x	10	$\frac{N_0}{x_0}\exp\left(-x/x_0\right)$
4	x	10	$\frac{N_0}{x_0}\left(x/x_0\right)\exp\left(-x/x_0\right)$
5	x	$x+x'$	$\frac{N_0}{x_0}\exp\left(-x/x_0\right)$

Table 6.2: Simultaneous growth and aggregation: Moments M_0 and M_1 of the distributions

Case	Moments
$\beta(x,x')=\beta_0$	$M_0=\frac{2N_0}{2+\beta_0 N_0 t}$
$G(x)=G_0$	$M_1=N_0x_0\left[1-\frac{2G_0}{\beta_0 N_0 x_0}\ln\left(\frac{2}{2+\beta_0 N_0 t}\right)\right]$
$\beta(x,x')=\beta_0$	$M_0=\frac{2N_0}{2+\beta_0 N_0 t}$
$G(x)=G_0\,x$	$M_1=N_0x_0\exp(\beta_0 t)$
$\beta(x,x')=\beta_0(x+x')$	$M_0=N_0\exp\left[\frac{\beta_0 N_0 x_0}{G_0}(1-\exp(G_0 t)\right]$
$G(x)=G_0\,x$	$M_1=N_0x_0\exp(\beta_0 t)$

discontinuity of the number density profile and is in good agreement in the other regions.

There are some differences between the first scheme results and analytical solutions on the far left side of the number density profile for $t = 0.01$ in Figure 6.4 and similar but not visible differences in all other simulations in Figure 6.3. These are due to the fact that analytical solution in this range breaks down, see also [49]. Ramabhadran et al. [98] have pointed out that for approximately equal growth and aggregation rates, their analytical solution for $G(x) = G_0$ and $\beta(x,x') = \beta_0$ is valid for only large particle sizes. For the aggregation-dominated situation, the range of validity is increased, where as for the growth-dominated situation, the solution breaks down completely. The simulations given in Figures 6.3 and 6.4 are somehow aggregation-dominated cases in order to allow analytical solutions to hold in a reasonably wide range. For this problem with exponential initial distribution the extent of aggregation $M_0(t)/M_0(0)$, as growth processes conserve

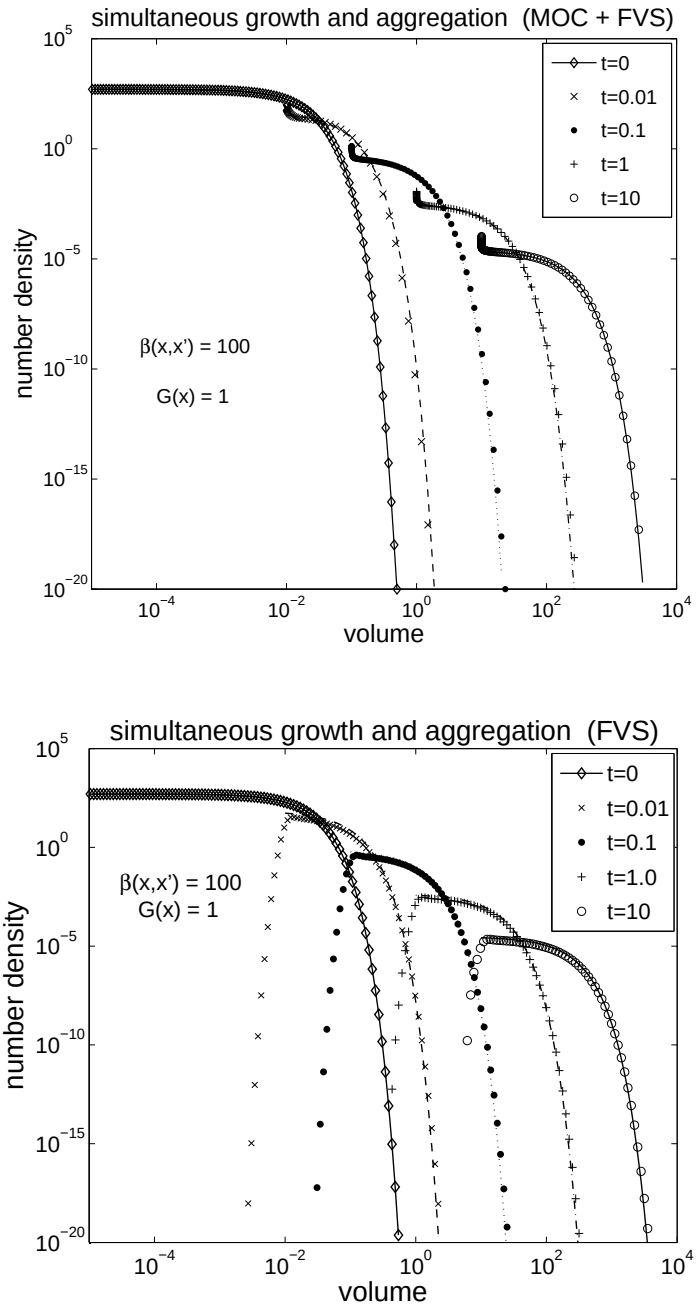

Figure 6.3: Simultaneous growth and aggregation: The comparison of numerical results (symbols) with analytical solutions (lines) for constant growth and constant aggregation (Case 1 of Table 6.1).

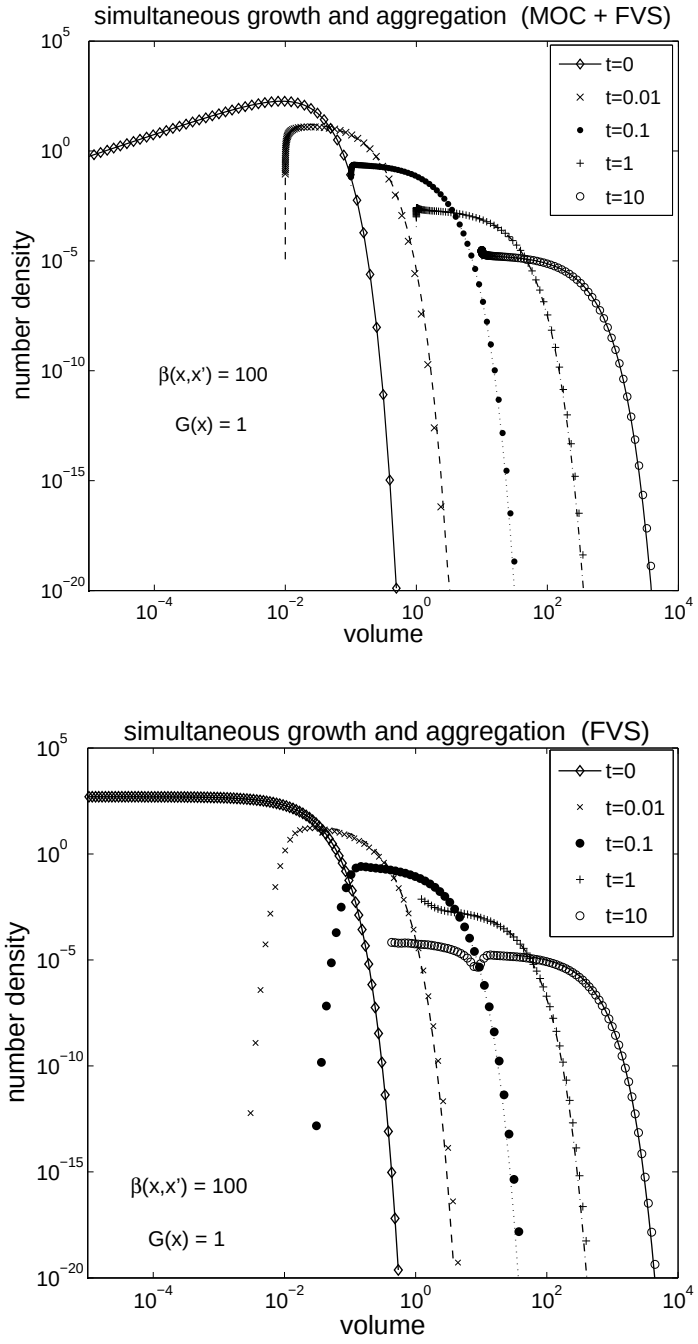

Figure 6.4: Simultaneous growth and aggregation: The comparison of numerical results (symbols) with analytical solutions (lines) for constant growth and constant aggregation (Case 2 of Table 6.1).

total number, is 0.288 and $3.998 \cdot 10^{-4}$ at times $t = 10^{-2}$ and $t = 10$, respectively. Similarly the extent of growth processes $M_1(t)/M_1(0)$, as the aggregation process conserve mass, is 1.501 and 4.13 at times $t = 10^{-2}$ and $t = 10$, respectively.

Linear growth and constant aggregation: In this case we consider $G(x) = G_0 x$ and $\beta(x, x') = \beta_0$. Figures 6.5 and 6.6 show evolving size distributions for cases 3 and 4 of Table 6.1. The numerical results are once again in very good agreement with the analytical results and those in [49]. Again, there is a visible smearing in the second method results at far left end of the number density profiles, while are in good agreement with analytical and MOC solutions in other regions. In case of exponential initial distribution the extent of aggregation $M_0(t)/M_0(0)$ is 0.039 and $3.98 \cdot 10^{-3}$ at times $t = 1$ and $t = 10$, respectively. Similarly the extent of growth processes $M_1(t)/M_1(0)$ is 2.72 and $2.2 \cdot 10^4$ at times $t = 1$ and $t = 10$, respectively.

Linear growth and sum aggregation: Here we consider $G(x) = G_0 x$ and $\beta(x, x') = \beta_0(x + x')$. The numerical results for the case 5 of Table 6.1 are presented in Figure 6.7. It shows that even with size dependent rate functions, the analytical and the numerical results of first and second methods are in excellent agreement. However, in the results of the second method there is a visible smearing at the left end of the number density profiles and very slight over prediction at the right end.

The above test simulations clearly show that the proposed techniques are quite robust and yield very good results for simultaneous growth and aggregation. Here the extent of aggregation $M_0(t)/M_0(0)$ is 0.92 and 0.39 at times $t = 1$ and $t = 3$, respectively. Similarly extent of growth processes $M_1(t)/M_1(0)$ is 2.72 and 20.09 at times $t = 1$ and $t = 3$, respectively.

6.2.3 Simultaneous nucleation and growth

In this section we consider some numerical test problems in order to test the proposed schemes for simultaneous nucleation and growth processes. These numerical results were also considered by Kumar and Ramkrishna [49] in order to test their scheme. In both methods we use again geometric grid with $q = 6$. We take 100 mesh points in both numerical examples.

Constant growth and exponential nucleation: In this case we take $G(x) = G_0$, and $\mathcal{Q}^+_{\text{nuc}}(x) = B_0/x_{0,n} \exp(-x/x_{0,n})$. As an initial condition we take the exponential initial distribution of the form $f_0(x) = N_0/x_0 \exp(-x/x_0)$. For numerical simulation we take $G_0 = 1$, $N_0 = 10$, $x_0 = 0.01$, $x_{0,n} = 0.001$, and $B_0 = 10^5$. The analytical solution for this

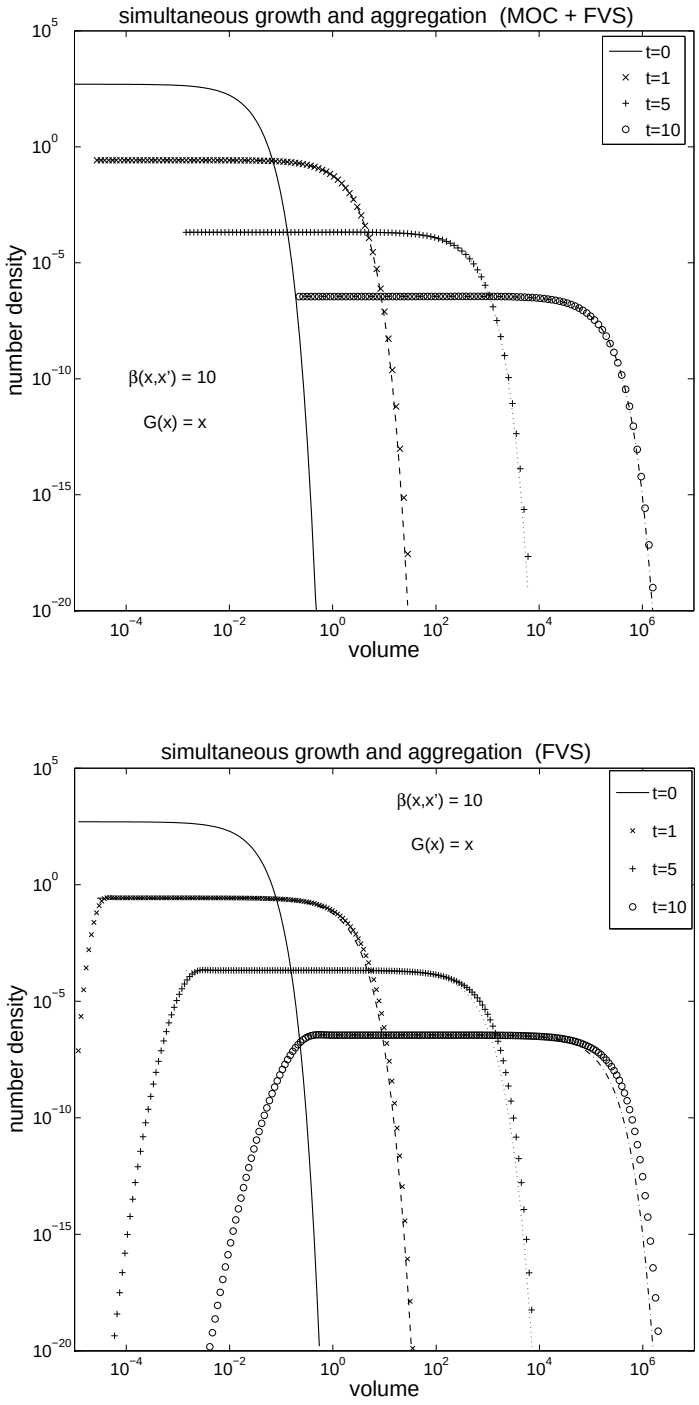

Figure 6.5: Simultaneous growth and aggregation: The comparison of numerical results (symbols) with analytical solutions (lines) for linear growth and constant aggregation (Case 3 of Table 6.1).

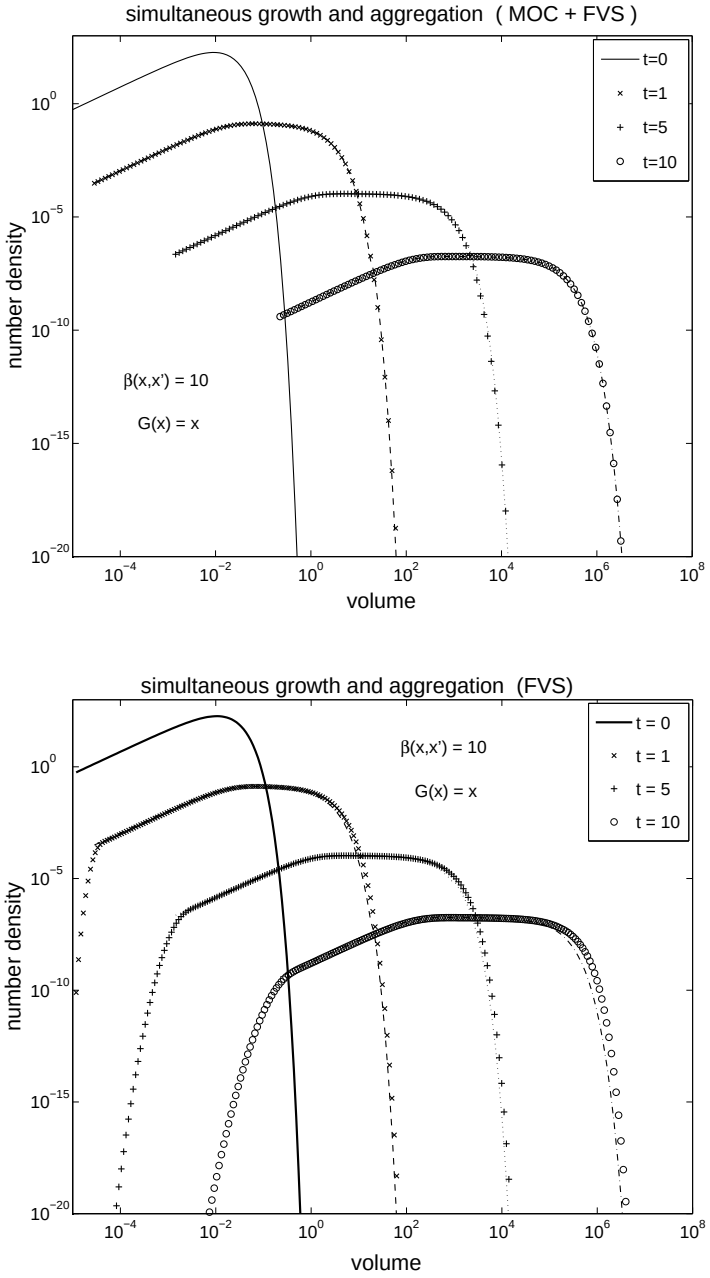

Figure 6.6: Simultaneous growth and aggregation: The comparison of numerical results (symbols) with analytical solutions (lines) for linear growth and constant aggregation (Case 4 of Table 6.1).

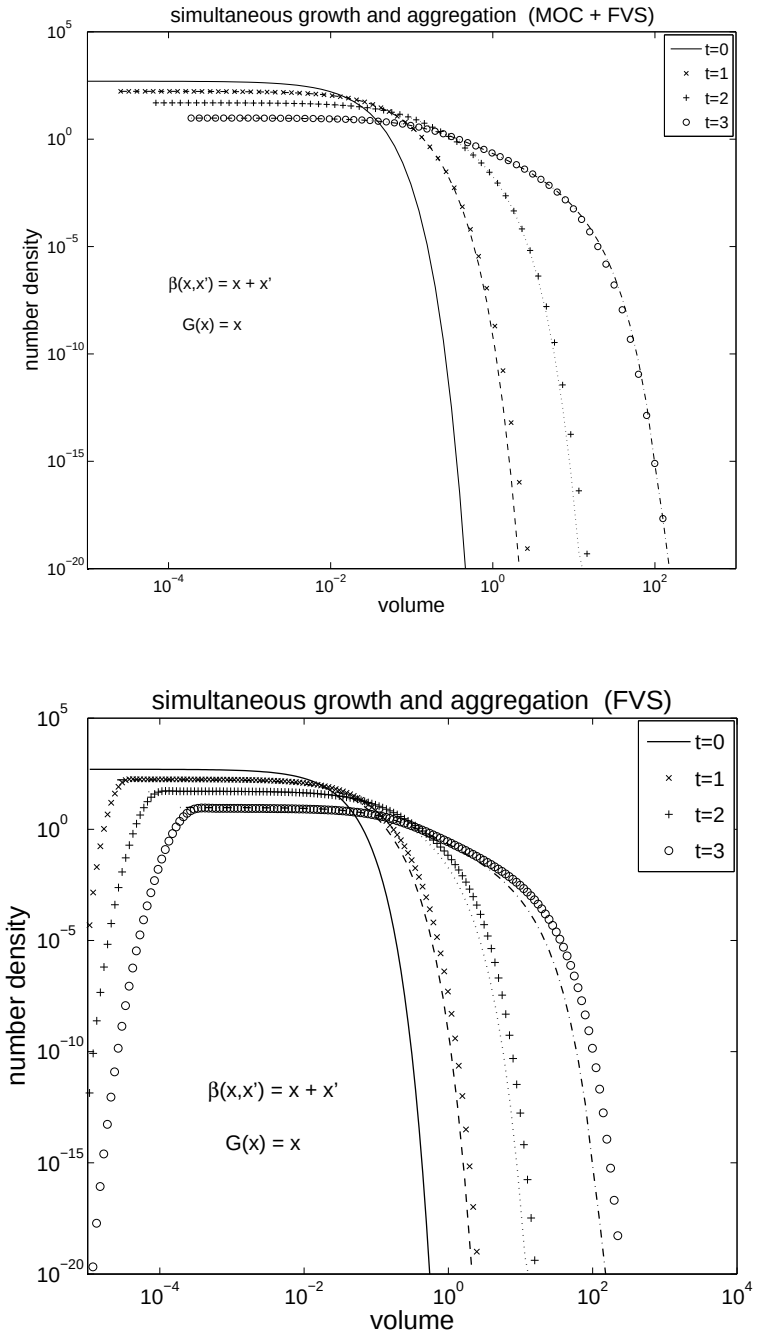

Figure 6.7: Simultaneous growth and aggregation: The comparison of numerical results (symbols) with analytical solutions (lines) for linear growth and sum aggregation (Case 5 of Table 6.1).

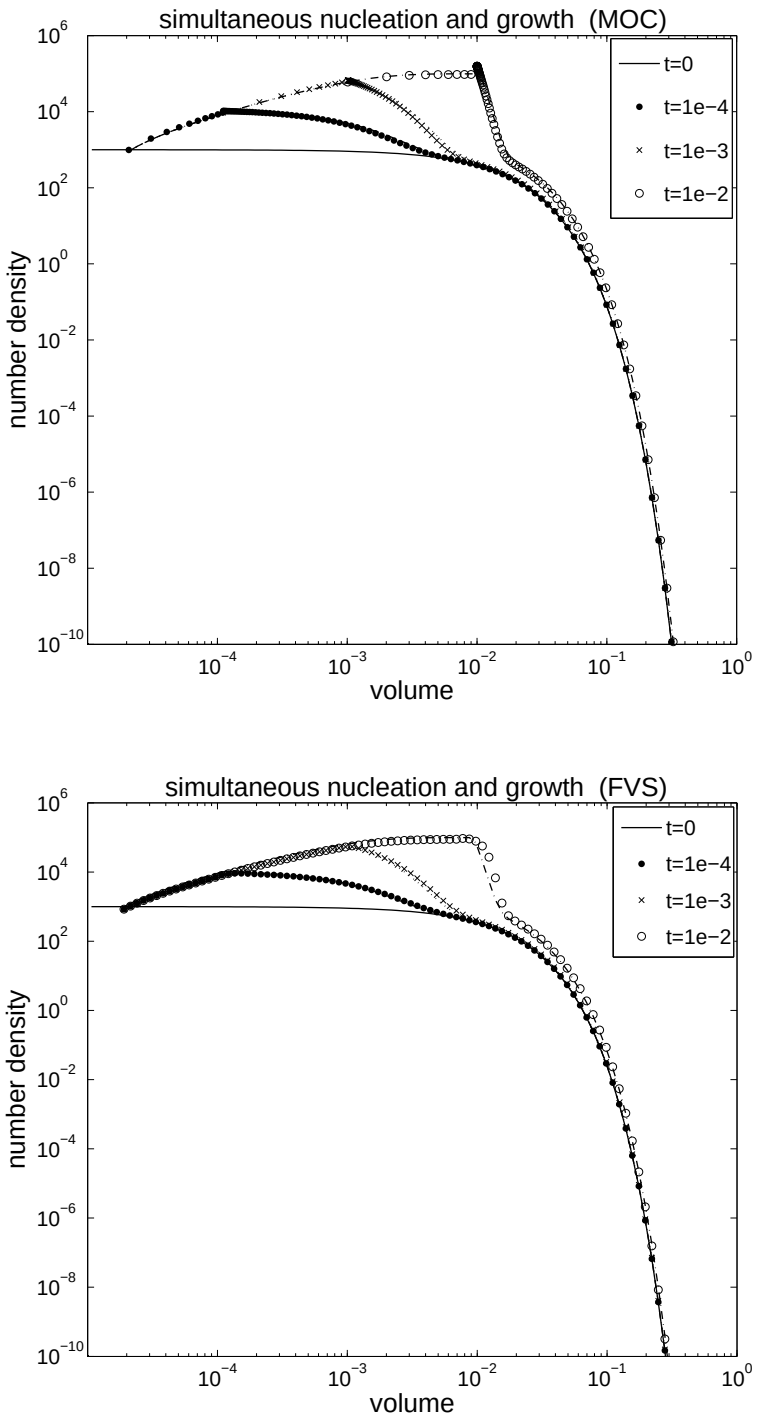

Figure 6.8: Simultaneous nucleation and growth: The comparison of numerical results (symbols) with analytical solutions (lines) for constant growth and exponential nucleation.

case is given as [49]

$$f(t,x) = f_0(x - Gt) + \frac{B_0}{G_0}\left[\exp\left(-\frac{x_{low}}{x_{0,n}}\right) - \exp\left(-\frac{x}{x_{0,n}}\right)\right], \tag{6.34}$$

$$x_{low} = \max(x_1, x - G_0 t)\,. \tag{6.35}$$

Here x_1 represent the center of the first cell in the mesh. Since now nucleation takes place, we have to add a new cell of nuclei size at each time step. In order to keep the number of cells fixed we delete the end cell at the same time level. The numerical results are shown in Figure 6.8. Again the numerical results of both methods are in very good agreement with the analytical solutions. The results of the second method are also excellent with a minor dissipation in the numerical result at $t = 10^{-2}$.

Linear growth and exponential nucleation: Here the initial data and the nucleation term have the same formulation as given in the last example but now $G(x) = G_0 x$. Here we take $G_0 = 1$, $N_0 = 10$, $x_0 = 0.01$, $x_{0,n} = 0.001$, and $B_0 = 10$. The analytical solution for this case is given as [49]

$$f(t,x) = f_0\left(xe^{-G_0 t}\right)\exp(-G_0 t) + \frac{B_0}{G_0 x}\left[\exp\left(-\frac{x_{low}}{x_{0,n}}\right) - \exp\left(-\frac{x}{x_{0,n}}\right)\right],$$

$$x_{low} = \max\left(x_1, xe^{-G_0 t}\right)\,. \tag{6.36}$$

The numerical results are shown in Figure 6.9. The results of the MOC are in excellent agreement with the analytical solution. However, there is visible dissipation in the numerical results of the FVS. From these results one can conclude that MOC become more important when the growth term is not constant.

6.2.4 Simultaneous nucleation, growth and aggregation

Unfortunately, there is no analytical solution available in this case. We consider the constant growth rate $G(x) = G_0$, exponential nucleation rate $\mathcal{Q}^+_{\text{nuc}}(x) = B_0/x_{0,n}\exp\left(-x/x_{0,n}\right)$ and a constant aggregation kernel $\beta(x,x') = \beta_0$. As an initial condition we take the exponential initial distribution of the form $f_0(x) = N_0/x_0\exp\left(-x/x_0\right)$. For numerical simulation we take $G_0 = 1$, $N_0 = 10$, $x_0 = 0.01$, $B_0 = 1$, $x_{0,n} = 0.001$, $\beta_0 = 100$, and 100 mesh points. The numerical results for both methods are compared with each other in Figure 6.10. The second plot in Figure 6.10 represents the results of both methods in the absence of aggregation. The first plot shows that first method resolve the discontinuities very well as compared to the second method. A comparison of both plots, i.e. with and without aggregation, shows that aggregation significantly effects the distribution of particles present initially and those born afterwards. Particularly, the distribution of the nucleated particles, which lie on the left hand side of discontinuity in the size range, is changed completely in the presence of aggregation.
In the second plot since the analytical solutions and MOC solutions were completely overlapping, therefore we omit the analytical solution here. The numerical results of both

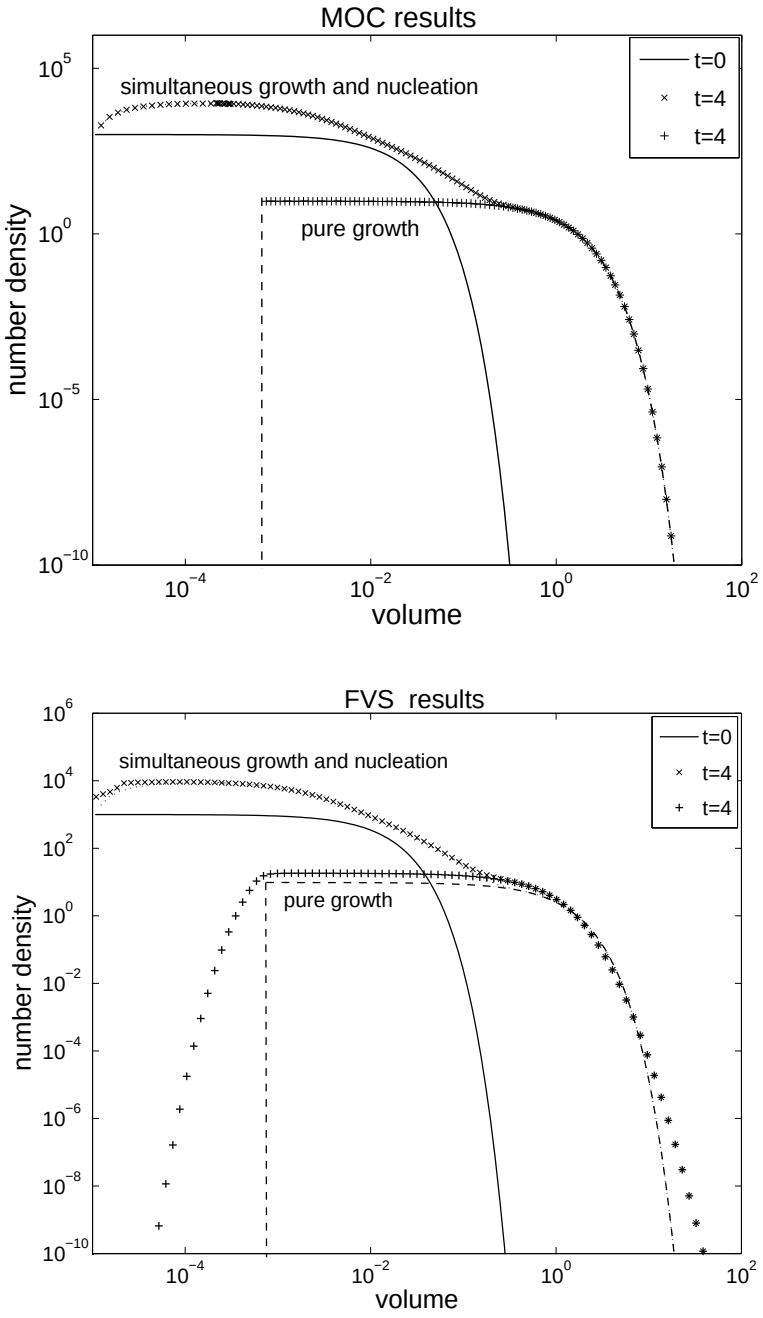

Figure 6.9: Simultaneous nucleation and growth: The comparison of numerical results (symbols) with analytical solutions (lines) for linear growth and exponential nucleation.

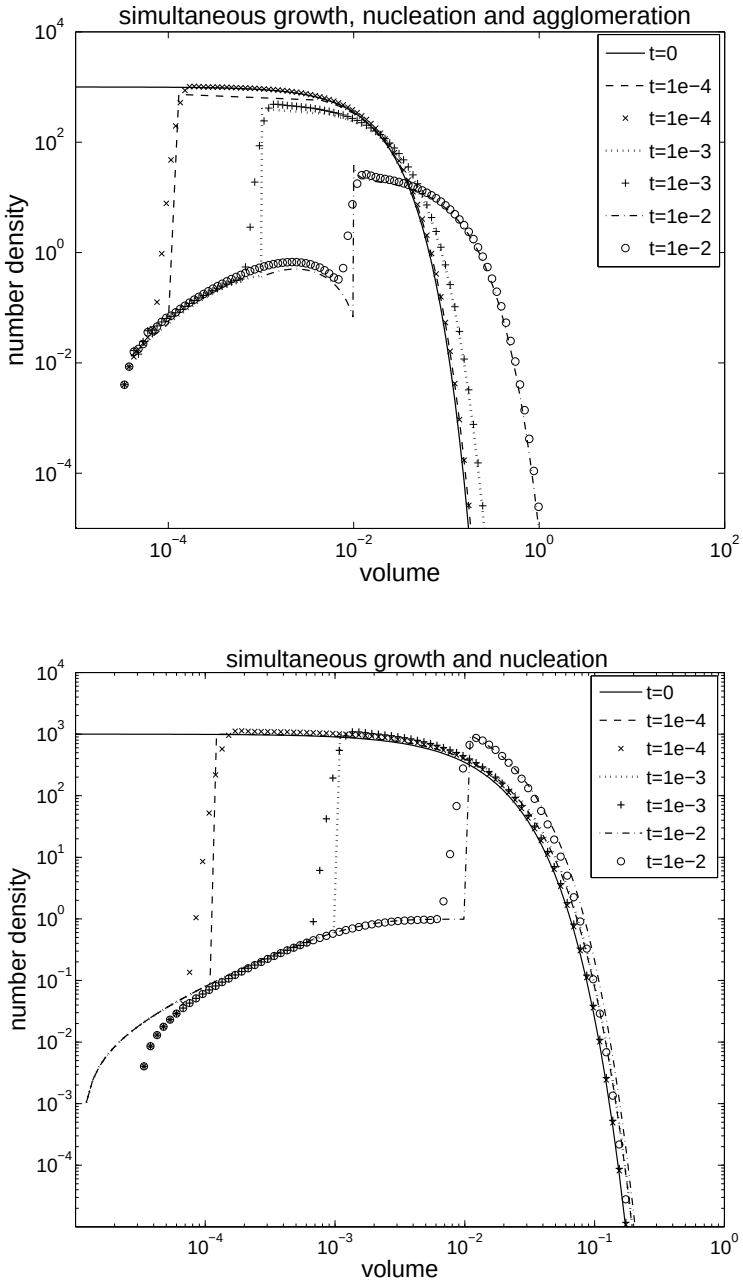

Figure 6.10: Simultaneous nucleation, growth and aggregation: The comparison of FVS and MOC+FVS results with each other and analytical results.

methods are in good agreement with each other. However, the results of the first method are more resolved as compared to the second method where dissipation is visible at the steep discontinuities.

6.2.5 Simultaneous aggregation and breakage

Here, we consider numerical test problems for simultaneous aggregation and breakage processes. The numerical results are compared with the available analytical solutions obtained by Patil and Andrews [82]. Later on these solutions were slightly simplified by Lage [51] to a form which we have used here. The analytical solution are given in the Appendix B.2. These analytical solutions were derived for a special case where the number of particles stays constant. They considered a uniform binary breakage $b(x, x') = 2/x'$, linear selection function $S(x) = S_0\, x$, and constant aggregation kernel $\beta(x, x') = \beta_0$. The two types of initial conditions which they considered are given by (B.9) and (B.11).

Apart from conservation of mass these problems have the spatial property that both aggregation and breakage processes have to conserve total number as well. Further, the solution of (B.9) is stationary.

A geometric grid discretization has been used for this problem with $q = 3$ and $N = 60$. The final simulation time is $t = 6$. Figures 6.11 and 6.12 show the numerical results at both log-log and semi-log scales. The results of the finite volume scheme are in agreement with analytical solutions. However a small under prediction is present in the solution at smaller volume range. We have observed that this under prediction is not increasing if we increase the simulation time. Secondly the under prediction is almost the same for both types initial conditions. In contrast, the fixed pivot technique gives over predicting solution in smaller volume range for this problem [44]. However, the cell averaged technique [44] which is an improved version of the fixed pivot technique gives good results for this problem.

6.2.6 Simultaneous aggregation and nucleation

In this case we test our algorithm for simultaneous nucleation and aggregation problem. As a simple case we take zero initial distribution with constant aggregation and mono-dispersed nucleation. Normally,such systems with zero initial population leads to oscillation in the particle size distribution. However, numerical results show that the finite volume scheme gives oscillations free results. The analytical solutions for the first two moments are reported by Alexopoulos and Kiparissides [3] and are given in Appendix B.3. We take the aggregation kernel $\beta = \beta_0 = 1.0$, and the nucleation term $Q^+_{\text{nuc}} = B_0\delta(x - x_1)$, where $B_0 = 1$ and x_1 represents the first cell of discretized domain. In the analytical solutions we consider $N_0 = 1$. The volume domain is discretized into 45 cells with minimum particle size $x_{\min} = 10^{-6}$.

Numerical results are shown in Figure 6.13. The first plot gives the comparison of analytical and numerical solutions for the first two moments. The numerical results are in good agreement with the analytical solutions. The moments plot shows that after certain time, the total number of particles in the system is invariant. A dynamic equilibrium with total number has been reached at that time. This means that particles nucleation rate becomes

equal to the total particles aggregation rate. On the other hand the total mass increases linearly with process time. Unfortunately there is no analytical solution for the number density distribution. The second plot shows the number density plots of the finite volume scheme at different times. A complicated but symmetric behavior of the results can be observed and are free from oscillations.

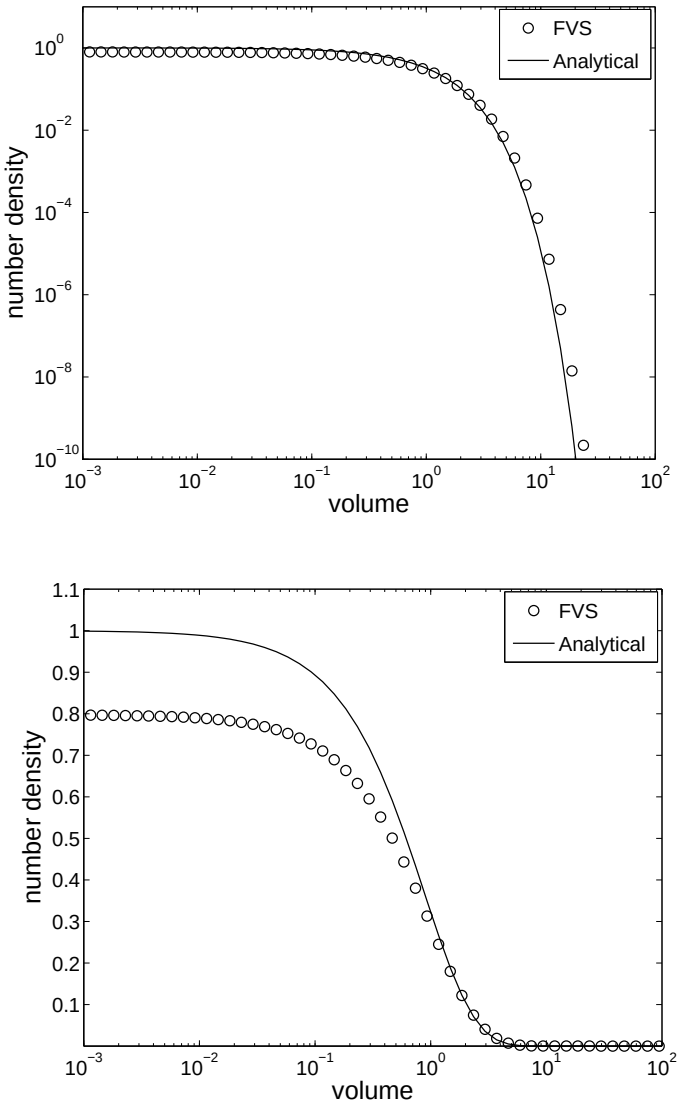

Figure 6.11: Simultaneous aggregation and breakage: Numerical results for the initial conditions (B.9) at $t = 6$.

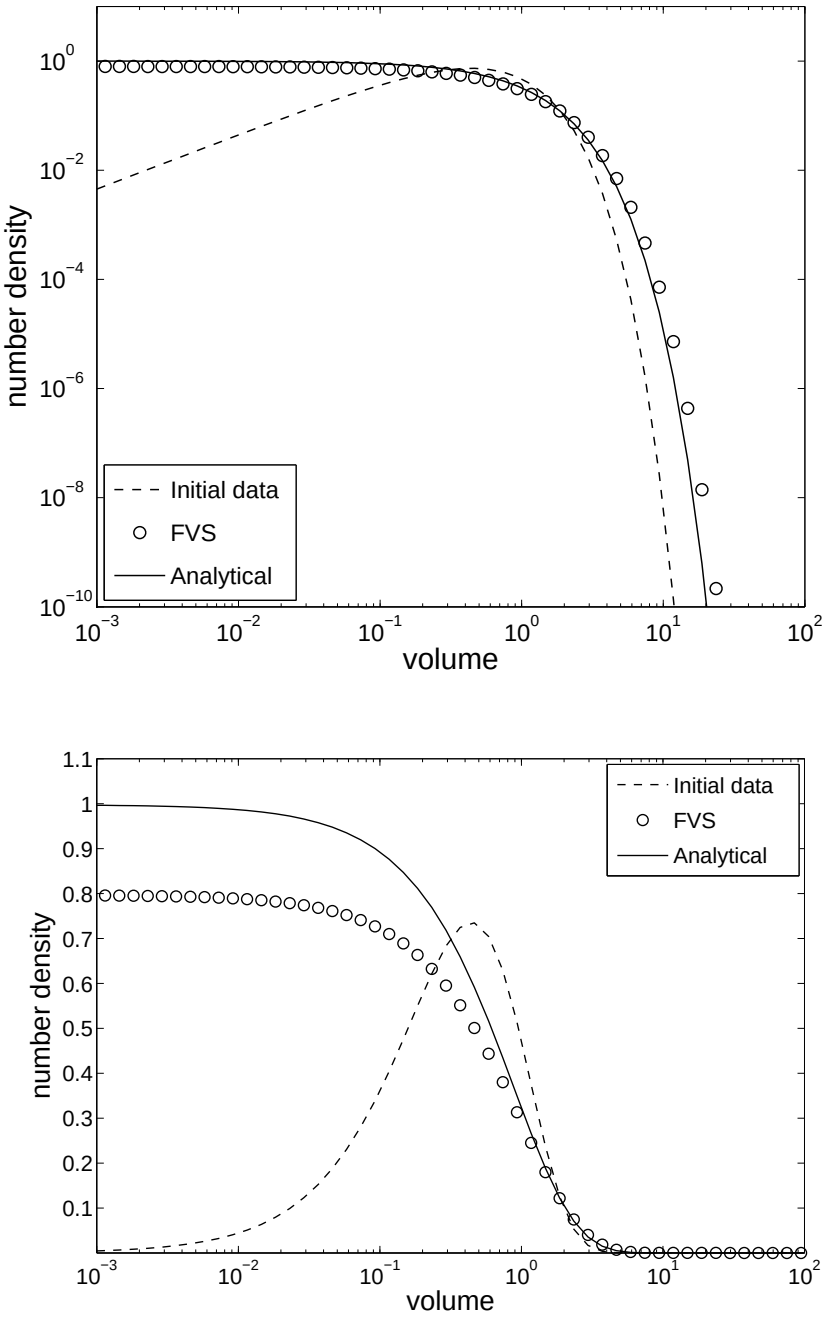

Figure 6.12: Simultaneous aggregation and breakage: Numerical results for the initial conditions (B.11) at $t = 6$.

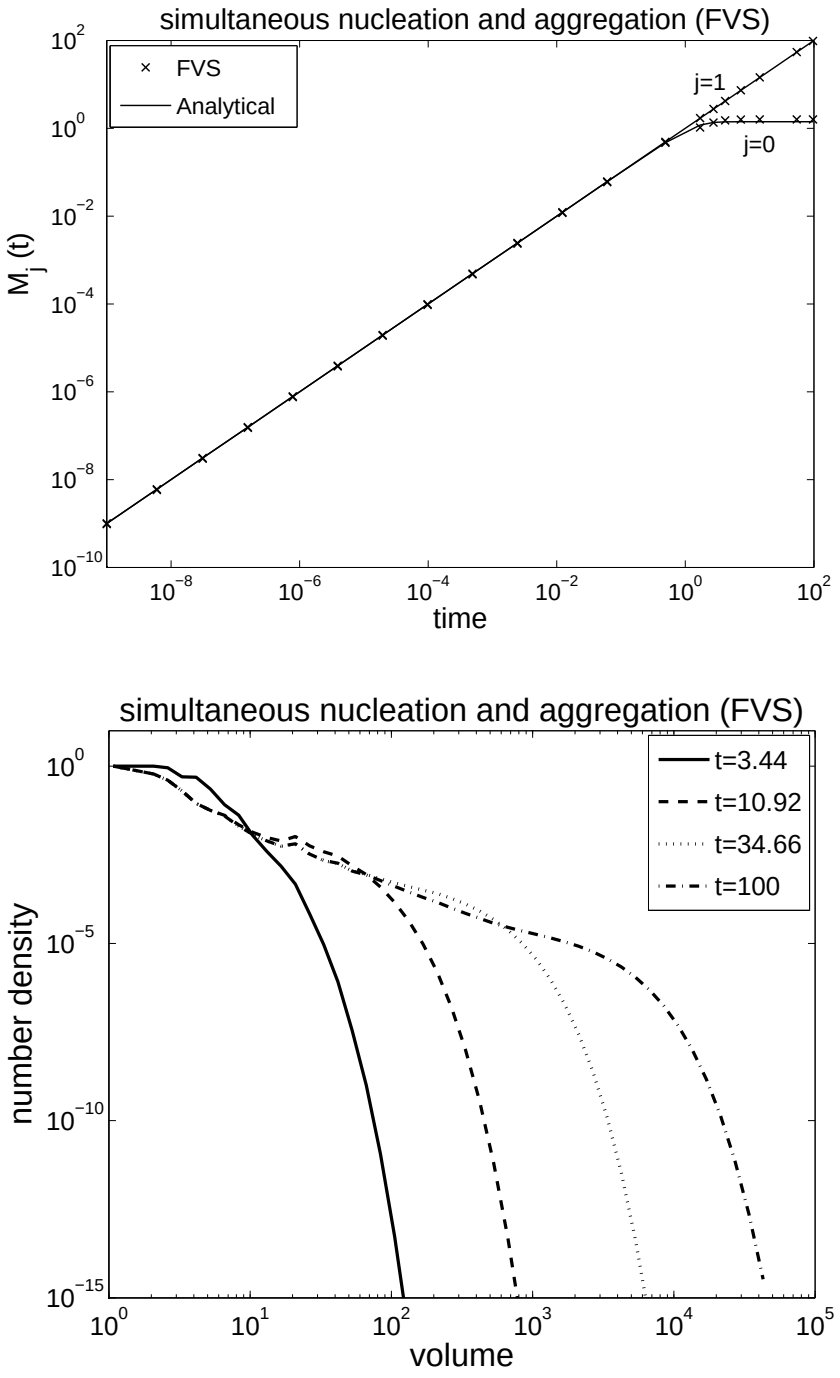

Figure 6.13: Simultaneous aggregation and nucleation: Numerical results at $N = 45$.

6.2.7 All processes simultaneously

This problem was considered by Lim et al. [61]. Suppose that the stiff nucleation takes place at a minimum particle size ($x_0 = 0$) as a function of time

$$f(t,0) = 100 + 10^6 \exp(-10^4 (t - 0.215)^2)\,. \tag{6.37}$$

Hence, we consider the PBE (6.1) with nucleation as a left boundary condition. The particle size and time ranges are $0 \le x \le 2.0$ and $0 \le t \le 0.5$, respectively. The square step initial condition for the number density is given as

$$f(0,x) = \begin{cases} 100 & \text{for } 0.4 \le x \le 0.6\,, \\ 0.01 & \text{elsewhere}\,. \end{cases} \tag{6.38}$$

Here we consider constant growth rate with $G = 1.0$. The analytical solution for only growth and nucleation is given as [61]

$$f(t,x) = \begin{cases} 100 + 10^6 \exp(-10^4((Gt - x) - 0.215)^2) \text{ for } 0.0 \le x \le Gt\ , \\ 100 \qquad\qquad\qquad\qquad \text{for } 0.4 \le x - Gt \le 0.6\,, \\ 0.01 \qquad\qquad\qquad\qquad \text{elsewhere}\,. \end{cases} \tag{6.39}$$

In this solution, a square step discontinuous shock and a narrow wave which is originated from nucleation move along the propagation path-line, $x = x_0 + Gt$. The numerical test is carried out on 200 grid points. The kinetic parameters from aggregation and breakage are $\beta = 1.5 \cdot 10^{-5}$, $b(t,x,x') = \frac{2}{x'}$ and $S(x) = x^2$.

Figure 6.14, which is obtained from method 1 (MOC+FVM), depicts the effects of the growth, nucleation, aggregation, and breakage terms on the particle size distribution (PSD). The solid line is the analytical solution for pure growth and nucleation problem but without aggregation and breakage. The numerical results of MOC for pure growth and nucleation are overlapping with the the analytical solution as shown in Figure 6.14. The stiff nucleation at the left boundary, produces a sharp peak. The aggregation term causes peaks of the PSD to be smeared and increases the population of large size particles. In contrast, the breakage term increases the population of small size particles. Therefore, the PSD of the PBE with the four kinetics is dispersed more broadly. Similar results which are obtained from the pure finite volume schemes are given in Figure 6.15. In comparison to method 1, more numerical diffusion is visible in the steep gradients of the solutions. However, the high resolution scheme still resolves all the profiles of the solution quite well.

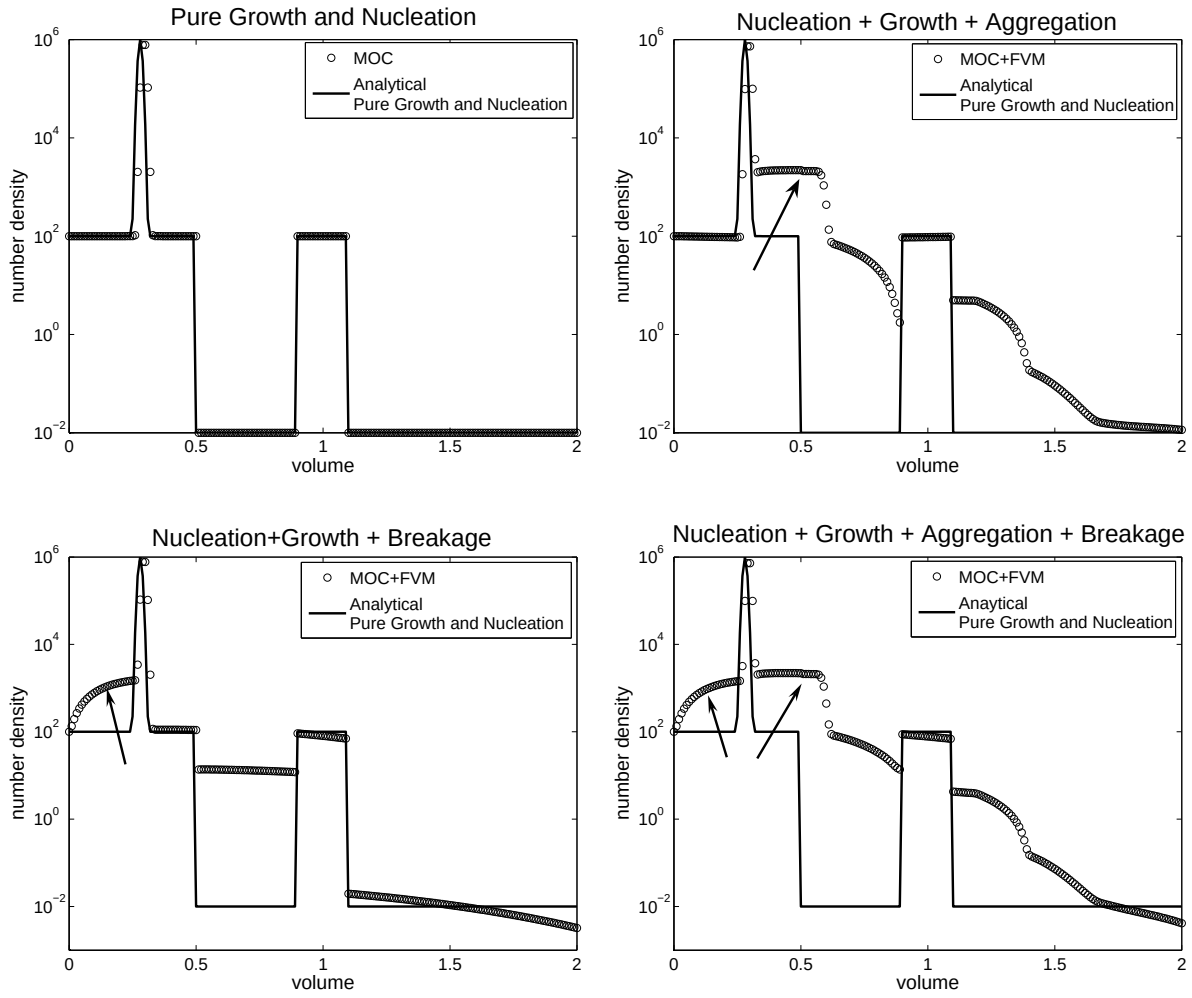

Figure 6.14: All processes: Results of Method 1 (MOC+FVM) at $t = 0.5$ and $N = 200$ mesh points.

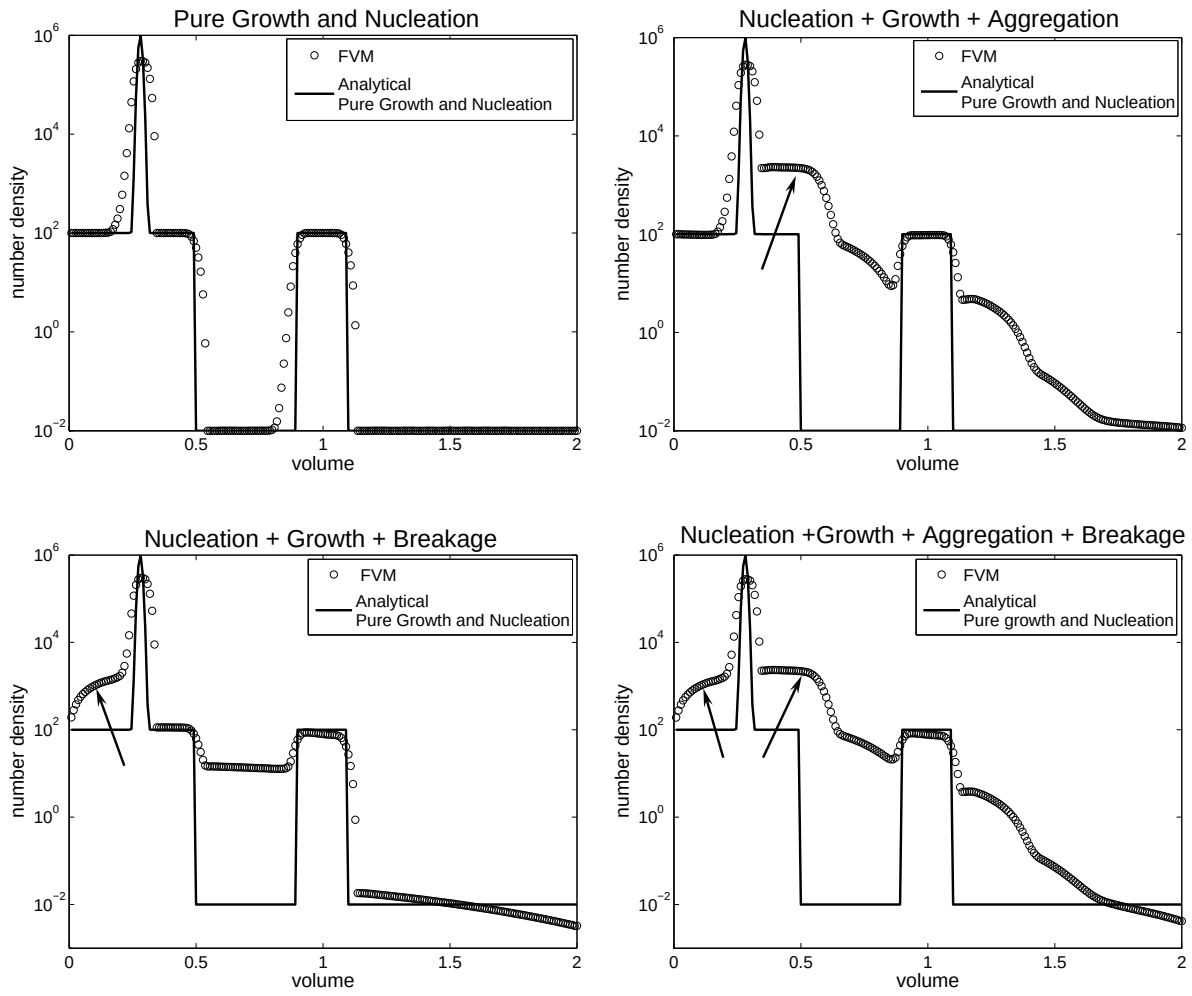

Figure 6.15: All processes: Results of Method 1 (MOC+FVM) at $t = 0.5$ and $N = 200$ mesh points.

Chapter 7

Conclusions

7.1 Outlook

In this thesis, we studied several population balance models. The numerical approximations and modeling of population balances for the simulation of different particulate processes occurring in process engineering were the main focus points of this work. Semi-discrete high resolution finite volume schemes [40, 57, 58] and the method of characteristics (MOC) [49, 61] are proposed for the numerical solutions of the resulting models. In this study nucleation, growth, aggregation and breakage processes are considered. For the one-dimensional batch crystallization model we also studied the local existence and uniqueness of the solution. With the help of inverse Laplace transformation, we have derived a new method which can be used to solve the given Batch crystallization model. The resulting method was found to be more efficient and accurate. However, this method is restricted to size independent growth processes.

The semi-discrete high resolution schemes are proposed for the numerical approximations of one and two-dimensional batch crystallization processes where nucleation and growth phenomena are considered while neglecting the aggregation and breakage. Having semi-discrete formulation, the schemes are discrete in property coordinates while continuous in time. The resulting ordinary differential equations can be solved by any standard ODE solver. In this work an adaptive RK45 method is used, which is an embedded Runge-Kutta method of order four and five. We also studied the issue of positivity (monotonicity), consistency, stability and convergence of the proposed schemes.

To improve the numerical accuracy further the high resolution schemes can be easily combined with an adaptive mesh refinement technique. For solving multidimensional PBEs, development of effective and robust adaptive grid methods becomes necessary because uniform grids can be very expensive and may result in loss of accuracy. The resulting numerical solutions may be far away from the real physical phenomena. Successful implementation of the adaptive grid strategy can increase the accuracy of the numerical approximations

and can also decrease the overall computational cost. In this dissertation a moving mesh technique of H. Tang and T. Tang [114] is considered for both one and two-dimensional PBEs which model batch crystallization processes. The current moving mesh technique is independent of the numerical scheme, hence can be applied to any numerical scheme.

The numerical test problems show clear advantages of the current finite volume schemes. The results of the schemes are highly resolved and free from numerical dispersion. The current moving mesh technique has further improved the numerical results. The high resolution schemes with the current moving mesh technique need approximately half of the mesh points to achieve the same accuracy in comparison to the same schemes without moving mesh technique. The schemes are simple, easy to implement, and computationally efficient. The overall computational cost of the schemes was further reduced by using moving mesh technique.

In the present work, a model is derived for batch preferential crystallization of enantiomers with fines dissolution unit. The model is further elaborated by considering the isothermal and non-isothermal conditions. In this model, the crystallization of the preferred enantiomers is assumed to take place in a single crystallizer with a fines dissolution loop. The extracted solution is screened by filters and assumed to be free of larger crystals. Therefore, only small particles are withdrawn to the fines dissolution loop. In order to assure a crystal-free liquid exchange, the withdrawn liquid in the fines dissolution loop is heated, so that the liquid becomes undersaturated and the withdrawn small particles dissolve. Before re-entering into the crystallizer, this liquid is assumed to be cooled down again. The attrition, breakage and agglomeration processes are not considered in this study. The model is further extended for a coupled batch preferential crystallization process with isothermal and non-isothermal conditions. In this setup, the crystallization of the two enantiomers is assumed to take place in two separate crystallizers, coupled by their fines dissolution loops. There are two main advantages of considering two coupled crystallizers which are interconnected by two fines dissolution units. The first one is that one gets both enantiomers at the same time in separate crystallizers. Secondly, because of the fines dissolution, the amount of small particles reduces which further enhances the particle growth. Both high resolution schemes and the method of characteristics are implemented for solving the models under consideration. These methods are used for the first time to model such processes. The numerical test problems show clear advantages of our proposed numerical schemes. The method of characteristics was found to be computationally efficient and highly resolved as compared to the finite volume schemes. However, the finite volume schemes still give very accurate results and the computational time is still less.

In this dissertation we have also extended the conservative finite volume scheme for the one-component pure aggregation [23] to two component aggregation problem. For this purpose the integro-ordinary differential equation for two-component aggregation process is reformulated to a partial differential equation (PDE) coupled with an integral equation. The resulting PDE was then solved by a semi-discrete finite volume scheme which also em-

ploys the geometric grid discretization technique [33, 31, 34]. The current extended finite volume scheme for two-component aggregation uses the basic ideas of the finite volume scheme for one-component aggregation derived in [23]. Therefore, for reader convenience the finite-volume scheme for the one-component aggregation is also presented with a slight modification as compared to that in [23]. Even though the scheme in [23] is derived for an arbitrary grid, the authors have used a uniform grid in their numerical test problems. Here, we have given further numerical test problems which were solved on geometric grids. Moreover, we also studied the stability of the proposed scheme for the one-component aggregation problem. In this case again a reformulated PBE was solved with a finite volume scheme. The use of geometric grid and semi-discrete formulation makes the current finite volume scheme comparable to those schemes which were specifically derived for aggregation problems. Instead of the number density the current scheme uses the volume (mass) density as unknown, which makes the scheme very suitable for the simulation of aggregation process. In aggregation process volume (mass) is conserved, which is guaranteed by the conservative finite volume formulation of the current scheme with volume (mass) density as conservative variable. The comparison of the finite volume scheme results for the one- and two-component aggregation processes with those polished in [46, 47] and [118] show that current schemes performed very well in both cases. In most of the test problems, it was found that current schemes gives better accuracy and especially volume (mass) is perfectly conserved. The current finite-volume schemes for both one and two-component aggregation processes are second order accurate in property coordinates and time if at least second order accurate ODE solver is used for the resulting system of ODEs. In the case of one-component aggregation, the CPU time for the current scheme is almost similar to the schemes in [46, 47]. However, in two-component aggregation the CPU time for the current finite volume scheme is about two times more than the CPU time of the scheme in [118]. The reason for this extra computational time are the extra summation terms appearing in advection part of the scheme. However, one can reduce the computation cost by paying more attention to the way these integral terms are programmed. The implementation of the scheme is simple, the main part which need more attention are the integrals appearing in the aggregation term. The scheme is explicit and new values at each time step are calculated from the values at previous time step. Similar to the one-component aggregation, we have also reformulated the PBE for the pure one-component breakage process. The resulting reformulated PBE for breakage process was then solved with the same finite volume scheme. Finally, we have analyzed stability and convergence of the proposed numerical scheme for the one-component breakage problem. From the above discussion it is clear that, the application of the finite volumes to aggregation and breakage problems prove their generality, flexibility, efficiency, and applicability as reliable schemes.

The proposed numerical schemes are further investigated by solving population balance equations with simultaneous nucleation, growth, aggregation and breakage processes. For that purpose once again a reformulated PBE is used where numerical methods calculate the volume (mass) density instead of the number density. However, as stated above one can easily recover the discrete values of the number density at the end of the simulation. Two

methods are proposed for this purpose. In the first method, the method of characteristics (MOC) is used for growth process [49] while a finite volume scheme for aggregation and breakage processes [23, 44]. In the second method, semi-discrete finite volume schemes (FVS) are used for all processes. Note that, in both methods the aggregation and breakage kinetics are solved with the same finite volume formulations. Various combinations of nucleation, growth, aggregation and breakage processes for different choices of nucleation, growth, aggregation and breakage rates are considered. A geometric grid discretization technique has been used in all test problems presented here. However, one can also use regular grid if needed. The main difference in both methods is the way they calculate the growth term, for example in the MOC the mesh is moved with the characteristic speed, whereby the linear advection is treated exactly. However, the second method uses a finite volume scheme to discretize the advection term. The efficiency and accuracy of the resultant methods are analyzed by comparing their numerical results with each other and with available analytical solutions. For handling nucleation term in the first scheme, the MOC is combined with a procedure of adding a cell of nuclei size at each time level. The same procedure was also used in [49]. A standard ODE solver can be used to solve the resultant ODEs. There are two main differences between the first method and the one used in [49]. In the current method aggregation and breakage terms are treated with a finite volume scheme, while in [49] the authors have used the fixed pivot technique for this purpose. Secondly, our numerical method uses a reformulated PBE instead of the original one. This reformulation is necessary in order to apply the finite volume schemes effectively. The numerical results show that both methods are very successful for the the simulation of simultaneous processes. Especially, the combination of FVS and MOC was found to be more successful with less computational cost and better accuracy instead of using purely finite volume scheme for all processes.

7.2 Future Recommendations

This work has a lot of potential for future extensions which are outlined below.

The proposed finite volume schemes and the method of characteristics should also be analyzed for the simulation of more general PBEs modeling different phenomena, such as batch and continuous crystallization processes. The latter is used for the production of large amount of bulk commodity chemicals. Especially, it will be more interesting to analyze the schemes for coupled PBEs with computational fluid dynamics (CFD). In this case the models become more complicated and the solutions have strong discontinuities. In such applications high resolution schemes will be good candidates as the application of the MOC alone may not be possible due its several limitations. For example in the case of CFD model, the flux terms can be non-linear functions of conservative variables which are in turn function of time and external coordinates. Hence, the MOC will be not applicable to the CFD models. However, one may use the MOC for the internal property variables

and the finite volume schemes for the external coordinates. Furthermore, the MOC is already adaptive due its built in moving mesh procedure and high resolution schemes can be easily combined with an adaptive mesh refinement procedure which are more important in PBE-CFD applications. The use of adaptive mesh refinement will not only reduce the numerical errors in the solutions but also the overall computational time.

In the current study of the preferential crystallization a model system of amino acid-H_2O was considered for our computational study. In this model no significant interdependence between the preferred- and counter-enantiomer on crystallization kinetics has been observed. The same was also experimentally observed by the process engineering group of Max-Planck Institute Magdeburg. However, in their experiments for mandelic acid-H_2O model system they observed a strong influence of the counter-enantiomer on the growth rate of the preferred-enantiomer, see [63] for further details. Moreover, it can be shown that in the latter case the counter-enantiomer may even change growth rates of particular crystal faces which results in different crystal shapes, see Figure 7.1. Hence, a detailed study on the influence of the counter-enantiomer on the growth rate and morphology of the seeded enantiomer is required. To model such processes and to study the different evolution of crystal faces a multidimensional population balance model has to be derived along with correct growth and nucleation rate kinetics whose results matches with the experimental results. This in turn also leads inevitably to a higher requirement of the efficient numerical discretization techniques. Currently, work is in progress on the mathematical derivation of the multidimensional population and mass balance models for the numerical simulation of this process.

The work for simultaneous processes can be further extended for the simulation of two-component problems involving nucleation growth, aggregation and breakage processes. The use of only finite volume scheme may be somehow expensive, especially on the regular grid. In this case one may need a refined mesh, even with a simple growth function, in order to avoid the numerical diffusion. However, with the use of regular refined mesh the calculation of the aggregation and breakage terms may be very expensive. Alternatively, one may use the adaptive mesh refinement technique instead of a regular grid which will considerably reduce the overall computational cost for the same desired accuracy. The scheme can become faster further if the methods of characteristics (MOC) is used for the growth term and finite volume scheme for the aggregation and breakage terms.

The aggregation and breakage problems can be analyzed mathematically. With the mathematical analysis one may find a more sophisticated procedure for the approximation of the integral terms. As pointed above, they pose a considerable numerical difficulties in the simulation of multidimensional PBEs. Therefore, they need attention and mathematical investigation.

Furthermore, one can use the proposed numerical methods for the study and design of control strategies in crystallization processes. In this direction it will be more interesting

to concentrate on the less restrictive models of crystallization processes and derive control strategies for both batch and continuous crystallizers.

Finally, one can implement the proposed schemes for other particulate processes, namely precipitation, polymerization, food processes, pollutant formation in flames, size distribution (PSD) of crushed material and rain drops, and growth of microbial and cell populations.

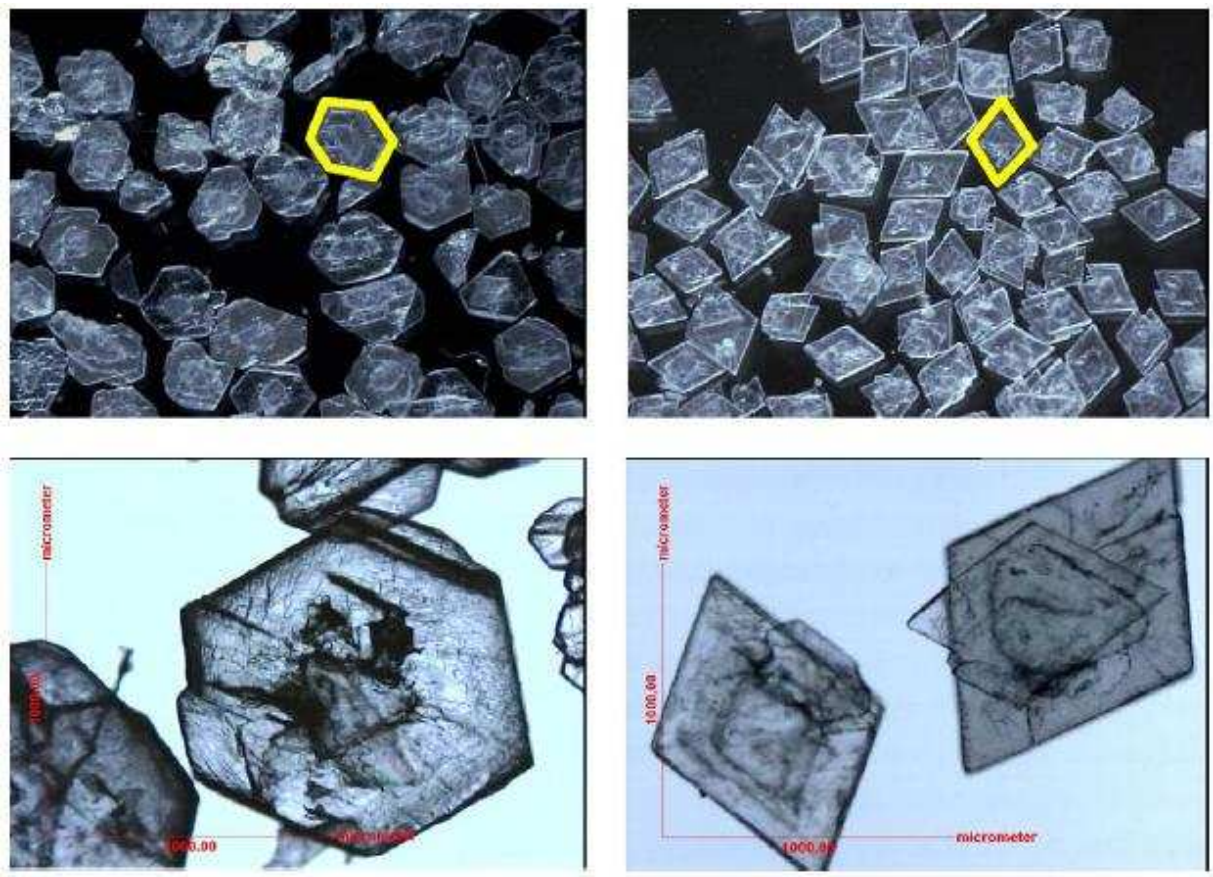

Figure 7.1: Illustration of the fact that crystal shape can depend on the enantiomeric composition in the solution. Results of isothermal (30 °C) seeded growth experiments with mandelic acid in water. Left:without counter enantiomer; Right: with counter-enantiomer (this figure is taken from [63, 83]).

Appendix A

Mathematical Derivations

A.1 Equivalence of Equation (2.5) with (2.8)

In this section we want to show that equations (2.5) and (2.7) are equivalent with (2.8) and (2.9). For this purpose, we start with equations (2.8) and (2.9) and derive back equations (2.5) and (2.7). By using (2.9) in (2.8) and taking the x-derivatives of $\tilde{\mathcal{F}}_{\text{agg}} := \tilde{\mathcal{F}}_{\text{agg}}(t,x)$, we obtain through product rule

$$\begin{aligned} x\frac{\partial f}{\partial t} &= -\frac{\partial \tilde{\mathcal{F}}_{\text{agg}}}{\partial x} = -\frac{\partial}{\partial x}\left(\int_0^x \int_{x-u}^{\infty} u\,\beta(t,u,v)\,f(t,u)\,f(t,v)\,dvdu\right) \\ &= -\int_0^{\infty} x\,\beta(t,x,v)\,f(t,x)\,f(t,v)\,dv + \int_0^x u\,\beta(t,u,x-u)\,f(t,u)\,f(t,x-u)\,du\,. \end{aligned} \tag{A.1}$$

Due to the symmetry of the kernel function, we have

$$\beta(t,x,x') = \beta(t,x',x)\,. \tag{A.2}$$

By changing the integration variables, i.e. $x-u=w$, the second integral of (A.1) gives

$$\int_0^x u\,\beta(t,u,x-u)\,f(t,u)\,f(t,x-u)\,du = \int_0^x (x-w)\,\beta(t,x-w,w)\,f(t,x-w)\,f(t,w)\,dw \tag{A.3}$$

which implies

$$\int_0^x u\,\beta(t,u,x-u)\,f(t,u)\,f(t,x-u)\,du = \frac{1}{2}\int_0^x x\,\beta(t,x-u,u)\,f(t,x-u)\,f(t,u)\,du\,. \tag{A.4}$$

By replacing the second integral in (A.1) by (A.4) and after canceling the term x on both sides of the equality, we get

$$\frac{\partial f}{\partial t} = \frac{1}{2}\int_0^x \beta(t, x-x', x')\, f(t, x-x')\, f(t, x')\, dx' - \int_0^\infty \beta(t, x, x')\, f(t, x)\, f(t, x')\, dx' \quad \text{(A.5)}$$

which comes out to be the same as given by equations (2.5) and (2.7). One can reverse these steps. This gives the equivalence.

A.2 Length Based Aggregation and Breakage Terms

In what follows, the birth and death terms of the length based aggregation and breakage (see equations (2.27) and (2.28)) are rigorously derived. These derivations are taken from [13]. First of all it is important to emphasize that the volume-based and length-based kernels are related as

$$S(x) = S(l^3) = S'(l)\,, \quad \text{and} \quad \beta(t, x, x') = \beta(t, l^3, l'^3) = \beta'(t, l, l')\,. \quad \text{(A.6)}$$

$$\mathcal{B}_{\text{agg}}(t, x) = \frac{1}{2}\int_0^x \beta(t, x-x', x')\, f(t, x-x')\, f(t, x')\, dx' \quad \text{(A.7)}$$

$$\Rightarrow\ \mathcal{B}_{\text{agg}}(t, l^3) = \frac{1}{2}\int_0^l \beta'(t, (l^3-l'^3)^{\frac{1}{3}}, l')\, f(t, l^3-l'^3)\, f(t, l'^3)\, 3l'^2\, dl' \quad \text{(A.8)}$$

$$= \frac{1}{2}\int_0^l \beta'(t, (l^3-l'^3)^{\frac{1}{3}}, l')\, \frac{3(l^3-l'^3)^{\frac{2}{3}}}{3(l^3-l'^3)^{\frac{2}{3}}}\, f(t, l^3-l'^3)\, n(t, l')\, dl' \quad \text{(A.9)}$$

$$= \frac{1}{2}\int_0^l \beta'(t, (l^3-l'^3)^{\frac{1}{3}}, l')\, \frac{n(t, (l^3-l'^3)^{\frac{1}{3}})}{3(l^3-l'^3)^{\frac{2}{3}}}\, n(t, l')\, dl' \quad \text{(A.10)}$$

and thus using $\mathcal{B}'_{\text{agg}}(t, l) = 3l^2\, \mathcal{B}_{\text{agg}}(t, l^3)$ we find that

$$\mathcal{B}'_{\text{agg}}(t, l) = \frac{l^2}{2}\int_0^l \beta'(t, (l^3-l'^3)^{\frac{1}{3}}, l')\, \frac{n(t, (l^3-l'^3)^{\frac{1}{3}})}{(l^3-l'^3)^{\frac{2}{3}}}\, n(t, l')\, dl'\,. \quad \text{(A.11)}$$

The death rate due to aggregation is given by

$$\mathcal{D}_{\text{agg}}(t,x) = \int_0^\infty \beta(t,x,x')\, f(t,x)\, f(t,x')\, dx' \tag{A.12}$$

$$\Rightarrow\ \mathcal{D}_{\text{agg}}(t,l^3) = \int_0^\infty \beta(t,l^3,l'^3)\, f(t,l^3)\, f(t,l'^3)\, 3l'^2\, dl' \tag{A.13}$$

$$= \int_0^\infty \beta'(t,l,l')\, f(t,l^3)\, n(t,l')\, dl' \tag{A.14}$$

$$\tag{A.15}$$

and thus using $\mathcal{D}'_{\text{agg}}(t,l) = 3l^2\, \mathcal{D}_{\text{agg}}(t,l^3)$ we find that

$$\mathcal{D}'_{\text{agg}}(t,l) = \int_0^\infty \beta'(t,l,l')\, n(t,l)\, n(t,l')\, dl'\,. \tag{A.16}$$

Hence

$$\mathcal{K}^{\pm}_{\text{agg}} = \mathcal{B}'_{\text{agg}}(t,l) - \mathcal{D}'_{\text{agg}}(t,l) \tag{A.17}$$

$$= \frac{l^2}{2} \int_0^l \frac{\beta'(t,(l^3-l'^3)^{\frac{1}{3}},l')}{(l^3-l'^3)^{\frac{2}{3}}}\, n(t,(l^3-l'^3)^{\frac{1}{3}})\, n(t,l')\, dl' - \int_0^\infty \beta'(t,l,l')\, n(t,l)\, n(t,l')\, dl'$$

which comes out to the same equation as given by (2.27).

The breakage term is given by

$$\mathcal{Q}^{\pm}_{\text{break}}(t,x) = \int_x^\infty b(t,x,x')\, S(x')\, f(t,x')\, dx' - S(x)\, f(t,x) \tag{A.18}$$

$$\Rightarrow\ \mathcal{Q}^{\pm}_{\text{break}}(t,l^3) = \int_l^\infty b(t,l^3,l'^3)\, S(l'^3)\, f(t,l'^3)\, 3l'^3\, dl' - S(l^3)\, f(t,l^3) \tag{A.19}$$

$$\Rightarrow\ 3l^2\, \mathcal{Q}^{\pm}_{\text{break}}(t,l^3) = 3l^2 \int_l^\infty b(t,l^3,l'^3)\, S(l')\, n(t,l')\, dl' - 3l^2\, S(l)\, f(t,l^3)\,. \tag{A.20}$$

Due to equation (2.30) we have $b'(t,l,l') = 3l^2\, b(t,l^3,l'^3)$, hence

$$\mathcal{K}^{\pm}_{\text{break}}(t,l) = 3l^2\, \mathcal{Q}^{\pm}_{\text{break}}(t,l^3) = \int_l^\infty b'(t,l,l')\, S(l')\, n(t,l')\, dl' - S(l)\, n(t,l) \tag{A.21}$$

which is the same as given by (2.28).

A.3 To Verify the Left Hand Side Relations in (2.36)

In this section we want to prove the relations given (2.36). By taking the l-derivatives of $\mathcal{F}_{\rm agg}(t,x)$ in (2.34), one gets by using the product rule

$$\begin{aligned}
\frac{\partial \tilde{\mathcal{F}}'_{\rm agg}(t,l)}{\partial l} =& \frac{\partial}{\partial l}\left(\int_0^l \int_{(l^3-u^3)^{\frac{1}{3}}}^{\infty} u^3\,\beta'(t,u,v)\,n(t,u)\,n(t,v)\,dvdu\right)\\
=& \int_0^{\infty} l^3\,\beta'(t,l,v)\,n(t,l)\,n(t,v)\,dv\\
&- \int_0^l u^3\,\beta'(t,u,(l^3-u^3)^{\frac{1}{3}})\,n(t,u)\,n(t,(l^3-u^3)^{\frac{1}{3}})\frac{\partial (l^3-u^3)^{\frac{1}{3}}}{\partial l}\,du\\
=& \int_0^{\infty} l^3\,\beta'(t,l,v)\,n(t,l)\,n(t,v)\,dv\\
&- \int_0^l \frac{u^3}{(l^3-u^3)^{\frac{2}{3}}}\,l^2\,\beta'(t,u,(l^3-u^3)^{\frac{1}{3}})\,n(t,u)\,n(t,(l^3-u^3)^{\frac{1}{3}})\,du\,. \qquad \text{(A.22)}
\end{aligned}$$

Let us define $(l^3-u^3)^{\frac{1}{3}}=w$, then

$$u^3 = l^3 - w^3 \quad \text{and} \quad du = \frac{-w^2}{(l^3-w^3)^{\frac{2}{3}}}\,dw\,. \qquad \text{(A.23)}$$

Now using (A.23) and keep in view the symmetry of β' function, we get

$$\begin{aligned}
&\int_0^l \frac{u^3}{(l^3-u^3)^{\frac{2}{3}}}\,l^2\,\beta'(t,u,(l^3-u^3)^{\frac{1}{3}})\,n(t,u)\,n(t,(l^3-u^3)^{\frac{1}{3}})\,du\\
&= \int_0^l \frac{l^3-w^3}{(l^3-w^3)^{\frac{2}{3}}}\,l^2\,\beta'(t,(l^3-w^3)^{\frac{1}{3}},w)\,n(t,w)\,n(t,(l^3-w^3)^{\frac{1}{3}})\,dw\,. \qquad \text{(A.24)}
\end{aligned}$$

This implies

$$\begin{aligned}
&\int_0^l \frac{u^3}{(l^3-u^3)^{\frac{2}{3}}}\,l^2\,\beta'(t,u,(l^3-u^3)^{\frac{1}{3}})\,n(t,u)\,n(t,(l^3-u^3)^{\frac{1}{3}})\,du\\
&= \frac{1}{2}\int_0^l \frac{l^3}{(l^3-u^3)^{\frac{2}{3}}}\,l^2\,\beta'(t,(l^3-u^3)^{\frac{1}{3}},u)\,n(t,(l^3-w^3)^{\frac{1}{3}})\,n(t,u)\,du\,. \qquad \text{(A.25)}
\end{aligned}$$

Finally (A.22) and (A.25) implies

$$\mathcal{K}^{\pm}_{\text{agg}} = -\frac{1}{l^3}\frac{\partial \tilde{\mathcal{F}}'_{\text{agg}}(t,l)}{\partial l} = \frac{l^2}{2}\int_0^l \frac{\beta'(t,(l^3-u^3)^{\frac{1}{3}},u)}{(l^3-u^3)^{\frac{2}{3}}}\, n(t,(l^3-w^3)^{\frac{1}{3}})\, n(t,u)\, du - \int_0^\infty \beta'(t,l,v)\, n(t,l)\, n(t,v)\, dv\,, \tag{A.26}$$

which comes out to the same equation as given by (2.27).

A.4 Equivalence of Equation (5.30) with (5.34)

In this section we want to show that equations (5.30) and (5.32) are equivalent with (5.34) and (5.37). For this purpose, we start with equations (5.34) and (5.37) and derive back equations (5.30) and (5.32). By taking the x-derivatives of $\tilde{\mathcal{F}}_{\text{agg}}(t,x,y)$ in (5.35), one gets by using the product rule:

$$\begin{aligned}\frac{\partial \tilde{\mathcal{F}}_{\text{agg}}}{\partial x}(t,x,y) =& \frac{\partial}{\partial x}\left(\int_0^x \int_{x-u}^\infty \int_0^\infty (u+y)\,\beta(t,u,y,v,w)\, f(t,u,y)\, f(t,v,w)\, dwdvdu\right)\\ =& \int_0^\infty \int_0^\infty (x+y)\,\beta(t,x,y,v,w)\, f(t,x,y)\, f(t,v,w)\, dwdv \\ &- \int_0^x \int_0^\infty (u+y)\,\beta(t,u,y,x-u,w)\, f(t,u,y)\, f(t,x-u,w)\, dwdu\,.\end{aligned} \tag{A.27}$$

Similarly the y-derivatives of $\tilde{\mathcal{G}}_{\text{agg}}(t,x,y)$ in (5.35) implies:

$$\begin{aligned}\frac{\partial \tilde{\mathcal{G}}_{\text{agg}}}{\partial y}(t,x,y) =& \frac{\partial}{\partial y}\left(\int_0^y \int_{y-v}^\infty \int_0^\infty (x+v)\,\beta(t,x,v,u,w)\, f(t,x,v)\, f(t,u,w)\, dwdudv\right)\\ =& \int_0^\infty \int_0^\infty (x+y)\,\beta(t,x,y,u,w)\, f(t,x,y)\, f(t,u,w)\, dwdu \\ &- \int_0^y \int_0^\infty (x+v)\,\beta(t,x,v,y-v,w)\, f(t,x,v)\, f(t,y-v,w)\, dwdv\,.\end{aligned} \tag{A.28}$$

Finally, the x and y-derivative of $\tilde{\mathcal{H}}_{\text{agg}}(t,x,y)$ gives:

$$\begin{aligned}
\frac{\partial^2 \tilde{\mathcal{H}}_{\text{agg}}}{\partial x \partial y}(t,x,y) =& \frac{\partial^2}{\partial x \partial y}\left(\int_0^x \int_0^y \int_{x-u}^{\infty} \int_{y-v}^{\infty} (u+v)\,\beta(t,u,v,w,z)\,f(t,u,v)\,f(t,w,z)\,dzdwdvdu\right) \\
=& \frac{\partial}{\partial y}\left(\int_0^y \int_0^{\infty} \int_{y-v}^{\infty} (x+v)\,\beta(t,x,v,w,z)\,f(t,x,v)\,f(t,w,z)\,dzdwdv\right. \\
& \left. - \int_0^x \int_0^y \int_{y-v}^{\infty} (u+v)\,\beta(t,u,v,x-u,z)\,f(t,u,v)\,f(t,x-u,z)\,dzdvdu\right) \\
=& \int_0^{\infty} \int_0^{\infty} (x+y)\,\beta(t,x,y,w,z)\,f(t,x,y)\,f(t,w,z)\,dzdw \\
& - \int_0^y \int_0^{\infty} (x+v)\,\beta(t,x,v,w,y-v)\,f(t,x,v)\,f(t,w,y-v)\,dwdv \qquad \text{(A.29)} \\
& - \int_0^x \int_0^{\infty} (u+y)\,\beta(t,u,y,x-u,z)\,f(t,u,y)\,f(t,x-u,z)\,dzdu \\
& + \int_0^x \int_0^y (u+v)\,\beta(t,u,v,x-u,y-v)\,f(t,u,v)\,f(t,x-u,y-v)\,dvdu\,.
\end{aligned}$$

By using equations (A.27), (A.28) and (A.29) in (5.34) we get after simplification

$$\begin{aligned}
(x+y)\frac{\partial f}{\partial t} =& \int_0^x \int_0^y (u+v)\,\beta(t,u,v,x-u,y-v)\,f(t,u,v)\,f(t,x-u,y-v)\,dvdu \\
& - \int_0^{\infty} \int_0^{\infty} (x+y)\,\beta(t,x,y,w,z)\,f(t,x,y)\,f(t,w,z)\,dzdw\,. \qquad \text{(A.30)}
\end{aligned}$$

Due to the symmetry of the kernel function, we have

$$\beta(t,x,y,x',y') = \beta(t,x',y',x,y)\,. \qquad \text{(A.31)}$$

By changing the integration variables, i.e. $x-u=w$ and $y-v=z$, in the second integral of (A.30) we obtain

$$\int_0^x \int_0^y (u+v)\,\beta(t,u,v,x-u,y-v)\,f(u,v)\,f(t,x-u,y-v)\,dvdu$$
$$= \int_0^x \int_0^y (x+y-(w+z))\,\beta(t,x-w,y-z,w,z)\,f(t,x-w,y-z)\,f(t,w,z)\,dzdw \quad \text{(A.32)}$$

which implies

$$\int_0^x \int_0^y (u+v)\,\beta(t,u,v,x-u,y-v)\,f(t,u,v)\,f(t,x-u,y-v)\,dvdu$$
$$= \frac{1}{2}\int_0^x \int_0^y (x+y)\,\beta(t,x-u,y-v,u,v)\,f(t,x-u,y-v)\,f(t,u,v)\,dvdu\,. \quad \text{(A.33)}$$

By replacing the second integral in (A.30) by (A.33) and canceling the term $(x+y)$ on both sides of the equality, we get

$$\frac{\partial f}{\partial t} = \frac{1}{2}\int_0^x \int_0^y \beta(t,x-u,y-v,u,v)\,f(t,x-u,y-v)\,f(t,u,v)\,dvdu$$
$$- \int_0^\infty \int_0^\infty \beta(t,x,y,u,v)\,f(t,x,y)\,f(t,u,v)\,dvdu \quad \text{(A.34)}$$

which comes out to be the same as equations (5.30) and (5.32). One can reverse these steps. This gives the equivalence.

A.5 Approximation of Equation (5.38)

Here, we explain the numerical approximation of (5.38) with (5.46). Let us start with equation (5.38), we have

$$\mathcal{F}(t,x,y) = \int_0^x \int_{x-u}^{R_x} \int_0^{R_y} (u+y)\,\beta(t,u,y,v,w)\,f(t,u,y)\,f(t,v,w)\,dwdvdu\,,$$
$$= \int_0^x \int_0^{R_y} \int_{x-u}^{R_x} (u+y)\,\beta(t,u,y,v,w)\,f(t,u,y)\,f(t,v,w)\,dvdwdu\,. \quad \text{(A.35)}$$

The above equation at the cell interface can be written as

$$\mathcal{F}(t)_{i+1/2,j} = \int_0^{x_{i+1/2}} (u+y_j) f(t,u,y_j) \int_0^{R_y} \int_{x_{i+1/2}-u}^{R_x} \frac{\beta(t,u,y_j,v,w)}{v+w} (v+w) f(t,v,w)\, dvdwdu\,. \tag{A.36}$$

According to our definition $\tilde{f}(t,x,y) := (x+y)\cdot f(t,x,y)$. Using this definition in the above equation we get

$$\mathcal{F}(t)_{i+1/2,j} = \int_0^{x_{i+1/2}} \tilde{f}(t,u,y_j) \int_0^{R_y} \int_{x_{i+1/2}-u}^{R_x} \frac{\beta(t,u,y_j,v,w)}{v+w} \tilde{f}(t,v,w)\, dvdwdu\,. \tag{A.37}$$

Let us omit the time variable for simplicity. Then for each $-1 \le i \le N_x$, we have

$$\mathcal{F}_{i+1/2,j} = \sum_{k=0}^{i} \int_{C_{k,j}} \tilde{f}(u,y_j) \int_0^{R_y} \int_{x_{i+1/2}-u}^{R_x} \frac{\beta(u,y_j,v,w)}{v+w} \tilde{f}(v,w)\, dvdwdu\,. \tag{A.38}$$

In the current finite volume scheme $\tilde{f}(x,y)$ is a conservative variable which is taken as the cell averaged values $\tilde{f}_{i,j}$ in each cell $C_{i,j}$. Keeping in view $\tilde{f}_{i,j}$ as the cell averaged values, we obtain from (A.38)

$$\begin{aligned}\mathcal{F}_{i+1/2,j} = &\sum_{k=0}^{i} \Delta x_k \tilde{f}_{k,j} \sum_{m=0}^{N_y} \Delta y_m \left\{ \int_{x_{i+1/2}-x_k}^{\alpha_{i,k}-1/2} \frac{\beta(x_k,y_m,x',y_j)}{x'+y_j} dx' \tilde{f}_{\alpha_{i,k}-1,m} \right. \\ &\left. + \sum_{l=\alpha_{i,k}}^{N_x} \int_{C_{lj}} \frac{\beta(x_k,y_m,x',y_j)}{x'+y_j} dx' \tilde{f}_{l,m} \right\}. \end{aligned} \tag{A.39}$$

By using the symmetry of aggregation kernel β and rearranging the terms in the brackets, we get

$$\begin{aligned}\mathcal{F}_{i+1/2,j} = &\sum_{k=0}^{i} \Delta x_k \tilde{f}_{k,j} \sum_{m=0}^{N_y} \Delta y_m \left\{ \sum_{l=\alpha_{i,k}}^{N_x} \int_{C_{lj}} \frac{\beta(x',y_j,x_k,y_m)}{x'+y_j} dx' \tilde{f}_{l,m} \right. \\ &\left. + \int_{x_{i+1/2}-x_k}^{\alpha_{i,k}-1/2} \frac{\beta(x',y_j,x_k,y_m)}{x'+y_j} dx' \tilde{f}_{\alpha_{i,k}-1,m} \right\}. \end{aligned} \tag{A.40}$$

Here, the integer $\alpha_{i,k}$ corresponds to the index of the cell such that $x_{i+1/2} - x_k \in C_{\alpha_{i,k}-1,j}$. Similarly one can derive the approximations (5.47) and (5.48) of the integrals given by (5.39) and (5.40), respectively.

Appendix B

Analytical Solutions

B.1 Simultaneous Growth and Aggregation

There are several combinations of growth rates and aggregation kernels where analytical solutions are available. These solution were derived by Ramabhadran et. al [98]. Since two simultaneous processes are taking place, the dynamics of the particle size distribution depends on two characteristic times, one for aggregation and other for growth. The ratio of these two times is the basic dimensionless parameter of the problem. Let us define Λ as the ratio of the characteristic times of growth and aggregation. The analytical solution for two initial distribution and different combinations of the growth and aggregation rates are given below.

Constant growth and constant aggregation: For the constant growth $G(x) = G_0$ and size independent aggregation kernel $\beta(x, x') = \beta_0$, the analytical solution with exponential initial distribution

$$f(0, x) := f_0(x) = \frac{N_0}{x_0} \exp\left(-\frac{x}{x_0}\right) \tag{B.1}$$

is given as

$$f(t, x) = \frac{M_0^2/M_1}{1 - 2\Lambda x_0 \left(\frac{N_0 - M_0}{M_1}\right)} \exp\left[-\frac{M_0}{M_1} \frac{\left(x - 2\Lambda x_0 \left(\frac{N_0}{M_0} - 1\right)\right)}{1 - 2\Lambda x_0 \left(\frac{N_0 - M_0}{M_1}\right)}\right], \tag{B.2}$$

where $\Lambda = \frac{G_0}{\beta_0 N_0 x_0}$. The moments M_0 and M_1 are given in Table 6.2.

For Gaussian-type initial distribution

$$f(0, x) := f_0(x) = \frac{N_0 x}{x_0^2} \exp\left(-\frac{x}{x_0}\right) \tag{B.3}$$

the analytical solution is given by

$$f(t,x) = \frac{M_0/x_0^2}{R(g1-g2)}\left(\exp\left[g_1\left(x-2\Lambda x_0\left(\frac{N_0}{M_0}-1\right)\right)\right] - \exp\left[g_2\left(x-2\Lambda x_0\left(\frac{N_0}{M_0}-1\right)\right)\right]\right). \tag{B.4}$$

Here $\Lambda = \frac{G_0}{\beta_0 N_0 x_0}$ and

$$\begin{aligned} g_1 &= -\frac{Q+\sqrt{Q^2-R}}{Rx_0}, \quad g_2 = -\frac{Q-\sqrt{Q^2-R}}{Rx_0}, \\ Q(x) &= \chi - \Lambda(\chi - 1 - \chi\ln\chi), \quad \chi = \frac{N_0}{M_0}, \\ R(\chi) &= \chi - (2\Lambda)^2\left[\chi(\chi-1-\ln\chi) - (\chi-1)^2\right]. \end{aligned} \tag{B.5}$$

Linear growth and constant aggregation: In case of linear growth $G(x) = G_0 x$ and size independent aggregation kernel $\beta(x,x') = \beta_0$, the analytical solution for exponential initial distribution (B.1) is given by

$$f(t,x) = \frac{M_0^2}{M_1}\exp\left(-\frac{M_0}{M_1}x\right). \tag{B.6}$$

For Gaussian-type initial distribution (B.3) the analytical solution is given as

$$f(t,x) = \frac{M_0^2}{M_1}\frac{1}{\sqrt{1-M_0/N_0}}\exp\left(-\frac{N_0 x}{M_1}\right)\sinh\left(\sqrt{1-\frac{M_0}{N_0}}\frac{N_0 x}{M_1}\right). \tag{B.7}$$

The moments M_0 and M_1 for this case are given in Table 6.2.

Linear growth and sum aggregation: For the case that $G(x) = G_0 x$ and $\beta(x,x') = \beta_0(x+x')$, the analytical solution for exponential initial distribution (B.1) is given as

$$f(t,x) = \frac{M_0}{x\sqrt{1-M_0/N_0}}\exp\left[-\frac{M_0}{M_1}\left(\frac{2N_0}{M_0}-1\right)x\right] I_1\left(2\sqrt{1-\frac{M_0}{N_0}}\frac{N_0 x}{M_1}\right), \tag{B.8}$$

where I_1 is the modified Bessel function of first kind of order one. The moments M_0 and M_1 for are given in Table 6.2.

B.2 Simultaneous Aggregation and Breakage

The analytical solutions for simultaneous aggregation and breakage are given by Patil and Andrews [82] for a special case where the total number of particles is constant. Later on the solutions were slightly simplified by Lage [51]. They considered a uniform binary

breakage $b(x, x') = 2/x'$, linear selection function $S(x) = S_0 x$, a constant aggregation kernel $\beta(x, x') = \beta_0$ and two types of initial distributions.

The first initial distribution is given by

$$f(0, x) = M_0 \cdot \frac{M_0}{M_1} \exp\left(-\frac{M_0}{M_1} x\right) . \tag{B.9}$$

It can be proved that the total number is constant by choosing the values of the problem parameters to satisfy $\sqrt{2S_0 M_1/\beta_0} = M_0$. Here, M_0 and M_1 represent the zero and first moments, respectively. The analytical solution has the form

$$f(t, x) = \frac{M_0^2}{M_1} \exp\left(-\frac{M_0}{M_1} x\right) . \tag{B.10}$$

The second initial distribution has the form

$$f(0, x) = M_0 \left(\frac{M_0}{M_1}\right)^2 x \, \exp\left(-2\frac{M_0}{M_1} x\right) \tag{B.11}$$

which has analytical solution

$$f(t, x) = \frac{M_0^2}{M_1} \, \Phi(\tau, \zeta) \, , \tag{B.12}$$

where

$$\Phi(\tau, \zeta) = \sum_{i=1}^{2} \frac{K_1(\tau) + p_i K_2(\tau)}{L_1(\tau) + 4p_i} \exp(p_i \zeta) \, , \quad \forall \, \tau > 0 \, . \tag{B.13}$$

Here $\tau = M_0 \beta_0 \, t$ and $\zeta = \frac{x \, M_0}{M_1}$. Moreover

$$K_1(\tau) = 7 + \tau + \exp(-\tau) \, , \tag{B.14}$$
$$K_2(\tau) = 2 - 2 \exp(-\tau) \, , \tag{B.15}$$
$$L_1(\tau) = 9 + \tau - \exp(-\tau) \, , \tag{B.16}$$
$$p_1 = \frac{1}{4}[\exp(-\tau) - \tau - 9] + \frac{1}{4}\sqrt{d(\tau)} \, , \tag{B.17}$$
$$p_2 = \frac{1}{4}[\exp(-\tau) - \tau - 9] - \frac{1}{4}\sqrt{d(\tau)} \, , \tag{B.18}$$

where

$$d(\tau) = \tau^2 + [10 - 2 \exp(-\tau)]\tau + 25 - 26 \exp(-\tau) + \exp(-2\tau) \, . \tag{B.19}$$

B.3 Simultaneous Aggregation and Nucleation

The analytical solution for the first two moments of this problem are reported by Alexopoulos and Kiparissides [3]. The analytical solutions for the zero initial population with a constant aggregation kernel and a constant nucleation rate are given by

$$M_0(t) = \tilde{\eta}\, \tanh\left(\tilde{\eta}\tau/2\right)\,, \quad M_1(t) = \sigma\,\tau\,, \tag{B.20}$$

where

$$\sigma = B_0/(\beta_0\, N_0^2)\,, \quad \tau = M_0(0)\beta_0\, t \quad \text{and} \quad \tilde{\eta} = \sqrt{2\sigma}\,.$$

Appendix C

Nomenclature

Abbreviations

CSD	crystal size distribution
FVS	finite volume schemes
MOC	method of characteristics
PBE	population balance equation
PBM	population balance model
PDE	partial differential equation
PSD	particle size distribution
TVD	total variation diminishing
ODE	ordinary differential equation

Latin Symbols

$\mathcal{B}$	birth term	$m^{-3}s^{-1}$
B_{nuc}	volume based nucleation rate	s^{-1}
B_0	nucleation rate at minimum particle size	s^{-1}
b	volume based breakage function	m^{-3}
b'	length based breakage function	m^{-3}
c	solution concentration	kgm^{-3}
c_p	specific heat capacity of solvent	J/K
c_{sat}	saturated concentration	kgm^{-3}
c_{mat}	metastable concentration	kgm^{-3}
$\mathcal{D}$	death term	$m^{-3}s^{-1}$
$\mathcal{D}_{\text{dis}}$	dissolution rate	$m^{-3}s^{-1}$
$\tilde{\mathcal{F}}_{\text{agg}}$	volume based aggregation flux	m^3s^{-1}
$\tilde{\mathcal{F}}_{\text{break}}$	volume based breakage flux	m^3s^{-1}
$\tilde{\mathcal{F}}'_{\text{agg}}$	length based aggregation flux	ms^{-1}
$\tilde{\mathcal{F}}'_{\text{break}}$	length based breakage flux	ms^{-1}

Latin Symbols (Continued)

f	volume base number function	m^{-3}
f_0	initial volume based distribution	m^{-3}
f_{in}	number density of inflow particles	m^{-3}
f_{out}	number density of outflow particles	m^{-3}
$\tilde{f}$	volume density function	$-$
$\tilde{f}_0$	initial volume density function	$-$
G	volume based growth rate	$m^3 s^{-1}$
G'	length based growth rate	$m \cdot s^{-1}$
ΔH_c	heat of crystallization	kg/Kg
h	death function	$-$
$\mathcal{K}^{+}_{\text{nuc}}$	length based nucleation term	$m^{-1}s^{-1}$
$\mathcal{K}^{\pm}_{\text{agg}}$	length based aggregation term	$m^{-1}s^{-1}$
$\mathcal{K}^{\pm}_{\text{break}}$	length based nucleation term	$m^{-1}s^{-1}$
$k_b^{(k)}$	nucleation rate constant of component k	$-$
k_g	growth rate constant	$-$
k_v	volume shape factor	$-$
L	length of dissolution unit (pipe)	m
$\mathbf{l}$	particle length coordinate vector	m
l	internal length coordinate	m
$\tilde{l}$	length coordinate in moving mesh	m
$\overline{l}$	mean size of the crystal	m
M_0	Total number of particles	$-$
M_1	Total volume of particles	m^3
$m^{(k)}$	mass of component k	kg
m_w	mass of water	kg
$\dot{m}_{in}^{(k)}$	incoming mass of component k	$kg \cdot min{-}1$
$\dot{m}_{out}^{(k)}$	outgoing mass of component k	$kg \cdot min{-}1$
$\mathcal{Q}^{+}_{\text{nuc}}$	volume based nucleation term	$m^{-3}s^{-1}$
$\mathcal{Q}^{\pm}_{\text{agg}}$	volume based aggregation term	$m^{-3}s^{-1}$
$\mathcal{Q}^{\pm}_{\text{break}}$	volume based nucleation term	$m^{-3}s^{-1}$
$\dot{\mathcal{Q}}_{\text{in}}$	inflow rate	$m^{-3}s^{-1}$
$\dot{\mathcal{Q}}_{\text{out}}$	outflow rate	$m^{-3}s^{-1}$
N	Total number of mesh points	$-$
n	length base number function	m^{-1}
n_0	initial length based distribution	$-$

Latin Symbols (Continued)

r	radius of dissolution unit (pipe)	m
S	relative supersaturation	$-$
$S^{(k)}$	relative supersaturation for enatiomers	$-$
T	temperature	C^o
T_c	cooling temperature	C^o
t	time	s
$U\,A_c$	heat coefficient·heat transfer area	$J/(s\,K)$
V	volume of the system	m^3
$\dot{V}_{\text{in}}$	volumetric inlet flow rate	$m^3 s^{-1}$
$\dot{V}_{\text{out}}$	volumetric outlet flow rate	$m^3 s^{-1}$
$\dot{V}$	volumetric flux rate	$m^3 \cdot min^{-1}$
$\mathbf{v}$	velocity vector	m/s
$w^{(k)}$	weight fraction	kg/kg
$w_{eq}^{(k)}$	equilibrium weight fraction	kg/kg
$\mathbf{x}$	particle state vector	m^3
x	internal volume coordinate	m^3

Greek Symbols

β	volume based aggregation kernel	s^{-1}
β'	length based aggregation kernel	s^{-1}
μ_3	third moment of component of $n(t,l)$	m^3
$\mu_3^{(k)}$	third moment of component of $n^{(k)}(t,l)$	m^3
ρ_c	density of crystals	kg/m^3
ρ_s	density of solvent	kg/m^3
τ_1	residence time in crystallizer	min
τ_2	residence time in pipe	min
$\xi\,,\eta$	volume coordinates in 2D	m^3
ω	monitor function	$-$

Subscripts and Superscripts

A	crystallizer A
agg	agglomeration
B	crystallizer B
break	breakage
c	counter (unseeded) enantiomer
dis	dissolution
in	inflow of crystallizer
liq	liquid phase
mat	metastable
nuc	nucleation
p	preferred (seeded) enantiomer
sat	saturation
out	outflow of crystallizer

Exponents

b	exponent of nucleation rate m^{-3}	
$b^{(k)}$	exponent of nucleation rate for component k	$-$
g	exponent of growth rate	$-$
$g^{(k)}$	exponent of growth rate for component k	$-$

Bibliography

[1] Abramowitz, M., Stegun, I. A., Handbook of mathematical functions with Formulas, Graphs, and Mathematical Tables, New York: Dover, (1972).

[2] Ain, Q., Qamar, S., Warnecke, G., A high resolution space-time conservative method for nonlinear hyperbolic conservation laws, accepted in *Int. J. Comput. Methods (IJCM)*, (2006).

[3] Alexopoulos, A. H., Kiparissides, C. A., Part II: Dynamic evolution of the particle size distribution in particulate processes undergoing simultaneous particle nucleation, growth and aggregation, *Chem. Eng. Sci.*, **60**, (2005), 4157-4169.

[4] Alvarez-Rodrigo, A., Lorenz, H., and Seidel-Morgenstern, A., Online monitoring of preferential crystallization of enantiomers, *Chirality*, **16**, (2004), 499-508.

[5] Amann, H., Ordinary differential equations: An introduction to nonlinear analysis, Walter de Gruyter, Berlin-New York, (1990).

[6] Angelov, I., Raisch, J., Elsner, M. P., Seidel-Morgenstern, A., Optimal operation of enantioseparation by batch-wise preferential crystallization, accepted in the special issue of *Chem. Eng. Sci.*, (2006).

[7] Barrett, J. C., Jheeta, J. S., Improving the accuracy of the moments method for solving the aerosol general dynamic equation *J. Aerosol Sci.*, **27**, (1996), 1135-1142.

[8] Bolley, C., Crouzeix, M., Conservation de la positivité lors de la discrétisation des problémes d'évolution paraboliques, *R.A.I.R.O Analyse Numérique*, **12**, (1978), 237-245.

[9] Bourgade, J. -P., Filbet, F., Convergence of a finite volume scheme for the coagulation-fragmentation equations, accepted in *Maths. of Comp.*, (2007).

[10] Bubovskii, P. B., Galkin, V. A., Stewart, I. W., Exact solutions for the coagulation-fragmentation, *Journal of Physics A: Mathematical and General*, **25**, (1992), 4737-4744.

[11] Chang, S. C., The method of space time conservation element and solution element -A new approach for solving the Navier Stokes and Euler equations, *J. Comput. Phys.*, **119**, (1995), 295-324.

[12] Chang, S. C., Wang, X. Y. and Chow, C. Y., The space-time conservation element and solution element method: A new high resolution and genuinely multidimensional paradigm for solving conservation laws, *J. Comput. Phys.* , **156**, (1999), 89-136.

[13] Daniele, L. M., Dennis, R. V., Rodney, O. F., Quadrature method of moments for aggregation-breakage processes, *J. Colloid Interface Sci.*, **258**, (2003), 322-334.

[14] David, L. M., Danesh, K. T., and Richard D. B., High-resolution simulation of multi-dimensional crystal growth, *Ind. Eng. Chem. Res.*, **41**, (2002), 6217-6223.

[15] David, R., Villermaux, J., Marchal, P., Klein, J. P., Crystallization and precipitation engineering-IV. Kinetic model to adipic acid crystallization, *Chem. Eng. Sci.*, **46**, (1991), 1129-1136.

[16] Dreyer, W., Qamar, S., Kinetic flux-vector splitting schemes for the hyperbolic heat conduction, *J. Comput. Phys.*, **198**, (2004), 403-423.

[17] Dreyer, W., Qamar, S., Second order accurate explicit finite volume schemes for the solution of Boltzmann-Peierls equation, *J. Appl. Math. Mech.*, **85**, (2005), 4-22.

[18] Dubovskiĭ, P. B., Stewart, I. W., Existence, uniqueness and mass conservation for the coagulation-fragmentation equation, *Math. Methods Appl. Sci.*, **19**, (1996), 571-591.

[19] Elsner, M. P., Lorenz, H., and Seidel-Morgenstern, A., Preferential crystallization for enantioseparation - New experimental insights indispensable for a theoretical approach and an industrial application, *10th International Workshop on Industrial Crystallization* BIWIC 2003, Mainz Verlag, ISBN-10:3861301989, (2003), 18-25.

[20] Elsner, M. P., Fernández Menéndez, D., Alonso Muslera, E., and Seidel-Morgenstern, A., Experimental study and simplified mathematical description of preferential crystallization, *Chirality*, **17**, (2005), 183-195.

[21] Ernst, M. H., Ziff, R. M., Hendriks, E. M., Coagulation processes with a phase transition, *J. Colloid Interface Sci.*, **97**, (1984), 266-277.

[22] Everson, R. C., Eyre, D., Campbell, Q. P., Spline method for solving continuous batch grinding and similarity equations, *Comp. & Chem. Eng.*, **21**, (1997), 1433-1440.

[23] Filbet, F., Laurençot, P., Numerical simulation of the Smoluchowski coagulation equation, *SIAM J. Sci. Comput.*, **25**, (2004), 2004-2048.

[24] Filbet, F., Laurençot, P., Mass-conserving solutions and non-conservative approximation to the Smoluchowski coagulation equation, *Archiv der Mathematik*, **30**, (2004), 558-567.

[25] Gelbard, F., Seinfeld, J. H., Coagulation and growth of a multicomponent aerosol, *J. Colloid Interface Sci.*, **63**, (1978), 357-375.

[26] Gelbard, F., Tambour, Y., and Seinfeld, J. H., Sectional representations for simulating aerosol dynamics, *J. of Colloid and Interface Sci.*, **76**, (1980), 541-556.

[27] Gerstlaur, A., Herleitung und Reduktion populationsdynamischer Modelle am Beispiel der Flüssig-Flüssig-Extrakion, Ph.D. thesis, University of Stutgart, Germany, (1999).

[28] Gunawan, R., Fusman, I., Braatz, R. D., High resolution algorithms for multidimensional population balance equations, *AIChE J.*, **50**, (2004), 2738-2749.

[29] Gunawan, R., Ma, D. L., Fujiwara, M., Braatz, R. D., Identification of kinetic parameters in a multidimensional crystallization process, *Int. J. Mod. Phys. B*, **16**, (2002), 367.

[30] Hill, P. J., Ng, K. M., New discretization procedure for the breakage equation, *AIChE J.*, **41**, (1995), 11204-1216.

[31] Hounslow, M. J., A discretized population balance for continuous systems at steady-state, *AIChE J.*, **36**, (1990), 106-116.

[32] Hounslow, M. J., Pearson, J. M. K., Instone, T., Tracer studies of high shear granulation: Population balance modeling, *AIChE J.*, **47**, (2001), 1984-1999.

[33] Hounslow, M. J., Ryall, R. L., Marshall, V. R., A discretized population balance for nucleation, growth, and aggregation, *AIChE J.*, **34**, (1988), 1821-1832.

[34] Hounslow, M. J., Wynn, E. J. W., Short-cut models for particulate processes, *Comp. & chem. Eng.*, **17**(**5**/**6**), (1993), 505-516.

[35] Hulburt, H. M., Katz, S., Some problems in particle technology, *Chem. Eng. Sci.*, **19**, (1964), 555-574.

[36] Hundsdorfer, W. H., Koren, B., Verwer, J. G., A positive finite-difference advection scheme applied on locally refined grids, Department of Numerical Mathematics, NM-R9309, ISSN: 0169-0388, (1993).

[37] Hundsdorfer, W. H, Verwer, J. G., Numerical solution of time-dependent advection-diffusion-reaction equations, Springer-Verlag, New York, First Edition, (2003).

[38] Immanuel, C. D., Doyle III, F. J., Computationally-efficient solution of population balance models incorporating nucleation, growth, and coagulation, *Chem. Eng. Sci.*, **58**, (2003), 3681-3698.

[39] Kim, Y. P., Seinfeld, J. H., Simulation of multicomponent aerosol dynamics, *J. Colloid Interface Sci.*, **149**, (1992), 425-449.

[40] Koren, B., A robust upwind discretization method for advection, diffusion and source terms. In C. B. Vreugdenhil, B. Koren, editors, *Numerical Methods for Advection-Diffusion Problems*, Volume 45 of Notes on Numerical Fluid Mechanics, chapter 5, pages 117-138, Vieweg Verlag, Braunschweig, (1993).

[41] Kostoglou, M., Karabelas, A. J., An assessment of low-order methods for solving the breakage equation, *Powder Technology*, **127**, (2002), 116-127.

[42] Kostoglou, M., Karabelas, A. J., Optimal low order methods of moments for solving the fragmentation equation, *Powder Technology*, **143 – 144**, (2004), 116-127.

[43] Kraaijevanger, J. F. B. M., Absolute monotonicity of polynomials occurring in the numerical solution of initial value problems, *Num. Math.*, **48**, (1986), 303-322.

[44] Kumar, J., Numerical approximations of population balance equations in particulate systems, Ph.D. thesis, Faculty of Mathematics, Otto-von-Guericke University, (2006).

[45] Kumar, J., Peglow, M., Warnecke, G., Heinrich, S., Mörl, L., A discretized model for tracer population balance equation: Improved accuracy and convergence, *Coput. Chem. Eng.*, **30**, (2006), 1278-1292.

[46] Kumar, J., Peglow, M., Warnecke, G., Heinrich, S., Mörl, L., Improved accuracy and convergence of discretized population balances: The cell average technique, *Chem. Eng. Sci.*, **61**, (2006), 3327-3342.

[47] Kumar, S., Ramkrishna, D., On the solution of population balance equations by discretization -I. A fixed pivot technique, *Chem. Eng. Sci.*, **51**, (1996), 1311-1332.

[48] Kumar, S., Ramkrishna, D., On the solution of population balance equations by discretization -I. A moving pivot technique, *Chem. Eng. Sci.*, **51**, (1996), 1333-1342.

[49] Kumar, S., Ramkrishna, D., On the solution of population balance equations by discretization -III. Nucleation, growth and aggregation of particles, *Chem. Eng. Sci.*, **52**, (1997), 4659-4679.

[50] Kurganov, A., Tadmor, E., New high-resolution central schemes for nonlinear conservation laws and convection-diffusion equations, *J. Comput. Phys.*, **160**, (2000), 241-282.

[51] Lage, P. L. C., Comments on the "An analytical solution to the population balance equation with coalescence and breakage-the special case with constant number of particles", by D. P. Patil and J. R. G Andrews, *Chem. Eng. Sci.*, **57**, (2002), 4253-4254.

[52] Lapidus, L., Pinder, G. F., Numerical solutions of partial differential equations in science and engineering, Wiley, New York, U.S.A., (1982).

[53] Laurenzi, I. J., Bartels, J. D., Diamond, S. L., A general algorithm for exact simulation of multicomponent aggregation processes, *J. Comput. Phys.*, **177**, (2002), 418-449.

[54] Lee, K., Matsoukas, T., Simultaneous coagulation and breakage using constant -N Monte Carlo, *Powder Technology*, **110**, (2000), 82-89.

[55] van Leer, B., Upwind-difference methods for aerodynamic problems governed by the Euler equations. In B.E. Enguist, S. Osher, and R.C.J. Somerville, editors, *Large-scale computations in fluid mechanics*, pages 327-336. AMS Series, American Mathematical Society, Providence, RI, (1985).

[56] Leonard, B. P. and Niknafs, H. S., Sharp monotonic resolution of discontinuities without clipping of narrow extrema, *Computers & Fluids*, **19**, (1991), 141-154.

[57] LeVeque, R. J., *Numerical methods for conservation laws*, Birkhäuser Verlag, Bassel, Germany (1992).

[58] LeVeque, R. J., Finite volume methods for hyperbolic problems, Cambridge Univ. Press, New York, NY (2002).

[59] LeVeque, R. J., Mihalas, D., Dorfi, E. A., Müller, E., *Computational methods for astrophysical fluid flow*, Springer-Verlag, Berlin, Germany (1998).

[60] Leyvraz, F., Tschudi, H. R., Singularities in the kinetics of coagulation processes, *J. Phys. A*, **14**, (1981), 3389-3405.

[61] Lim, Y. I., Lann,J-M. L., Meyer,X. M., Joulia, X., Lee, G. and Yoon, E. S., On the solution of population balance equation (PBE) with accurate front tracking method in practical crystallization processes, *Chem. Eng. Sci.* , **57**, (2002), 3715-3732.

[62] Litster, J. D., Smith, D. J., and Hounslow, M. J., Adjustable discretized population balance for growth and agglomeration, *AIChE J.*, **41**, (1995), 591-603.

[63] Lorenz, H., Perlberg, A., Sapoundjiev, D., Elsner, M. P., Seidel-Morgenstern, A., Crystallization of enantiomers, *Chem. Eng. Proc.*, **45**, (2006), 863-873.

[64] Lushnikov, A. A., Evolution of coagulating systems III. Coagulating mixtures, *J. Colloid Interface Sci.*, **54**, (1976), 94-101.

[65] Ma, A., Tafti, D. K., and Braatz, R. D., Optimal control and simulation of multidimensional crystallization processes, *Comp. & Chem. Eng.*, **26**, (2002), 1103-1116.

[66] Ma, A., Tafti, D. K., and Braatz, R. D., High resolution simulation of multidimensional crystal growth, *Ind. Eng. Chem. Res.*, **41**, (2002), 6217-6223.

[67] Madras, G., McCoy, B. J., Reversible crystal growth-dissolution and aggregation breakage: Numerical and moment solutions for population balance equations, *Powder Technology*, **143 − 144**, (2004), 297-307.

[68] Maisels, A., Kruis, F. E., Fissan, H., Direct Monte Carlo simulations of coagulation and aggregation, *J. Aerosol Sci., Suppl.*, **30**, (1999), S417-S418.

[69] Makino, J., Fukushige, T., Funato, Y., Kokubo, E., On the mass distribution of planetesimal in the early runaway stage, *New Astronomy*, **3**, (1998), 411-417.

[70] Marchal, P., David, R., Klein, J. P., Villermaux, J., Crystallization and precipitation engineering I: An efficient method for solving population balance in crystallization with agglomeration, *Chem. Eng. Sci.*, **43**, (1988), 59-67.

[71] Marchisio, D. L., Vigil, R. D., Fox, R. O., Quadrature method of moments for aggregation-breakage processes, *J. Colloid Interface Sci.*, **258**, (2003), 322-334.

[72] Mattheij, R. M. M, Molenaar, J., *Ordinary differential equations in theory and practice*, John Wiley & Sons, Chichester-New York-Brisbane-Toranto-Singapore, (1997).

[73] McGraw, Description of aerosol dynamics by the quadrature method of moments, *Aer. Sci. Tech.*, **27**, (1997), 255-265.

[74] Mersmann, A., *Crystallization Technology Handbook*, Marcel Dekker, Inc., Second Edition, (2001).

[75] Miller, S. M., Rawlings, J. B., Model identification and quality control strategies for batch cooling crystallizers, *AIChE J.*, **40**, (1994), 1312-1327.

[76] Mishra, B. K., Monte Carlo simulation of particle break process during grinding, *Powder Technology*, **110**, (2000), 246-252.

[77] Motz, S., Mitrović, A., Gilles, E. D., Comparison of numerical methods for the simulation of dispersed phase systems, *Chem. Eng. Sci.*, **57**, (2002), 4329-4344.

[78] Muhr, H., David, J., Villermaux, J., and Jezequel, P. H., Crystallization and precipitation engineering VI: Solving population balance in the case of the precipitation of Silver Bromide crystals with high primary nucleation rate by using first order upwind differentiation, *Chem. Eng. Sci.*, **51**, (1996), 309-319.

[79] Nessyahu, H., Tadmor, E., Non-oscillatory central differencing fo hyperbolic conservation Laws, *SIAM J. Comput. Phys.* **87**, (1990), 408-448.

[80] Nicmanis, M., Hounslow, M. J., Finite element methods for steady-state population balance equations, *AIChE J.*, **44**, (1998), 2258-2272.

[81] Patankar, S. V., Numerical heat transfer and fluid flow, Hemisphere, New York, (1980).

[82] Patil, D. P., Andrews, J. R. G., An analytical solution to continuous population balance model describing floc coalescence and breakage, *Chem. Eng. Sci.*, **53**, (1998), 599-601.

[83] Perlberg, A., Untersuchungen zum Einfluss des Gegenenantiomers bei der enantioselektiven Krystallisation aus Lösungen, Ph.D. thesis, Otto-von-Guericke University Magdeburg, (2006).

[84] Perry, R-H., Green, D. W., editors, Perry's chemical engineers' handbook, McGraw-Hill, New York, Seventh Edition, 1997.

[85] Qamar, S., Warnecke, G., Simulation of multicomponent flows using high order central schemes, *Appl. Num. Math.*, **50**, (2004), 183-201.

[86] Qamar, S., Warnecke, G., A high order kinetic flux-spitting method for the special relativistic magnetohydrodynamics, *J. Comput. Phys.*, **205**, (2005), 182-204.

[87] Qamar, S., Warnecke, G., Application of space-time CE/SE method to shallow water magnetohydrodynamics equations, *J. Comput. Appl. Math.*, **196**, (2006), 132-149.

[88] Qamar, S., Warnecke, G., A space-time conservative method for hyperbolic systems with stiff and non stiff source terms, *Commun. in Comput. Phys. (CiCP)*, **1**, (2006), 451-480.

[89] Qamar, S., Elsner, M.P., Angelov, I., Warnecke, G., Seidel-Morgenstern, A., A comparative study of high resolution schemes for solving population balances in crystallization, *Comp. & Chem. Eng.*, **30**, (2006), 1119-1131.

[90] Qamar, S., Warnecke, G., Solving population balance equations for two-component aggregation by a finite volume scheme, *Chem. Eng. Sci.*, **62**, (2006), 679-693.

[91] Qamar, S., Angelov, I., Elsner, M. P., Ashfaq, A., Seidel-Morgenstern, A., Warnecke, G., Numerical approximations of a population balance model for coupled batch preferential crystallizers, accepted in the special issue of *Appl. Num. Math.*, (2007).

[92] Qamar, S., Ashfaq, A., Elsner, M. P., Angelov, I., Warnecke, G., Seidel-Morgenstern, A., Adaptive high resolution schemes for multidimensional population balances in crystallization processes, *Comp. & Chem. Eng.*, **31**, (2007), 1296-1311.

[93] Qamar, S., Ashfaq, A., Angelov, I., Elsner, M. P., Warnecke, G., Seidel-Morgenstern, A., Numerical solutions of population balance models in preferential crystallization, *Chem. Eng. Sci.*, **63**, (2008), 1342-1352..

[94] Qamar, S., Warnecke, G., Numerical solution of population balance equations for nucleation growth and aggregation processes, *Comp. & Chem. Eng.*, **31**, (2007), 1576-1589.

[95] Qamar, S., Warnecke, G., Elsner, M. P., Numerical simulation of population balances for combined particulate processes, submitted to *Chem. Eng. Sci.*, (2007).

[96] Qamar, S., Warnecke, G., Analytical and numerical investigations of a batch crystallization model, accepted in *Comp. Appl. Math.*, doi:10.1016/j.cam.2007.12.012, (2008).

[97] Qamar, S., Warnecke, G., Elsner, M. P., Seidel-Morgenstern, A., A Laplace transformation based technique for reconstructing crystal size distributions regarding size independent growth, accepted in *Chem. Eng. Sci.*, (2008).

[98] Ramabhadran, T. E., Peterson, T. W., and Seinfeld, J. H., Dynamics of aerosol coagulation and condensation, *AIChE J.*, **22**, (1976), 840-851.

[99] Ramkrishna, D., Statistical models of cell populations, *Advances in Biochemical Engineering*, **11**, (1979), 1-47.

[100] Ramkrishna, D., The status of population balances, *Rev. chem. Eng.*, **3**(**1**), (1985), 49-95.

[101] Ramkrishna, D., *Population Balances: Theory and applications to particulate systems in engineering*, Academic Press, San Diego, CA (2000).

[102] Randolph, A., Larson., M. A., Theory of particulate processes, Academic Press, Inc., San Diego, CA, Second Edition, (1988).

[103] Rawling, J. B., Miller, S. M., Witkowski, W. R., Model identification and control of solution crystallization process, *Chem. Eng. Sci.*, **32**, (1993), 1275-1296.

[104] Rawling, J. B., Slink, C. W., Miller, S. M., Control of crystallization process, A. S. Myerson (Ed.), Handbook of Industrial Crystallization, Second ed., (2001), 201-230.

[105] Scott, W. T., Analytic studies of cloud droplet coalescence, *Journal of the Atmospheric Sciences*, **25**, (1968), 54-65.

[106] Shah, B. H., D. Ramkrishna, and J. D. Borwanker, Simulation of particulate systems using concept of the interval of quiescence, *AICHE J.*, **23**, (1977), 897-904.

[107] Shi, D., El-Farra, N. H., Li, M., Mhaskar, P., Christofides, P. D., Predictive control of particle Size distribution in particulate processes, *Chem. Eng. Sci.*, **61**, (2006), 268-281.

[108] Shi, D., P. Mhaskar, N. H. El-Farra, P. D. Christofides, Predictive control of crystal size distribution in protein crystallization, *nanotechnology*, **16**, (2005), 562-574.

[109] Singh, P. N., Ramkrishna, D., Solution of population balance equations by MWR, *Comp. & chem. Eng.*, **1**, (1977), 23-31.

[110] Smit, D. J., Hounslow, M. J., Paterson, W. R., Aggregation and gelation -I Analytical solutions for CST and batch operation, *Chem, Eng. Sci.*, **49**, (1994), 1025-1035.

[111] Song, M., Qiu, X. J., Alternative to the concept of the interval of quiescence (IQ) in the Monte Carlo simulation of population balances, *Chem. Eng. Sci.*, **54**, (1999), 5711-5716.

[112] Sun, N., Immanuel, C. D., Efficient solution of population balance models employing a hierarchical solution strategy based on a multi-level discretization, *Trans. Inst. Measurement and Control*, **27**, (2005), 347-366.

[113] Sweby, P. K., High resolution schemes using flux limiters for hyperbolic conservation laws, *SIAM J. Numer. Anal.*, **21**, (1984), 995-1011.

[114] Tang, H. -Z., Tang, T., Adaptive mesh methods for one- and two-dimensional hyperbolic conservation laws, *SIAM J. Numer. Anal.*, **41**, (2003), 487-515.

[115] Tang, T., Moving mesh methods for computational fluid dynamics, proceedings of the international conference on recent advances on adaptive computation, May 24-28, (2004), 141-173.

[116] Togkalidou, T., Fujiwara, M., Patel, S., Braatz, R. D., Solute concentration prediction using chemometrics and ATR-FTIR spectroscopy, *J. Cryst. Growth*, **231**, (2001), 534-543.

[117] Toro, E. F., Riemann solvers and numerical method for fluid dynamics, Second Edition, Springer-Verlag, (1999).

[118] Vale, H. M., Mckenna, T. F., Solution of the population balance equation for two-component aggregation by an extended fixed pivot technique, *Ind. Eng. Chem. Res.*, **44**, (2005), 7885-7891.

[119] Vanni, M., Discretization procedure for the breakage equation. *AIChE J.*, **45**, (1999), 916-919.

[120] Vanni, M., Approximate population balance equations for aggregation-breakage processes, *J. Colloid Interface Sci.*, **221**, (2000), 143-160.

[121] Vollmer, U., Control of crystallization based on population balances, Ph.D. thesis, Faculty of Electrical Engineering and Information Technology, Otto-von-Guericke University, (2005).

[122] Wulkow, M., Gerstauer, A., Nieken, U., Modeling and simulation of crystallization processes using PARSIVAL, *Chem, Eng. Sci.*, **56**, (2001), 2575-2588.

[123] Ziff, R. M., McGray, E. D., The kinetics of cluster fragmentation and depolymerization, *Journal of Physics A: Mathematical and General*, **18**, (1985), 3027-3037.

[124] Ziff, R. M., New solution to the fragmentation equation, *Journal of Physics A: Mathematical and General*, **24**, (1991), 2821-2828.